

Satellite remote sensing of aerosols using geostationary observations from MSG-SEVIRI

Citation for published version (APA):

Bennouna, Y. S. (2009). *Satellite remote sensing of aerosols using geostationary observations from MSG-SEVIRI*. [Phd Thesis 2 (Research NOT TU/e / Graduation TU/e), Applied Physics and Science Education, Universite du Sud Toulon - Var]. Technische Universiteit Eindhoven. <https://doi.org/10.6100/IR642972>

DOI:

[10.6100/IR642972](https://doi.org/10.6100/IR642972)

Document status and date:

Published: 01/01/2009

Document Version:

Publisher's PDF, also known as Version of Record (includes final page, issue and volume numbers)

Please check the document version of this publication:

- A submitted manuscript is the version of the article upon submission and before peer-review. There can be important differences between the submitted version and the official published version of record. People interested in the research are advised to contact the author for the final version of the publication, or visit the DOI to the publisher's website.
- The final author version and the galley proof are versions of the publication after peer review.
- The final published version features the final layout of the paper including the volume, issue and page numbers.

[Link to publication](#)

General rights

Copyright and moral rights for the publications made accessible in the public portal are retained by the authors and/or other copyright owners and it is a condition of accessing publications that users recognise and abide by the legal requirements associated with these rights.

- Users may download and print one copy of any publication from the public portal for the purpose of private study or research.
- You may not further distribute the material or use it for any profit-making activity or commercial gain
- You may freely distribute the URL identifying the publication in the public portal.

If the publication is distributed under the terms of Article 25fa of the Dutch Copyright Act, indicated by the "Taverne" license above, please follow below link for the End User Agreement:

www.tue.nl/taverne

Take down policy

If you believe that this document breaches copyright please contact us at:

openaccess@tue.nl

providing details and we will investigate your claim.

**Satellite Remote Sensing
of Aerosols
using Geostationary Observations
from MSG-SEVIRI**

Yasmine Bennouna

The work described in this thesis was performed at the TNO Defence, Security and Safety *Netherlands Organisation for Applied Scientific Research*, The Hague, The Netherlands, and financially supported by the *Netherlands Institute for Space Research (SRON)* (project number EO-077).

The PhD project was conducted in the framework of a dual-doctoral degree program between the *Eindhoven University of Technology (TUE)*, The Netherlands, and the *University of the South Toulon Var (USTV)*, France.

A catalogue record is available from the Eindhoven University of Technology Library

Bennouna, Yasmine Sarah
Satellite Remote Sensing of Aerosols using Geostationary Observations from MSG-SEVIRI

ISBN 978-90-386-1881-4

**Satellite Remote Sensing
of Aerosols
using Geostationary Observations
from MSG-SEVIRI**

PROEFSCHRIFT

ter verkrijging van de graad van doctor aan de
Technische Universiteit Eindhoven, op gezag van de
rector magnificus, prof.dr.ir. C.J. van Duijn, voor een
commissie aangewezen door het College voor
Promoties in het openbaar te verdedigen
op dinsdag 7 juli 2009 om 16.00 uur

door

Yasmine Sarah Bennouna

geboren te Rennes, Frankrijk

Dit proefschrift is goedgekeurd door de promotoren:

prof.dr. H.M. Kelder
en
prof.dr. J. Piazzola

Copromotor:
prof.dr. G. de Leeuw

Promotiecommissie: prof.dr.ir. K. Kopinga
Technische Universiteit Eindhoven, The Netherlands

prof.dr.ir. P.J.H. Builtjes
Free University of Berlin, Germany

dr.hab. M. Chami
University Pierre & Marie Curie, France

prof.dr. P. Levelt
Technische Universiteit Eindhoven, The Netherlands

prof.dr. P. Fraunie
University of the South Toulon-Var, France

Comme la vie n'a rien d'un long fleuve tranquille...
A vous tous qui me donnez des ailes,
pour poursuivre mon humble et petit bout de chemin...

”اعْمَلْ لِذُنُوبِكَ كَأَنَّكَ تَمُوتُ غَدًا،
تَتَقَفَّ كَأَنَّكَ تَعِيشُ أَبَدًا.“

*”Vis comme si tu devais mourir demain,
apprends comme si tu devais vivre toujours”*

*”Live as if you were to die tomorrow,
learn as if you were to live forever.”*

(Mahatma Gandhi)

Acknowledgements

Undoubtedly, nothing in life is worth living without the people we meet along the way.... Therefore the following words are meant to thank all the people who by their knowledge, skills, support, friendship, love and affection have somehow contributed to this little achievement in my life. The following text is written in French and/or in English depending whom it may concern.

Sans aucun doute, rien dans la vie ne vaudrait la peine d'être vécu sans les gens que l'on croise sur notre chemin... De fait, les mots qui suivent s'adressent à tous ceux qui par leurs connaissances, compétences, leur soutien, amitié, amour et affection, ont, d'une certaine manière, contribué à l'accomplissement de cette étape de ma vie. Le texte qui suit est écrit en Français et/ou en Anglais, selon les personnes concernées.

First of all, I am very grateful to all members of the PhD examining board for accepting and fulfilling this role.

In particular, I would like to express my gratitude to *Gerrit de Leeuw* who supervised my work during these four years. I am grateful that you gave me the opportunity to conduct this PhD at TNO. I have surely learned a lot from your experience. Despite the fact you left The Netherlands halfway through my PhD, we remained in close contact and you always kept track of my progress. Thank you for guiding me carefully through all steps until I could finally see "the light at the end of the tunnel"! Thanks for your patience when you were reading and correcting this manuscript and related articles.

Je voudrait aussi exprimer ma grande reconnaissance à *Jacques Piazzola* sans qui cette aventure n'aurait probablement jamais vu le jour. Je te remercie donc d'avoir pensé à moi et de m'avoir fait confiance, en m'introduisant auprès de *Gerrit*. Merci d'avoir continué à suivre de près mon travail malgré l'éloignement, et merci pour tes incessants encouragements. Tu t'es aussi toujours soucié de mon bien-être pendant ces quatre longues années, et tes attentions m'ont beaucoup touchée.

I would like to thank *Hennie Kelder* for making it possible to defend my thesis at the University of Eindhoven, for taking care of all the paperwork, and for taking the time to have regular meetings.

Thanks a lot to *Rob Roebeling* for his help and the fruitful discussions we had regarding cloud detection.

I could not resist to thank you *Duane*, for the wonderful experience you gave me a long while ago, and for your comprehension for the thesis work we did not carry out together... I guess it was just not the right time.... In the end I went back to my

first idea of doing a PhD though! Now I wish I could propose you: "Let's go for a second ride!", but as you can certainly understand, I think one PhD for one lifetime is enough... Thank you again for your kind support especially during the last few months.

I often think of a person I admired a lot: *Petra Udelhofen*, a researcher in atmospheric science. I will never forget her sudden departing that Spring... When I happen to look at clouds, I cannot help thinking I somehow get closer to her.

J'aimerais tout particulièrement remercier une personne qui a beaucoup compté dans les prémices de mon éducation scientifique. Il s'agit de mon professeur *Mme El Maïzi*, qui a guidé mes premiers pas en Physique, et qui est incontestablement pour beaucoup dans mes choix de carrière... J'espère qu'elle aura l'occasion de lire ces quelques mots un jour.

Since not much could have been achieved without efficient technical support, I would like to express my thanks to *Ronald Scharroo* for being so eager and able to solve my LINUX-related problems, and for gaining the upper hand over my computer!

I would like to thank *Connie van der Bijl* who printed my manuscript, for her help and patience when I was preparing the final printable version of my manuscript.

Jolanta, my dear roommate, I am very grateful for the long time we spent together in the same office. You were always willing to help, and you always had very good advice on both work and personal issues. It was such a pleasure to start every day with your morning smile, and there is nothing as such to start a good day!

Comme tu dis si bien *Lyana*, si "galère" certes il y a, heureusement "compagne de galère" il y a aussi! Tu m'as convaincue qu'il ne fallait pas rester sur une première impression, et que la patience récompensait celui qui cherche à apprivoiser... Je tâcherai de toujours m'en rappeler. Nos échanges ont été pour moi très enrichissants, j'ai appris beaucoup à tes côtés, et "la collègue" y est incontestablement pour beaucoup dans chaque étape du produit final.

Je dis un grand merci à mon compagnon du "LateX fan club", j'ai nommé *Mathieu*, qui fut un fervant joueur des devinettes LateX ces derniers mois! Bon courage à toi pour la suite et les futures "humeurs" de notre ami LateX.

Who said The Netherlands was a cold country? I owe so much to my "northern suns": *Myriam & Frank*, *Lyana* (you again) & *Menno*, *Benoît & Elise*, *Christophe & Daniela*, *Mauro*, *Giovanni*, *Jacqueline*, *Fanette*, *Marianne*, *Mathieu* (you again), *Ronald Poell*... You are like insidious factors aggravating the constant and dangerous advance of global warming that we had better pay attention to! Coffee breaks, never ending discussions, cozy evenings, dinners, concerts, surprise parties, and so much more to mention... It was my great pleasure to share a piece of your life in the Flat Country. Please never lose your smile, your spirit and profound generosity! May these suns shine forever, wherever you go.

Qui a dit qu'il faisait toujours gris au Plat Pays? Je dois beaucoup à tous mes soleils du Grand Nord, qui sont des facteurs du réchauffement climatique que la communauté scientifique devrait s'enquérir de surveiller de près: *Myriam & Frank*, *Lyana* (sous une autre casquette) & *Menno*, *Benoît & Elise*, *Christophe & Daniela*, *Mauro*, *Giovanni*, *Jacqueline*, *Marianne*, *Mathieu* (et oui encore toi), *Fanette*, *Ronald Poell*... Les pauses café, les soirées au coin du feu, les sorties, les dîners, les concerts,

les surprises parties...etc La liste est trop longue! Partager un bout de chemin auprès de vous fût un réel plaisir. Gardez précieusement votre sourire, votre bonne humeur, et cette générosité débordante qui nous inonde! Que ces soleils brillent toujours, ici ou ailleurs, là où vos chemins vous mèneront.

Parmi ces derniers se cachent mes anges gardiens (et un trio infernal) que je ne pouvais pas m'empêcher de réunir: *Lyana, Myriam et Benoît*. Quel mérite vous avez à m'avoir supportée (et surtout à m'avoir écoutée) pendant si longtemps! Je vous aime très fort, merci pour TOUT, vous savez bien...

Thanks to all other colleagues who brightened my stay at TNO: *Lex, Harm, Harald, Jan Olijslager, Eric van der Veen, Gertjan, Adam*, with special thoughts for people of the Acoustics Group who kindly adopted me for lunch and coffee breaks: *Simonette, Paul, Ton, Jeroen, Sander, Rene, Frans Peter, Peter, Lianke, Sander, Pieter, Jan Cees, Henri, Frank, Camiel*...etc.

A vous qui m'avez aimée dès le premier instant, qui m'avez appris, protégée et soutenue contre vents et marées... vous qui m'avez laissé m'envoler sans jamais pour autant me quitter des yeux... aucun mot ne saurait exprimer mon amour et ma gratitude envers vous mes chers parents. Et j'ai bien peur qu'une vie ne me suffise pas à vous rendre tout ce que vous m'avez déjà donné.

Merci ma soeur, tout simplement car tu demeureras la seule et unique soeur que j'aurai jamais *Sarah*. Tu n'oscutes peut-être pas les nuages, mais tu sembles si proche d'eux, comme eux tu rends nos vies plus légères et moins monotones! Je t'en prie reviens-nous vite...

Je remercie de tout mon coeur mes chers grands parents, *Michel & Suzanne* (alias *Papi & Mamie*), qui n'ont jamais cessé de veiller sur moi et de m'entourer de toute leur affection.

Cela va sans dire, comme tout un chacun la famille de coeur compte aussi pour beaucoup. Je pense entre autres à mes bien aimés "oncles" et "tantes": *Hamid & Khadija, Monique & Nouredine, Kamal & Leïla, Jalal & Latifa*, et toutes leurs petites familles que je considère comme miennes. Il y a aussi mes adorables "familles d'accueil" qui m'ont choyée comme leur propre fille: *Christine & Pascal, Dominique & Véronique, André & Edith*.

Ma tendre *Juliette*, ni la distance ni le temps n'ont eu raison de nous... Toi qui a toujours été fidèle aux rendez-vous hebdomadaires, et dont les mots ont souvent su consoler mes peines, apaiser mes peurs, mais aussi partager mes joies, mes rires et mes bonheurs. Tu sais déjà trop bien ce que je n'ai plus besoin de dire... alors comme on dit: pourvu que ça dure, et espérons-le, pour le meilleur!

Quand je pense à ma terre de coeur en Provence, je pense à d'autres amis qui me sont très précieux: *Marie* (jusqu'aux bouts du monde toujours elle m'a toujours retrouvée), *Tatiana & Greg* (sans oublier mon *Janny* et *Raphaël*), *Jean-Paul, Sophie & James, Isabelle & Matthieu* (celui d'Isa), *Karine & Pierre*. Il y a aussi plusieurs personnes de l'équipe du Labo de l'Université de Toulon, qui sont bien plus que de simples collègues: *Elena, Sabrina, Deborah, Clothilde, Tathy, Marc, et Romain*.

Je remercie aussi tous les amis de longue date qui repondent toujours présent à l'appel: *Fatim, Claire, Nada, Gaëlle, Ozlëm, et Oznür*. Après tout ce temps rien ne paraît avoir changé, et si vous saviez combien cela me comble! Un merci tout

particulier à *Fatim* qui s'est si gentiment attelée aux préparatifs de ma nouvelle vie, celle de "l'après-thèse". Muchas gracias a mi querida amiga por cuidarme desde los primeros momentos de mi nueva vida en España.

Enfin, je voudrais aussi remercier tous ceux qui seront présents ce fameux jour J, je serais très touchée de les savoir à mes côtés. Mes sincères excuses à tous ceux que je pourrais avoir oubliés sur le papier, et merci quand même...

Finally, I would like to thank all the people who will attend this defense the D-day, I will be touched to have them beside me. My sincere apologies to people I may have forgotten to mention, many thanks to you too...

En (pas si) bref:

In (not so) short:

Merci beaucoup,

Thanks a lot,

Dan u wel,

Muchas gracias,

Gracie mille,

شُكْرًا جَدًّا،

Un manuscript de thèse n'est pas seulement le fruit d'un travail, c'est également un accomplissement personnel dans une belle aventure humaine. On est rien seule, cette thèse n'est donc pas mienne, elle est nôtre!

A thesis is not only the results of long and hard work, it is a great human adventure. We are nothing alone, hence this thesis is not mine but ours!

Je me sens particulièrement chanceuse de vous avoir tous rencontrés! Aujourd'hui une page se tourne, demain une autre s'ouvre, et j'espère vous y retrouver...

I feel so incredibly lucky to have met all of you! Today a page is turned, tomorrow a new one starts, and I hope to see you there...

Abstract

Satellite Remote Sensing of Aerosols using Geostationary Observations from MSG-SEVIRI

Aerosols play a fundamental role in physical and chemical processes affecting regional and global climate, and have adverse effects on human health. Although much progress has been made over the past decade in understanding aerosol-climate interactions, their impact still remains one of the largest sources of uncertainty in climate change assessment. The wide variety of aerosol sources and the short lifetime of aerosol particles cause highly variable aerosol fields in both space and time. Ground-based measurements can provide continuous data with high accuracy, but often they are valid for a limited area and are not available for remote areas. Satellite remote sensing appears therefore to be the most appropriate tool for monitoring the high variability of aerosol properties over large scales.

Passive remote sensing of aerosol properties is based on the ability of aerosols to scatter and absorb solar radiation. Algorithms for aerosol retrieval from satellites are used to derive the aerosol optical depth (AOD), which is the aerosol extinction integrated over the entire atmospheric column. The aim of the work described in this thesis was to develop and validate a new algorithm for the retrieval of aerosol optical properties from geostationary observations with the SEVIRI (Spinning Enhanced Visible and Infra-Red Imager) instrument onboard the MSG (Meteorological Second Generation) satellite. Every 15 minutes, MSG-SEVIRI captures a full scan of an Earth disk covering Europe and the whole African continent with a high spatial resolution. With such features MSG-SEVIRI offers the unique opportunity to explore transport of aerosols, and to study their impact on both air quality and climate.

The SEVIRI Aerosol Retrieval Algorithm (SARA) presented in this thesis, estimates the AOD over sea and land surfaces using the three visible channels and one near-infrared channel of the instrument. Because only clear sky radiances can be used to derive aerosol information, a stand-alone cloud detection algorithm was developed to remove cloud contaminated pixels. The cloud mask was generated over Europe for different seasons, and it compared favorably with the results from other cloud detection algorithms - namely the cloud mask algorithm of Meteo-France for MSG-SEVIRI, and the MODIS (Moderate Resolution Imaging Spectroradiometer) algorithm. The aerosol information is extracted from cloud-free scenes using a method

that minimizes the error between the measured and the simulated radiance. The signal observed at the satellite level results from the complex combination of the surface and the atmosphere contributions. The surface contribution is either parameterized (over sea), or based on *a priori* values (over land). The effects of atmospheric gases and aerosols on the radiance are simulated with the radiative transfer model DAK (Doubling-Adding-KNMI) for different atmospheric scenarios.

The algorithm was applied for various case studies (i.e. forest fires, dust storm, anthropogenic pollution) over Europe, and the results were validated against ground-based measurements from the AERONET database, and evaluated by comparison with aerosol products derived from other space-borne instruments such as the Terra/-Aqua-MODIS sensors. In general, for retrievals over the ocean, AOD values as well as their diurnal variations are in good agreement with the observations made at AERONET coastal sites, and the spatial variations of the AOD obtained with the SARA algorithm are well correlated with the results derived from MODIS. Over land, the results presented should be considered as preliminary. They show reasonable agreement with AERONET and MODIS, however extra work is required to improve the accuracy of the retrievals based on the proposed method.

Résumé

Téledétection satellite des aérosols à partir d'observations géostationnaires du capteur MSG-SEVIRI

Les particules d'aérosols jouent un rôle fondamental dans les processus physico-chimiques de l'atmosphère impliqués dans régulation climatique et dans la qualité de l'air, aussi bien à l'échelle régional qu'à l'échelle globale. Malgré les progrès considérables accomplis au cours des deux dernières décennies dans le domaine de la caractérisation des aérosols et dans la compréhension des mécanismes d'interaction aérosols-climat, il existe encore une large plage d'incertitude dans les projections climatiques liées à l'estimation de l'impact radiatif des aérosols. En raison de leur courte durée de vie, et de l'hétérogénéité des sources naturelles et anthropiques, la distribution des aérosols présentent une grande variabilité temporelle et spatiale. A l'heure actuelle, les mesures d'aérosol effectuées depuis le sol permettent de fournir des données en continu qui constituent la plus fiable des sources d'information existantes. Cependant, ces données ne sont souvent disponibles que sur un domaine limité, voire même totalement absentes dans certaines régions. A cet égard, le satellite représente le seul outil capable de produire des observations à grande échelle indispensables à une description approfondie des propriétés des aérosols atmosphériques.

La téledétection passive des aérosols exploite les propriétés diffusantes et absorbantes des aérosols. Les algorithmes de téledétection des aérosols à partir des données satellite, permettent de restituer l'épaisseur optique des aérosols, qui correspond à l'intégration verticale du coefficient d'extinction sur la colonne atmosphérique. Le système de balayage du capteur SEVIRI (Spinning Enhanced Visible and Infra-Red Imager) embarqué sur le satellite géostationnaire MSG (Meteorological Second Generation) permet d'acquérir l'image d'un disque terrestre complet couvrant principalement l'Europe, le continent Africain, et les mers adjacentes, à intervalles réguliers de 15 minutes. Grâce de telles caractéristiques, l'instrument SEVIRI offre un potentiel unique et sans précédent pour suivre le transport des aérosols, et pour mieux comprendre et quantifier leur influence sur la qualité de l'air et sur le changement climatique. L'objectif de ce travail de thèse consistait au développement et à la validation d'un nouvel algorithme pour l'extraction des propriétés optiques des aérosols à partir des observations du radiomètre MSG-SEVIRI.

L'algorithme SARA (SEVIRI Aerosol Retrieval Algorithm) présenté dans cette thèse, permet d'estimer l'épaisseur optique des aérosols sur terre et sur mer, dans

les canaux du visible et du proche infrarouge de l'instrument. La restitution des aérosols ne pouvant être réalisée qu'à partir d'observations en ciel clair, les données SEVIRI contaminées par la présence de nuages ont été filtrées grâce à une technique de détection des nuages qui a été implémentée au sein de l'algorithme. Les masques de nuages obtenus au-dessus de l'Europe pour différentes saisons, ont été comparés aux résultats d'autres algorithmes de détection de nuage, à savoir le masque de nuage de Météo France développé pour MSG-SEVIRI et celui de MODIS (Moderate Resolution Imaging Spectroradiometer). Ces intercomparaisons ont démontré une efficacité raisonnable de la technique mise en oeuvre pour la détection nuageuse. L'information sur les aérosols est dérivée des données en ciel clair en utilisant une méthode qui consiste à minimiser l'écart entre le signal mesurée et le signal simulé. Le signal observé par le satellite au sommet de l'atmosphère résulte d'une combinaison complexe des effets de la traversée de l'atmosphère et des propriétés réfléchives de la surface. La contribution de la surface est basée sur une paramétrisation au-dessus de la mer, et sur l'utilisation de valeurs a priori d'une base de donnée d'albedo de surface sur la terre. Les propriétés optiques de l'atmosphère sont estimées au moyen de données pré-calculées par le code de transfert radiatif DAK (Doubling-Adding-KNMI), pour différents scénarios atmosphériques.

Cet algorithme a été appliqué à différents cas d'étude au-dessus de l'Europe, et les résultats obtenus ont été validés à l'aide de mesures au sol du réseau AERONET, et comparés avec les produits aérosols dérivés des mesures spatiales de Terra-MODIS. Au-dessus de la mer, en général, les valeurs d'épaisseur optique ainsi que les variations diurnes sont en bon accord avec les observations réalisées aux sites côtiers AERONET, et les variations spatiales de l'épaisseur optique obtenues avec l'algorithme SARA présentent une bonne corrélation avec les résultats du produit aérosol de MODIS. Au-dessus de la terre, les résultats obtenus doivent être considérés comme préliminaires. Ils sont en accord satisfaisants avec les données MODIS et AERONET, cependant un effort supplémentaire sera nécessaire pour améliorer la précision de ces résultats dans le cadre de la démarche proposée.

Contents

Acknowledgements	xi
Abstract	xv
Résumé	xvii
1 Aerosols, climate and air quality	1
1.1 Context of study	1
1.2 Atmospheric aerosols	2
1.2.1 General information	2
1.2.2 Physical and chemical characterization	4
1.2.3 Ambient aerosol models	7
1.2.4 Radiative properties	10
1.3 The role of aerosols in climate and air quality	13
1.3.1 The Earth's energy balance	13
1.3.2 Aerosol radiative forcing	16
1.3.3 Health effects of aerosol pollution	20
1.4 Remote sensing	21
1.4.1 Ground-based measurements	21
1.4.2 Satellite observations	23
1.5 This thesis	27
1.5.1 Motivation	27
1.5.2 Outline	27
2 MSG-SEVIRI and satellite-based aerosol retrievals	29
2.1 Introduction	29
2.2 MSG-SEVIRI, instrument description	29
2.3 Illumination-observation geometry	31
2.3.1 Illumination	32
2.3.2 Observation	33
2.3.3 Scattering geometry	35
2.4 Theory for space-based retrievals	38
2.4.1 Atmosphere-surface coupling	38

2.4.2	Radiative transfer equations	42
2.4.3	Radiative transfer model	43
2.4.4	Retrieval method	44
2.5	Ancillary data	45
2.5.1	Land-sea mask and topography	45
2.5.2	Chlorophyll concentrations	46
3	Cloud detection	47
3.1	Introduction	48
3.2	Overview of cloud detection methods	49
3.3	TNO stand-alone Cloud Detection Algorithm	50
3.3.1	General principles of the method	50
3.3.2	Test description	51
3.3.3	Detection scheme and results	55
3.4	Comparison with other cloud masks	60
3.4.1	MSG-SEVIRI comparisons	60
3.4.2	MODIS-TERRA comparisons	70
3.5	Conclusions and perspectives	78
4	Aerosol retrievals over the ocean	79
4.1	Introduction	80
4.2	Algorithm description	82
4.2.1	MSG-SEVIRI radiance data	82
4.2.2	Cloud Mask	82
4.2.3	LUTs	82
4.2.4	Reflectance model over sea	86
4.2.5	The retrieval method	90
4.3	Sets for data evaluation	91
4.3.1	AERONET data set	91
4.3.2	MODIS aerosol product	91
4.4	Case studies	92
4.4.1	Transport of forest-fire smoke over the Atlantic Ocean	92
4.4.2	Saharan dust storm across the eastern Mediterranean Sea	96
4.5	Conclusions	113
5	Aerosol retrievals over land: exploration of a method and applica- tion	115
5.1	Introduction	116
5.2	Method and algorithm description	117
5.2.1	Simulation of the satellite signal	117
5.2.2	Aerosol models and atmospheric optical properties	118
5.2.3	Land surface albedo	119
5.2.4	Retrieval assumptions	120
5.2.5	Minimization process and AOD retrieval	120
5.3	Aerosol observations over Europe for summer 2006	121

5.3.1	Results	121
5.3.2	Evaluation against AERONET	122
5.3.3	Evaluation against MODIS	123
5.4	Conclusion	130
6	Conclusion and Outlook	135
	Bibliography	139
	List of Figures	161
	List of Tables	169
	Curriculum Vitae	171

Chapter 1

Aerosols, climate and air quality

1.1 Context of study

Atmospheric aerosols originate from various sources from both natural and anthropogenic origins, and present a very large diversity of size and chemical composition. Since the past two decades, there has been increased interest in aerosols because they have significant environmental and health impacts. Extreme weather events have yet demonstrated the devastating consequences Earth's warming can have. According to scientific forecasts, these climate events are likely to be more intense and more frequent in the near future, thus associated to huge human, environmental and economical damage costs. In the past few years, scientific studies on climate change have confirmed that the current warming is very likely to be due to human activities. In the most optimistic scenarios, which assume extremely conservative greenhouse gas emissions, climate models predict a global surface temperature rise of 2.4° above the pre-industrial reference in the 21st century [IPCC, 2007]. Like green-house gases, atmospheric aerosols affect the Earth's radiation balance. They have the potential to influence climate directly by affecting the amount of radiation reaching the Earth surface due to scattering and absorption, and indirectly by playing a key role in the formation and behaviour of clouds in the climate system. At the global scale, aerosol tend to counteract the effect of greenhouse gases, by contributing to global cooling. However, anthropogenic aerosols alter air quality, and increased levels of small particles can be responsible for serious health hazards. Therefore, the relative impact of natural aerosols and those of human origin has to be accurately quantified. The variability in particle chemical composition, physical and optical properties renders it difficult to assess both their effect on human health, and their influence on long-term global climate change. The most reliable measurements of aerosols are currently provided by ground-based stations. Nevertheless, spatial extrapolation from such

measurements is difficult. The retrieval of aerosol properties from space-based observations, which is a relatively recent discipline in aerosol science, is a unique tool that allows for measurements on regional and global scales. The purpose of this research work was to develop and to validate a new algorithm for the retrieval of aerosol optical properties over both land and ocean from geostationary observations provided by the SEVIRI (Spinned Enhanced Visible and Infrared Radiometer) instrument on-board the MSG (Meteosat Second Generation) spacecraft. The uniqueness of these observations resides in the unprecedented sampling frequency (15 minutes) which allows for a detailed description of spatio-temporal characterization of aerosols which in turn provides crucial information for the study of air quality and climate-related issues.

1.2 Atmospheric aerosols

1.2.1 General information

Definition

An aerosol can be defined as an ensemble of airborne solid and/or liquid particles in a gas [Seinfeld and Pandis, 1998c]. Thus, atmospheric aerosol refers to particles suspended in air. In atmospheric science, aerosol usually refers to the particulate component. Atmospheric aerosols reside mainly in the two lowest layers of the atmosphere: the troposphere, and the stratosphere. Most aerosols are characterized by sizes ranging from a few nanometers to more than a hundred micrometers.

Sources and Formation

Atmospheric aerosols can originate from both natural and anthropogenic sources, or be formed by chemical processes in the atmosphere. Aerosol particles that are directly injected into the atmosphere are called *primary aerosols*. Natural primary aerosols such as sea spray, mineral dust, volcanic ash, plant and animal debris, are produced by mechanical means. The desintegration and the dispersion of vegetal and animal fragments, and microbes blown off from various surface types, represent the biogenic component of primary aerosol. During a volcanic eruption, a large amount of particles can be released into the atmosphere, and some particles can be injected at very high altitudes (>10 km) into the stratosphere [Rampino and Self, 1984, Robock, 2000, Thomason and Pitts, 2008]. Similarly, human activities such as industry, traffic, households, biomass burning, and agriculture produce primary anthropogenic aerosols. The presence of precursor gases from both natural and anthropogenic origin such as SO_2 , NO_2 , and Volatil Organic Compounds (VOC) are responsible for gas-to-particle conversion, thus producing *secondary aerosols*. Table 1.1 summarize the strengths of the different aerosol sources in terms of aerosol mass fluxes [Andreae, 1995].

Table 1.1: Sources of natural and anthropogenic aerosols with the global annual burden of their emission (after [Andreae \[1995\]](#)).

Source	Annual Emissions (Tg.yr ⁻¹)
Natural Particles	
<i>Primary</i>	
Soil and rock debris	1500
Forest fires and slash burning	50
Sea salt	1300
Volcanic debris	33
<i>Gas to particle conversion</i>	
Sulfate from sulfure gases	102
Nitrate from NO _x	22
VOC from plants exhalation and fires	55
Subtotal (Natural)	3060
Anthropogenic Particles	
<i>Primary</i>	
Industrial, transportation, etc.	120
<i>Gas to particle conversion</i>	
Sulfate from SO ₂ and H ₂ S	120
Nitrate from NO _x	36
VOC conversion	90
Subtotal (Anthropogenic)	366
Total	3430

Transport and life cycle

Once in suspension, aerosols are mixed and transported in the atmosphere during a period that can last from a few hours to a few weeks. They may travel over large distances, sometimes as far as thousands of kilometers away from their sources. During their journey, the size, shape and chemical characteristics of airborne particles can change by various chemical and physical processes. They can be subject to chemical reactions, coagulation with other particles (i.e. the process by which small particles collide and join together to form larger particles), condensation and evaporation.

Two types of processes can cause their removal from the atmosphere: *dry deposition* and *wet deposition* [Seinfeld and Pandis, 1998a,b]. Dry deposition includes all mechanisms involved in the direct transport of particles onto surfaces (such as gravitation, collisions with obstacles). In wet deposition or *precipitation scavenging*, a particle is intercepted by cloud or fog drops, rain or snow. Due to the time scales characterizing these processes, the residence time of aerosols in the atmosphere is relatively short compared to those of most greenhouse gases.

Their relatively short lifetime together with the heterogeneity of the sources render aerosol concentrations and composition over the globe highly variable in both space and time. In consequence, aerosol pollution is mainly observed over developing countries, in the European region, over North America and China. Biomass burning aerosols are mostly found over South America and Africa. The major sources of dust aerosols are located in the 'Dust Belt' [Prospero et al., 2002], a belt of strongly emitting desert dust sources, including the Sahara desert and in Central Asia [Schütz et al., 1981, D'Almeida, 1987]. Saharan dust can be transported across the Mediterranean and Caribbean seas into northern South, Central, and North America, and Europe [Prospero, 1996, Swap et al., 1992, Goudie and Middleton, 2001]. The Gobi Desert is another source of dust in the atmosphere, which affects eastern Asia and western North America [Jaffe et al., 2003, Husar et al., 2001].

1.2.2 Physical and chemical characterization

Size classification

Atmospheric aerosols are often classified according to their size range or *mode*. According to the classification proposed by Whitby and Cantrell [1976], *coarse* particles generally have a diameter greater than $2.5\ \mu\text{m}$, below this limit they are referred to as *fine* aerosols (see Figure 1.1). This distinction in size in general, is also valid in terms of sources, formation, chemical composition, optical properties, removal processes, and health effects. It should be noted, however, that other definitions for fine/coarse mode aerosols are used as well. Coarse mode aerosols consist of mechanically produced natural and anthropogenic aerosols. Because of their large size, these particles do not remain suspended for long before falling out of the atmosphere by dry deposition. The fine mode can distinguish two submodes: a smaller mode called the nuclei or the Aitken mode, and a larger mode called the accumulation mode. Particles in the nuclei mode have typical diameters below $0.1\ \mu\text{m}$. They are usually secondary aerosol which are formed by nucleation or condensation of atmospheric

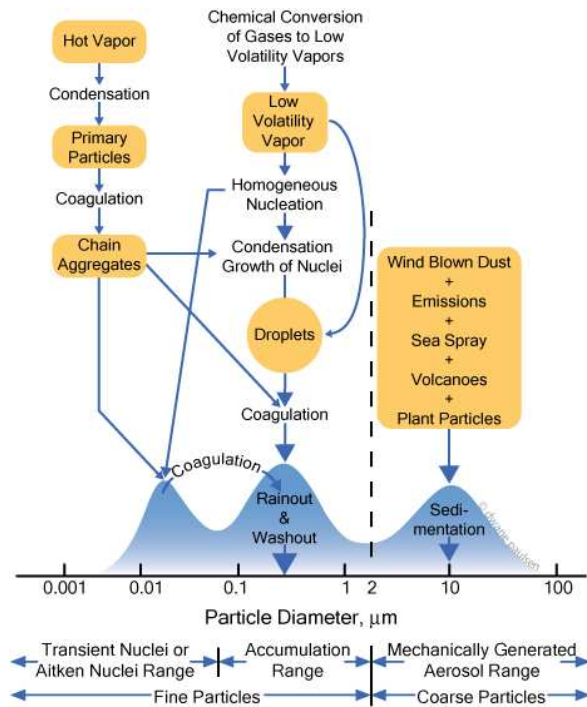


Figure 1.1: Conceptual representation of the principal size ranges for atmospheric particles and their associated sources, and removal processes, adapted from the work of [Whitby and Cantrell \[1976\]](#). The blue curve is a plot of the idealized surface area distribution of an atmospheric aerosol, and blue arrows identify the different physical and the chemical processes responsible for aerosol formation and changes in size. Source: <http://www.dwanepaulsen.net/blog/category/aerosols/>.

gas compounds, but also primary sea salt particles have been observed in this mode. Their number concentration in the atmosphere is the highest, however they represent only a small mass fraction of the total aerosol load. For these particles, brownian motion is the dominant mechanism for deposition, and is responsible for their short lifetime in the atmosphere. Accumulation mode particles are produced by the growth of Aitken particles by either coagulation or condensation of gases, and have sizes in the range of $0.1 \mu\text{m}$ to $2.5 \mu\text{m}$. Removal processes have little effect on these particles, and thus have a long residence time in the atmosphere (\sim weeks), which is principally reduced due to washout and rainout (i.e. wet scavenging) [Hoppel et al., 1994]. In the literature the terms "giant" [Kim et al., 1990], or "ultrafine" [Bates et al., 1998b] are also employed, and the number of different modes can reach 4. The terminology used to refer to the different modes depends very much on the authors.

Hygroscopicity and Chemical composition

The ability of aerosol particles to absorb water vapor is expressed by its hygroscopicity. Dry hygroscopic aerosols retain their solid state at relative humidity up to the deliquescence point, which corresponds to the relative humidity where the aerosol goes from a solid dry phase to an aqueous or mixed solid-aqueous phase [Wexler, 1991]. When the relative humidity increases, liquid aerosols made of aqueous solution grow in size [Tang and Munkelwitz, 1994, Tang et al., 1997, Chan et al., 2000].

The principal chemical constituents of atmospheric aerosols are: sulfate, ammonium, nitrate, chloride, black carbon, organics, trace metals, and water. According to their chemical composition, aerosols can be divided in five major categories: sea salt, sulfate, nitrate, mineral dust and carbonaceous aerosols.

Sea salt aerosols are produced by bursting bubbles at the surface of the ocean during wave breaking, and by spume drops generated from surface tearing at the wave crests. The chemical composition of the sea spray droplets reflects the nature of the sea water enriched by material present in the sea-surface microlayer. Sea salt aerosols consist primarily of sodium chloride (NaCl) [Tang et al., 1997], and contain small amounts of other salts like sulfate, calcium and potassium, as well as halogens. O'Dowd and de Leeuw [2007] determined the organic component in sea spray aerosol which can represent as large as 70% of the mass concentration over biologically active waters. Sea salt particles are highly soluble, and their size can vary over a wide range (0.01 - $100 \mu\text{m}$ diameter) [O'Dowd and de Leeuw, 2007]. Although liquid in the marine environment, they may crystallize when carried inland or to high altitudes.

Sulfate aerosols are produced from the oxidation of sulfur dioxide (SO_2) of anthropogenic or natural origin. Over land, sulfate dioxide is emitted by fossil fuel combustion and volcano eruptions. Over the ocean, phytoplankton produces Dimethyl Sulfide (DMS) which oxidates in the atmosphere to form SO_2 [Andreae and Raemdonck, 1983, Andreae, 1986]. Sulfate aerosols are liquids under almost all conditions, and present mainly in the fine mode ($< 2.5 \mu\text{m}$).

Similarly to sulfate, nitrate aerosols are formed by oxidation processes applying to nitrate dioxide (NO_2). Anthropogenic NO_2 is released in the atmosphere due to the combustion of fossil fuels. It is also naturally produced by microbial activity in soils

and by lightning [Bond et al., 2002]. Nitrate aerosols are present in both the coarse and the fine modes.

Mineral dust aerosol forms during storms over arid areas and deserts. These particles, which are irregularly shaped [Dick et al., 1998], are composed of minerals such as aluminium, silicon, iron oxide and carbonates [Sokolik and Toon, 1999]. Most of them belong to the coarse particle mode. Although nonsoluble, they usually mix with sulfate and organic compounds which constitute a thin liquid layer around the solid cores. In the presence of such a layer, dust particles might become hygroscopic and grow with increasing relative humidity.

Carbonaceous aerosols are composed of organic carbon and black carbon (or elemental carbon) [Kanakidou et al., 2005]. Carbonaceous aerosols emitted in the atmosphere during incomplete combustion processes, e.g., fossil fuel burning or forest fires, are commonly referred to as soot particles [Pöschl et al., 2004]. Soot contains elemental carbon in the form of particle aggregates which are always mixed with organic species. Although soot is not soluble, aging particles may become hygroscopic due to chemical transformation [Chughtai et al., 1999, Decesari et al., 2002]. Biogenic aerosols (i.e. pollen, plant debris, animal fragments etc) constitute the natural source of carbonaceous aerosols. Secondary organic aerosols are formed by oxidation and condensation of VOC. Fresh organic carbon from biogenic sources tend to be solid like, but as they age in the atmosphere their chemical and physical properties are affected by oxidation processes in the presence of OH and NO_x.

1.2.3 Ambient aerosol models

Size distribution

As shown in the previous paragraphs, the chemical composition of aerosol particles is very diverse and their size can vary over a broad range of diameters. In consequence, since the nature of ambient aerosols over a region depends on both the local sources and dynamic processes in the atmosphere (i.e. transformation by physical and chemical processes, removal processes), the characteristics of ambient aerosols can be highly variable. Several models have been proposed to describe the physical properties, chemical composition and mixing state of typical ambient aerosols. In the environment, the aerosol mixing state lies between the extreme cases described by the *internal* and the *external* mixture [Clarke et al., 2004]. In an internal mixture, multiple components reside within a particle. When the different components are physically separated (i.e. in different particles), it is an external mixture [Lesins et al., 2002]. The model proposed by Shettle and Fenn [1979] distinguishes 4 different air masses or *background aerosols* qualified as: maritime, urban, rural, and free troposphere (i.e. mid- and upper troposphere, above clouds). In this model, the chemical composition of each aerosol type is described by the relative contribution of sea salt, soil dust, sulfate, and black carbon, expressed as a fraction of the total number concentration.

The full description of an ambient aerosol, also requires the description of the size distribution. Aerosol size distribution represents the number of particles as function of the particle diameter or radius. The number size distribution of a polydispersed

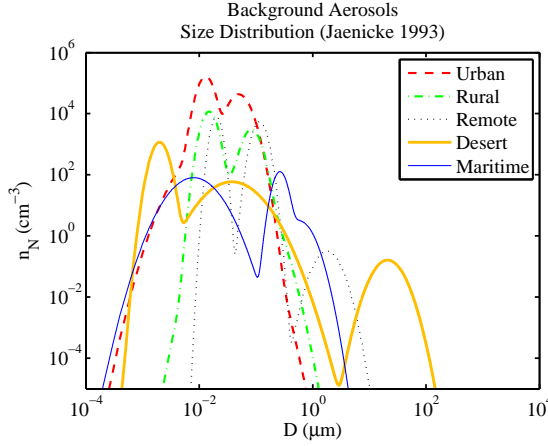


Figure 1.2: Number size distributions as described by the trimodal lognormal parametrization proposed by Jaenicke [1993] for urban, rural, remote, desert and marine environments.

aerosol type can be well described by the superposition of one or several lognormal distribution functions:

$$n_N(D) = \frac{dn}{dD} = \sum_{i=1}^k \frac{n_i}{D \cdot \sqrt{2\pi} \cdot \ln \sigma_{g,i}} \exp \frac{-(\ln D - \ln \bar{D}_{g,i})^2}{2 \cdot \ln^2 \sigma_{g,i}} \quad (1.1)$$

With this parametrization, the number size distribution is fully determined by k pairs of parameters: the mean geometric diameter $\bar{D}_{g,i}$ and the geometric standard deviation $\sigma_{g,i}$ of each mode i . From this expression, a similar description can be derived for the size distribution of the aerosol surface area $n_S(D_{gS}, \sigma_g)$, and volume $n_V(D_{gV}, \sigma_g)$. Hence:

$$\ln \bar{D}_{gS,i} = \ln \bar{D}_{g,i} + 2 \cdot \sigma_{g,i}^2 \quad (1.2)$$

$$\ln \bar{D}_{gV,i} = \ln \bar{D}_{g,i} + 3 \cdot \sigma_{g,i}^2 \quad (1.3)$$

In the model proposed by Jaenicke [1993], the size distribution of the different ambient aerosols is described by the sum of three lognormal modes, for marine, urban, rural, continental, and desert environments. Based on the data of this study, Figure 1.2 shows a representation of the surface number size distribution for these backgrounds. A dominant accumulation mode in the number size distribution indicates the presence of aged particles, and a trimodal structure is usually observed for rural and natural aerosols [Mäkelä et al., 2000]. Aerosols found in the remote maritime environment

have a very broad size distribution, and are generally characterized by three modes, in the nuclei, the accumulation and the coarse mode. Although most of the mass is contained in the coarser mode [Fitzgerald, 1991], the number of particles is higher for the finer modes. The largest particles are produced by wave-wind interactions at the sea surface e.g. [de Leeuw, 1986], and the number concentration and the size distribution are strongly dependent on both wind speed e.g. [Andreas, 1998.] and fetch i.e. the wind's trajectory over water [Piazzola et al., 2002, Piazzola and Despiou, 1997]. Urban aerosols are mainly influenced by primary emissions from human activities, therefore most particles have a radius below $0.1 \mu m$. For many urban sites, it was shown that the mass distribution has two modes in the accumulation and in the coarse mode [Lioy et al., 1987, Aceves and Grimalt, 1993]. The size distribution of aerosols is highly variable within an urban area, and the highest concentration levels are found at the sites downwind of the sources. The rural continental background mainly contains aerosols of natural origin, and undergoes a moderate influence from nearby urban areas. The size distribution of ultrafine particles in urban and rural regions is modulated by many parameters such as photochemical generation during the summer months, vehicle emissions at rush hours, and downwind long-range transport of particles originating from highly polluted industrial or urban sites to rural areas [Kim et al., 2002]. In remote continental regions or desert, the anthropogenic influence is negligible, and the number size distribution is trimodal. The desert dust number distribution spreads over a wide range of diameters, and the shape of the distribution is strongly related to wind speed [Schütz and Jaenicke, 1974, Longtin et al., 1988].

Vertical profile

The Planetary Boundary Layer (PBL) represents the lowest part of the troposphere where large scale atmospheric flows interact with the earth's surface [Stull, 1988]. Due to the action of atmospheric turbulence, a substance injected in this layer is gradually dispersed throughout this layer. In the absence of sinks and sources, this substance would be completely mixed throughout the PBL, therefore the PBL is also referred to as the mixing layer [Seibert et al., 2000]. In the simplest models, aerosols are confined in a single and well mixed layer, with an extent of a few kilometers above the surface. In this ideal case, there is a good correspondence between the aerosol layer height and the height of the mixing layer. For a typical background aerosol, it is common to characterize the vertical profile of the mass concentration by an exponential decrease with altitude [Gras, 1991]:

$$M(z) = M(0) \cdot \exp - \left(\frac{z}{H_s} \right) \quad (1.4)$$

where $M(0)$ is the mass concentration at the surface level, z is the altitude above the ground, and H_s the scale height describing the slope of the profile. In Hess et al. [1998], different values for the scale height and the altitude of the aerosol layer are proposed for different aerosol background types. The shape of a real vertical profile can significantly differ from the exponential model. It is highly variable close to sources,

and strongly influenced by the meteorological conditions. In practice, aerosols can be transported above the mixing layer and aerosols can occur in disconnected layers, with different aerosol content and properties [Gobbi et al., 2003, 2004, Sicard et al., 2006]. These layers are formed due to diurnal variations in the meteorological processes [Stull, 1988]. In addition, terrain elevation can also be a mechanism responsible for the transport of aerosols above the boundary layer [De Wekker et al., 2004].

1.2.4 Radiative properties

Absorption and Scattering

Aerosol particles can absorb and/or scatter electromagnetic radiation at different wavelengths. For interactions of solar radiation with molecules and particles in the atmosphere, the specific form of scattering is *elastic scattering*. In this process, when a photon encounters a particle, the kinetic energy of the system photon-particle is conserved. The light scattered has the same wavelength as the incident beam, only the trajectory of the scattered photon is modified. Scattering and absorption properties of a particle are determined by its chemical composition, size, and the wavelength of the incident radiation. These processes are governed by two wavelength (λ) dependent parameters, the refractive index m and the dimensionless size parameter x :

$$m(\lambda) = n(\lambda) + i \cdot k(\lambda) \quad (1.5)$$

$$x = \frac{\pi \cdot D}{\lambda} \quad (1.6)$$

The real part of the refractive index n represents scattering and its imaginary part k is responsible for absorption. The refractive index of a particle is strongly related to its chemical composition. In equation 1.6, D is the characteristic length of the particle (diameter for spherical particles). The angular distribution of the scattered intensity is controlled by the value of both the refractive index and the size parameter. Based on the value of the size parameter, three regimes of scattering can be distinguished (see Figure 1.3): Rayleigh scattering ($x \ll 1$), Mie scattering ($x \sim 1$) and Geometric scattering ($x \gg 1$). Rayleigh scattering is an extreme case of elastic scattering. It usually refers to molecular scattering, but also applies to small aerosol particles. Mie theory provides an exact solution to Maxwell's equations [Mie, 1908] which can be used to describe scattering for most aerosol particles. This analytical solution is calculated considering spherically shaped particles. As regards irregularly shaped aerosols, Mishchenko [1991] proposes an alternative for scattering by homogeneous, rotationally symmetric nonspherical particles in fixed and random orientations. The geometric regime of scattering concerns larger particles including cloud droplets and ice crystals. The scattered intensity depends on the angle between the direction of incidence and the direction of observation. This property is described by the phase function of the particle, which corresponds to the angular distribution of the scattered

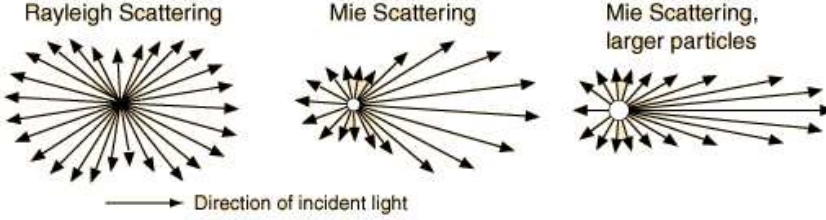


Figure 1.3: Schematic description of light scattering by particles with different size parameters. The size parameter is increasing from left to right. Source: <http://hyperphysics.phy-astr.gsu.edu/Hbase/atmos/blusky.html>.

intensity:

$$P(\Theta, x, m) = \frac{I(\Theta, x, m)}{\int_0^\pi I(\Theta, x, m) \cdot \sin \Theta d\Theta} \quad (1.7)$$

where $I(\Theta, x, m)$ is the intensity scattered in the direction forming an angle Θ with the incident direction of the light. When there is no preferred direction (i.e. isotropic scattering), the spherically symmetric phase function can be written as:

$$P(\Theta, x, m) = \frac{1}{\cos \Theta} \quad (1.8)$$

To give an indication on the degree of asymmetry of scattering it is common to define the asymmetry parameter. Its expression is derived from the cosine weighted average of the phase function over the scattering plane:

$$g(\Theta, x, m) = \frac{1}{2} \int_0^\pi P(\Theta, x, m) \cdot \cos \Theta \cdot \sin \Theta d\Theta \quad (1.9)$$

Forward scattering refers to the observation directions for which $\Theta < 90^\circ$, and backward scattering refers to the observation directions for which $\Theta > 90^\circ$. As shown in Figure 1.3, usually the Rayleigh phase function is symmetrical in forward and backward directions, whereas higher size parameters favor forward scattering ($g > 0$).

Extinction

Due to scattering and absorption, when a light beam passes through a medium, only part of the incident radiation is transmitted in the forward direction (i.e. direction of the incident light). Following the Beer-Lambert-Bouguer Law, the light attenuation over an infinitesimal path of length dz can be expressed by the ratio of the transmitted

to the incident intensity of the radiation:

$$\frac{dI(z)}{I_0} = \exp(-z \cdot \sigma_{ext}(z)) dz = \exp(-z \cdot (\sigma_s(z) + \sigma_a(z))) dz \quad (1.10)$$

In the above equation, σ_{ext} is called the total extinction coefficient which can be splitted into the extinction from scattering σ_s and from absorption σ_a . When particles are considered to be spherically shaped, the extinction due to a population of particles characterized by a number size distribution $n(r)$ (radius function) can be calculated by:

$$\sigma_{ext} = \int_0^R Q_{ext}(x, m) \cdot \frac{\pi D^2}{4} \cdot n(D) \cdot dD \quad (1.11)$$

with D and Q_{ext} representing respectively the diameter and the extinction efficiency of each single particle. Q_{ext} is a complex function of the refractive index and size parameter of the particle, which can be, like for the extinction coefficient, separated into Q_s and Q_a . Since scattering of particles in the Rayleigh domain is symmetrical and almost independent on the particle shape, [Bohren and Huffman \[1983\]](#) determined an analytical solution of Q_{ext} . In this case, Q_{ext} varies proportionnaly to λ^{-4} . For particles having a size close to the wavelength, the Mie-Debye-Lorentz theory [[Mie, 1908](#)] allows the calculation of Q_{ext} . Scattering in the Geometric regime is strongly dependent on the particle shape and on its orientation relative to the direction of the incoming radiation. For very high size parameters, Q_{ext} saturates at a limit value of 2. Instead of parameter Q_{ext} , it is also common to use the extinction cross section C_{ext} , which is defined as the product of the extinction efficiency by the geometrical cross section of the particle. For a sphere :

$$C_{ext} = Q_{ext}(x, m) \cdot \frac{\pi D^2}{4} \quad (1.12)$$

For a particle, the relative effect of scattering to the total extinction is quantified by the single scattering albedo:

$$w_0 = \frac{Q_s}{Q_{ext}} = \frac{C_s}{C_{ext}} \quad (1.13)$$

Hence single scattering albedo would be 1 for a fully scattering particle and 0 for a fully absorbing particle. In general, sea salt and water soluble aerosols predominantly scatter solar light with single scattering albedo approaching 1, whereas dust and carbonaceous aerosols are partially absorbing. Aerosols with a single-scattering albedo greater than 0.85 are generally considered to cool the planet, and those with less than 0.85 tend to warm the planet [[Hansen et al., 1981](#)].

Aerosol Optical Depth

In atmospheric radiative studies, the aerosol optical depth (AOD) is a dimensionless quantity that is often used. The AOD is defined as the integrated value of the extinction coefficient over the whole atmospheric layer (i.e. from the surface $z = 0$ to the Top of the Atmosphere $z = h_{TOA}$):

$$\tau(\lambda) = \int_0^{h_{TOA}} \sigma_{ext,aer}(\lambda, z) \cdot dz \quad (1.14)$$

Therefore, the AOD depends on the vertical profile of the aerosol extinction, which in turn is a complex function of its physical and chemical properties. Generally, aerosol models relate the phase function, the extinction coefficient, and the single scattering albedo to their physical and chemical characteristics [Shettle and Fenn, 1979, WMO, 1983, Hess et al., 1998]. With the use of a general circulation model, Reddy et al. [2005] could estimate the largest contributions of different aerosol types to the global AOD (0.12 at $0.55\mu\text{m}$): 58% for natural, 26% for fossil fuel and 16% for biomass burning.

The spectral dependance of the AOD is usually represented by power law function:

$$\tau(\lambda) \propto \lambda^{-\alpha} \quad (1.15)$$

The Ångström coefficient α decreases when the size distribution is dominated by relatively large particles, and increases when relatively small particles dominate [Kuśmierczyk-Michulec et al., 2001]. Its values range roughly between 0 and 3. In the presence of air masses dominated by large particles such as sea salt or dust, the Ångström coefficient has values close to zero, which can even become negative in the presence of very large particles like freshly produced sea salt or desert dust particles suspended during dust storms. In polluted areas where small sulfate and nitrate particles dominate, the Ångström coefficient can reach values in the order of 2 to 3. High values of the Ångström coefficient are also observed during biomass burning episodes. Scattering and absorption of solar light by aerosol particles induce perturbations in the Earth energy balance which have been shown to significantly affect the climate system at both regional and global scales.

1.3 The role of aerosols in climate and air quality

1.3.1 The Earth's energy balance

Sunlight is the primary source of energy for the Earth's oceans, atmosphere, land and biosphere. The energy emitted by the sun is mostly in the ultraviolet, visible, and near-infrared parts of the spectrum (shortwave), while the Earth radiates in the thermal infrared wavelengths (longwave). Assuming the sun is a black body at a temperature close to 6000 K, Planck's law provides the description of the spectral solar

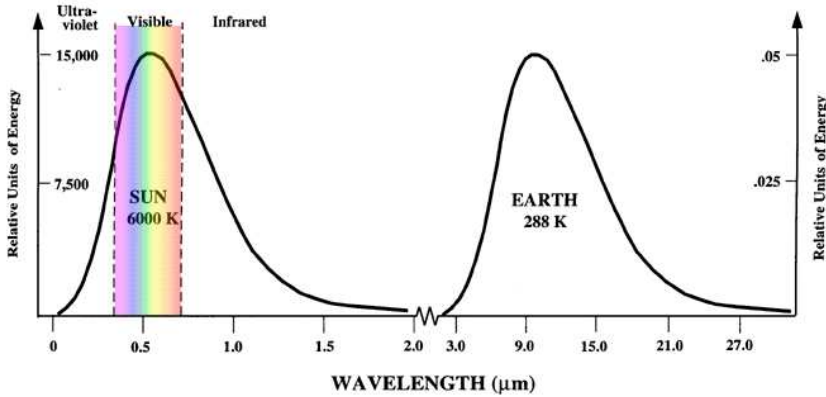


Figure 1.4: Sun and Earth emission spectrums. The spectrum of the solar radiation can be approximated by the spectrum of a black-body with a temperature of 6000 K. With this temperature, most of the radiation is emitted between 0.1 and 4 μm and the maximum of energy is reached for a wavelength of approximately 0.48 μm . The spectral distribution of the terrestrial radiation is similar to that of a black-body with a temperature of 288 K. The Earth radiates mainly in a range between 0.5 and 30 μm , and the wavelength of maximum emission is found around 10 μm . Source: http://ockhams-axe.com/global_warming.

irradiance as illustrated in Figure 1.4. The Earth system reaches a thermal equilibrium when the amount of longwave energy emitted is balanced by the shortwave solar energy absorbed. The radiative equilibrium maintains the Earth at the global temperature of about 288K. Due to the inclination of the Earth rotation axis, the sun energy is not uniformly distributed over the globe. Most of solar radiation benefits to the tropics where the sun rays are almost perpendicular to the Earth's orbit plane, whereas polar latitudes receive much less solar heating. On a yearly average, the whole globe receives 1370 J per second from the sun. In other words, at the top of the atmosphere, the solar flux across a surface of unit area normal to the solar beam is about $342 \text{ W}\cdot\text{m}^{-2}$. This energy is distributed among the different components of the Earth system through various reflection and absorption processes (see Figure 1.5). About one third of the shortwave radiation is reflected back to space by clouds, aerosols and atmospheric molecules ($\sim 77 \text{ W}\cdot\text{m}^{-2}$), and the surface ($\sim 30 \text{ W}\cdot\text{m}^{-2}$). In addition, a fraction of the incoming solar radiation that is transferred by the atmosphere to the surface is absorbed by greenhouse gases present in the atmosphere ($\sim 67 \text{ W}\cdot\text{m}^{-2}$). Therefore, only half of the direct shortwave radiation reaches the surface and is absorbed as heat ($\sim 168 \text{ W}\cdot\text{m}^{-2}$). Due to the ability of greenhouse gases to absorb longwave radiation, the thermal radiation emitted by the surface in turn heats the atmosphere. The thermal radiation emitted by both the atmosphere and the surface is absorbed by clouds and aerosols which re-emit longwave radiation,

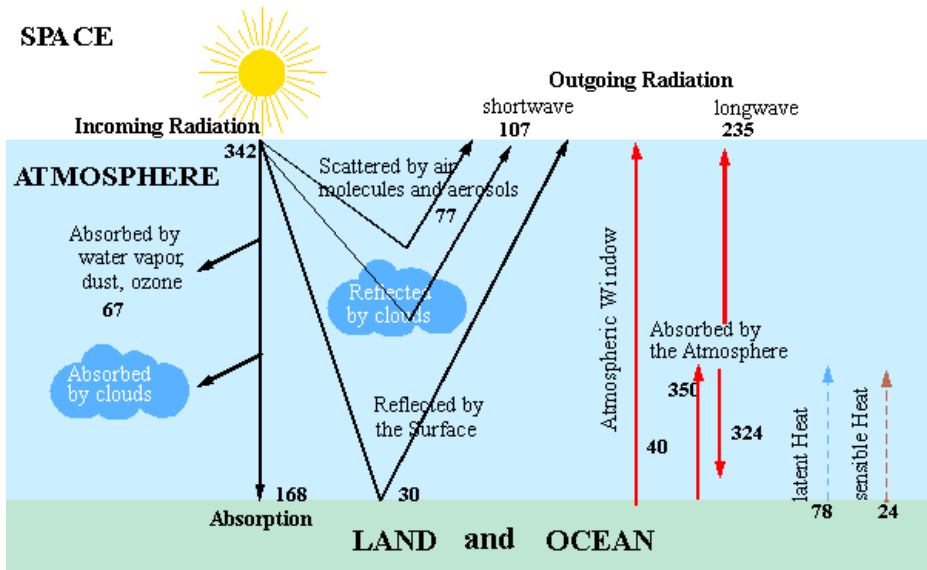


Figure 1.5: The global annual energy balance of the Earth. The contributions of the different components are expressed in Wm^{-2} . Straight lines represent either short-wave radiation (black) or long-wave radiation (red), and dotted lines illustrate the vertical heat transport due to evapo-condensation processes (latent heat) and uprising warm air masses (sensible heat). Source <http://www.hamburger-bildungsserver.de/welcome.phtml?untent=/klima/greenhouse/radiation.html>, based on data from Kiehl and Trenberth [1997], Figure 1.2 in Chapter 1 "The Climate System: an Overview" of the Working Group I Report in the 2001 Intergovernmental Panel on Climate Change.

thus trapping the energy between the Earth surface and cloud tops. In the absence of greenhouse gases, clouds and aerosols and their related processes, the mean temperature of the Earth would be 33° lower. With greenhouse gases, but no clouds or aerosols, this temperature would reach 293 K.

1.3.2 Aerosol radiative forcing

Since the first industrial revolution, which began in the eighteenth century, the concentrations of all long-lived greenhouse gases and aerosols have largely increased due to human activities. These anthropogenic emissions have brought external perturbations to the Earth's natural radiation balance which are referred to as *climate radiative forcing* [Myhre et al., 2001]. When climate forcing occurs, the solar energy absorbed by the Earth system is no longer in balance with the longwave radiation it emits, and the climate system evolves toward a new equilibrium. A net negative change in the Earth radiative budget is associated with a cooling effect of the atmosphere, whereas a net positive difference implies that the atmosphere is warming up. The globally averaged net effect of human activities since pre-industrial times (1750) has been estimated with great confidence to represent a warming of 1.6 W.m^{-2} [+0.6 to +2.4]¹ [Solomon et al., 2007]. The different radiative forcing agents, and the range of their contribution to the global average radiative forcing estimated for the year 2005 from pre-industrial times, are presented in Figure 1.6. As compared to aerosols, most of the significant greenhouse gases (e.g. CO₂, CH₄, N₂O) are long-lived (lifetime beyond a decade) and relatively well mixed. Consequently, their global impact on climate is easier to determine than that of aerosols. In the troposphere, they absorb the radiation in near-infrared wavelengths of the solar spectrum, which has a net positive change on the Earth radiation balance and produces the well-known *global-warming* effect. The increases in CO₂, CH₄, and N₂O concentrations, have contributed to this global-warming effect by 2.3 W.m^{-2} [+2.1 to +2.5]¹ [Solomon et al., 2007]. Anthropogenic aerosols are believed to globally cool the planet, and to substantially offset the positive radiative forcing from the increase in greenhouse gases [Haywood and Boucher, 2000, Penner et al., 2001]. However, their effect on climate is much more complex than that of greenhouse gases, and although large efforts are pursued in understanding aerosol-climate interactions, this remains one of the largest uncertainties in the climate system. Due to their short lifetime and variety of sources, aerosols are heterogeneously dispersed: generally concentrated downwind, at close distances from their sources, and strongly correlated to them. Thus, their radiative effects, which in turn are determined by their concentration, chemical composition, size and shape, are highly variable in both space and time. As a consequence, aerosols affect both regional and global climate. Aerosols influence climate in two different ways: a direct and an indirect effect. To investigate these effects and quantify their impact on climate, many studies have been carried out, either relying on analysis of ground-based [Yu et al., 2006] or satellite [Kaufman et al., 2005a, Bellouin et al., 2005] measurements, or from model calculations [Schulz et al., 2006, Forster et al., 2007]. Overviews

¹90% uncertainty interval around the best estimate

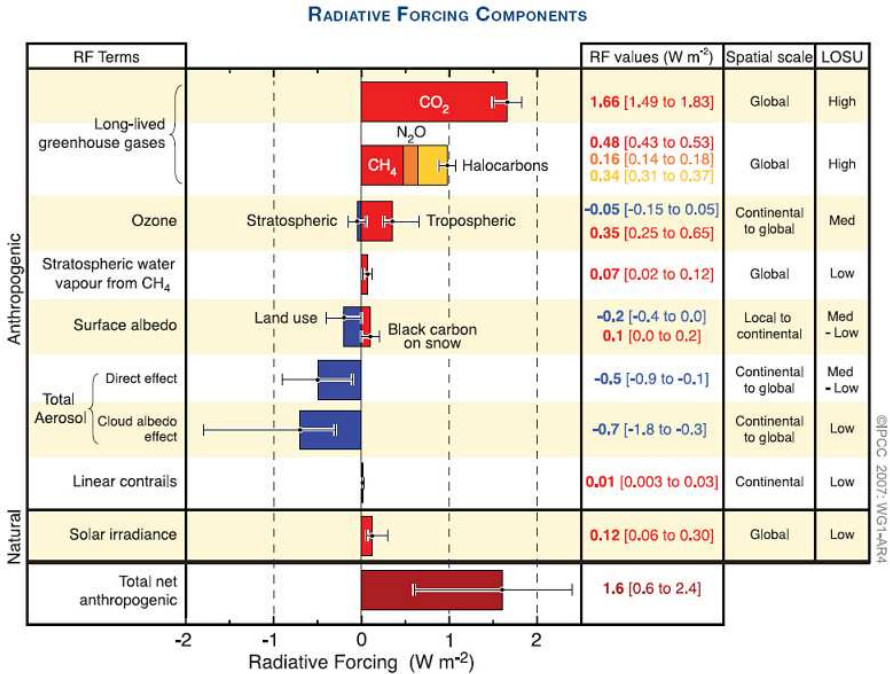


Figure 1.6: Global average estimates (in $W\cdot m^{-2}$) of the contributions from the different radiative forcing components of the Earth climate for the year 2005. For each component, the spatial scale and Level Of Scientific Understanding (LOSU) are presented in the right most columns. The amplitude and the uncertainty of the total net radiative effect due to the anthropogenic contribution is also available. Source: Figure SPM.2 from the Summary of Policymakers of the Working Group I Report in the 2007 Intergovernmental Panel on Climate Change.

on the assessment of global radiative forcing of aerosols on climate are discussed in [Haywood and Boucher \[2000\]](#) for the direct effect and in [Lohmann and Feichter \[2005\]](#) for the indirect effect. The most recent estimate of aerosol-induced radiative forcing represents a cooling of -1.3 Wm^{-2} $[-2.2 \text{ to } +0.5]^1$ [[Solomon et al., 2007](#)].

Direct effect

The direct effect is related to the ability of aerosols to absorb and scatter solar and thermal radiation [[Chylek and Coakley, 1974](#)]. These two processes reduce the amount of shortwave radiation reaching the Earth's surface. By reflecting the solar radiation back to space, aerosols contribute to cooling the atmosphere and the surface, whereas absorbing processes lead to positive climate forcing. Among the most recent studies, the study of [Yu et al. \[2006\]](#) based on satellite measurements evaluates the direct radiative effect of aerosols to be a global cooling of $-5.5 \pm 0.2 \text{ W.m}^{-2}$ over the ocean, and of $-4.9 \pm 0.7 \text{ W.m}^{-2}$ over land. The global and total direct radiative forcing accounting for the anthropogenic contributions for all main aerosol types represent -0.5 Wm^{-2} $[-0.9 \text{ to } -0.1]^1$ [[Solomon et al., 2007](#)]. [Reddy et al. \[2005\]](#) have estimated from general circulation modeling results that the major aerosol components (i.e. sulfate, black carbon, organic matter, dust and sea salt) contribute respectively -0.62 , $+0.55$, -0.33 , -0.28 and 0.30 W.m^{-2} to the global annual mean of the direct aerosol radiative perturbation in the shortwave range for all-sky conditions. In the longwave domain, these values were found to be approximatively half.

Indirect effect

Aerosols also perturb the Earth-atmosphere radiation balance by changing the albedo, the amount and the lifetime of clouds. All these processes contribute to the so-called indirect climate forcing by aerosols. Clouds are a collection of water droplets or ice crystals suspended in the atmosphere. To be formed, cloud droplets require the presence of aerosol particles which serve as cloud condensation nuclei (CCN), on which water vapour condenses when relative humidity increases. As they absorb water vapour, aerosol particles swell and eventually reach a critical diameter above which they become activated CCN [[Kohler, 1921](#)]. These activated CCN grow faster to become rain droplets. Therefore, the microphysical and radiative properties of a cloud are closely linked to the nature of the aerosols from which it forms. Anthropogenic processes produce large amounts of hygroscopic particles, which affect cloud microphysical and radiative properties in different ways. The first indirect effect refers to the increase in the number of CCN available for a fixed amount of water vapor. Less water vapor can thus condensate to each CCN, and as a result cloud droplets are smaller [[Twomey et al., 1984](#)]. When the droplets are smaller, the scattering within the cloud is enhanced, and the cloud has a higher albedo [[Twomey, 1977](#)]. The second indirect effect is related to the reduction of the precipitation efficiency induced by more numerous smaller droplets which precipitate less easily. This effect usually leads to longer cloud lifetime and greater cloud cover [[Albrecht, 1989](#)]. Besides, absorbing aerosols enhance the ability of clouds to absorb sunlight, thereby cooling the

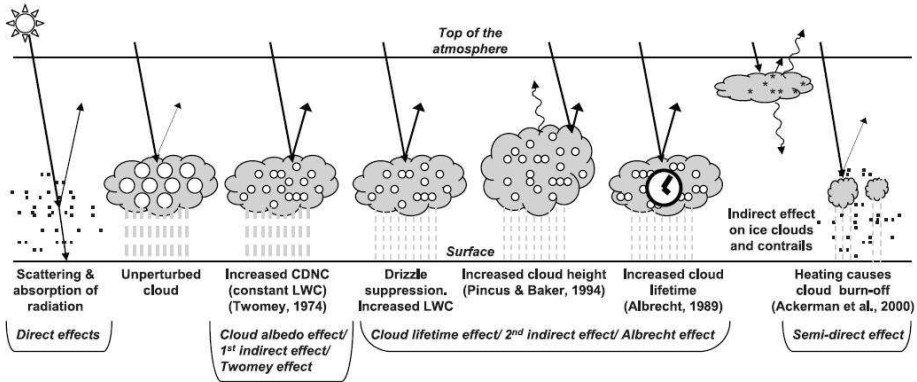


Figure 1.7: Schematic illustration of aerosol radiative effects on climate including the different direct and indirect effects (modified from Haywood and Boucher [2000]). Straight lines represent shortwave radiation, and wavy lines the longwave radiation. Black dots, circles, and stars represent respectively aerosols, cloud droplets, and cloud ice crystals. The precipitation amount is related to the thickness of the grey dashed lines. Source: Figure 2.10 from Chapter 2 "Changes in Atmospheric Constituents and in Radiative Forcing" of the Working Group I Report in the 2007 Intergovernmental Panel on Climate Change.

surface and heating the atmosphere. The consequence of this effect termed as the semi-indirect effect, is the inhibition of the cloud formation [Ackerman et al., 2000]. The schematic representation of the different effects induced by cloud-aerosol interactions is illustrated in Figure 1.7. Based on satellite data for the Amazon basin and Cerrado during the dry season, [Kaufman and Fraser, 1997] have shown that smoke particles from biomass burning were responsible for an increase of the cloud reflectance from 0.35 to 0.45, and reduce the droplet size from 14 to 9 μm . A more recent study relying also on satellite observations, reports the influence of smoke from biomass burning on the scattered cumulus cloud cover over the Amazon region during the dry season [Koren et al., 2004]. A 38% reduction of the scattered cumulus cloud cover was estimated in clean conditions, whereas no reduction occurred in the presence of heavy smoke. When the reduction applied, the instantaneous regional forcing reversed from $-28 \text{ W}\cdot\text{m}^{-2}$ up to $+8 \text{ W}\cdot\text{m}^{-2}$. In contrast, according to other satellite observations, aerosols lead to increases of the shallow cloud coverage of 0.2 to 0.4 over the Atlantic Ocean, in all conditions of smoke, dust and pollution. This change in the cloud coverage induces a radiative forcing of about $-7 \text{ W}\cdot\text{m}^{-2}$ at the top of the atmosphere [Kaufman et al., 2005b]. Using ground-based measurements around the globe, Kaufman and Koren [2006] found that generally the cloud cover increases with the aerosol column concentrations, whereas it is inversely dependent on aerosol absorption of sunlight. Due to the duality of these effects, the aerosol indirect forcing is credited with the greatest level of uncertainty among the known factors

of radiative forcing [IPCC, 2007]. The current best estimate for the contribution of anthropogenic aerosols to the global indirect cloud albedo radiative effect, is based on model calculations which associate this effect with a cooling of -0.7 W.m^{-2} $[-1.8$ to $0.3]$ [Solomon et al., 2007]. Therefore, aerosol particles certainly play an important role in the overall radiation budget of the Earth, and there is still a lot to learn about the relation between particles and cloud radiative properties.

1.3.3 Health effects of aerosol pollution

In addition to their effect on climate, aerosols affect air quality, thus having a detrimental effect on human health. In the last decades, the occurrence of asthma has dramatically increased, and aerosols can certainly trigger and aggravate respiratory problems [Lippmann et al., 1980]. Many epidemiological studies report that exposure to particulate air pollution produces excesses in cardio-pulmonary morbidity and mortality [Lippmann et al., 2000, 2003]. In densely populated areas and highly industrialized urban centers, the concentration levels of ambient particles alarms the health authorities, and air pollution particles are thought to kill more than 500 000 persons worldwide each year [Devlin et al., 2003]. Consequently, in addition to regular measurements of the contaminant gases (i.e. SO_2 , NO_2 , O_3 , CO etc), air quality policies/studies also rely on Particulate Matter (PM) indicators: PM10 and PM2.5. PM10 concentrations refer to mass concentrations of all aerosol particles with a dry aerodynamic diameter below 10 micrometers. Such particles can be inhaled into the nose and throat [Lippmann and Albert, 1969]. Particles with aerodynamic diameters of less than $2.5 \mu\text{m}$ (PM2.5) can penetrate deep into the lungs [Lippmann and Albert, 1969], and the finest can even enter the bloodstream via the lungs, thus affecting other parts of the human body. The main toxic effect of PM10 is cardiovascular diseases in populations, and respiratory diseases among children. Like other atmospheric pollutants, particulate matter might be responsible for some childhood cancers, due to prenatal exposure to PM10 that are inhaled by the mother during pregnancy [Knox, 2005]. With regards to these health issues, the various governments have set maximum standards. According to the European standards, daily levels of PM10 concentration below $50 \mu\text{g.m}^{-3}$ are considered to be clean days, for levels between $50 \mu\text{g.m}^{-3}$ and $200 \mu\text{g.m}^{-3}$ air quality is considered to be moderate, and for levels above $200 \mu\text{g.m}^{-3}$ is considered poor and designated as smog. Although air quality has in terms of PM improved during the past decade, The Netherlands, for which 45% of the aerosols are of anthropogenic origin, remains like many other states from the European Union among the countries that do not comply with the 24-hour average limit of $50 \mu\text{g.m}^{-3}$ imposed by the European norms [Buijsman et al., 2005]. A number of studies have demonstrated the efficiency of the policies in the reduction of PM related detrimental health effects, however the magnitude of health risk depends on a complex combination of factors involving particle size, concentration and chemical composition, and are therefore difficult to manage [Vincent et al., 1995]. In order to improve and explore environmental policy, aerosol measurements have become a crucial necessity.

1.4 Remote sensing

Aerosol physical and chemical properties, and thus their optical properties, are highly variable over scales ranging from local to regional to global, and vary with location on Earth and with the season. To better understand and quantify the radiative forcing effect of aerosol on climate, and for better management of air quality, more knowledge on the properties of aerosol at global and regional scales is needed. To this end, several measurement techniques are used. Aerosol properties can be measured directly by analyzing in-situ samples, or derived from remotely sensed data acquired at ground-based stations or by instruments carried on satellites. Some methods used for in-situ measurements have the unique advantage to provide a direct and complete determination of the physical and the chemical properties of the particles.

Remote sensing is defined as the acquisition of information about an object without being in physical contact with it [Elachi, 1987]. This technique make use of the properties of electromagnetic radiation emitted, reflected or diffracted by the objects. A remotely sensed object of interest can be observed either passively or actively. In passive remote sensing, the sensor measures the radiation which originates from natural sources. Natural sources refer to either the radiation emitted by the sun or by the earth-atmosphere sytem. Observations in the UV (Ultra Violet) or the visible wavelengths use the sun as a source of radiation, whereas terrestrial radiation is mainly used for longwave measurements ($>8 \mu\text{m}$). In active remote sensing, the sensors detect the response scattered back by the object, based on the use of artificially-generated energy sources. Theses techniques use instruments such as RADAR (RAdio Detection And Ranging) and LIDAR (LIght Detection And Ranging) which operate in a spectral domain ranging from the UV to the microwave region. Thus, depending on the optical properties of the atmosphere, the radiation observed from above or below it is more or less affected, and aerosol properties can be derived by the change induced in the backscattered radiation.

1.4.1 Ground-based measurements

Field campaigns in different regions of the globe have contributed to improve the understanding of atmospheric aerosol and their effects on climate. Some major experiments were focused either on the remote marine atmosphere or areas downwind of continental aerosol source regions. They integrated dedicated ship cruises, using fully equipped vessels over oceanic regions, and intrumented aircrafts and balloon-sondes, to perform atlitude profiling over selected regions. Among these campaigns, the first Aerosol Characterization Experiment ACE-1 was carried out over the South-West Pacific to determine the properties characterizing aerosols in the remote marine atmosphere, and to quantify the impact of the controlling factors involved in aerosol radiative forcing and climate [Bates et al., 1998a]. The Tropospheric Aerosol Radiative Forcing Observational Experiment (TARFOX) conducted along the east coast of the USA in the summer of 1996 was designed to assess the anthropogenic impact on climate change where one of the world's major plumes of urban/industrial haze

is advected off the continent over the Atlantic Ocean [Russell et al., 1999]. A central objective of the Southern African Regional Science Initiative campaign (SAFARI 2000) during the dry season was to investigate the emissions from fires and from soils impacted by burning in the African savannas [Swap et al., 2002]. The Saharan Dust Experiment (SHADE), which took place in September 2000 on the west coast of Africa, used a wide range of measurements to improve knowledge about the radiative impact of mineral dust [Tanré et al., 2003]. More recently, the objective of the ICARB (Integrated Campaign for Aerosols, gases, and Radiation Budget in Spring 2006) which is the largest and most exhaustive field campaign that has ever been conducted in the Indian region, was to characterize the physico-chemical properties and radiative effects of atmospheric aerosols and trace gases over the Indian landmass and the adjoining oceanic regions of the Arabian Sea, northern Indian Ocean, and Bay of Bengal through intensive, simultaneous observations [Moorthy et al., 2008].

However large field campaigns occur rarely, and remain relatively limited in space and time. Thanks to ground-based networks, long term climatologies provide the context needed for intensive field campaigns which focus on regional issues. These ground-based networks can include in-situ and/or remote-sensing instrumentation. Aerosol measurements at NOAA GMD/ERDL (Global Monitoring Division / Earth Research Laboratory) have begun to provide information about the trends and the factors of aerosol particles that influence climate forcing since the early seventies [Ogren, 2004]. Aerosol properties monitored by ESRL/GMD include both in situ and remote-sensed data from baseline and regional stations [Ogren, 2004]. NASA has established an international network of ground-based sunphotometers: the Aerosol Robotic Network (AERONET) [Holben et al., 1998] which performs passive measurements of aerosols at more than 300 locations all over the world. AERONET stations use CIMEL sunphotometers to measure the radiance angular distribution in 4 or more spectral bands. For this purpose, radiance observations are made both in the almucantar (i.e. azimuthal angle relative to the sun) and the principal plane (i.e. direction away from the sun direction). The aerosol optical depth is recorded every 15 minutes based on the transmission of direct sunlight inferred from the radiance measurement in the sun direction. The collection of radiance data from the different directions is used in combination with the aerosol optical depth to derive aerosol properties such as size distribution, complex refraction index, partition spherical/non spherical. The latter are retrieved using *Direct Sun* inversion algorithms [Nakajima et al., 1983, Dubovik and King, 2000] routinely applied to clear sky data (i.e. no clouds) [Smirnov et al., 2000]. The phase function and single scattering albedo are calculated on the basis of the retrieved parameters. AERONET data can be freely accessed on the web and are available for three quality levels: Level 1.0 for raw data i.e. unscreened (AOD), Level 1.5 for automatically cloud filtered data (AOD and inversion products), and Level 2 quality assured, automatically cloud filtered and manually inspected (AOD and inversion products). Except for Level 2 data which have post-field yearly calibration applied, all products are provided on a near-real time basis.

Since its creation in February 2000, the EARLINET (European Aerosol Lidar Network) is a joint project of 20 European lidar groups to establish a quantitative comprehensive statistical data base of both horizontal and vertical distribution of

aerosols on a continental scale [Bösenberg et al., 2001]. Most of the measurements performed by these lidars are performed on fixed schedules, or at specific time and location to explore particular issues. In addition to vertical/horizontal monitoring, LIDARs have the advantage to operate under all sky conditions whereas other remote sensing measurements require cloud screening.

1.4.2 Satellite observations

Satellite remote sensing of aerosols is the only technique allowing to monitor the high variability of aerosols in both space and time. Moreover, aerosols affect the remote sensing of other geophysical parameters (i.e. ocean color, atmospheric ozone, surface albedo, etc), therefore aerosol remote-sensed data are also essential for atmospheric correction [Kaufman et al., 1997b]. Space-based aerosol observations are based on inversion algorithms using radiative transfer simulations of the signal received by the sensor at the satellite level (cf. Chapter 2). The radiative simulations require the use of *a priori* information on the aerosol type and usually on the surface reflectance/properties. Aerosol measurements from space make use of instruments such as radiometers, spectrometers, spectroradiometers, or polarimeters for passive techniques, and of LIDARs in active detection [King et al., 1999]. These various sensors can be carried on either polar orbiting spacecrafts (i.e. sunsynchronous) also called Low-Earth Orbit Satellites (LEO), or geostationary satellites for having Geosynchronous (GEO) (see Figure 1.8).

Despite the fact they were not designed for aerosol retrievals, the instruments onboard the first meteorological satellites, such as Nimbus-7-TOMS (Total Ozone Mapping Spectrometer), NOAA-AVHRR (Advanced Very High Resolution Radiometer) and ERS-2 (European Remote Sensing)-GOME (Global Ozone Monitoring Experiment) [Burrows et al., 1999] were used for that purpose. Carried on the NOAA's polar orbiting platforms since 1978, AVHRR is a broad band scanner with 4 to 5 channels in the solar spectrum and in the thermal infrared [Kidwell, 1995]. It is a standard instrument for global mapping of vegetation, sea surface temperature and ice cover, that has also provided the first aerosol information from space-based measurements. The first aerosol retrieval algorithm using channel 1 (0.58-0.68 μm) of AVHRR was implemented by Griggs [1975], and started to provide operational aerosol observations in 1988 [Rao et al., 1989]. The single-channel methodology was improved and applied to channel 2 (0.73-1.10 μm) [Stowe et al., 1997], and channel 3 (1.58-1.64 μm) [Ignatov et al., 2004]. For application over land, Holben et al. [1992] proposed two different techniques to retrieve the aerosol optical depth in channel 1 of AVHRR. First TOMS, then GOME and OMI (Ozone Monitoring Instrument) series of polar orbiting sensors, aimed at monitoring the long term global changes in stratospheric ozone. During almost 30 years, the nadir-viewing spectrometer TOMS (1978-2007) supplied global ultraviolet radiance data for 6 wavelengths in the range of 308.6-360.44 nm, every 3 days at a rather coarse resolution of 25-60 km^2 . Torres et al. [2002] have tested a retrieval method that makes use of the unique near-UV remote sensing feature of the TOMS instrument onboard Nimbus-7 (1979-1992) and Earth Probe (since mid-1996) to produce a long term record of aerosol optical depth

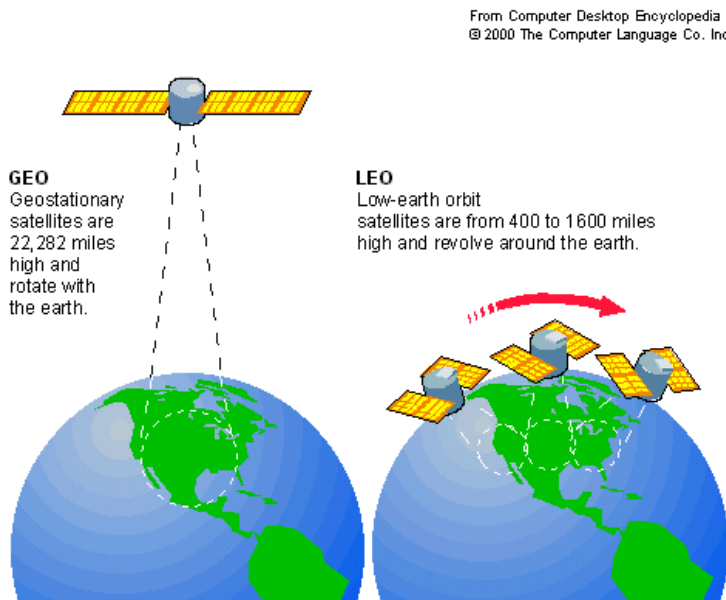


Figure 1.8: Description of GEosynchronous Orbit (GEO) and Low Earth Orbit (LEO) satellites. GEO satellites have geosynchronous orbits characterized by their circularity, an altitude of 35000 km directly above the Earth's equator (0° latitude), and a period equal to the revolution period of the Earth. For an observer on the Earth surface, geostationary satellites appear motionless. Orbits of LEO satellites are commonly defined as orbits with an altitude below 2000 km. These orbits are elliptical or circular with a period of the order of a hundred minutes. Polar orbits are LEO orbits for applications with the purpose to view the same place on Earth at the same time each day. Image Credit: Reproduced with permission from Computer Desktop Encyclopedia (c) 2008 The Computer Language Company Inc.

over land. With a larger footprint (40x320 km²) than TOMS, GOME (1995-present) achieves a complete scan of the Earth within 1 day. GOME performs nadir observations of the spectrum between 237 nm and 794 nm, in 4 broad-band channels and with a spectral resolution of 0.2 to 0.4 nm. The algorithm proposed by Kuśmierczyk-Michulec and de Leeuw [2005] allows to derive the aerosol optical depth over both land and water from GOME data at 6 wavelengths in the range of 380-670 nm. The Ozone Monitoring Instrument (OMI) flown on Aura [Levelt and Noordhoek, August 2002] is a nadir viewing imaging spectrograph, which combines the advantages of GOME and TOMS. It measures a complete spectrum in the ultraviolet and the visible wavelength range, with a spectral resolution of about 0.5 nm and has the advantage to make a full scan of the Earth within one single day at a spatial resolution of 13x24 km². A recently developed algorithm, cf. Curier et al. [2008], dedicated to OMI, has been used to derive the aerosol properties in the near-UV, based on the multi-wavelength approach proposed by Torres et al. [2002]. Starting 1991, the series of Along Track Scanning Radiometers (ATSR-1, ATSR-2 and AATSR) have the goal to measure the surface temperature with the climate standard accuracy [Edwards et al., 1990, Llewellyn-Jones et al., 2001]. These instruments provide the radiance in the visible, near-infrared and far-infrared ranges, with the advantage to perform quasi-simultaneously measurements for two viewing angles (i.e. 55° forward and nadir), at a spatial resolution of 1 km for the nadir view. The dual-view feature of this radiometer allowed for the retrieval of the aerosol optical depth (at 0.550, 0.67, 0.87 and 1.6 μm), without using any *a priori* on the surface contribution to the top of the atmosphere radiance [Veefkind, 1999].

Accurate retrieval of aerosol properties from remotely sensed data requires the use of sensors with very narrow bands and multispectral characteristics. Furthermore, the accuracy of these retrievals can be significantly improved when the sensors provide measurements for multiple viewing angles and information on the polarization. Over the past decade, a new generation of instruments well suited for aerosol applications has emerged. In that respect POLDER (Polarization of Directionality of the Earth Reflectance) [Deschamps et al., 1994], and two instruments from the A-Train satellite constellation [Savtchenko et al., 2007] namely MODIS (MODerate resolution Imaging Spectroradiometer)[Salomonson et al., 1989b] and MISR (Multi-angle Imaging SpectroRadiometer) [Diner et al., 1998], are imagers that were designed with the aim to provide regular measurements on a large scale for aerosol related issues. The large 2300 km swath of MODIS onboard the NASA's Terra (launched in 1999) and Aqua (launched in 2002) spacecrafts, allows the acquisition of a global coverage within a period of 1 to 2 days. With its 36 spectral bands between 0.4 and 14.4 μm, the MODIS sensor exhibits enhanced spectral and spatial resolution (250-500 m) which are well suited for the derivation of aerosol information. The aerosol retrieval algorithm for MODIS which uses 7 wavebands of the instrument in the visible to near-infrared range (0.259-2.15 μm), is based on the work of Tanré et al. [1997] over the ocean and of Kaufman et al. [1997c] over land. The derivation of aerosol optical depth from the MODIS single-view instrument is based on the ratio of the visible to the near-infrared reflectance [Kaufman et al., 1997a]. The POLDER instrument which was developed by CNES (French National Space Agency) for the Japanese ADEOS (Advanced Earth

Satellite System) missions (launched in 1996), has 15 spectral bands which range from 443 nm to 910 nm. The spectral measurements are made for 12 different directions in 6 km² grid boxes, and in addition to the intensity field, the sensor provides the 2nd and the 3rd parameter of the Stokes vector characterizing the upwelling radiance [Deschamps et al., 1994]. The polarization feature of this spectroradiometer makes it far more advanced than the other instruments to determine the type of aerosols. Deuzé et al. [1999] and Deuzé et al. [2001] describe the aerosol retrieval methodology and the global distribution of tropospheric aerosols obtained from the daily global data of POLDER. The algorithm uses the 670 nm and 865 nm channels of POLDER to derive the aerosol optical depth and Ångström coefficient. In addition to MODIS, the Terra platform carries the MISR instrument, which measures the radiation in four spectral bands of the solar spectrum (0.446, 0.558, 0.672, and 0.866 μm) at 9 different viewing angles: a nadir view and 8 other symmetrical views (26.1, 45.6, 60.0, and 70.5) spread out forward and aftward of nadir. MISR data are provided at a spatial resolution of 275 m at all off-nadir angles and 250 m at nadir. With a 360 km swath, the multi-angle repeat cycle is achieved every 9 days at the equator, and every 2 days at highest latitudes. Martonchik et al. [1998, 2002] describe the technique used by the MISR Heterogeneous Land and Dark Water aerosol retrieval algorithm and its applicability to a wide variety of atmospheric conditions. Based on realistic aerosol and surface models, this algorithm derives simultaneously the aerosol and surface optical properties in boxes of 17.6x17.6 km². The major advantage of this algorithm is that it requires no assumption on land reflectance, the angular signatures allow to separate the surface-leaving reflectance from the intrinsic atmospheric radiance.

More recently (2006), the Cloud-Aerosol Lidar and Infrared Pathfinder Satellite Observation (CALIPSO) mission, established in the framework of a collaboration between CNES and NASA, provides a unique opportunity to improve our understanding of the role of aerosols and clouds in climate [Winker et al., 2003]. Like Terra, CALIPSO flies as part of the so-called A-Train constellation of Earth-orbiting spacecraft. The active Cloud-Aerosol Lidar with Orthogonal Polarization (CALIOP) onboard CALIPSO enhances the current capabilities in space-based aerosol observation, by delivering global information on their vertical distribution over all types of surface during both day and night. CALIOP is equipped with 2 laser transmitters which produce light pulses at 532 nm and 1064 nm at a repetition rate of 20 Hz. The receiver provides backscatter profiles from the surface to 40 km, with a vertical resolution of 30-60 km and horizontal resolution of 333 m. From these backscatter data, the profiles of cloud and aerosol backscatter and extinction coefficients as well as their respective layer heights can be retrieved [Vaughan et al., 2004]. In addition, the linearly polarized laser and the polarization sensitivity of the receiver can be used to calculate the linear depolarization from the two-channel lidar measurement, which allows the detection of non-spherical particles, and the distinction between ice and water clouds.

With the recent emergence of all these new spaceborne instruments, there has been significant progress in the development and the validation of algorithms dedicated to the retrieval of aerosol information, over large scales and at a high spatial resolution. However, ground-based aerosol products are less affected by uncertainties

than satellite-based information, and therefore constitute a reliable *ground truth* reference, which is of crucial importance for the evaluation and the validation of satellite retrievals.

1.5 This thesis

1.5.1 Motivation

Space-based aerosol observations represent a great potential for climate forcing and air quality research associated with aerosol particles, at both global and regional scales [Kaufman et al., 2002, Engel-Cox et al., 2004, Gupta et al., 2006, Al-Saadi et al., 2005, Schaap et al., 2009]. The research work described in this thesis aims to contribute to the development, the application and the validation of scientific methods for the retrieval of aerosol properties from satellite observations. In this respect, a new algorithm for the retrieval of aerosol optical properties over cloud-free scenes has been implemented. This algorithm uses the data from the SEVIRI (Spinned Enhanced Visible and Infrared Radiometer) imager onboard the European geostationary satellite MSG (Meteosat Second Generation) launched in August 2002, which delivers an image of a full Earth hemisphere every 15 minutes. The results generated by SARA (SEVIRI Aerosol Retrieval Algorithm) have been tested successfully with data from both space-based and ground-based measurements, and for various case studies (e.g. forest fires, dust storm, anthropogenic pollution). The high temporal sampling of this radiometer offers the unique opportunity to monitor aerosol diurnal variability and to follow the transport of atmospheric pollutants over Europe and the entire African continents.

1.5.2 Outline

The next chapter of this thesis is dedicated to the main principles and the data involved in aerosol remote sensing using the MSG-SEVIRI instrument. It starts with a detailed description of the measurements provided by this instrument, followed by an explanation of the general theory behind aerosol remote sensing from space observations, and by the description of the different ancillary data needed to perform aerosol retrievals with MSG-SEVIRI.

The third chapter explains the cloud detection method used for the stand-alone cloud screening process implemented within the aerosol retrieval algorithm for MSG-SEVIRI. The cloud detection process which consists of 4 main tests, generates a cloud mask that has been compared to another MSG-SEVIRI cloud mask obtained with the KNMI/MF algorithm, and to the cloud product derived for the MODIS instrument. This chapter has been accepted for publication in the International Journal of Remote Sensing in October 2008.

In Chapter 4, the method used for the retrieval of the aerosol optical properties over the ocean is presented. The reflectances measured in the visible and the near-infrared channels of the SEVIRI instrument are used to retrieve physical parameters such as the optical depth and the Ångström coefficient, which provide information on the aerosol load and size distribution. The results obtained for two case studies

were evaluated by means of comparisons with the aerosol product of MODIS, and with AERONET AOD measurements at coastal stations. This chapter has been submitted to the Journal of Geophysical Research in December 2008.

Chapter 5 deals with the methodology implemented for the extraction of aerosol information over land surfaces. This technique requires the use of a priori information on the spectral albedo of the land surface. For that purpose, MSG-SEVIRI measurements are used in synergy with the MODIS surface albedo/parameter product. The spectral AOD is validated with ground-based observations from the AERONET network, and evaluated against the results of the MODIS aerosol retrieval algorithm.

The 6th chapter provides conclusions and outlook for the research work described in this manuscript. This synthesis explores the potential benefit of the results together with their limitations, and proposes some perspectives for improvements and future investigations.

Chapter 2

MSG-SEVIRI and satellite-based aerosol retrievals

2.1 Introduction

Space-based passive aerosol remote sensing uses sensors that are designed to measure the upwelling radiance at the top of the atmosphere, from which the optical properties of aerosols can be derived. In inversion algorithms dedicated to aerosol retrievals, the most complex task is to separate the contribution of the surface from that of the atmosphere. When this distinction cannot be achieved in a straightforward manner, several assumptions and approximations have to be made. In this thesis, the Spinning Enhanced Visible Radiometer (SEVIRI) flown on the Meteosat Second Generation (MSG) satellite was considered. The first part of this chapter provides a description of the principal features of the MSG-SEVIRI imager. The second part of the chapter summarizes the main principles and the different assumptions behind the theory of aerosol retrieval in general, and those used within the SEVIRI Aerosol Retrieval algorithm. In addition, SARA retrievals rely on radiative transfer simulations using the Doubling-Adding KNMI (DAK) radiative transfer model, and require the use of ancillary data such as terrain elevation and chlorophyll concentration data for which details are given at the end of the chapter.

2.2 MSG-SEVIRI, instrument description

The new series of European geostationary satellites Meteosat Second Generation (MSG) operated by EUMETSAT (European Organisation for the Exploitation of Meteorological Satellites) was created to provide high quality data needed to forecast global weather conditions and monitor climate until the year 2012 [Schmetz et al.,

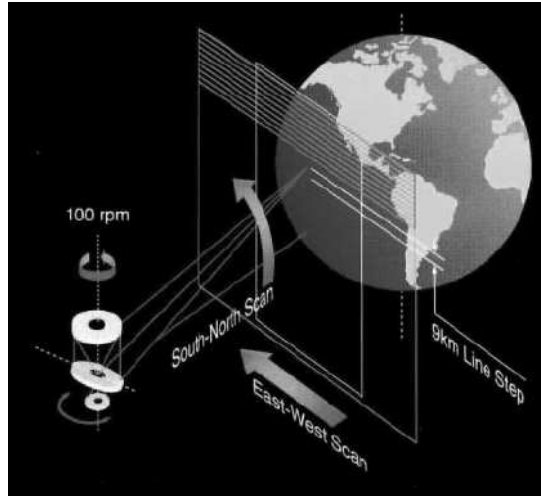


Figure 2.1: Schematic representation of the scanning principle used by the MSG-SEVIRI instrument, showing the line-by-line process, the spin rate of the satellite, the spatial resolution, and the spatial coverage of the observation. Source: Figure from [Aminou, 2002].

2002]. The MSG satellite is a spin-stabilized satellite rotating at a spin rate of 100 rotations per minute, and flying at an altitude of about 36 000 km above the Earth surface. The first satellite of this program MSG-1 also called METEOSAT-8, was launched in August 2002 and started routine operations in January 2004. MSG-1 has a nominal position centered over the equator and 0° in longitude. The Spinning Enhanced Visible Radiometer (SEVIRI) [Schmid, 2000] onboard the MSG satellite is a line by line radiometer that provides a complete scan of an Earth hemisphere with a repeat cycle of 15 minutes (see Figure 2.1). Thus, the SEVIRI imager carried on the MSG-1 spacecraft continuously observes Europe, the entire African continent and parts of the Indian and Atlantic Oceans. The SEVIRI instrument measures the upwelling radiance in 11 narrow bands and one broad band. The narrow channels which include 3 solar (0.6, 0.8 and $1.6 \mu\text{m}$) and 8 infrared wavelengths (3.9, 6.2, 7.3, 8.7, 9.7, 10.8, 12.0 and $13.4 \mu\text{m}$), provide data at a spatial resolution of $3 \times 3 \text{ km}^2$ at the sub-satellite point. The broadband channel covers the spectral range between 0.4 and $1.1 \mu\text{m}$, and has a higher spatial resolution than the standard channels with $1 \times 1 \text{ km}^2$ at nadir. The spectral features of the SEVIRI instrument, including the band width and the nominal wavelength of the different channels are summarized in Table 2.1. MSG-SEVIRI images complement the present measurements of polar orbiting sensors, by combining their multi-spectral features and high spatial resolution, with continuous observations at high temporal frequency. The infrared channels of MSG-SEVIRI can produce accurate pictures of the temperature of clouds, and of land

Table 2.1: Spectral features characterizing the SEVIRI channels.

Channel	Nadir resolution (km)	Central wavelength (μm)	Spectral band (μm)	Gaseous absorber / window	
1	VIS.0.6	3	0.635	0.56 - 0.71	window
2	VIS0.8	3	0.810	0.74 - 0.88	window
3	NIR1.6	3	1.64	1.5 - 1.78	window
4	IR3.9	3	3.90	3.48 - 4.36	window
5	WV6.2	3	6.25	5.35 - 7.15	Water Vapor
6	WV7.3	3	7.35	6.85 - 7.85	Water Vapor
7	IR8.7	3	8.70	8.30 - 9.10	window
8	IR9.7	3	9.66	9.38 - 9.94	Ozone
9	IR10.8	3	10.8	9.80 - 11.80	window
10	IR12.0	3	12.0	11.0 - 13.0	window
11	IR13.4	3	13.40	12.40 - 14.40	window
12	HRV	1	-	0.4 - 1.1	Carbon dioxide

and sea surfaces, at all times of the day and night. Using channels in the absorption band of ozone, water vapour and carbon dioxide, MSG-SEVIRI also provides information on the characteristics of atmospheric air masses. The solar channels 'VIS0.6', 'VIS0.8' and 'NIR1.6' of SEVIRI are crucial for cloud detection (cf. Chapter 3), and can be used to retrieve both aerosols and surface properties. Thus, the combination of channels supplied by MSG-SEVIRI offers a unique opportunity to monitor the weather conditions as they develop, and to study long-range transport of atmospheric constituents and their impact on the climate system. SEVIRI solar channels give measurements at similar wavelengths as channels from AVHRR, MODIS and GOES. The comparison with measurements from MODIS and GOES have shown that the calibration accuracy of these channels is within 5% [Govaerts et al., 2004, Doelling et al., 2004].

2.3 Illumination-observation geometry

The radiance measured by the sensor at the satellite level depends on the radiative properties of the atmospheric constituents and surface below. These properties depend on both the wavelength and the geometry of the illumination-observation. In remote sensing, several angles are used to describe both the sun illumination and the sensor observation geometries. The horizontal coordinate system is a celestial system of coordinates which uses the horizon of a specific observation point as the fundamental plane. With respect to this reference, for each location on the Earth surface, the apparent position of the sun and the sensor are specified by the zenith and azimuth angles (see Figure 2.2). The zenith angle describes the position of the sun (satellite) relative to the local normal to the horizontal plane. The azimuth angle is the angle on the horizontal plane, formed between a reference direction and the point directly

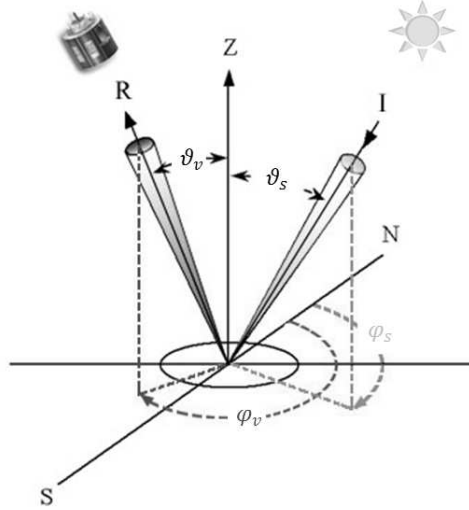


Figure 2.2: Schematic representation of the illumination-viewing geometry for satellite observations: θ_s and θ_v are the sun and viewing zenith angles, ϕ_s and ϕ_v the azimuth angles for the sun and the satellite.

beneath the sun (satellite). Here sun (satellite) azimuth is defined clockwise with respect to true north (i.e. geographic north). Thus azimuthal angles vary from 0 to 360° starting with true north as 0. The zenith and azimuth angles can be calculated from various formulas based on spherical trigonometry formulas.

2.3.1 Illumination

For the sun, the zenith angle is a function of the location latitude lat , the solar declination δ and the time angle h :

$$\cos(\theta_s) = \sin(lat_p) \sin(\delta) + \cos(lat_p) \cos(\delta) \cos(h) \quad (2.1)$$

The time angle defines the angle the Earth has turned since local solar noon. Local solar noon corresponds to the time during the day, when the sun is highest in the sky. Hence the time angle expression can be written as:

$$h = \frac{\pi t}{12} + lon_p - \pi + e_t \quad (2.2)$$

where lon_p is the longitude of the location on the Earth surface and t is time in the Universal Time Coordinate system. The hour angle can also be defined as the difference between the longitude of the observation and the longitude below the sun

(i.e. sun nadir). The eccentricity and the obliquity of the Earth orbit around the sun cause variations in the Earth's rate of rotation. As a result, solar noon differs by a correction offset e_t which is calculated using the Equation of Time (in hour unit) [Velds et al., 1992]:

$$e_t(f) = 0.0072 \cdot \cos(f) - 0.0528 \cdot \cos(2f) - 0.0012 \cdot \cos(3f) \\ - 0.1229 \cdot \sin(f) - 0.1565 \cdot \sin(2f) - 0.0041 \cdot \sin(3f)$$

in which f is a function of the day number d taken between 0 and 366:

$$f = \frac{2\pi}{366} \cdot d \quad (2.3)$$

The solar declination measures the angle between the sun rays and the equatorial plane of the Earth (counted positive northward and negative southward). It is analogous to the latitude of the sub-solar point. Due to the tilt of the Earth's rotation axis with respect to its orbital plane around the sun, the declination varies between approximately $+23.5^\circ$ in June (Summer solstice) to -23.5° in December (winter solstice). The declination angle can be calculated as a function of the day number [Spencer, 1971]:

$$\delta(f) = 0.006918 - 0.399912 \cdot \cos(f) - 0.006758 \cdot \cos(2f) - 0.002697 \cdot \cos(3f) \\ - 0.070257 \cdot \sin(f) - 0.000907 \cdot \sin(2f) - 0.00148 \cdot \sin(3f)$$

The azimuth angle of the sun can be calculated using:

$$\cos(\phi_s) = \frac{\sin(\delta) - \sin(lat_p) \cos(\theta_s)}{\cos(lat_p) \sin(\theta_s)} \quad (2.4)$$

$$\sin(\phi_s) = \frac{\sin(h) \cos(\delta)}{\sin(\theta_s)} \quad (2.5)$$

2.3.2 Observation

The zenith angle θ_v associated to the sensor position, is determined using the formula:

$$\tan(\theta_v) = \frac{\sin(\psi)}{\cos(\psi) - \frac{R_e}{R_e + A}} \quad (2.6)$$

The factor $\frac{R_e + A}{R_e}$ takes into account the Earth curvature with the Earth radius R_e , and a sensor orbit with an altitude A , which is assumed to be circular. ψ is the great circle angle (i.e. angle to the center of the Earth) between the subsatellite point

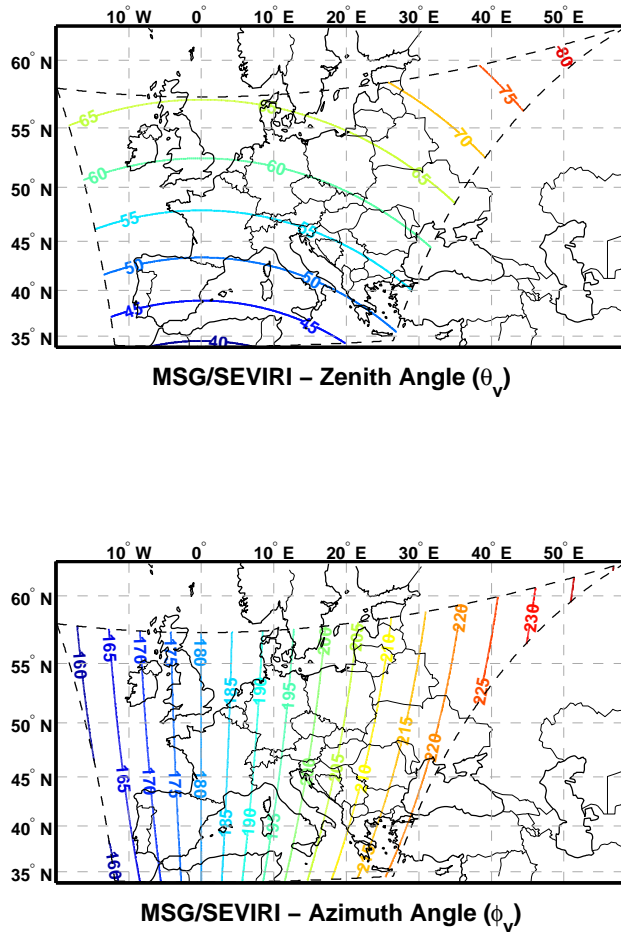


Figure 2.3: Observation geometry for MSG-SEVIRI: map of viewing zenith angle (upper panel) and viewing azimuth angle (lower panel).

(lat_v, lon_v) and the observed point (lat_p, lon_p) . This angle is calculated with:

$$\cos(\psi) = \sin(lat_p) \sin(lat_v) + \cos(lat_p) \cos(lat_v) \cos(lon_p - lon_v) \quad (2.7)$$

Since the subsatellite point of MSG is located at $(0^\circ, 0^\circ)$:

$$\cos(\psi) = \cos(lat_p) \cos(lon_p) \quad (2.8)$$

The azimuth angle of the satellite is a function of the geolocation coordinate and the aforementioned great circle angle ψ . It can be calculated with similar expression to those of the sun azimuth using the following equations:

$$\cos(\phi_v) = \frac{\sin(lat_v) - \sin(lat_p) \cos(\psi)}{\cos(lat_p) \sin(\psi)} \quad (2.9)$$

$$\sin(\phi_v) = \frac{\sin(lon_p - lon_v) \cos(lat_v)}{\sin(\psi)} \quad (2.10)$$

Like for the expression of ψ , due to the nominal position of the satellite, simplifications can be applied to obtain:

$$\cos(\phi_v) = \frac{-\sin(lat_p)}{\tan(\psi)} \quad (2.11)$$

$$\sin(\phi_v) = \frac{\sin(lon_p)}{\sin(\psi)} \quad (2.12)$$

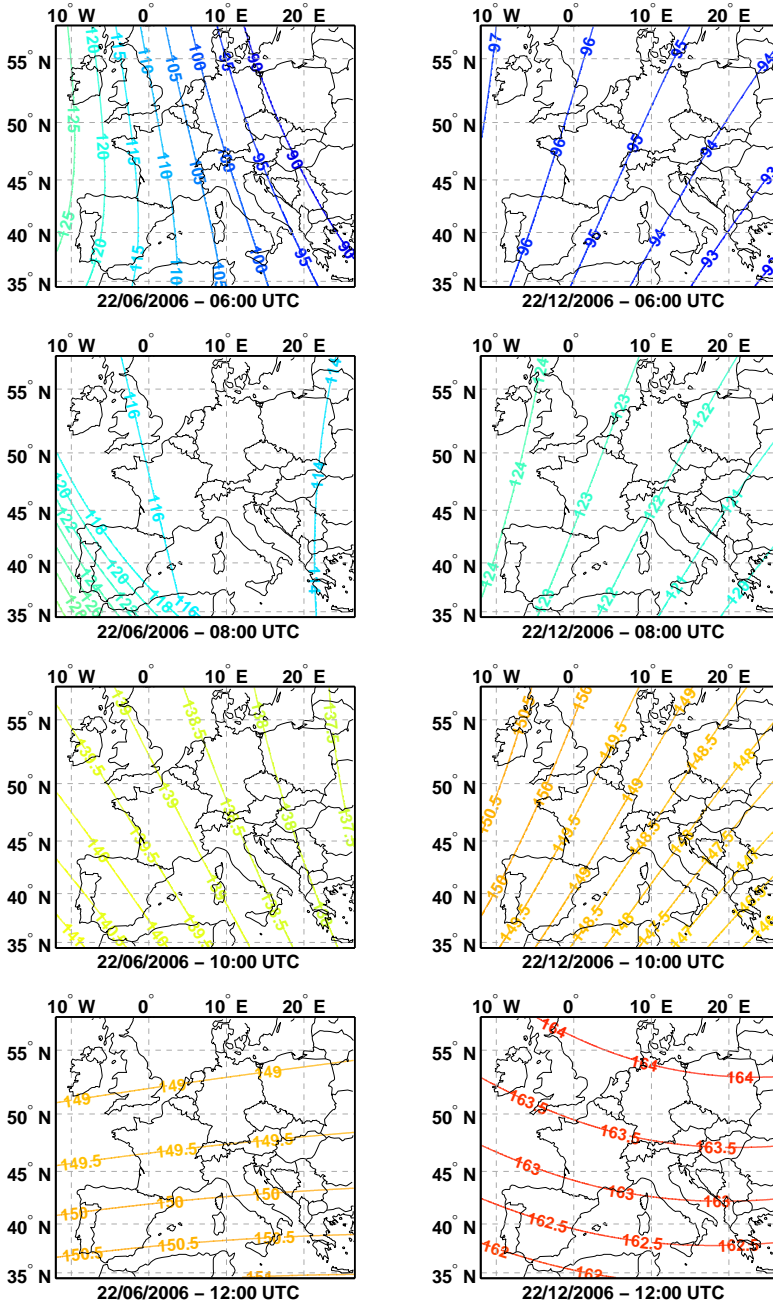
As an example, Figure 2.3 describes the viewing geometry of MSG-SEVIRI over Europe, with the maps of the satellite zenith and azimuth angle.

2.3.3 Scattering geometry

The combination of the illumination and the viewing geometry determines the scattering and the glint angle. The scattering angle Θ is defined by the angle formed between the incident direction of the radiation, and the direction of the radiation reflected toward the sensor. It is derived from:

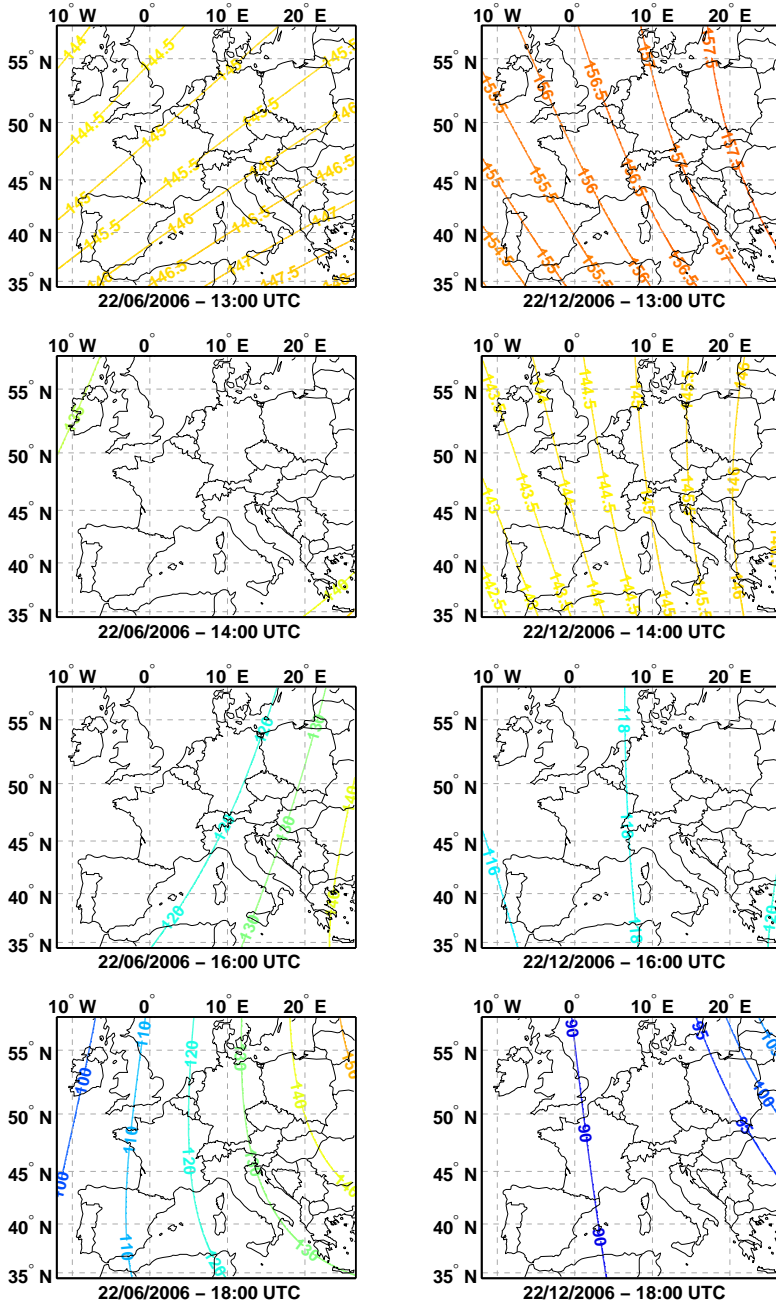
$$\cos(\Theta) = \cos(\theta_s) \cos(\theta_v) + \sin(\theta_s) \sin(\theta_v) \cos(\phi_r) \quad (2.13)$$

where ϕ_r which is the absolute difference between the satellite azimuth and the solar azimuth angles. Figure 2.4(a) presents an example of the diurnal variations of the scattering angles observed by MSG-SEVIRI over Europe for two days. June 22 and December 22 represent the two extreme cases corresponding respectively to the summer and the winter solstice, when the sun reaches its most northern or most



(a) First part

Figure 2.4: Maps of scattering angle for MSG-SEVIRI observations for 22 June (summer solstice) and for 22 December (winter solstice) 2006.



(b) Second part

Figure 2.4: Maps of scattering angle for MSG-SEVIRI observations the 22 June (summer solstice) and 22 December (winter solstice) 2006. (Con't)

southern position. During the course of a day, the scattering angle isolines rotate with the Earth rotation. The scattering angle reaches a maximum around noon, when the geometry of the observation gets the closest to backscattering, and this maximum is larger in the winter than in the summer. Another angular reference that is often used in remote-sensing is the glint angle. The glint angle is the angle in the scattering plane formed between the direction of backscattering ($\Theta = 180^\circ$) and the direction of scattering associated to the sensor field of view. The glint angle θ_g can therefore be obtained using:

$$\cos(\theta_g) = \cos(\theta_s) \cos(\theta_v) - \sin(\theta_s) \sin(\theta_v) \cos(\phi_r) \quad (2.14)$$

2.4 Theory for space-based retrievals

Assuming a plane parallel homogeneous atmosphere, the spectral bidirectional reflectance ρ at the Top of the Atmosphere (TOA) is a dimensionless parameter that can be derived from the radiance measurements $L(W.m^{-2}.s^{-1})$ provided by the satellite instrument using:

$$\rho(\lambda, \mu_s, \mu_v, \phi_r) = \frac{\pi \cdot L(\lambda, \mu_s, \mu_v, \phi_r)}{\mu_s \cdot F_0(\lambda)} \quad (2.15)$$

In this equation, μ_s , μ_v and ϕ_r are the cosine of the solar zenith angle, the cosine of the viewing zenith angle, and the relative azimuth angle ($\phi_s - \phi_v$). F_0 ($W.m^{-2}.s^{-1}$) is the extraterrestrial solar irradiance at the wavelength λ . It is the solar radiation incident at the top of the atmosphere, which is on average $1367 W.m^{-2}$ and varies within 3% as the earth orbits around the sun.

2.4.1 Atmosphere-surface coupling

The bidirectional reflectance observed at the TOA results from the contribution of scattering by the various constituents of the atmosphere (i.e. including gas molecules and aerosols), of the reflective properties of the underlying surface, and the scattering processes resulting from multiple surface-atmosphere interactions. The formulation of [Tanré et al. \[1979\]](#) models the TOA reflectance including all the different paths a photon could follow in the atmosphere before reaching the sensor:

$$\rho = \underbrace{\rho_{atm}}_{(1)} + \underbrace{T^\downarrow \rho_{sfc,dir} T^\uparrow}_{(2)} + \underbrace{t^\downarrow \rho_{sfc,dif} T^\uparrow}_{(3)} + \underbrace{T^\downarrow \rho'_{sfc,dif} t^\uparrow}_{(4)} + \underbrace{t^\downarrow \rho_{sfc,iso} t^\uparrow}_{(5)} \quad (2.16)$$

In this equation all terms depend on the wavelength and the sun-satellite geometry. Each numbered term is associated to the different type of light paths (see [Figure 2.5](#)). Term (1) corresponds to the intrinsic reflectance of the atmospheric layer which is commonly called the *path reflectance* of the atmosphere. It represents the part

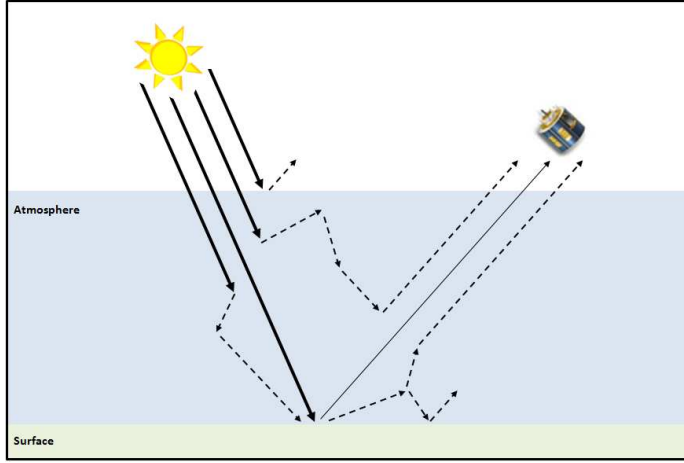


Figure 2.5: Schematic representation of the different paths a photon from the sun beam can follow before reaching the satellite sensor.

of the radiation which is reflected by the atmospheric constituents (i.e. gases and aerosols) toward the sensor.

On its way upward and downward across the entire atmospheric layer, the radiation is attenuated by absorption and scattering occurring within the atmosphere. This effect is represented by the different transmission coefficients (T, t). Both downward and upward transmissions are splitted into a direct (T^\downarrow, T^\uparrow) and a diffuse component (t^\downarrow, t^\uparrow) of the radiation. The direct transmissions accounts for photons that are not redirected by scattering on their way downward (upward), whereas diffuse transmissions accounts for photons that have undergone multiple scattering events on their way downward (upward).

Terms (2), (3), (4) and (5) are related to the various interactions between the radiation and the surface. In the above formulation, the directionality of the radiation reflected by the surface is taken into account. The surface reflectance is described by different components: a specular component $\rho_{sfc,dir}$, two diffused components $\rho_{sfc,dif}$, $\rho'_{sfc,dif}$, and an isotropic component $\rho_{sfc,iso}$. Term (2) considers both illumination and reflection through a direct path. $\rho_{sfc,dir}$ is the Bidirectional Reflectance Distribution Function (BRDF), which quantifies the angular distribution of the radiance reflected by an illuminated surface. In term (3) only the diffuse illumination of the surface is considered. $\rho_{sfc,dif}$ is the fraction of diffuse irradiance scattered in the viewing direction (μ_v, ϕ_v) under solar incidence μ_s . This quantity corresponds to the average of the surface BRDF weighted by the contribution of the downward diffuse

radiation to the total downward radiation over all directions of incidence:

$$\rho_{sfc,dif} = \bar{\rho}_{dir}(\lambda, \mu_s, \mu_v, \phi_r) = \frac{\int_0^{2\pi} \int_0^1 \mu \cdot L^\downarrow(\mu_s, \mu, \phi') \cdot \rho_{sfc,dir}(\mu, \mu_v, \phi' - \phi_r) d\mu d\phi'}{\int_0^{2\pi} \int_0^{\frac{\pi}{2}} \mu \cdot L^\downarrow(\mu_s, \mu, \phi') d\mu d\phi'} \quad (2.17)$$

Assuming reciprocity of $\rho_{sfc,dif}$ when μ_s and μ_v are interchanged, $\rho'_{sfc,dif}$ can be inferred from equation 2.17 using:

$$\rho'_{sfc,dif}(\lambda, \mu_v, \mu_s, \phi_r) = \rho_{sfc,dif}(\lambda, \mu_s, \mu_v, \phi_r) \quad (2.18)$$

In equation 2.16, term (5) combines downward and upward diffuse radiation ($t^\downarrow \cdot t^\uparrow$), and therefore has a small impact on the total signal observed at the TOA. Additionally, the diffuse radiation becomes isotropic after very few scattering events. This allows to approximate the surface reflection in term (5) by the value of by the hemispherical albedo of the surface target $\rho_{sfc,iso}$:

$$\rho_{sfc,iso} = \bar{\rho}_{dir}(\lambda) = \int_0^1 \mu \int_0^{2\pi} \int_0^1 \mu' \rho_{sfc,dir}(\mu, \mu', \phi' - \phi_r) d\mu' d\phi' d\mu \quad (2.19)$$

When the underlying surface reflects the radiation equally in all directions, it is referred to as a *Lambertian surface*. Under the Lambertian assumption, equation 2.16 is replaced by the widely used expression proposed by Chandrasekhar [1960]:

$$\rho = \rho_{atm} + \frac{\rho_{sfc}}{1 - S_{atm} \cdot \rho_{sfc}} T_{tot} \quad (2.20)$$

where T_{tot} is the total transmission of the atmosphere, including both diffuse and direct components of the radiation, for upward and downward paths ($T_{tot} = T_{tot}^\downarrow \cdot T_{tot}^\uparrow$). In expression 2.20, ρ_{sfc} is the albedo of the underlying surface. The factor $\frac{\rho_{sfc}}{1 - S_{atm} \cdot \rho_{sfc}}$ accounts for multiple-orders of scattering between the surface and the atmosphere, in which S_{atm} represents the spherical albedo of the atmosphere.

For the shortest wavelengths of the solar spectrum (i.e. uv range), the surface reflectivity is low for most surface types (except for snow and ice cover), with values ranging between 2 % and 8 % for both land and water bodies regardless of the season [Herman and Celarier, 1997, Herman et al., 2001, Koelemeijer et al., 2003]. The low near-UV surface albedo results in reduced sensitivities to errors in values associated with neglecting BRDF effects [Torres et al., 2002]. Consequently, the Lambertian approximation is satisfactory in this wavelength range.

In the visible and the near-infrared parts of the spectrum, surfaces such as the ocean or densely vegetated areas are dark for most geometries. However, these surfaces may be very bright when they are viewed under certain angles. This occurs

when the glint angle corresponds to the directions of specular reflectance which are related to the specific surface properties. As regards water bodies, this effect is called the *sun glint*. Over the ocean, the directions of specular reflectance can be calculated using the Fresnel coefficient formula applied to a flat or a wavy sea surface. For a perfectly flat ocean surface, the unique direction of specular reflection is determined by the Snell-Descartes law. Considering the ocean as a rough surface, the wave facets present various slopes, and behave as a collection of inclined mirrors. The sea state is described by the wave slope distribution which is related to the wind speed. Most models are based on the parametrization of the wave slope distribution proposed by [Cox and Munk, 1954]. Away from the sun glint, the reflectance of the sea surface is mostly due to its isotropic components namely the reflectance oceanic whitecaps and subsurface scattering from water constituents (see details in Chapter 4). Over land surfaces, there is a large variety of different surface cover types. The vegetation BRDF is a complex function of the zenith and the azimuth angles describing the illumination and the viewing geometry [Li and Strahler, 1992]. The most notable feature characterizing the directional signature of vegetation BRDFs is the *hot spot*. This effect occurs when the geometry of the observation gets close to backscattering and can lead to a significant and sharp increase of the surface reflectance. Away from the surface hot-spot, a Lambertian surface may be assumed. Sparsely vegetated or arid areas are very bright targets in the visible and the near-infrared, and they show more isotropic surface reflectances as compared to vegetated ones [Bacour et al., 2006]. Over the desert, the retrieval of aerosol can be done under the Lambertian assumption with reasonable accuracy [Takemata et al., 2000].

To retrieve aerosol over land, the surface contribution may be derived using a surface BRDF/albedo database when available. Under the assumption of a Lambertian surface, some aerosol retrieval techniques use the minimum LER (Lambertian Equivalent Reflectance) to estimate the surface reflectance [Kuśmierczyk-Michulec and de Leeuw, 2005, Koelemeijer et al., 2003]. The LER is the value of the reflectance for an isotropic surface, required to match the TOA measurement in an atmosphere devoid of aerosols. In this case, the surface reflectance of a target is determined from the minimum value of the LER observed over that target during a certain period. The shape of the BRDF can be simulated using different types of models. The parameters of these models are determined by fitting atmospherically corrected data to the chosen models. Analytical models such as the three-parameter linear Ross-Li model [Ross, 1981, Li and Strahler, 1992, Roujean et al., 1992], or the nonlinear Rahman-Pinty-Verstraete (RPV) model [Rahman et al., 1993, Minnaert, 1941, Henyey and Greenstein, 1941] have produced accurate fitting of atmospherically corrected observations from POLDER [Maignan et al., 2004], MISR [Lavergne et al., 2007], and from MODIS-MISR [Jin et al., 2003, Wanner et al., 1997]. The use of a relationship between the surface reflectance at visible and mid-infrared wavelengths is a mean to avoid the necessity of a surface *a priori* over land [Levy et al., 2007]. Assuming the shape of the BRDF to be much less dependent on the wavelength than on the viewing angle [Flowerdew and Haigh, 1997], Veeffkind [1999] used the dual-view feature of the AATSR (Advanced Along Track Scanning Radiometer) to correct for the surface contribution.

When aerosol retrievals make use of polarized light, the fact that atmospheric scattering is much more polarized than the radiation reflected from the surface allows another approach, as proposed by [Deuzé et al., 2001] for POLDER. The SEVIRI channels in the visible and the near-infrared, are close to some of the MODIS channels. Therefore, the parameters from the MODIS BRDF/albedo database [Schaaf et al., 2002] can be used to reproduce the surface reflectance over land for the appropriate geometry of SEVIRI observations (see details in Chapter 5). Atmospheric reflectance and transmission functions are pre-calculated by a radiative transfer model (see details in section 2.4.3).

2.4.2 Radiative transfer equations

Remote sensing of atmospheric constituents is based on radiative transfer theory. When radiation propagates through a medium, its energy is affected by scattering, absorption and emission processes. The radiative transfer equation provides a mathematical expression of these phenomena. The nature of this equation depends on the specific geometry and the physical properties of the propagation medium. The radiative transfer equation can be expressed for the monochromatic radiance L , with a general form that is valid regardless of the problem geometry [Lenoble, 1985]:

$$\vec{\Omega} \cdot \nabla L(\lambda, \vec{r}, \vec{\Omega}) = -\sigma_{ext}[L(\lambda, \vec{r}, \vec{\Omega}) - J(\vec{r}, \vec{\Omega})] \quad (2.21)$$

In this equation, \vec{r} defines the position of the point considered, and $\vec{\Omega}$ the direction of propagation of the radiation. The function $J(\vec{r}, \vec{\Omega})$ is called the source function, it represents both internal and external radiation sources. Equation 2.21 is solved for specific boundary conditions. In atmospheric applications, the plane parallel assumption is often used. In this case, a simplified form of the radiative transfer equation can be expressed in terms of the dimensionless optical depth τ . Thus, for a plane parallel atmosphere overlaying a black surface:

$$\mu \frac{dL(\lambda, \tau, \mu, \phi)}{d\tau} = L(\tau, \mu, \phi) - \frac{\omega_0}{4\pi} \int_0^{2\pi} p(\lambda, \tau, \mu, \phi, \mu', \phi') L(\lambda, \tau, \mu, \phi) d\mu' d\phi' \quad (2.22)$$

where p is the phase function and w_0 the single scattering albedo of an atmospheric layer with optical depth τ (see definitions in Chapter 1). The boundary conditions are defined by the upwelling and the downwelling radiances $L^-(\tau_{TOA}, \mu, \phi)$ and $L^+(0, \mu, \phi)$. Aerosol retrievals based on passive remote sensing techniques make use of the solar radiation as the source of light. Therefore downwelling radiance at the top of the atmosphere is determined from the direction (μ_s, ϕ_s) and the intensity of the incident solar radiation. For MSG-SEVIRI retrievals, the various interactions of the radiation with the surface are taken into account using the equations described in section 2.4.1, provided that the reflectance and the transmission functions of the atmosphere are known. For this purpose, the above equation is solved using a radiative

transfer model.

2.4.3 Radiative transfer model

Different approaches can be used to solve atmospheric radiative transfer equations, e.g., the Discrete Ordinate method (DISORT) [Stamnes et al., 1988], the Doubling Adding method [de Haan et al., 1987, Stamnes, 2001], Successive Order of Scattering (SOC) [Vermote et al., 1997], the Monte-Carlo method [Macke et al., 1999], the Spherical Harmonic Discrete Ordinate Method [Evans, 1998]. In these models the discretisation of the atmosphere is treated in different ways, either taking into account the sphericity or assuming a plane parallel geometry of the Earth-Atmosphere system. Some of them correct for the refraction, and/or perform polarization calculations. The radiative transfer equations are solved monochromatically, or provide spectral or broad band computations. The most complicated models allow to investigate two-dimensional and even three-dimensional effects. Therefore, depending on the application, an appropriate solver must be chosen. The classical radiative transfer models which treat a medium as a superposition of horizontally uniform plane-parallel layers, are well suited for the study of aerosol interactions with solar radiation. The basic assumptions state that particles in the medium are well separated, and that interferences from the light scattered by the neighboring particles can be neglected. The latter condition is satisfied when the distance between the particles is much larger than wavelength.

To simulate the signal measured by SEVIRI at the satellite level in different atmospheric scenarios, the Doubling-Adding KNMI (DAK) radiative transfer is used. This model has been developed at KNMI (Royal Netherlands Meteorological Institute) and performs monochromatic or narrow band multiple scattering calculations under the assumption of a plane parallel homogeneous atmosphere [de Haan et al., 1987, Stamnes, 2001]. DAK determines the radiative fluxes through the entire atmospheric layer subdivided in several sublayers. These calculations can include scattering due to aerosol and/or molecular scattering provided that the vertical profile of each atmospheric constituent is given as an input. Different aerosol models (i.e. scattering matrix, and single scattering albedo) can be associated to the different layers, and the turbidity of each layer is defined by setting its aerosol optical depth. The doubling-adding method consists of two steps which are repeated until the total optical depth of the layer is reached. When the "doubling" step starts, the transmission and the reflection are calculated for an optically thin layer so that only single scattering applies. In the second step or "adding" procedure, an identical layer is added on top of the previous layer, and the optical properties of the combined layer are calculated including internal scattering. Thus, the "doubling" allows to take into account multiple scattering. The two steps are successively repeated until the radiative fluxes between all layers are determined. To truncate the phase function and to determine the number of streams for multiple scattering calculations, DAK discretizes the zenith angles and the azimuth angles using respectively Gaussian points, and Fourier terms. The accuracy of DAK simulations is partly dependent on the numbers of Gaussian points and Fourier terms used. The number of zenith angles required for integration

increases with the anisotropy of the phase function.

2.4.4 Retrieval method

Given an appropriate model to represent atmosphere-surface interactions (see section 2.4.1), the outputs from the radiative transfer model are used to reproduce the reflectance measured by SEVIRI at the visible and the near-infrared wavelengths for different atmospheric 'scenarios'. These atmospheric 'scenarios' for use over Europe account for the presence of gases using the standard Mid-Latitude Winter (MLW) or Summer (MLS) profiles [McClatchey et al., 1972], and different aerosol loads defined by the aerosol optical depth at the reference wavelength of 500 nm. Rayleigh (i.e. gas) absorption and scattering are calculated for ozone, with cross sections based on the work of Bass and Paur [1984]. Several aerosol models are used to produce different Look Up Tables (LUT) in which reflectance, transmittance and transmission data are stored. The rayleigh LUT represents the case of an atmosphere devoid of aerosols (i.e. $\tau = 0$). The retrieval splits the TOA reflectance into two individual contributions:

$$\rho(\lambda) = \rho_0(\lambda) + \rho_{aer}(\lambda) \quad (2.23)$$

ρ_0 is the TOA reflectance for the case of a purely molecular atmosphere, and ρ_{aer} the reflectance caused by the presence of aerosols. The TOA reflectance is related to the aerosol optical depth by assuming a linear function of the AOD [Durkee et al., 1986]:

$$\rho(\lambda) = \rho_0(\lambda) + C(\lambda) \cdot \tau(\lambda) \quad (2.24)$$

The linearity of the above equation is not valid for high optical depths [Veeffkind, 1999, Kokhanovsky et al., 2009]. Although in most cases this approximation is sufficient, for dust events, the optical depth can reach values much larger than 1. For such situations, a third order polynomial approximation was used to interpolate the LUTs data. The reflectance at the top of the atmosphere is calculated for an external mixture of two aerosol types representing the dominant aerosol type for the fine and the coarse mode. The reflectance of the mixture can be approximated by the weighted average of the reflectance due to the individual contributions of each mode [Wang and Gordon, 1994]:

$$\rho_{aer}(\lambda) = \nu \cdot \rho_f(\lambda) + (1 - \nu) \cdot \rho_c(\lambda) \quad (2.25)$$

The atmospheric scenario (i.e. coarse-fine combination and AOD at 500 nm) that minimizes the least square error ϵ :

$$\epsilon_{w,f,c,\tau_{500}} = \sum_{i=1}^n \left(\frac{\rho^{meas}(\lambda_i) - \rho^{lut}(\lambda_i, \tau_{500})}{\rho^{meas}(\lambda_i) - \rho_0^{lut}(\lambda_i) + 0.01} \right)^2 \quad (2.26)$$

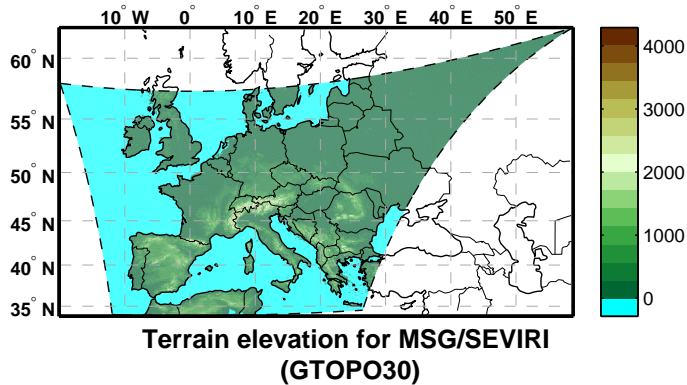


Figure 2.6: Map of terrain elevation over Europe, obtained from GTOPO30 data, and remapped for the projection grid of MSG-SEVIRI.

determines the aerosol model selected to derive the AOD. In the expression of ϵ , the wavelengths corresponding to the first three channels of SEVIRI are used, ρ^{lut} and ρ^{meas} refer to the modeled and the measured reflectance. The constant of 0.01 has been added to the denominator to avoid numerical overflows.

2.5 Ancillary data

2.5.1 Land-sea mask and topography

Since the reflectance properties of ocean and land surfaces differ strongly, the surface correction used in aerosol retrievals is performed differently over these two types of surface. Consequently, land pixels have to be distinguished from sea pixels. Moreover, since surfaces of equal aerosol extinction roughly follow the terrain contours, local elevation adjustment must be taken into account in the atmospheric correction. Here, pre-calculated atmospheric parameters are specified for a target at sea level. The measured reflectance is therefore adjusted by a factor corresponding to the ratio of the pressure at the ground elevation to the reference pressure, which is calculated using an hydrostatic vertical pressure profile. For these two purposes, the data from Global 30-Arc-Second Digital Elevation Model (GTOPO30) [U.S. Geological Survey, 1997] are used. The remapping of these ancillary data onto the MSG-SEVIRI images is done with a nearest neighbor interpolation to generate a land sea mask, and a bi-linear interpolation for elevation data. Terrain elevation values interpolated from the GTOPO30 dataset over Europe are displayed in Figure 2.6.

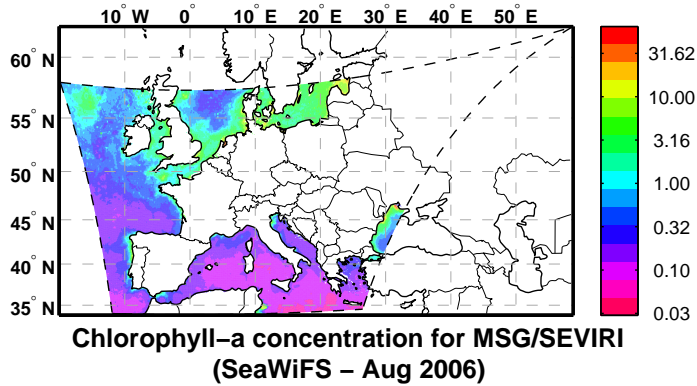


Figure 2.7: Map of chlorophyll-*a* concentration over Europe for August 2006, obtained from SeaWiFS data, and remapped for the projection grid of MSG-SEVIRI.

2.5.2 Chlorophyll concentrations

As mentioned in section 2.4.1, one of the effects that has to be taken into account for the sea surface reflectance is subsurface scattering. Subsurface scattering refers to the reflectance of the water constituents. Some substances present in suspended particles can enhance light scattering e.g., in sediments such as sand, silt, whereas others absorb the radiation at certain wavelengths and alter its characteristics. The most important light-absorbing substance in the ocean is chlorophyll, a green pigment used by phytoplankton organisms during photosynthesis. Chlorophyll absorbs preferentially in the blue and the red region of the solar spectrum [Hovis et al., 1980]. Therefore the contribution of chlorophyll to subsurface scattering is not expected to have a significant impact on the TOA radiation in the solar channels of SEVIRI (i.e. VIS0.6, VIS0.8, VIS1.6). It is accounted for using a parametrization of the upwelling radiance as a function of the chlorophyll concentration. The values of the chlorophyll concentration are obtained from the Level-3 monthly global dataset of SeaWiFS [Campbell et al., 1995]. In this dataset, the chlorophyll concentrations were derived using the ocean color algorithm for SeaWiFS [O'Reilly et al., 1998, Gregg and Casey, 2004]. Level-3 products of SeaWiFS are space/time averaged fields binned on a standard 9 km grid. Within the aerosol retrieval algorithm for SEVIRI, the value of the chlorophyll concentrations in a SEVIRI pixel is estimated by using a bilinear interpolation of the SeaWiFS data. Figure 2.7 shows an example of the chlorophyll concentration observed over a European scene for August 2006.

Chapter 3

Cloud detection*

Abstract

Since February 2003, the Spinning Enhanced Visible and Infrared Imager (SEVIRI) aboard the first Meteosat Second Generation (MSG) provides radiance data in 12 spectral bands for a full earth hemisphere every 15 minutes. This high frame rate renders it an excellent tool for studies of atmospheric transport of pollutants, aerosol and clouds. TNO (Netherlands Organisation for Applied Scientific Research) is currently developing an algorithm for the retrieval of aerosol properties from MSG-SEVIRI observations over cloud-free scenes. This requires rigorous cloud screening for which a fast and stand-alone algorithm is developed. The detection technique described in this paper which is based on ATSR-2 (Along Track Scanning Radiometer 2) cloud screening algorithm, can be easily implemented, and satisfactorily identifies clouds. The study presented here focuses on West-Europe for the year 2006. Cloud detection results are compared to the KNMI/MF (Royal Netherlands Meteorological Institute/Meteo-France) and the MODIS cloud detection algorithms. According to the statistics, the results obtained with our algorithm show good agreement (> 80%) with these data sets.

*Y.S. Bennouna, R.L. Curier, G. de Leeuw, J. Piazzola, R. Roebeling, and P. de Valk. An automated day-time cloud detection technique applied to MSG-SEVIRI data over Western Europe. *International Journal of Remote Sensing*. Accepted for publication: October 2008.

3.1 Introduction

The Meteosat Second Generation (MSG) geostationary satellite was launched in August 2002 and started routine operations in January 2004. The Spinning Enhanced Visible Infrared Radiometer SEVIRI [Schmetz et al., 2002] aboard the MSG satellite gives a full scan of the earth dish centered on the Equator and Greenwich meridian for 11 spectral bands. Compared to the original Meteosat radiometer, it has enhanced spectral characteristics, with double temporal sampling rate with an image every 15 minutes and increased horizontal resolution of 3 km at the sub-satellite point except for the High Resolution Visible (HRV) channel (1 km at the sub-satellite point). The spectral capabilities of the instrument allow various environmental remote sensing applications, and the need for accurate satellite-based cloud detection is particularly important because a number of these applications require cloud masking (i.e. aerosol retrievals, sea surface temperature retrievals, ocean color retrievals, surface albedo retrievals, sea ice mapping). Clouds generally have much higher reflectances than blue sky which causes strong reflection of the solar radiation at the Top of the Atmosphere (TOA). The magnitude of this effect depends on cloud type and cloud microphysical properties. Accurate cloud filtering is essential for retrievals of surface and aerosol properties, which are based on satellite observed spectral reflectances or brightness temperatures in case of cloud free conditions. As regards aerosol retrievals, any remaining cloud contamination can lead to large overestimation of the Aerosol Optical Depth (AOD). Therefore, the robustness of satellite retrievals of AOD depends largely on the accuracy of the cloudy and cloud contaminated pixels. During the last twenty years, various methods have been proposed for the detection and the classification of clouds using VIS/IR imaging radiometers: multispectral thresholding methods applied to individual pixels [Reynolds and Vonder Haar, 1977, Schiffer and Rossow, 1983, Saunders and Kriebel, 1988, Derrien, 1993, Feijt et al., 1999], spatial coherence methods [Coakley and Bretherton, 1982, Simmer et al., 1982], dynamic cloud clustering analysis [Desbois et al., 1982, Seze and Desbois, 1987], pattern recognition techniques [Ebert, 1987], and artificial neural networks techniques [Bankert, 1994]. The aim of this paper is to outline the cloud detection methodology used in the aerosol retrieval algorithm for MSG-SEVIRI, which is currently under development at TNO (Netherlands Organisation for Applied Scientific Research). It presents the development of a simple, stand-alone, fast and efficient day-time cloud detection process which doesn't use any ancillary data. Except over extremely bright or cold surfaces such as the desert and snow, clouds are generally brighter and colder than the underlying surfaces, and the screening process can be based on pre-defined thresholds for both reflectance and temperature. The determination of these thresholds is done through a histogram technique proposed by Koelemeijer et al. [2001], that was already used in the aerosol retrieval algorithm [Robles-Gonzalez, 2003] for the ERS-2 (European Research Satellite 2) ATSR-2 (Along Track Scanning Radiometer 2). The procedure was adapted to the MSG-SEVIRI spectral bands and updated according to recent improvements of the AVHRR Processing scheme Over cLOUDs, Land and Ocean (APOLLO) analysis tool [Kriebel, 2003]. Since aerosol retrievals are problematic over snow, the applicability of the cloud detection over snow covered areas is

not needed. The accuracy of this cloud screening technique has been evaluated over Europe (where desert areas are not common) by means of comparisons with other cloud mask products derived either from the same radiometer or from a different instrument on another platform such as Terra-MODIS (MODerate resolution Imaging Spectroradiometer).

3.2 Overview of cloud detection methods

The threshold methods are of two types, radiative transfer methods, and statistical methods. In radiative transfer methods, both cloud detection and cloud classification apply physical thresholding of the VIS/IR radiances on individual pixels. On the other hand, statistical methods are applied to image segments and use statistical properties of the radiance data.

Radiative transfer methods detect clouds through the spatial and the temporal variations they induce in infrared and visible radiance data. Thus clouds that do not alter or weakly alter radiances remain undetected. The radiance changes are determined by means of comparison between the surface properties inferred from satellite measurements at a given place and time and its simulated estimates in clear conditions calculated with a radiative transfer model [Rossow and Garder, 1993]. The decision tools involve one or a few selected spectral bands, and the cloud pixels are classified in cloud classes according to their radiative characteristics. This technique, which is certainly the simplest, was mainly developed during the 1980s and remains the most commonly used approach in cloud remote sensing. However, this method suffers from several problems: the high variability of clouds, the difficulty to accurately estimate surface emissivity over land (where the background is more uncertain), and to determine the most suitable bands. In consequence, the development of statistical methods has recently received increasing attention.

The statistical approach is based on the representation of one image segment in the spectral space. Assuming homogeneous targets, a surface or a cloud type can be identified by a high density peak in the bi- or multidimensional histograms. To improve the clustering process, statistical methods are applied on time-accumulated samples. Thus cloudy from clear conditions can be distinguished from statistical properties of an image ensemble. Statistical methods are generally more accurate than traditional threshold methods. They have the advantage of utilizing all available bands simultaneously to extract the information on a type of target. In addition, statistical analysis provides better separation of two types of targets with overlapping characteristics. However, the performance of statistical methods is limited by either the need of a training phase to build regional-based sets like in neural network approaches, or the requirement of *a priori* information on the data distribution in Bayesian methods. Threshold methods which are not affected by location and data distribution, are therefore more suitable for global applications. Another disadvantage of the statistical approach is that it lacks physical basis.

Cloud detection using only spectral bands becomes an extremely difficult task when spectral signatures in all bands are similar. Over bright and cold surfaces like

in the polar regions, the visible and the thermal contrast between cloud and the surface is very small, and in consequence threshold techniques are not reliable. As an alternative, the pattern recognition approach makes use of textural features which can also be combined with spectral features for a better detection accuracy [Ebert, 1987]. In this technique, the image is divided into homogeneous regions that are then used to classify each cell. However the calculation of texture features is computationally complex and time-consuming, so in areas where it is not necessary their use should be avoided.

3.3 TNO stand-alone Cloud Detection Algorithm

Since our aerosol retrieval algorithm is meant to derive aerosol properties using reflected solar radiation in the SEVIRI visible wavelengths during day-time, the cloud mask is generated by TNO stand-alone Cloud Detection Algorithm (TNO-CDA) for day-time only. The method used to identify cloud contaminated pixels is based on the work of Saunders and Kriebel [1988] that was carried out for detecting clear sky and cloudy radiances from the Advanced Very High Resolution Radiometer (AVHRR) on TIROS-N/NOAA polar orbiters. The main structure of the routines implemented for SEVIRI is similar to the automated version implemented by [Robles-Gonzalez, 2003] for ATSR-2, which is based on the algorithm developed by [Koelemeijer et al., 2001]. The code was adapted to fit the characteristics of MSG-SEVIRI, and updated according to the improvements implemented in the APOLLO cloud analysis tool [Kriebel, 2003].

3.3.1 General principles of the method

For the MSG-SEVIRI stand-alone cloud detection algorithm developed by TNO, a multispectral dynamic thresholding technique is adopted. This method can be easily applied with a limited number of channels. It relies on the simple physical principle that clouds are generally brighter and colder than most surface features. If the reflectance (visible range) of a pixel is above a certain threshold, or if the brightness temperature (infrared range) of a pixel is lower than a certain minimum value, this pixel is likely to be cloudy. However, the accuracy of the cloud detection depends on the extent of the clouds compared to the spatial resolution of the satellite scanner.

Determination of the threshold value remains the major difficulty in this method, because it depends on the range of reflectances and temperatures characterizing the selected area at the time of acquisition. Sea is usually much darker than land, with rather small horizontal gradients within hundreds of kilometers for both reflectance and surface temperature. On the other hand, the wide variety of land cover type provides a wide range of surface reflectances. As a consequence, the application of a fixed threshold would certainly lead to large errors. Therefore accurate cloud detection requires the determination of image-dependent thresholds to take into account surface properties as well as day to day variation of the meteorological conditions.

To this end image data sets of temperature and reflectance data are clustered to

form two different types of histograms. The automatic determination of appropriate thresholds requires the calculation of extreme points values (including minima, maxima, and inflection points) of these histograms. For this purpose, the cloud detection algorithm uses numerical methods from Numerical Recipes [Press et al., 1992]. The histograms are first smoothed with a low-pass filter which is based on a Fast Fourier Transform approach. Once the smoothing process has been performed, a Lagrangian interpolation by cubic splines is applied to compute the extreme points (i.e. where the first derivative becomes null). From the latter, appropriate thresholds can be derived to make the distinction between cloud-free and cloud-contaminated pixels. However, due to the fixed size of the bins, some images might produce smoothed histograms with a shape which prevents the correct computation of extreme points. In such cases, to prevent a test from being completely disabled, the threshold is set to a default value.

The method further includes tests involving pseudo-channels created from linear or non-linear combinations of actual channels. For instance, brightness temperature differences or reflectance ratios of two channels are commonly employed and provide information beyond what can be extracted from a single spectral band. Additionally, the spatial uniformity of clouds is checked through threshold tests on the standard deviation for temperature and reflectance data.

Thus, this histogram technique which is rather easy to implement, enables fast detection of cloud contaminated radiances without the use of auxiliary data from external sources (i.e. numerical weather prediction model or in-situ observations).

3.3.2 Test description

The cloud detection technique developed for MSG-SEVIRI makes use of the same satellite data needed in the aerosol retrieval algorithm, namely reflectances at $0.635 \mu\text{m}$ (channel 1), $0.810 \mu\text{m}$ (channel 2), and $1.64 \mu\text{m}$ (channel 3), together with brightness temperature measurements at $10.8 \mu\text{m}$ (channel 9) and $12.0 \mu\text{m}$ (channel 10). The detection process applied in the TNO-CDA consists of 4 different tests. With the help of a land-sea mask, a distinction is made between land and ocean, for which different tests apply. The land-sea mask is derived from the Global 30-Arc-Second (GTOPO30) Digital Elevation Model (DEM) data [U.S. Geological Survey, 1997], which were remapped to the normalized geostationary projection of MSG (i.e. polar stereographic grid centered at (0,0)) at the resolution of the SEVIRI instrument ($3 \times 3 \text{ km}^2$ at the subsatellite point). This resampling is done through a nearest neighbor interpolation.

Test 1: The Infrared Gross Temperature Test

The Infrared Gross Temperature Test (test 1) uses brightness temperature at $12.0 \mu\text{m}$ to detect the coldest areas in the image. The latter correspond to medium or high clouds, [Derrien, 1993] characterized by cloud-tops much colder than most land and sea surfaces. The histograms are produced with the use of all pixels falling within a reasonable temperature range (i.e. 260 deg K and 310 deg K), and each bin has a

width of 1 degree. Over land, vegetated surfaces are identified using the threshold test described below (test4). For these clear vegetated pixels, the temperature threshold is calculated. Since plant evapotranspiration has a cooling effect, vegetated areas are generally colder than other land surfaces (soil, urban, sparsely vegetated). Vegetated areas thus can be used to determine a valid threshold for all land surfaces. This may not be true when a temperature inversion occurs, but this situation is so rare during day-time with clear sky that it is not expected to have a significant effect on the cloud mask. Due to potentially large spatial variability of surface temperatures over land, the temperature threshold associated with this test is latitudinally dependent. In this study, Europe has been divided in 7 horizontal zones (of equal size in pixels) for which 7 thresholds are calculated, one for each region. As regards to sea pixels, they are all used to produce a single histogram for the whole scene, from which the temperature threshold over sea is estimated.

Figure 3.1(a) shows an example of the temperature histogram analysis performed over land pixels in a single sub-zone of the scene, for a SEVIRI image acquired on 29 October 2006 at 10:00. The brown colored histogram corresponds to land pixels, and green bars display the same information for identified clear vegetated areas. For this subzone of the image, most pixels have temperatures lower than 300 K. In this example, the calculation of the second derivative by the "Spline" routine (see section 3.3.1) determines an inflection point at 277 K, which is used as threshold value for this part of the scene. Any land pixel showing a temperature below this limit is rejected as cloudy. For the whole scene, the temperature test applied to sea pixels is illustrated in Figure 3.1(b). In the same manner as for land, the inflection point below the peak temperature, which is found around 280 K, discriminates cloud free from cloud contaminated pixels over the ocean. All values to the left of this point indicate cloud presence.

Test 2: The Spatial Coherence Test

The Spatial Coherence Test (test 2) aims to detect small cloud amounts and clouds presenting low optical thickness (i.e. cloud edges, thin cirrus, and small cumulus) by using the standard deviation of the $10.8 \mu\text{m}$ brightness temperature in a 3×3 pixel array. To avoid misclassifications due to large horizontal variations of temperatures which may occur over land during the day, this test is applied only over the ocean. Each pixel where the temperature differs from its neighbours by more than 2 degrees is suspected to be cloudy. However, such variations in temperature can also be caused by oceanic upwellings. Therefore a second test needs to be done on reflectance standard deviation as well. Thus, the pixels are flagged as cloudy when both of the following criteria apply: (1) standard deviation in temperature above the limit, (2) they either have been determined as cloudy by any of the other tests or the variability between surroundings pixels is more than 5 percent in reflectance .

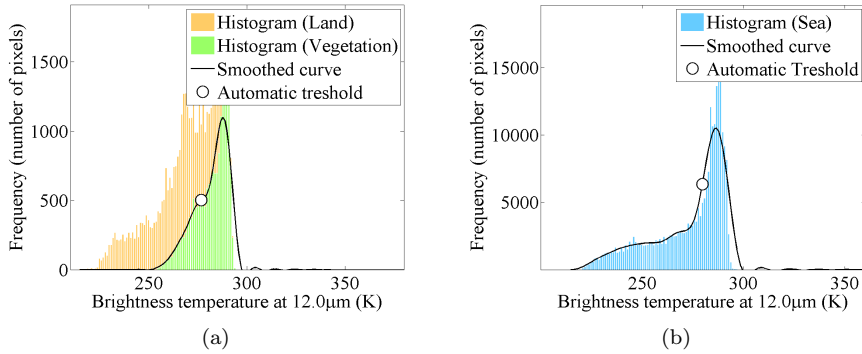


Figure 3.1: Infrared Gross Temperature Test histograms over Western Europe for 29 October 2006 at 10:00 UTC, in (a) Land case and (b) Sea case. Bars in orange and blue represent the histograms including all land, and sea pixels. Green bars correspond to pixels determined as clear vegetated by test 4 (see text for further explanation).

Test 3: The Dynamic Visible Test

The Dynamic Visible Test (test 3) takes advantage of the strong reflectance of clouds as compared to that of land and sea surfaces. This test has particular importance for the detection of low clouds [Derrien, 1993]. Clouds have similar reflectance signatures in the two visible channels, but sea surfaces reflect more radiation in channel 1, and land surfaces look brighter in channel 2. Therefore, to take advantage of an enhanced contrast between cloud and surface targets, this test uses the $0.635 \mu\text{m}$ reflectance over land, and the $0.810 \mu\text{m}$ reflectance over sea. Both land histograms and sea histograms are constructed with 1% reflectance bin width. Over sea, all pixels are used to construct one histogram. Over land, only cold land pixels identified by the temperature test are selected based on the visible test.

An example of a reflectance histogram at $0.635 \mu\text{m}$ is shown in Figure 3.2(a). In this particular situation, two peaks can be seen. The peak centered over much higher values indicates clouds with a reflectance around 0.7. The analysis also shows that land reflectivity spreads roughly between 0.1 and 0.3, with most land surfaces having a reflectance of approximately 0.2 and leading to a second peak in the histogram. The first inflection point encountered above the peak reflectance is calculated with the method described in section 3.3.1. Thus the reflectance threshold is set to 0.26. Land pixels with higher reflectivity are considered to be cloudy. Similarly, Figure 3.2(b) displays the reflectance histogram over sea areas for the same sample image. Sea surfaces are very dark, their reflectance can reach a maximum of approximately 0.15. For this case, the automatic process finds a threshold value of 0.14, and brighter sea pixels suggest cloud contamination.

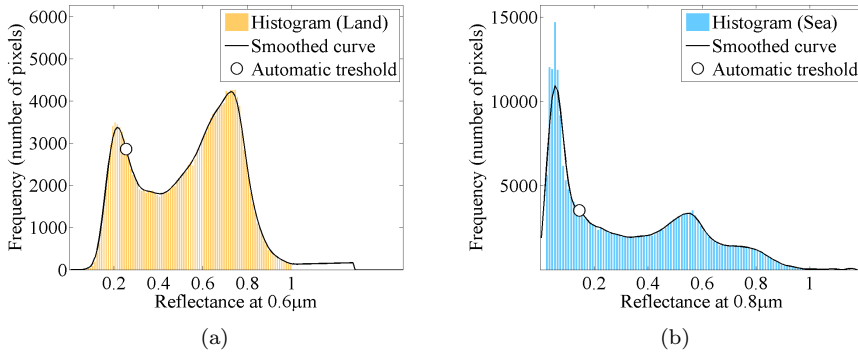


Figure 3.2: Dynamic Visible Test histograms over Western Europe for 29 October 2006 at 10:00 UTC, in (a) Land case and (b) Sea case (see text for further explanation).

Test 4: The Dynamic Ratio Test

The Dynamic Ratio Test (test 4) uses the ratio of the two visible reflectances provided by SEVIRI:

$$R = \frac{R_{0.8}}{R_{0.6}} \quad (3.1)$$

$R_{0.6}$ and $R_{0.8}$ are the reflectances centered at $0.635 \mu\text{m}$ and $0.810 \mu\text{m}$. Given the relative reflectivity of the different types of targets at these two wavelengths (see description of test 3), R is around 1 for clouds, whereas larger values are observed for land surface reflectances, and $R < 1$ for ocean surface reflectances. However, the reflectance ratio of poorly vegetated areas e.g. in central Europe reaches values close to 1, hence using the ratio to distinguish between clouds and sparsely vegetated land surfaces can lead to numerous mis-detections over land [Kriebel, 2003]. Consequently, the ratio test is not used to determine cloud contaminations over land. It is however used to isolate cloud-free vegetated areas with reasonable confidence. Thus all pixels with a ratio higher than 1.6 are classified as cloud-free vegetated targets.

Figure 3.3 shows the reflectance ratio histogram obtained for sea pixels. Cloudy pixels are grouped around the peak centered close to 1. Here, the Lagrangian interpolation (see section 3.3.1) determines a maximum which is reached for a reflectance of 1.09. The lower inflection point gives a limit of 0.98 below which all sea pixels are classified cloud free.

As mentioned before, depending on the scene observed, the smoothed histograms obtained are not necessarily gaussian shaped. When this is the case, the method used to calculate extreme points cannot be applied, and hence the cloud test cannot be applied either. To avoid significant underestimation of the cloud cover, the threshold is set to a default value for use in this particular situation. In Test 1, when no

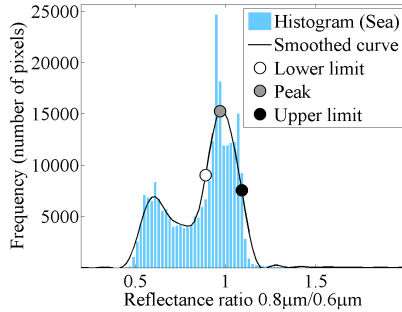


Figure 3.3: Dynamic Ratio Test histogram over Western Europe for 29 October 2006 at 10:00 UTC, as applied over sea (see text for further explanation).

automatic threshold is found, the minimum possible temperature of a surface target is set to 280 K (with no distinction in surface type). When Test 3 is used in default mode, it treats (independently of latitude and season) as cloudy: all land pixels with a reflectance above 25 % at $0.635 \mu\text{m}$, and all ocean pixels with a reflectance exceeding 10% at $0.810 \mu\text{m}$. Although the default limit of Test 3 over land would certainly fail over the desert, and might be slightly too strict for drylands in Southern Europe, it is suitable over most of Western Europe. Hence these default thresholds may have to be appropriately tuned for such bright surfaces. Whether the threshold is determined automatically or by a default value, due to their brightness and low temperatures, snow areas are not distinguished from clouds, and the corresponding pixels are flagged as cloudy. However, this limitation of the cloud detection algorithm is not much of an issue as aerosol retrievals cannot be performed over snow.

3.3.3 Detection scheme and results

The detection process consist of the 4 tests described in the previous section. From the histogram analysis, each single detection test suspects a group of pixels of being cloudy. Areas of the image suspected to be cloudy present a test flag equal to 1. A slightly different scheme applies over land and sea areas. The implementation of the 4 tests is schematically recapitulated in Figures 3.4 and 3.5, for scenes over land and sea, respectively. As mentioned in section 3.3.2, in term of cloud detection, Test 4 is not decisive over land (i.e. flag value not filled). Test 1 uses the group of pixels identified as 'clear vegetated' by Test 4 to determine a threshold. This threshold is then applied to all land pixels to identify cold land areas (Test 1 = 1). Test 3 applies differently depending on the output of Test 1, and it is meant to detect bright areas (Test 3 = 1). In the sea case, all the tests are applied independently except for Test 2. In the independent tests, the individual thresholds are inferred from all sea pixels, and applied to the latter. Test 1 detects cold areas (Test 1 =1), Test 3 bright areas (Test 3 =1), and Test 4 areas with a visible ratio close to 1 (Test 4 =1). Test 2 looks for pixels with high standard deviation in brightness temperatures among pixels with

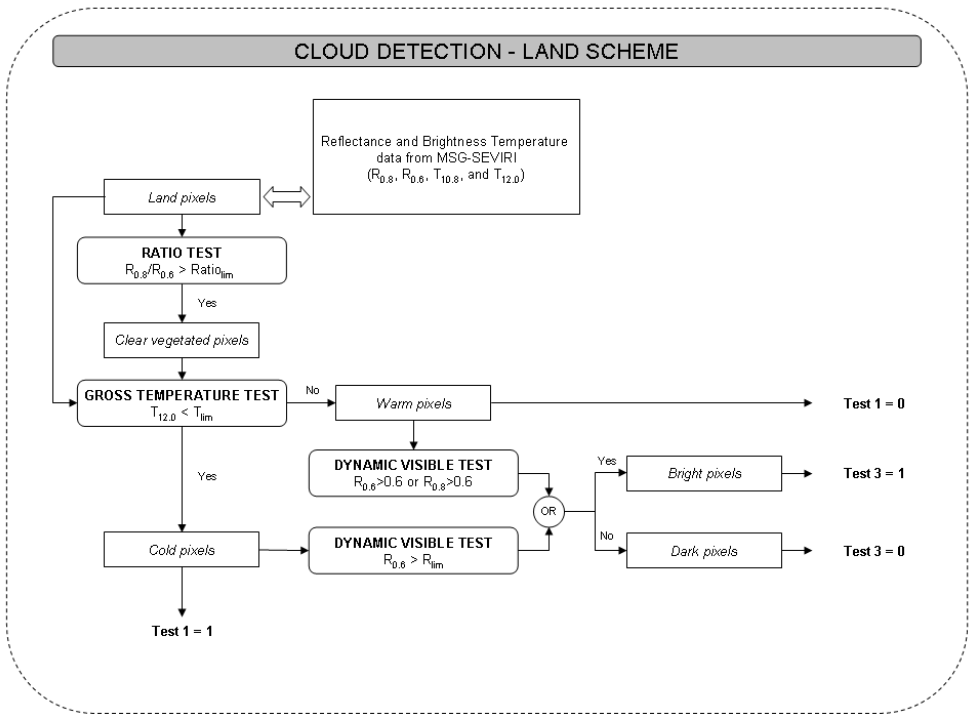


Figure 3.4: Description of the test sequences used in TNO-CDA developed for MSG-SEVIRI, for land pixels. Rectangles represent the data corresponding to a particular group of pixels within the image. These distinctions may be derived from the result of a test, and used as an input for other tests. For the areas suspected to be cloudy by a test, the test flag is set to 1, to 0 otherwise.

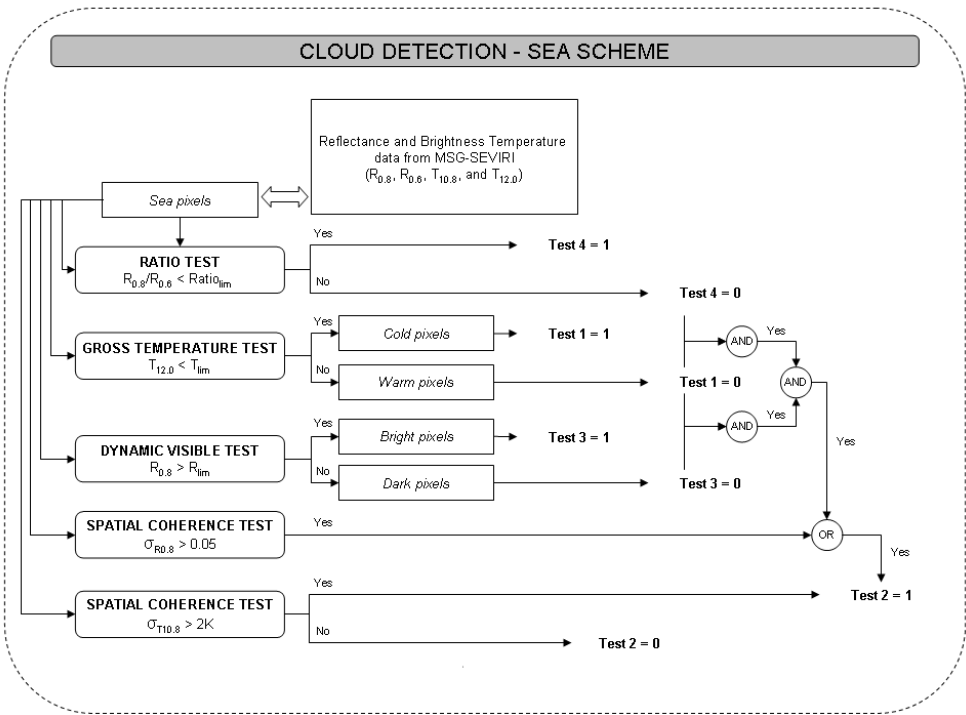


Figure 3.5: Description of the test sequences used in TNO-CDA developed for MSG-SEVIRI, for sea pixels. Rectangles represent the data corresponding to a particular group of pixels within the image. These distinctions may be derived from the result of a test, and used as an input for other tests. For the areas suspected to be cloudy by a test, the test flag is set to 1, to 0 otherwise.

a high standard deviation in reflectance or a null output for the other tests (Test 2 =1).

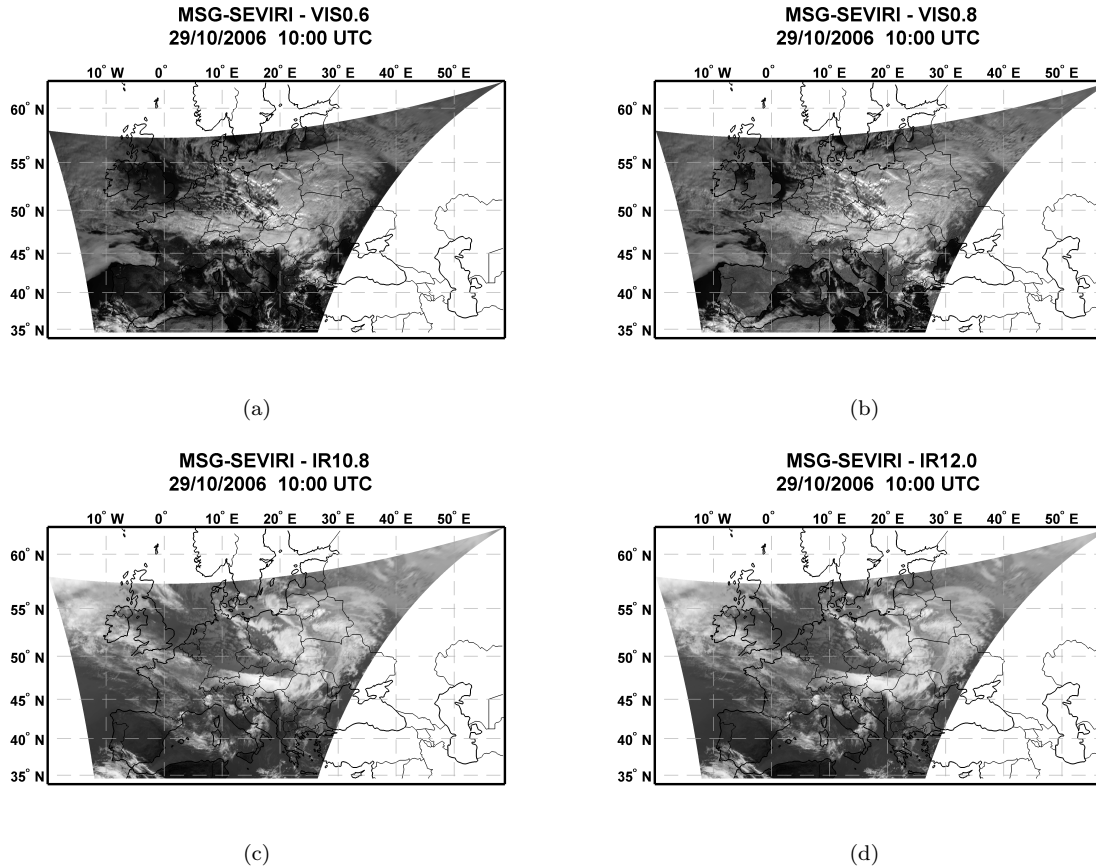


Figure 3.6: MSG-SEVIRI images over Western Europe for 29 October 2006 at 10:00 UTC, for the 4 channels used in the TNO cloud detection algorithm. (a) channel 1 - VIS0.6 (b) channel 2 - VIS0.8 (c) channel 9 - IR10.8 and (d) channel 10 - IR12.0.

The results from the cloud detection routines running in the aerosol retrieval algorithm, are stored in output files, which include the result of each individual test. To illustrate the type of information that is extracted from the data of 4 SEVIRI channels (see Figure 3.6), the map displayed in a mercator projection in Figure 3.7 shows the different combinations of tests identifying cloud occurrences, over Europe on the 27th of October 2006. The correspondence between the map colors and test combinations is explicated in Table 3.1. Over land, most areas flagged as cloudy by Test 1 are flagged as cloudy by Test 3 as well (dark blue). However, Test 3 seems less strict than Test 1 on the edges of clouds. For sea, Test 1, 3 and 4 generally identify the same areas as cloudy (yellow). Nevertheless, Test 4 seems to detect cloud targets that Test 1 fails to detect. Test 2, which is exclusively applied in the sea case, detects only a very small percentage of cloudy pixels located either on the edges of the clouds, or over broken cloud fields. From these results, a pixel is considered to be cloud contaminated if any of the individual tests has detected a contamination. A pixel is assumed to be clear only if it has been labeled as cloud free by all tests. Although no confidence flag is determined from these results, the number of tests that have flagged a pixel as cloudy can give an indication on the likelihood of cloud contamination.

3.4 Comparison with other cloud masks

To evaluate the accuracy of the cloud mask obtained through the stand-alone algorithm, the results have been compared to other cloud products generated with different algorithms: the KNMI/MF (Royal Netherlands Meteorological Institute/Meteo-France) algorithm for MSG-SEVIRI, and the MODIS algorithm. In the study presented here, the screening method has been applied to a limited area of the MSG-SEVIRI disk, covering mainly the western part of Europe. To test the applicability of the method in various conditions, it was applied in different seasons during the year 2006.

3.4.1 MSG-SEVIRI comparisons

KNMI/MF algorithm

KNMI has adopted the Cloud Mask (CMa) and Cloud Type (CT) algorithm developed by METEO-FRANCE [Derrien and le Gléau, 2005] in the Satellite Application Facility for Numerical Weather Prediction (SAFNWC) context. The cloud mask is determined by applying a number of tests depending on illumination: night, day, twilight and sunglint, and surface conditions (e.g. sea, land, snow covered and sea ice). Most thresholds are determined from satellite-dependent look-up tables using as input the viewing geometry (sun and satellite viewing angles), NWP forecast fields (surface temperature and total atmospheric water vapour content) and ancillary data (elevation and climatological data). These thresholds are computed at a user defined spatial resolution, which is specified by the number of SEVIRI infrared pixels. Some thresholds are empirical constants or satellite-dependent values. The threshold tests are applied both on a single spectral channel, and on the difference between

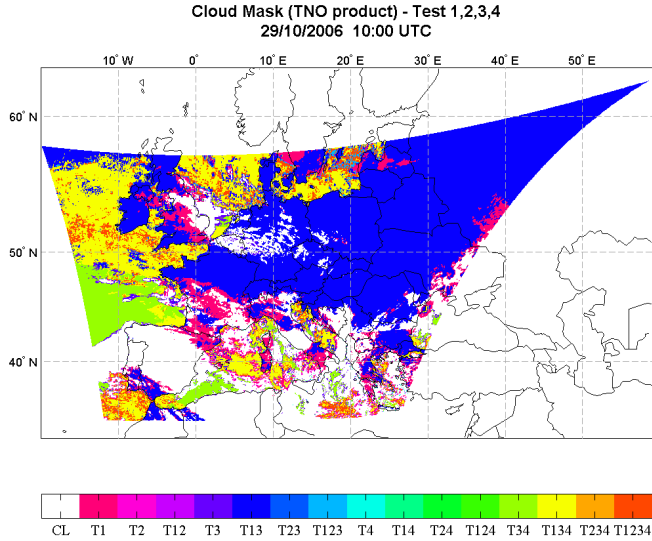


Figure 3.7: Cloud test results obtained with TNO-CDA, over Western Europe for 29 October 2006 at 10:00 UTC. Each color corresponds to a different combination of tests that have all flagged the same pixel as cloudy. (see Table 3.1 for details).

Table 3.1: Code signification for the result map of TNO cloud detection algorithm.

Legend Code	Test 1	Test 2	Test 3	Test 4
CL	Clear	Clear	Clear	Clear
T1	Cloudy	Clear	Clear	Clear
T2	Clear	Cloudy	Clear	Clear
T12	Cloudy	Cloudy	Clear	Clear
T3	Clear	Clear	Cloudy	Clear
T13	Cloudy	Clear	Cloudy	Clear
T23	Clear	Cloudy	Cloudy	Clear
T123	Cloudy	Cloudy	Cloudy	Clear
T4	Clear	Clear	Clear	Cloudy
T14	Cloudy	Clear	Clear	Cloudy
T24	Clear	Cloudy	Clear	Cloudy
T124	Cloudy	Cloudy	Clear	Cloudy
T34	Clear	Clear	Cloudy	Cloudy
T134	Cloudy	Clear	Cloudy	Cloudy
T234	Clear	Cloudy	Cloudy	Cloudy
T1234	Cloudy	Cloudy	Cloudy	Cloudy

two spectral channels. The threshold values themselves depend on surface type and illumination conditions. The local spatial texture is also used in the tests to discriminate clouds from clear conditions. The tests are performed per pixel in a sequential order until one of them is positive. The difference between the derived pixel value and the threshold value is also an indication of the quality of the test, e.g. a very cold temperature of a pixel well below the threshold value is very likely to be a cold cloud top. For a limited period the cloud mask has been compared to ground based observations. The comparison showed a high accuracy with a low false detection rate (i.e. number of false detection over the number of real detection) for both clear and cloudy conditions. Low clouds are most challenging to determine correctly. Also snow covered land poses a challenge in unfavorable illumination conditions. For the year 2006, the MSG-SEVIRI cloud mask product provided by KNMI is available every 15 minutes after Julian day 100, and at 3 hourly intervals before that date.

Comparison of KNMI/MF and TNO-CDA cloud masks

The results obtained with the TNO cloud detection algorithm and the KNMI cloud mask product were compared for 4 representative periods of one week in January, May, August, and October 2006. Except for the winter period (January), for which the KNMI product was available only on a 3-hourly basis, the comparison study involves all images acquired by SEVIRI between 6:00 and 18:00 UTC. The KNMI cloud mask product provides 5 different flags for a SEVIRI image: 'out of processing region', 'no cloud', 'possible cloud', 'cloud', 'snow' and 'not processed'. For this comparison study, no distinction was made between the three flags corresponding to 'out of processing region', 'snow', or 'not processed'. The associated pixels are set to a new flag: 'Not Determined'. Thus, no conclusions can be drawn from the comparison made for these pixels. This simplification has little influence on the results of the comparison study because the concerned regions usually represent very small areas.

The TNO cloud mask provides simple binary information: a pixel is either 'cloud free' or 'cloud contaminated', no confidence index is given. Because the KNMI cloud mask can show large regions identified as 'possible cloud', it has been converted as well to binary information by simply replacing the 'possible cloud' flag by a 'cloudy' flag. This leads to the type of comparison maps presented in Figures 3.8(a)-(d). Each map corresponds to a representative time within each of the 4 periods outlined above. The code for the colors used is given in Table 3.2. Each color corresponds to a unique combination of flags of the two products, and the related percentage appears in Table 3.3.

All image samples presented here were chosen because they were characterized by particularly cloudy conditions, where the cloud cover represents at least 40 % of the image. Regions identified as cloudy or as clear by both algorithms are represented respectively in blue and grey. Yellow and red colored areas indicate that the two different products disagree. The presence of yellow indicates a stricter behaviour of the KNMI cloud mask as compared to the TNO screening product, and visa versa for red.

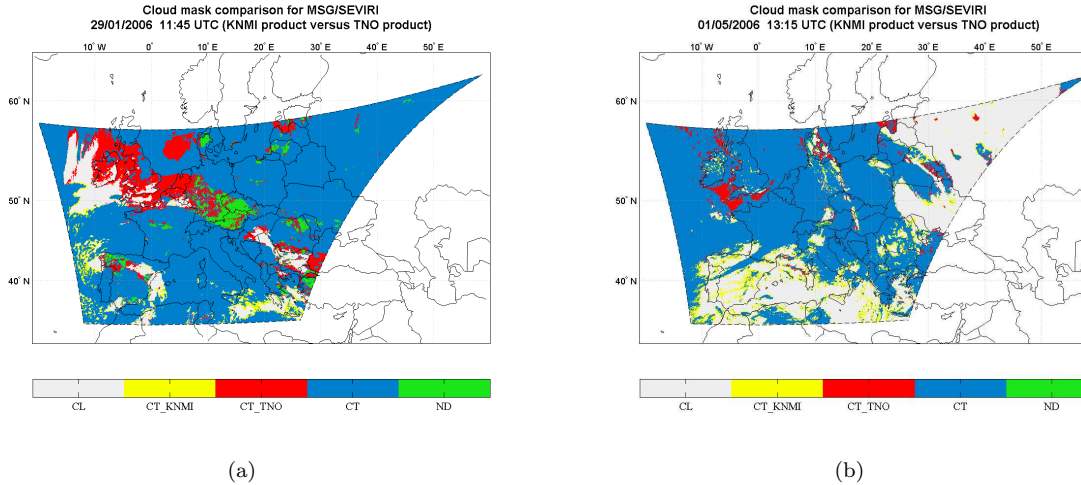


Figure 3.8: Comparison of the KNMI/MF and TNO-CDA products over Western Europe for (a) 29 January 2006 at 11:45 UTC, (b) 1 May 2006 at 13:15 UTC, (c) 4 August 2006 at 14:00 UTC and (d) 29 October 2006 at 10:00 UTC. The meaning of the different abbreviations used in the legend are explained in Table 3.2. The percentages represented by the different colors are available in Table 3.3.

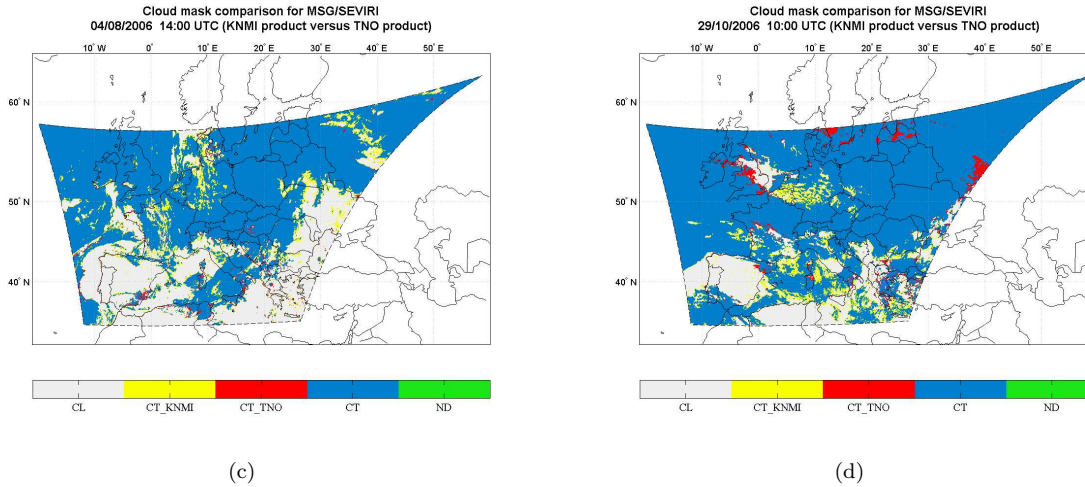


Figure 3.8: Comparison of the KNMI/MF and TNO-CDA products over Western Europe for (a) 29 January 2006 at 11:45 UTC, (b) 1 May 2006 at 13:15 UTC, (c) 4 August 2006 at 14:00 UTC and (d) 29 October 2006 at 10:00 UTC. The meaning of the different abbreviations used in the legend are explained in Table 3.2. The percentages represented by the different colors are available in Table 3.3. (Cont')

Table 3.2: Signification of the legend abbreviations used in the comparison maps with the KNMI/MF product (Figures 3.8).

Legend Code	MSG-SEVIRI (KNMI/MF)	MSG-SEVIRI (TNO)	Comparison
CL	Clear	Clear	Agreement
CT_KNMI	Cloudy	Clear	Disagreement
CT_TNO	Clear	Cloudy	Disagreement
CT	Cloudy	Cloudy	Agreement
ND	Not Determined	-	Not Determined

Table 3.3: Extent (in pixel percentage) of the different colored areas in the comparison maps with the KNMI/MF product (Figures 3.8).

Date-Time	CL (%)	CT_KNMI (%)	CT_TNO (%)	CT (%)	ND (%)	Agreement (%)	Disagreement (%)
29/01/2006 11:45	15.0	5.6	3.9	72.2	3.3	87.2	9.5
01/05/2006 13:15	32.7	9.8	2.4	55.1	0.0	87.8	12.1
04/08/2006 14:00	41.0	6.7	1.7	50.6	0.0	91.6	8.4
29/10/2006 10:00	24.4	7.7	2.3	65.6	0.0	90.0	10.0

For all periods, differences between the two cloud masks are mainly observed near the cloud edges and within areas with scattered clouds. In general, the KNMI algorithm appears more strict on cloud edges. The TNO detection routines seem to overestimate cloud occurrence in scattered cloud areas. This tendency appears the largest in the January examples shown in Figure 3.8(a), but never exceeds 10 % of the image area. Apart from these, the two products compare favorably, and the cloud structures observed in the cloud mask are rather similar for both algorithms.

A statistical analysis of the comparison maps was made. These statistics take into account all available images over the 4 selected periods, and provide the average of the different flag combinations (in pixel percentage). The results are presented in a histogram in Figure 3.9. Each bar of the histogram corresponds to a single period of study. The bars are grouped in 7 different groups distinguished by color. The first 5 groups (grey, yellow, red and blue) displayed correspond to the different flag combinations used in the comparison maps (see Table 3.2). The 2 other groups represented in pink and orange are derived from the first 5 groups. The bars representing the percentage of agreement is the sum of the bars in the 1st group (grey) and the 4th group (blue), and the sum of the 2nd (yellow) and the 3rd (red) groups gives the bars related to the percentage of disagreement.

The cloud cover is obviously more extended during the winter and fall periods than for the spring and the summer periods, and on average the percentage of agreement is between 80 and 90 %. The lowest value is found in January with 79 % of agreement. In January, only 25 images were available for the comparison study, whereas the statistics were made with about 300 pictures for all other periods. Moreover, certain cloud mask products provided by KNMI contain very large areas flagged as 'Not Determined' in January period.

To assess the applicability of the TNO algorithm within the area selected, the spatial distribution of cumulative agreement percentages is presented in Figure 3.10. To create these cumulative data sets, each pixel is associated to a counter which is incremented for every frame showing agreement between the two products at that particular location. The percentage for the specific pixel is obtained by dividing the value of this counter by the number of images over the given time interval. Here, one map represents a full week. The cumulative agreement percentage is rather satisfying for all periods, between 80 and 90 % over most regions in Europe. Poorest cumulative agreement is observed in January, in the eastern and the center part of the selection, when large regions show values smaller than 50 %. This weak agreement is due to the limited number of samples used to produce the January map, together with the gaps in the data provided by KNMI. In May, the agreement frequency over the North and the Baltic Sea is very low. These regions tend to be falsely identified as cloudy in the TNO detection process by the Infrared Gross Temperature test (Test 1) over the North Sea and the Dynamic Visible Test (Test 3) over the Baltic Sea. It is suggested that the application of a fixed sea surface temperature over the entire study area results in an overestimation of cloudiness at higher latitudes. Moreover, over the Baltic Sea the presence of algae blooms in spring time may result in higher surface reflectance, which may explain the high amount of falsely identified clouds over the Baltic Sea. Therefore, the application of a global sea temperature threshold

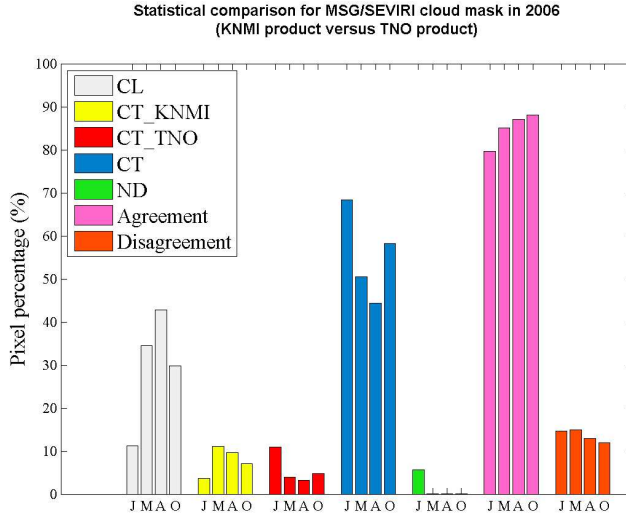


Figure 3.9: Statistical comparison of the KNMI/MF and TNO cloud detection results, over Western Europe for the 4 periods chosen in 2006 ('J', 'M', 'A', and 'O' refer to individual periods for January, May, August, and October, respectively). The abbreviations used in the legend are explained in Table 3.2.

calculated for the whole selection is not really suitable in this case.

The TNO cloud mask is generated regardless of the illumination conditions. Some areas among the images taken between 6:00 in the morning and 18:00 in the evening may present large solar zenith angles, and the algorithm which was designed for daytime only cannot perform well. Before retrieving aerosol AOD, cosine of solar zenith angles below 0.5 are filtered, therefore these artifacts do not have much impact on the retrievals.

The comparison study between the KNMI and TNO cloud masks shows that for the purpose of aerosol retrieval, and for solar zenith angles lower than 60° , the TNO cloud detection algorithm provides reasonable results.

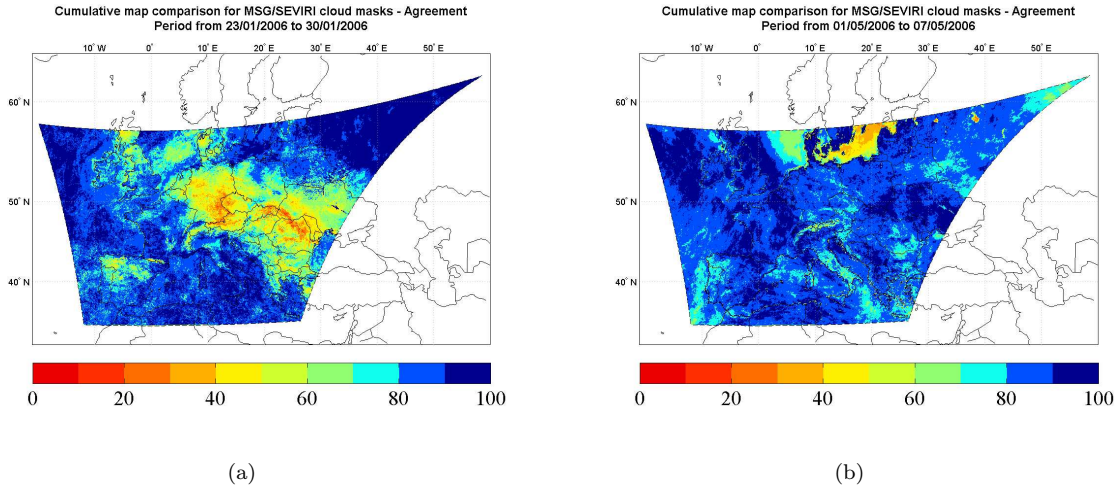
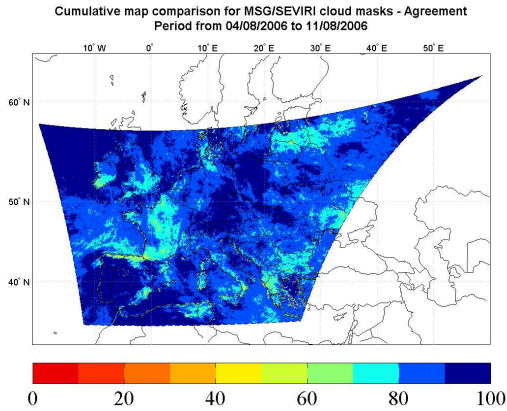
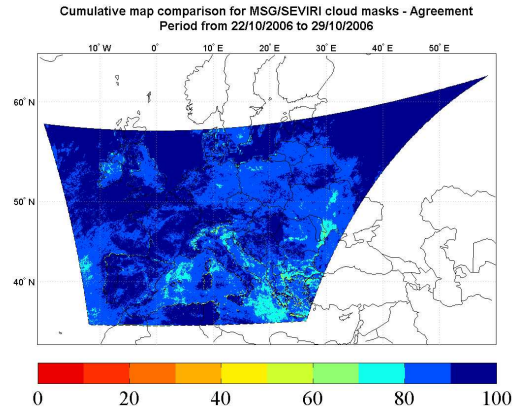


Figure 3.10: Geographic distribution of the cumulative agreement (in percentage) between KNMI/MF product and TNO product, over Western Europe for one week in (a) January 2006, (b) May 2006 (c) August 2006 and (d) October 2006.



(c)



(d)

Figure 3.10: Geographic distribution of the cumulative agreement (in percentage) between KNMI/MF product and TNO product, over Western Europe for one week in (a) January 2006, (b) May 2006 (c) August 2006 and (d) October 2006. (Cont')

3.4.2 MODIS-TERRA comparisons

MODIS Algorithm

A number of images from Terra-MODIS overlapping the study area have also been used for the evaluation of the TNO-CDA cloud mask. The MODIS Cloud Mask data product that was used for the comparison is part of the Earth Observation System (EOS) standard data products [Ackerman et al., 1998]. It is produced from the radiance data measured by the MODIS sensor mounted on the Terra platform, and generated for each image collected by Terra-MODIS with 1 km spatial resolution at nadir. This Cloud Mask is a Level 2 product from Collection 5. Like the TNO cloud algorithm, the MODIS algorithm is based on the principles of the APOLLO processing scheme. It employs a panel of visible and infrared thresholds, and makes use of the full spectral range offered by the 36 channels of the instrument. In addition, consistency tests related to the radiometrical accuracy of the radiances allow for the specification of the confidence for each single test. The final decision to determine whether a pixel is cloud-free or not is made by combining the confidence values from the individual test. The tests applied to the MODIS data can be divided in four groups depending on the type of clouds to be detected: the tests meant to identify high thick clouds from temperature thresholds, the reflectance tests for the detection of low clouds, the thin cirrus tests relying on both temperature and temperature difference tests, and the tests for thin clouds detected from temperature thresholds.

In every Terra-MODIS Cloud Mask data product file (MOD35_L2), the MODIS Cloud Mask Scientific Data Set (SDS) is coded on a 6 byte array. For each pixel, the different bits give various information such as cloudy conditions, illumination conditions, and surface type. In this study, only the flag named Unobstructed FOV Quality flag is used (i.e. bit 1 and bit 2). Thus the information extracted will determine whether a MODIS pixel is clear or cloudy with either probable or reliable confidence.

Comparison of TNO-CDA and MODIS cloud masks

In order to produce comparison maps, both the TNO cloud mask for MSG-SEVIRI and the MODIS data have been regridded on a regular grid at 0.05 degree resolution filled by bilinear interpolation. Figure 3.11 shows the results obtained by the two algorithms on the area covered by a MODIS graticule overlapping the selected area of the MSG-SEVIRI disk.

Like for the study with the KNMI product described in section 3.4.1, comparison maps are presented. The associated legends are detailed in Tables 3.4, and each map is an example for the 4 different study periods.

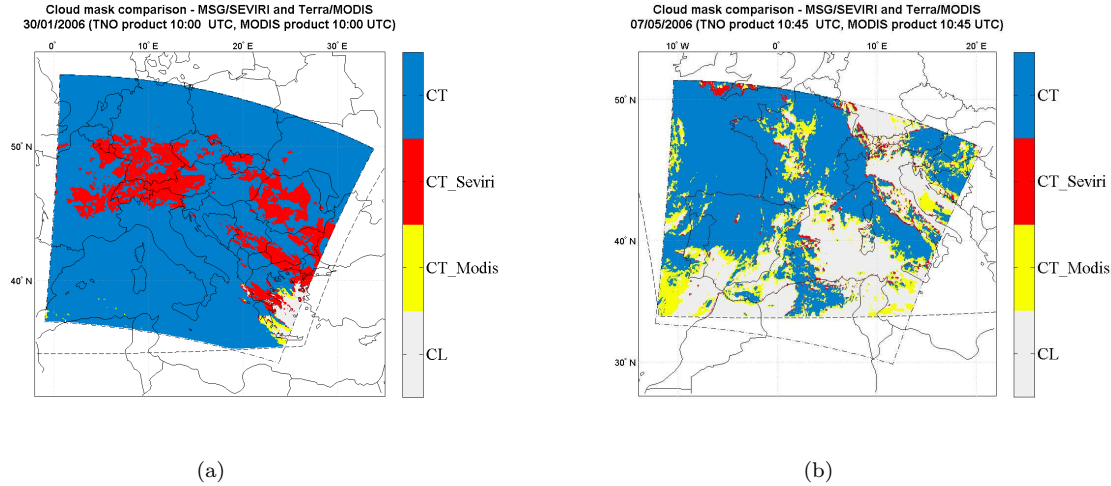


Figure 3.11: Comparison between MSG-SEVIRI (TNO product) and Terra-MODIS cloud detection over Western Europe for (a) 30 January 2006 at 10:00 UTC, (b) 7 May 2006 at 10:45 UTC, (c) 10 August 2006 at 10:00 UTC and (d) 29 October 2006 at 10:00 UTC. The meaning of the different abbreviations used in the legend are explained in Table 3.4. The percentage represented by the different colors are available in Table 3.5.

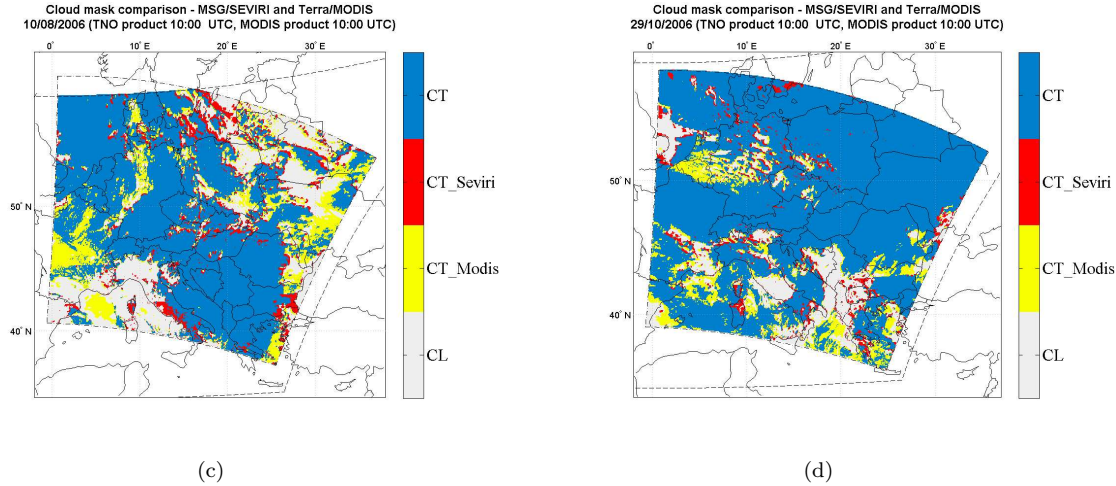


Figure 3.11: Comparison between MSG-SEVIRI (TNO product) and Terra-MODIS cloud detection over Western Europe for (a) 30 January 2006 at 10:00 UTC, (b) 7 May 2006 at 10:45 UTC, (c) 10 August 2006 at 10:00 UTC and (d) 29 October 2006 at 10:00 UTC. The meaning of the different abbreviations used in the legend are explained in Table 3.4. The percentage represented by the different colors are available in Table 3.5. (Cont²)

Table 3.4: Meaning of the legend abbreviations used in the comparison maps with the MODIS product (Figure 3.11).

Legend Code	MODIS	MSG-SEVIRI (TNO)	Comparison
CL	Clear	Clear	Agreement
CT_Modis	Cloudy	Clear	Disagreement
CT_Seviri	Clear	Cloudy	Disagreement
CT	Cloudy	Cloudy	Agreement

Table 3.5: Extent (in pixel percentage) of the different colored areas in the comparison maps with the MODIS product (Figure 3.11).

Date-Time	CL (%)	CT_Modis (%)	CT_Seviri (%)	CT (%)	Agreement (%)	Disagreement (%)
30/01/2006 10:00	1.5	0.6	15.3	82.5	84.1	15.9
07/05/2006 10:45	31.2	13.7	2.8	52.3	83.5	16.5
10/08/2006 10:00	21.5	13.2	7.0	58.3	79.8	20.2
29/10/2006 10:00	13.1	9.1	4.5	73.3	86.4	13.6

In the MODIS cloud mask, the zones flagged with the lowest confidence flag namely 'probably cloudy' and 'probably clear' are generally located on the edges of the clouds. To evaluate the performance of the TNO algorithm to screen clouds, MODIS lowest confidence flags are transformed to their respective confident flags. In this new configuration it becomes clear that an area that is initially considered as 'probably cloudy' by MODIS, is flagged as 'cloudy' by TNO algorithm, and areas flagged as 'probably clear' by MODIS are set to 'clear' for SEVIRI. Thus, when the MODIS information becomes simply binary, the agreement between the two algorithms increases.

The main differences between the two cloud masks reside in the definition of the cloud contours. Cloud edges are more accurately determined by MODIS due to its higher spatial resolution (1x1 km² vs 4x7 km² for SEVIRI over Europe). In addition, the TNO algorithm occasionally fails to distinguish clear areas within large broken clouds. This can be seen for the winter example displayed in Figure 3.11(a). Figures 3.11(b), (c), (d), show that during spring, summer and autumn periods, the agreement between the two products is good.

Comparison of KNMI/MF and MODIS cloud masks

The results of the KNMI/MF and the MODIS cloud masks for the same images selected in the comparison between TNO and MODIS algorithms (see section 3.4.2) are displayed in Figures 3.12(a)-(c). Results from the KNMI/MF product were not available for the 30 January 2006 at 10:00.

Like in section 3.4.2 the comparison maps display the combination of flags after they have been simplified to a binary information for both products (see Table 3.6). MODIS and KNMI/MF cloud mask products generally agree well, and the percentage of agreement is greater than 80% for the three examples (see Table 3.7). The KNMI/MF algorithm appears stricter than the MODIS algorithm by a few percent. Since the spatial resolution of the MODIS instrument is higher than that of SEVIRI, the MODIS cloud mask can be considered to be the most reliable of the three products presented here. The results from both the TNO and KNMI/MF cloud detection algorithms are consistent with the results of the MODIS algorithm. Comparison of Table 3.7 and Table 3.5 shows that the KNMI/MF algorithm is in better agreement with MODIS than the TNO-CDA. However, these differences are less than 3% in the total agreement.

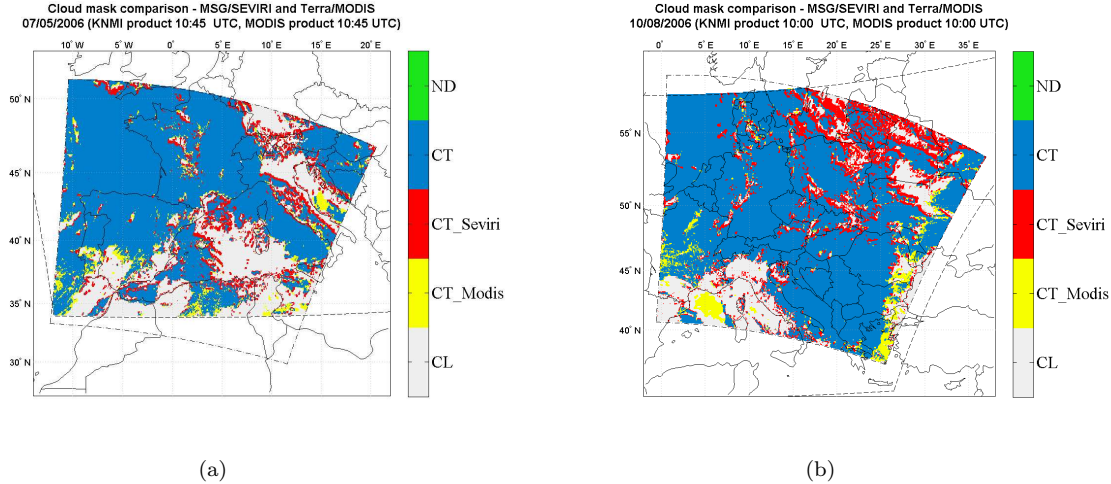
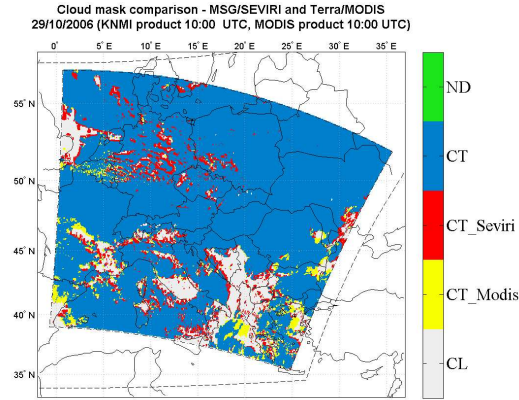


Figure 3.12: Comparison between MSG-SEVIRI (KNMI product) and Terra-MODIS cloud detection over Western Europe for (a) 7 May 2006 at 10:45 UTC, (b) 10 August 2006 at 10:00 UTC and (c) 29 October 2006 at 10:00 UTC. The meaning of the different abbreviations used in the legend are explained in Table 3.6. The percentage represented by the different colors are available in Table 3.7.



(c)

Figure 3.12: Comparison between MSG-SEVIRI (KNMI product) and Terra-MODIS cloud detection over Western Europe for (a) 7 May 2006 at 10:45 UTC, (b) 10 August 2006 at 10:00 UTC and (c) 29 October 2006 at 10:00 UTC. The meaning of the different abbreviations used in the legend are explained in Table 3.6. The percentage represented by the different colors are available in Table 3.7. (Cont')

Table 3.6: Meaning of the legend abbreviations used in the comparison maps with the MODIS product (Figure 3.12).

Legend Code	MODIS	MSG-SEVIRI (KNMI)	Comparison
CL	Clear	Clear	Agreement
CT_Modis	Cloudy	Clear	Disagreement
CT_Seviri	Clear	Cloudy	Disagreement
CT	Cloudy	Cloudy	Agreement
ND	-	-	Not determined

Table 3.7: Extent (in pixel percentage) of the different colored areas in the comparison maps with the MODIS product (Figure 3.12).

Date-Time	CL (%)	CT_Modis (%)	CT_Seviri (%)	CT (%)	ND (%)	Agreement (%)	Disagreement (%)
07/05/2006 10:45	24.3	4.5	9.6	61.6	0.0	85.8	14.2
10/08/2006 10:00	15.9	4.9	12.6	66.6	0.0	82.5	17.5
29/10/2006 10:00	10.6	3.9	7.0	78.5	0.0	89.1	10.9

3.5 Conclusions and perspectives

The cloud detection technique used by TNO in the AATSR aerosol retrieval algorithm [Robles-Gonzalez, 2003] has been transferred to MSG-SEVIRI. The test sequence of the detection scheme dedicated to MSG-SEVIRI includes the implementation of the modifications suggested by Kriebel [2003] for the improvement of the APOLLO scheme. The applicability of the day-time TNO stand-alone cloud detection algorithm over western Europe was verified by means of comparison with the KNMI/MF cloud product for MSG-SEVIRI, and cloud mask data from MODIS. Generally, TNO results are in good agreement with both products. Part of the differences between MODIS and MSG are caused by collocation differences due to re-projection uncertainties, to small differences in overpass time and to parallax differences. Most differences between the three cloud masks are observed near cloud edges. Due to the high resolution of the MODIS instrument, the MODIS product can be considered to represent cloud edges with more accuracy than the SEVIRI cloud masks. In case of TNO-CDA algorithm, it is noted that some problems still remain in the identification of clear areas within broken clouds. Such artefacts can be explained by the fact that no external dataset is used to constrain the determination of the thresholds, as it is for example in KNMI/MF algorithm. In the scope of aerosol retrievals, these mis-detections lead to an artificial increase in AOD near cloud edges [Koren et al., 2007]. Besides cloud contaminations at the cloud edges, these features are also related to the aerosol swelling effect, when water vapour is absorbed as relative humidity increases near clouds. Consequently, accurate identification of cloud edges is not a trivial task. However, most of these outliers can be screened out in a post-processing step [de Leeuw et al., 2007]. Over the domain selected, the sea temperature threshold, which for the current work was fixed over the whole area, should be replaced by latitudinally varying threshold as done over land. Regarding the winter comparison, the agreement found is weak as compared to the results from the other seasons. This may in part be due to the small data set available and the study should be repeated for a longer period, to arrive at a statistically more reliable data set allowing for more solid conclusions. Although the KNMI/MF cloud mask looks slightly stricter than both the MODIS and TNO cloud masks, it must be taken into account that the extrapolation of 'probable' flags to 'confident' flags may enhance or diminish the differences between the cloud mask products. In conclusion, the TNO algorithm appears reasonably efficient to detect clouds for application of cloud screening in aerosol retrievals, and this without the use of any ancillary data. For future investigations, it could be interesting to examine its applicability over other regions of the MSG disk, such as desert areas.

Acknowledgements

The authors would like to thank the NASA and the MODIS/Terra Science Teams for making available the data used in this study. The research work presented in this paper has been financially supported by SRON (project number EO-077).

Chapter 4

Aerosol retrievals over the ocean^{*}

Abstract

With its observational frequency of 15 minutes, the Meteosat Second Generation (MSG) geostationary satellite offers a great potential to monitor aerosol transport over the Atlantic Ocean and the Mediterranean Sea using Spinning Enhanced Visible and Infra-Red Imager (SEVIRI) data. To explore this potential, an algorithm for the retrieval of aerosol optical properties has been developed for use over the ocean. It is based on the Along Track Scanning Radiometer (ATSR-2) algorithm [Veeffkind and de Leeuw, 1998] which has been adapted to the corresponding channels of SEVIRI (635 nm, 0.810 nm and 1.640 nm). The SEVIRI Aerosol Retrieval Algorithm (SARA) provides the Aerosol Optical Depth (AOD) for these channels. To illustrate its capabilities, the application of this algorithm to two cases is presented: (1) a forest-fire smoke plume advected from Spain and Portugal over the Atlantic Ocean in August 2006, and (2) an outbreak of Saharan dust across the Western Mediterranean Sea in February 2006. The results obtained are validated with AERONET ground-based measurements for two coastal stations, and compared with the retrievals from the MODerate resolution Imaging Spectroradiometer (MODIS) on NASA's Terra and Aqua satellites. The diurnal variations of the aerosol optical depth observed at the AERONET sites are well reproduced, and the spatial patterns retrieved using the SARA algorithm are in reasonable agreement with those observed by MODIS.

^{*}Y.S. Bennouna, G. de Leeuw, J. Piazzola, and J. Kuśmierczyk-Michulec. Aerosol remote sensing over the ocean from MSG-SEVIRI images. *Journal of Geophysical Research - Atmospheres*. Submitted for publication: December 2008.

4.1 Introduction

Atmospheric aerosol refers to a suspension of solid or liquid particles in air [Seinfeld and Pandis, 1998d]. These particles have a typical size between 0.05 and 1 μm . Tropospheric aerosols originate from both natural and anthropogenic sources. They can be directly injected into the atmosphere (primary aerosols), or generated by gas-to-particle conversion (secondary aerosols). They can be transported over long distances, and their residence time in the troposphere ranges from a few days to a few weeks [Pandis et al., 1995]. Aerosol particles are involved in many atmospheric processes. By absorbing and scattering the incoming solar radiation, atmospheric particles affect the amount of radiation reaching the surface, and therefore influence directly the earth radiative balance. Since they can act as condensation nuclei (hygroscopic particles with submicrometer sizes) or as ice nuclei (e.g. dust particles), they also play a role in the formation of clouds. Urbanization and industrialization have largely contributed to the increase of aerosol concentrations and to the change of the chemical composition of the lower troposphere. When the number of Cloud Condensation Nuclei (CCN) increases (i.e. the number of droplets increases), less water is available for each droplet, and hence their size is smaller. These changes in the cloud microphysics modify the cloud albedo [Twomey, 1977, Twomey et al., 1984], influence cloud lifetime and reduce precipitation [Flossmann, 1998]. Because of the complexity of these processes, the role of aerosols remains one of the largest uncertainties in climate assessment [IPCC, 2007]. The significance of their impact on climate has been estimated by Kaufman et al. [2002]. Globally, effects of aerosols on the radiation balance is cooling as opposed to warming by greenhouse gases. Aerosol radiative forcing is of the same order of magnitude as that due to anthropogenic greenhouse gases: -0.1 to -0.9 W/m^2 for direct forcing, -0.3 to -1.8 W/m^2 for indirect forcing [IPCC, 2007].

Most aerosols have short lifetimes (days to weeks) and therefore their geographical distribution, physical, chemical and optical properties are highly variable in both space and time, and strongly related to their sources. To document this variability, satellites present an almost instantaneous view over a large spatial area using the same instrument and technique. Regarding Low Earth Orbiting (LEO) satellites, the revisit time is at best one day. The high temporal sampling of Geostationary Orbiting (GEO) satellites renders them very suitable for aerosol-climate and transport studies.

The use of passive remote sensing to retrieve aerosols is based on the separation of the surface from atmospheric contributions to the top of the atmosphere (TOA) radiance, in cloud free conditions. In most situations, the contribution of aerosols is similar to the signal from the surface except over very bright (desert, snow, ice) or dark (forests, ocean) surfaces.

In 1981, AVHRR (Advanced Very High Resolution Radiometer) provided the first aerosol information from space observation over oceans [Griggs, 1981]. Since then, a number of space-based instruments has emerged, e.g., TOMS (Total Ozone Monitoring Spectrometer), GOME (Global Ozone Monitoring Experiment), ATSR (Along Track Scanning Radiometer), MODIS (MODerate resolution Imaging Spectroradiometer), POLDER (POLarization and Directionality of Earth Reflectance), MISR (Multi-angle Imaging Spectro- Radiometer), MERIS (Medium- Resolution Imaging

Spectrometer), SeaWiFS (Sea-viewing Wide Field-of-view Sensor), and several algorithms dedicated to aerosol retrievals have been proposed, for application over both ocean and land. These algorithms require assumptions on ambient aerosol types, and most retrievals use algorithms which determine the best fit between the measured radiation at the TOA, and that calculated using a Radiative Transfer Model (RTM) for one or several aerosol models. When available, the use of polarization with radiance measurements reduces the dependency on the aerosol a priori, and improves the quality of the retrievals [Mishchenko et al., 1997].

The solar radiation reflected within the three spectral bands of SEVIRI centered at 635, 810 and 1640 nm, is sensitive to all major aerosol types. The aim of this paper is to present the method used in a newly developed algorithm: the SEVIRI Aerosol Retrieval Algorithm (SARA), for the retrieval of AOD and the Ångström coefficient over sea surfaces in the three solar channels. This methodology is based on the interpolation of Look Up Table (LUT) reflectance and transmittance data built for pre-defined aerosol types with monomodal particle size distributions. The parameters of the LUTs have been generated with the Doubling and Adding radiative transfer model developed by KNMI (DAK) [Stammes, 2001] for each selected aerosol type. The SARA algorithm is similar to the single view algorithm developed by Veefkind and de Leeuw [1998], which was first applied to ATSR-2 [Robles-Gonzalez, 2003] and more recently to AATSR [Curier et al., 2009]. In this algorithm, the reflectance of the sea surface is parameterized as a function of wind speed and chlorophyll concentration, and a least square fitting procedure selects the aerosol mixture (fine and coarse) that minimizes the difference between pre-calculated (contained in LUTs) and measured TOA reflectance.

The study presented here provides a description of the algorithm developed for MSG-SEVIRI, and its application to two cases: (1) a plume of smoke due to forest fires in Spain and Portugal and transported over the Atlantic Ocean, and (2) a Saharan dust outbreak across the eastern Mediterranean Sea. In order to investigate the ability of the geostationary retrievals to follow diurnal trends of the aerosol load, the results were evaluated against timeseries from sunphotometer measurements at two AERONET sites located on the coast. The AOD retrieved from SEVIRI radiances is also compared to the MODIS aerosol product, for two different time slots acquired during the aforementioned events.

4.2 Algorithm description

4.2.1 MSG-SEVIRI radiance data

METEOSAT-8, launched in August 2002, is the first in a new generation of highly advanced weather satellites within the Meteosat Second Generation (MSG) programme of EUMETSAT [Schmetz et al., 2002]. MSG is a spin stabilized satellite orbiting geosynchronously at about 36000 km above the earth surface. The SEVIRI instrument onboard the MSG satellite delivers a full scan of the earth disk centered over the Equator and the 0 longitude every 15 minutes. This radiometer measures simultaneously the radiance in 11 narrow spectral bands: 3 solar channels (0.6, 0.8 and 1.6 μm), 8 infrared channels, and in one broad band 0.3-0.7 μm . SEVIRI provides images at a resolution of 3 km at the subsatellite point for the 11 narrow bands, and at a higher resolution of 1 km for the broad band channel. In this study, MSG-SEVIRI data were provided by KNMI in numerical counts which have been converted to radiances using the calibration coefficients as provided by EUMETSAT. Since aerosol optical properties influence the measurement of the sensor in the shortwave range, SARA uses the SEVIRI data for two visible wavelengths, 0.635 nm and 0.810 nm, and one near-infrared wavelength: 1.64 μm .

4.2.2 Cloud Mask

The retrieval of aerosol properties is possible only for cloud free scenes. This requires rigorous cloud screening for which a fast and stand-alone algorithm has been implemented [Bennouna et al., 2008]. The method used to identify cloud contaminated pixels is based on the work of Saunders and Kriebel [1988]. The main structure of the routines implemented for SEVIRI is similar to the automated version implemented by Robles-Gonzalez [2003] for ATSR-2 which in turn is based on the algorithm developed by Koelemeijer et al. [2001]. The code was adapted to fit the characteristics of MSG-SEVIRI, and updated according to the improvements implemented in the APOLLO cloud analysis tool [Kriebel, 2003]. The dynamic thresholding technique adopted in the TNO stand-alone Cloud Detection Algorithm (TNO-CDA) is based on image histogram analysis which makes use of a limited number of channels. The detection process consists of 4 different tests: the Infrared Gross Temperature Test, the Spatial Coherence Test, the Dynamic Visible Test and the Dynamic Ratio Test. The evaluation of this cloud screening technique over Western Europe has been described in Bennouna et al. [2008].

4.2.3 LUTs

Aerosol Models

Optical properties of aerosols are determined by their size distribution and chemical composition which is related to the refractive index. In this study, 3 sets of LUTs have been created. Each of these sets is based on various sources of information including the Navy Oceanic Vertical Aerosol Model [de Leeuw et al., 1989],

Table 4.1: Size distribution parameters and microphysical properties for the aerosol models used to generate the different LUTs.

LUT Label	$R_g(\mu m)$	σ_g	$m(\lambda) = n + ik$		
			635 nm	810 nm	1640 nm
NAM6b1	0.03	2.03	1.37 + i0.00002	1.37 + i0.00004	1.36 + i0.00050
NAM6soc	0.24	2.03	1.39 + i0.00000	1.38 + i0.00000	1.37 + i0.00030
OPACwaso	0.03	2.24	1.40 + i0.00212	1.39 + i0.00327	1.37 + i0.00633
OPACssam	0.42	2.03	1.35 + i0.00000	1.35 + i0.00000	1.33 + i0.00015
OPACmiam	0.39	2.00	1.53 + i0.00450	1.53 + i0.00400	1.53 + i0.00609
OPACmitr	0.50	2.20	1.53 + i0.00450	1.53 + i0.00400	1.53 + i0.00609
MODISc8	0.60	1.82	1.53 + i0.00000	1.53 + i0.00000	1.46 + i0.00100
MODISc9	0.50	2.22	1.53 + i0.00000	1.53 + i0.00000	1.37 + i0.00100

the Optical Properties of Aerosols and Clouds (OPAC) database [Hess et al., 1998], and the MODIS aerosol retrieval algorithm [Remer et al., 2006]. The different size distribution parameters and refractive index used to build the different LUTs are listed in Table 4.1. Unlike dust, sea salt and water soluble aerosols are hygroscopic particles. Here, the mean geometric radius and the refractive indices have been determined at 80% relative humidity [Shettle and Fenn, 1979]. Two different models of sea salt and water soluble aerosols have been tested: the types labeled as 'NAM6b1' and 'NAM6soc' are defined from the NOVAM model, 'OPACwaso' and 'OPACssam' are based on the OPAC database. As regards dust particles, the mineral accumulation mode ('OPACmiam') and the mineral transported model ('OPACmitr') from OPAC were used, as well as the 2 dust aerosol types proposed in the MODIS aerosol retrieval algorithm ('MODISc8' and 'MODISc9'). For each aerosol type the parameters r_g (mean geometric radius) and σ_g (geometric standard deviation) define the distribution of the normalized number concentration n , represented by a monomodal lognormal function of the particle radius r [Seinfeld and Pandis, 1998c]:

$$n(r) = \frac{dn}{dr} = \frac{1}{r \cdot \sqrt{2\pi} \cdot \ln \sigma_g} \exp \frac{-(\ln r - \ln \bar{r}_g)^2}{2 \cdot \ln^2 \sigma_g} \quad (4.1)$$

In most climate and radiative transfer models, optical properties of aerosols are modeled assuming particle sphericity. This assumption is based on the simple physical principle that liquid aerosols have spherical shape because of surface tension. However, soot agglomerate and dust aerosols are non-hygroscopic solid aerosols which are typically irregularly shaped [DeCarlo et al., 2004, Kalashnikova and Sokolik, 2002]. The nonsphericity aspect of dust particles can have a significant impact on their optical properties in the solar spectrum [Yang et al., 2007]. Spheroid models can closely reproduce light scattering matrices obtained from laboratory measurements of desert dust particles [Volten et al., 2001]. In this study, the scattering matrices of spherical

Table 4.2: Spectral average extinction cross section (in μm^2) for the different aerosol types and wavelengths of SEVIRI.

LUT label	$C_{ext}(\lambda)$		
	635 nm	810 nm	1640 nm
NAM6b1	2.3124e-11	1.3417e-11	2.0394e-12
NAM6soc	1.3264e-08	1.2835e-08	8.3628e-09
OPACwaso	7.7462e-11	5.1359e-11	1.1746e-11
OPACssam	3.8268e-08	3.9259e-08	3.4102e-08
OPACmiam	3.1998e-08	3.3394e-08	3.3980e-08
OPACmitr	6.4656e-08	6.6841e-08	7.2833e-08
MODISc8	5.6892e-08	5.9713e-08	6.6271e-08
MODISc8 (non-spherical)	4.6905e-08	5.5673e-08	4.3161e-08
MODISc9	6.6372e-08	6.8582e-08	7.4196e-08
MODISc9 (non-spherical)	3.7230e-08	4.3404e-08	2.2725e-08

particles are calculated with the code developed by [de Rooij and van der Stap \[1984\]](#) based on the Lorentz-Mie theory [[Mie, 1908](#), [van de Hulst, 1957](#), [Kerker, 1969](#)]. The impact of the particle shape on the retrievals has been investigated with the T-matrix code [[Mishchenko and Travis, 1994](#)] which rigorously computes light scattering by randomly oriented spheroid particles. For both spherical and non-spherical models, the values of the average extinction cross section C_{ext} , single scattering albedo w_0 and asymmetry parameter of the phase function g are presented in Tables 4.2, 4.3 and 4.4, respectively.

Radiative transfer simulations

To model the TOA reflectance measured by SEVIRI, the algorithm uses pre-calculated LUTs which provide the modeled bidirectional reflectance/transmittance data, and transmission functions for a pre-defined atmosphere in the three channels 635, 810 and 1640 nm. Each LUT corresponds to a different type of aerosol (i.e. size distribution parameters and chemical composition), except the 'Rayleigh LUT' which represents the case of a purely molecular atmosphere, without aerosols. Various sets of aerosol models were used to build the LUTs dedicated to MSG-SEVIRI retrievals. The different aerosol types are described in section 4.2.3. Reflectance, transmittance, and transmission quantities which are stored in the LUTs are computed using the KNMI Doubling and Adding radiative transfer model (DAK) [[Stammes, 2001](#)]. DAK is developed for line-by-line or monochromatic multiple scattering calculations at UV, visible, and near-infrared wavelengths in a horizontally homogeneous atmosphere using the doubling adding method [[de Haan et al., 1987](#)]. For the results presented in this paper, the atmospheric profile for pressure, temperature and humidity is based on the Midlatitude Summer (MLS) and the Midlatitude Winter (MLW) reference atmospheres [[McClatchey et al., 1972](#)]. For all simulations, the aerosol layer was assumed

Table 4.3: Spectral single scattering albedo for the different aerosol types and wavelengths of SEVIRI.

LUT label	$\omega_0(\lambda)$		
	635 nm	810 nm	1640 nm
NAM6b1	0.9997	0.9994	0.9811
NAM6soc	1.0000	1.0000	0.9976
OPACwaso	0.9828	0.9708	0.9004
OPACssam	1.0000	1.0000	0.9984
OPACmiam	0.9080	0.9330	0.9471
OPACmitr	0.8589	0.8926	0.9148
MODISc8	1.0000	1.0000	0.9901
MODISc8 (non-spherical)	0.9999	0.9999	0.9951
MODISc9	1.0000	1.0000	0.9833
MODISc9 (non-spherical)	0.9999	0.9999	0.9948

Table 4.4: Spectral asymmetry parameter for the different aerosol types and wavelengths of SEVIRI.

LUT label	$g(\lambda)$		
	635 nm	810 nm	1640 nm
NAM6b1	0.6257	0.5759	0.3946
NAM6soc	0.7620	0.7660	0.7627
OPACwaso	0.6918	0.6680	0.5608
OPACssam	0.7844	0.7892	0.8050
OPACmiam	0.7170	0.6999	0.6875
OPACmitr	0.7622	0.7383	0.7041
MODISc8	0.6988	0.6824	0.7203
MODISc8 (non-spherical)	0.6255	0.6770	0.7420
MODISc9	0.7242	0.7096	0.7225
MODISc9 (non-spherical)	0.6627	0.7116	0.7050

to be 2 km high and concentrations decrease exponentially with altitude. The signal measured by the satellite is simulated for various scenarios, including multiple sun-satellite geometries and various aerosol loads: 15 solar and viewing zenith angles, 37 azimuth angles, and 11 optical depths at the reference wavelength of 500nm (ranging between 0.02 and 6). All physical parameters available in the LUTs are listed and described in Table 4.5.

4.2.4 Reflectance model over sea

Sea-surface reflectance

SARA accounts for the bidirectional reflectance of the ocean. The ocean reflectance is assumed to be the sum of specular reflection, reflection from oceanic whitecaps, and subsurface reflection [Koepeke, 1984]. Given the relative area covered with whitecaps proposed by Monahan and Muircheartaigh [1980] for a surface wind speed U in $m.s^{-1}$:

$$A_{wc} = 3.84 \cdot 10^{-6} \cdot U^{3.41} \quad (4.2)$$

the total sea surface reflectance can be expressed as:

$$\rho_{sea} = \underbrace{(1 - A_{wc})\rho_g}_{(1)} + \underbrace{A_{wc} \cdot \rho_{wc}}_{(2)} + \underbrace{(1 - A_{wc}) \cdot \rho_u}_{(3)} \quad (4.3)$$

In equation 4.3 the sea surface reflectance is composed of one bidirectional component also called *glint* (1) and two isotropic components (2 and 3). The first term describes the specular reflectance at the water surface, which applies in the absence of whitecaps (cf. $(1 - A_{wc})$ for area not covered by whitecaps). When the ocean surface can be approximated by a flat surface, the specular reflectance is calculated using the classical Fresnel coefficient formula [Fresnel, 1827]. When the roughness effect is taken into account, the Fresnel reflection coefficient of a wavy sea surface can be calculated using a probability distribution function of surface wave slope [Cox and Munk, 1954]. Term (2) quantifies the reflectance due to the presence of whitecaps. The spectral values of the foam reflectance ρ_{wc} are based on the laboratory measurements performed by Whitlock et al. [1982]. In situ measurements of foam reflectance have been carried out by e.g. Moore et al. [2000], Kokhanovsky [2004]. Term (3) represents the *water leaving reflectance* or *underlight* which is the reflectance caused by the water constituents below the ocean surface. The below- and above-water upwelling radiances and fluxes expressed by Gordon and Morel [1983] and Morel and Gentili [1996] lead to a relation which defines the water leaving reflectance by covering both effects of reflection and refraction at the air-sea interface [Ruddick et al., 2006]:

$$\rho_u = \pi \cdot \frac{(1 - \rho_w) \cdot (1 - \bar{\rho}_w)}{n_w^2} \cdot \frac{R}{Q} \quad (4.4)$$

In this equation, the index w refers to pure sea water, ρ_w (~ 0.021) is the Fresnel

Table 4.5: Variables stored in the LUTs.

Parameter	Symbol	Dependence	Dimension
Surface pressure	p	-	1
Wavelength	λ	-	3
Reference AOD at 500nm	τ_{500}	-	11
Cosine of solar Zenith Angle	μ_s	-	15
Cosine of viewing Zenith Angle	μ_v	-	15
Relative Azimuth Angle	ϕ	-	37
Single Scattering Albedo	w_0	(λ)	3
Asymmetry Parameter	g	(λ)	3
Spectral AOD	τ	(λ, τ_{500})	(3,11)
Bidirectional reflectance at the TOA	ρ_{atm}	($\lambda, \tau_{500}, \mu_s, \mu_v, \phi$)	(3,11,15,15,37)
Bidirectional transmittance at the surface	T_{bd}	($\lambda, \tau_{500}, \mu_s, \mu_v, \phi$)	(3,11,15,15,37)
Transmission function of the atmosphere	T_{tot}	($\lambda, \tau_{500}, \mu_s, \mu_v$)	(3,11,15,15)
Total downward transmission of the atmosphere	T_{tot}^{\downarrow}	($\lambda, \tau_{500}, \mu_s$)	(3,11,15)
Total downward diffuse transmission of the atmosphere	t^{\downarrow}	($\lambda, \tau_{500}, \mu_s$)	(3,11,15)

reflectance for upwelling radiance from water to air, $\bar{\rho}_w$ (~ 0.043) is the coefficient for downwelling flux from air to water, and n_w the refractive index of water (~ 1.33 in the visible and near infrared). R is the irradiance reflectance, and Q relates the radiance to the irradiance. [Gordon et al. \[1988\]](#) have shown that for case 1 water, the ratio $\frac{R}{Q}$ can be approximated by:

$$\frac{R}{Q} = 0.11 \cdot \frac{b_b}{K_d} \quad (4.5)$$

Thus the water leaving reflectance is related to its inherent optical properties, i.e. the total backscatter coefficient b_b and the diffuse attenuation coefficient K_d .

[Morel and Prieur \[1977\]](#) have proposed a classification of sea water according to their constituents. For case 1 water, it was shown that water color mainly depends on phytoplankton concentrations. Therefore, the index usually adopted to specify the bio-optical state of case 1 water is its chlorophyll concentration [[Smith and Baker, 1978](#)]. Both the backscatter and diffuse attenuation coefficients can be expressed as the sum of specific coefficients related to pure sea water (b_{bw}, K_{dw}) and chlorophyll (b_{bc}, K_{dc}):

$$b_b = b_{bw} + b_{bc} \quad (4.6)$$

$$K_d = K_{dw} + K_{dc} \quad (4.7)$$

The values used for the coefficients of pure sea water are based on the measurements of [Smith and Baker \[1981\]](#). ρ_u can be expressed as a function of the chlorophyll-*a* concentration Chl , using the bio-optical models formulated by [Morel \[1988\]](#) for the backscatter coefficient:

$$b_{bc}(\lambda) = 0.30 \cdot Chl^{0.62} \cdot \left(2 \cdot 10^{-3} + 2 \cdot 10^{-2} \cdot (0.50 - 0.25 \cdot \log Chl) \cdot \frac{0.550}{\lambda} \right) \quad (4.8)$$

and by [Baker and Smith \[1982\]](#) for the diffuse attenuation coefficient:

$$K_{dc}(\lambda) = k_c(\lambda) \cdot Chl \cdot \exp(-k'_c(\lambda) \cdot \log(2 \cdot Chl))^2 + 0.001 \cdot Chl^2 \quad (4.9)$$

In equation 4.9, k_c and k'_c are fitting parameters. Regarding the results presented in this paper, the surface wind speed has been fixed to a value of $5 \text{ m}\cdot\text{s}^{-1}$ for the whole area of study. The sea-surface chlorophyll concentration is extracted from monthly data of the SeaWiFS Level-3 product for chlorophyll-*a* concentration [[Campbell et al., 1995](#)].

TOA reflectance

By combining the bidirectional reflectance of the sea-surface with atmospheric scattering, the total TOA reflectance overlaying an ocean surface can be expressed as the sum of five terms corresponding to the different paths a photon might follow in the atmosphere [Tanré et al., 1979]:

$$\rho = \underbrace{\rho_{atm}}_{(1)} + \underbrace{T^\downarrow \rho_{sea,dir} T^\uparrow}_{(2)} + \underbrace{t^\downarrow \rho_{sea,dif} T^\uparrow}_{(4)} + \underbrace{T^\downarrow \rho'_{sea,dif} t^\uparrow}_{(3)} + \underbrace{t^\downarrow \rho_{sea,iso} t^\uparrow}_{(5)} \quad (4.10)$$

All the above terms are functions of the wavelength and the sun-view geometry (i.e. sun and satellite zenith angles, and relative azimuth angle). The first term ρ_{atm} is called the path reflectance by aerosols and molecules (i.e. gases), which corresponds to the reflectance of the atmospheric layer containing both aerosol and gases as if there was no underlying surface. T and t (\uparrow upward or \downarrow downward) stand for the direct and diffuse transmission of the atmosphere. Direct transmissions are assumed to be an exponential function of the aerosol optical depth τ :

$$T = \exp\left(\frac{-\tau}{\mu}\right) \quad (4.11)$$

where μ is either the cosine of the solar zenith angle (μ_s) for the direct transmission in the downward direction, or the cosine of the viewing angle (μ_v) for the direct transmission in the upward direction. The downward diffuse transmission is directly provided by the LUT (cf. Table 4.5). The transmission downward (upward) is considered to be the sum of the diffuse and the direct transmissions downward (upward). The diffuse transmission in the upward direction can thus be derived from the LUTs data using:

$$t^\uparrow = \frac{T_{tot}}{(T^\downarrow + t^\downarrow)} - T^\uparrow \quad (4.12)$$

In equation 4.10, terms (2), (3), (4) and (5) include the contributions of the specular reflection, oceanic whitecaps and underlight from the sea surface. $\rho_{sea,dir}$, $\rho_{sea,dif}$ ($\rho'_{sea,dif}$), and $\rho_{sea,iso}$, are respectively the directional, the diffuse and the isotropic components of the sea surface reflectance. A wavy ocean, as described by Cox and Munk [1954], is assumed for the computation of the term related to the direct contribution (2), and a flat interface is assumed for the computation of the diffuse components (3, 4 and 5). As it was shown by Takashima and Masuda [1985], the latter approximation has very little effect on the retrievals.

4.2.5 The retrieval method

The method applied by SARA for aerosol ocean retrievals is similar to the single view algorithm that was developed for ATSR-2 [Veefkind, 1999]. This method is used to derive the AOD at the 3-km pixel level of SEVIRI (nadir resolution), in the three solar channels of the instrument. In the retrieval method, the first assumption relies on the separation of the TOA reflectance into the TOA reflectance of an atmosphere-ocean system in the absence of aerosols (ρ_0), and the reflectance caused by the presence of aerosols (ρ_{aer}):

$$\rho(\lambda) = \rho_0(\lambda) + \rho_{aer}(\lambda) \quad (4.13)$$

In the algorithm, an external mixture of two aerosol types is considered: one type represents the dominant aerosol type for the fine mode (anthropogenic/pollution), and the other the dominant aerosol type for the coarse mode (natural particles). In the same way as it is done in the retrieval scheme of MODIS [Remer et al., 2005], the TOA reflectance for the mixture of two aerosols is approximated as a weighted average of the reflectances from the individual modes, as if they were alone in the atmosphere [Wang and Gordon, 1994]. If the fraction associated with the contribution of the fine mode to the TOA reflectance is called ν , the TOA reflectance can thus be expressed by:

$$\rho_{aer}(\lambda) = \nu \cdot \rho_f(\lambda) + (1 - \nu) \cdot \rho_c(\lambda) \quad (4.14)$$

where ρ_f and ρ_c represent the reflectance due to the fine and the coarse mode respectively. With the help of equation 4.10 and the variables from the LUTs interpolated to the appropriate geometry, the TOA reflectance is calculated both for a purely molecular atmosphere (ρ_0^{lut}), and for an atmosphere composed of both aerosol and gases (ρ^{lut}). ρ^{lut} is determined for different fine/coarse aerosol mixtures, and for all tabulated values of the AOD at the reference wavelength at 500 nm. The best model is chosen by minimizing the least square error ϵ expressed as:

$$\epsilon_{\nu, f, c, \tau_{500}} = \sum_{i=1}^n \left(\frac{\rho^{meas}(\lambda_i) - \rho^{lut}(\lambda_i, \tau_{500})}{\rho^{meas}(\lambda_i) - \rho_0^{lut}(\lambda_i) + 0.01} \right)^2 \quad (4.15)$$

This regression compares the sensor measurements ρ^{meas} in n selected channels of the instrument, with ρ^{lut} , the estimate of the TOA reflectance provided by the LUT data for the same wavelengths. The additional value of 0.01 in the denominator is only here to avoid numerical overflows. For weakly absorbing aerosols and small optical depths [Veefkind, 1999, Kokhanovsky et al., 2009] we can assume a linear relationship between the reflectance due to aerosols and the AOD noted τ [Durkee et al., 1986], hence:

$$\rho_{aer}(\lambda) = C(\lambda) \cdot \tau(\lambda) \quad (4.16)$$

The spectral values of C depend on the aerosol type. The fine-coarse combination and the fraction ν that best fits the remote sensed data determine the model (i.e. spectral values of C) used to derive the AOD. Given the two aerosol types (fine and coarse) and ν for which $\epsilon_{\nu,f,c,\tau_{500}}$ is minimal, $C(\lambda)$ is estimated for each wavelength:

$$C(\lambda) = \frac{\rho_{aer}^{lut}}{\tau^{lut}} = \frac{\nu \cdot \rho_f^{lut}(\lambda, \tau_{500}) + (1 - \nu) \cdot \rho_c^{lut}(\lambda, \tau_{500})}{\nu \cdot \tau_f^{lut}(\lambda, \tau_{500}) + (1 - \nu) \cdot \tau_c^{lut}(\lambda, \tau_{500})} \quad (4.17)$$

and the spectral AOD can be derived as follows:

$$\tau(\lambda) = \frac{\rho_{aer}^{meas}}{C(\lambda)} = \frac{(\rho_0^{meas}(\lambda) - \rho_0^{lut}(\lambda))}{C(\lambda)} \quad (4.18)$$

In the SARA algorithm, the set of equations is solved for the first three bands of the MSG-SEVIRI instrument (i.e. 635, 810 and 1640 nm), and the fraction ν is chosen among 50 regularly spaced values between 0 and 1. For high AODs, the linear approximation mentioned in equation 4.16 cannot be used because the TOA reflectance plateaus for large AOD values. For this reason, if the best model corresponds to an AOD higher than 1, a third-order polynomial approximation is used to derive the AOD.

4.3 Sets for data evaluation

4.3.1 AERONET data set

AERONET is an international network of automated sun-photometers [Holben et al., 1998] established by NASA. AERONET involves more than 300 automatically operating instruments worldwide. Standardization imposes sun and sky measurements of the downwelling radiation for a number of defined wave bands (340, 380, 440, 500, 675, 870, 1020nm). The aerosol optical depth derived from these measurements is available from a free-access database. This database also provides other inversion products [Dubovik and King, 2000] characterizing aerosol optical, microphysical and radiative properties which are of great interest for aerosol research studies and satellite validation. In the current study, we used Level 1.5 (cloud-screened) and Level 2.0 (cloud-screened and quality-assured) data from two AERONET stations: Cabo da Rocca (38N, 9W), and Forth Crete (35N, 25E).

4.3.2 MODIS aerosol product

The polar-orbiting MODIS [Salomonson et al., 1989a] aboard Terra and Aqua spacecrafts acquires data for the entire Earth every 1 to 2 days. It measures the radiance in a large spectral range composed of 36 spectral bands between 0.405 and 14.385 μm , at three spatial resolutions of 250 m, 500 m, and 1000 m, with a wide swath of 2330 km. With such characteristics, this instrument was uniquely designed for monitoring

ambient aerosols, clouds, and further allows the derivation of various products for remote sensing applications over land, ocean, and atmosphere. Aerosol retrievals over land and ocean from MODIS is done through two independent algorithms. The theoretical basis of the algorithms for application over land is described by Kaufman et al. [1997c], and over ocean by Tanré et al. [1997]. Ocean and land retrievals have been validated by means of comparison with AERONET data [Ichoku et al., 2002, Chu et al., 2002, Remer et al., 2002, Levy et al., 2003, 2005]. The accuracy of the AOD retrievals over the ocean is: $\delta\tau = \pm 0.15\tau \pm 0.05$ as reported after revision of pre-launch estimation [Remer et al., 2005]. The MODIS algorithm relies on a LUT approach. The MODIS algorithm models the ambient aerosol as a combination of one fine and one coarse mode following individual log-normal distributions. The measurement is compared to pre-calculated radiative transfer calculations for 9 aerosol types (4 'fine', and 5 'coarse'), and the inversion finds two solutions: the best and the average least square fit. In the Level-2 Atmosphere products of MODIS collection 5 [Remer et al., 2006], both Terra and Aqua MODIS aerosol products (MOD04/MYD04-C005) provide global spectral AOD values over the ocean and the continents for cloud free regions at 10 km resolution. These products also include the fractional contribution of the fine aerosol mode to the total AOD at 0.55 μm , and the type of aerosol identified by the retrieval. The SEVIRI channels in the visible and near-infrared are close to channels on Terra/Aqua MODIS. Therefore, aerosol retrievals derived from these two instruments can provide relevant comparisons to study the spatial variability of the AOD obtained with SARA.

4.4 Case studies

The applicability of the SARA algorithm for MSG-SEVIRI data over sea was tested for two case studies. The first event presented is the advection of strong forest-fire plumes from Portugal and Galicia (Spain) over the Atlantic Ocean. The second concerns a dust outbreak from the Saharan desert over the Western Mediterranean Sea. The values of the AOD and its diurnal variability are validated against AERONET measurements which are considered as 'ground truth'. In addition, the ability to reproduce the spatial variations is evaluated through comparisons with data from the MODIS aerosol product.

4.4.1 Transport of forest-fire smoke over the Atlantic Ocean

Large forest fires contribute to global warming in a "positive feedback loop": huge amounts of carbon dioxide and other "planet-warming" greenhouse gases are released into the atmosphere, and global warming enhances the conditions that favours forest fires. In Europe, climate change seems to induce more frequent and longer heat waves of high intensity, with increasing likelihood of forest fires in the Mediterranean regions.

In summer 2006, the Iberian peninsula experienced one of its most severe droughts. By August 7, many severe wildfires occurred across Galicia (Spain) and northern Portugal. Figure 4.1(a) shows the smoke plumes produced by forest fires which can

be seen in the MODIS RGB picture (Terra) at 11:10 UTC.

SEVIRI retrieval results

For the forest-fire case, SEVIRI aerosol retrievals were performed for two different sets of aerosols, namely the 'OPAC' and the 'NAM' sets (see section 4.2.3). Since the results obtained with the 'NAM' and the 'OPAC' models are very similar, only the 'OPAC' retrievals which give a slightly better agreement with AERONET, are presented here. The AOD retrieved from MSG-SEVIRI radiance data at 11:15 UTC is shown in Figure 4.1(b). High values of the AOD located in the middle of the smoke plume contrast with the clean maritime background characterized by low AOD values (<0.1). The AOD at 635 nm retrieved with the SARA algorithm in the plume ranges mostly between 0.3 and 0.5, with maxima around 0.7. Outside the plume, high AOD values also appear near cloud edges. These are artefacts due to remaining cloud contamination.

The Ångström coefficient was inferred from the AOD retrieved at the two visible wavelengths:

$$\alpha_{635-810} = -\frac{810}{635} \cdot \ln \frac{\tau_{635}}{\tau_{810}} \quad (4.19)$$

The spatial variation of the Ångström coefficients is presented in Figure 4.1(c). It shows that α has values in the plume of 0.6-1, whereas outside the plume they are around 0. This indicates the presence of small particles within the plume. Figure 4.1(d) shows that the high AOD observed over the plume is mostly due to the contribution of the fine mode, with values of ν mainly above 0.8.

Validation with AERONET

To validate the results of SARA, the latter were compared to AOD measured at the AERONET site of Cabo da Rocca (38N,9W), see Figure 4.2. For the comparison, both timeseries (Figure 4.2(a)) and scatterplots (Figure 4.2(b)) are presented. The AERONET observations represent measurement average within 15 minutes. To estimate the AOD at the AERONET site, the AOD retrieved with SARA over the ocean (spatial resolution of about $5 \times 7 \text{ km}^2$ over Central Europe), has been averaged over an area of 10 km radius around the Cabo da Rocca location. Although the SARA retrievals were analyzed on a three day period, the timeseries are presented only for 7 August 2006, to better show diurnal variations. The scatterplot comprises the results for the entire period from 6 to 8 August 2006. In the timeseries for 7 August, a maximum of 0.4 in the AOD was observed at Cabo da Rocca around 13:00 (UTC), when the edge of the smoke plume crossed over the AERONET station. The AOD estimated from SARA shows a good agreement with AERONET, and the diurnal variations of the AOD are very well reproduced at all wavelengths. The correlation coefficient between SARA retrievals and AERONET is about 90% for the visible wavelengths. The correlation is weaker for the near-infrared channel, because small particles have less

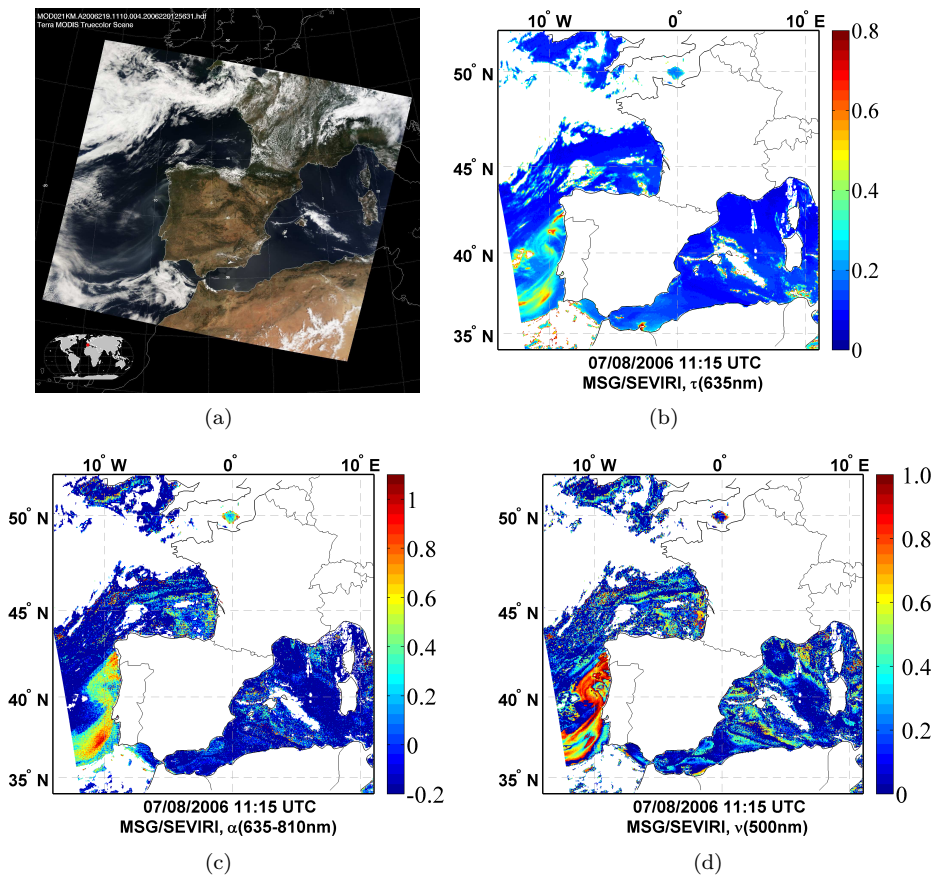
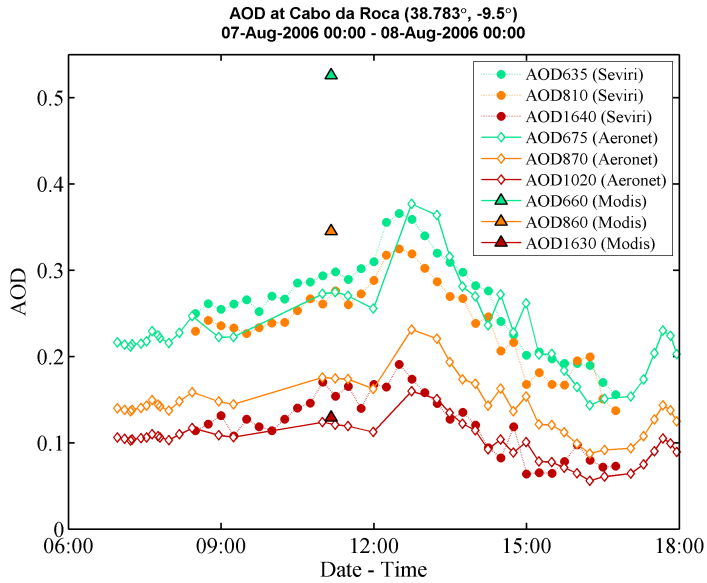
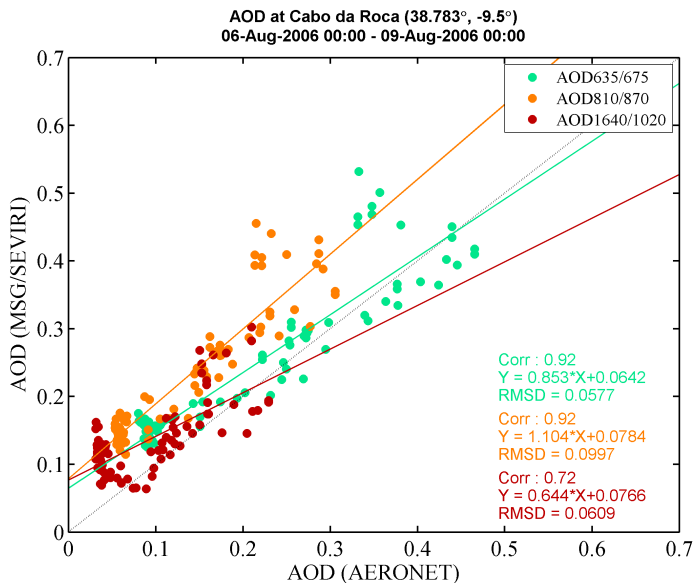


Figure 4.1: True Color image from the MODIS Terra/Aqua collection (a) and results from SARA retrievals (b,c,d) for the smoke plume from forest-fires in Portugal advected over the Atlantic Ocean on 7 August 2006 at 11:15 UTC. Map (resolution $\sim 5 \times 7 \text{ km}^2$) of (b) AOD at 635 nm, (c) Ångström coefficient 635-810 nm, and (d) weight of the Fine/Coarse mode aerosol on the AOD at 500 nm.



(a)



(b)

Figure 4.2: Comparison of the AOD retrieved using SARA with AERONET data at Cabo da Roca for the period 6 - 8 August 2006: (a) Timeseries (7 August 2006). (b) Scatter plots (6 - 8 August 2006). The open diamonds stand for AERONET data, the dots represent SARA retrievals, and the triangles the aerosol product for the MODIS overpass.

impact on the measurement at longer wavelengths. The AOD retrieved with SARA at 810 nm is overestimated, with a positive bias of about 0.08.

Comparison with MODIS

For this forest-fire case study, MODIS and SEVIRI 11:15 overpasses were within 5 minutes. AOD spatial patterns for the first visible channel of SEVIRI show consistency with the MODIS aerosol product at 660 nm (see Figure 4.3(a)). Over the ocean, the AOD at 660 nm derived from MODIS data, shows high optical depths along the west coast of the Iberian peninsula due to smoke advected from land over the Atlantic Ocean. According to MODIS retrievals, the smoke plume is mainly characterized by AOD values between 0.4 and 0.6, with higher values in the center of the plume, to larger than 1. The AOD differences between the two instruments ($\tau_{seviri,635} - \tau_{modis,660}$) are presented in Figure 4.3. For this comparison, the AOD has not been adjusted to a common wavelength because an adjustment (using Ångström coefficient of 1) changes AOD by less than 88%. They are generally within ± 0.1 with higher values in the tail of the distributions. The comparison analysis includes: the map (Figure 4.3(b)) and the histogram (Figure 4.3(d)) of the AOD differences, as well as the scatterplot (Figure 4.3(c)). The map of the AOD differences shows that in the plume the AOD estimated by SEVIRI is in general lower than the AOD estimated by MODIS, and visa versa outside the plume. This explains the double-peak feature of the histogram. These differences can reach values between -0.1 and -0.2 in the middle of the plume. However, about 80% of the pixels differ by less than 0.05. The largest positive differences (> 0.4) are located on cloud edges and can therefore be ascribed to cloud mask screening failure in SARA. According to the density scatterplot in Figure 4.3(c), there is a good correlation between the two datasets ($\sim 90\%$). At Cabo da Roca the AOD retrieved for the collocated pixel from the MODIS overpass was also shown in the timeseries of AERONET (see Figure 4.2(a) in previous section). As noticed in the comparison with AERONET at Cabo da Roca, the scatterplot confirms that MODIS overestimates the AOD in the forest-fire case.

4.4.2 Saharan dust storm across the eastern Mediterranean Sea

The Mediterranean Sea is among the areas with the highest aerosol optical depth over the ocean in the world [Prospero et al., 2002], and especially during Saharan desert dust outbreaks. The Saharan desert is the major source of mineral aerosols on the Earth [Papayannis et al., 2005], and dust aerosols have an important effect on climate [Tanré et al., 2003], marine chemistry and sedimentation in the Mediterranean Sea [Guerzoni and Chester, 1996]. It is mostly transported in the form of pulses during high wind periods, and can be advected over long distances as a consequence of the injection to high altitudes up to 10 km [Gobbi et al., 2000]. On February 25, 2006, a thick dust cloud was observed over the eastern Mediterranean Sea. It originated from a dust storm in the Saharan Desert that had started two days before. The MODIS RGB image (see Figure 4.4) shows a dense dust layer extending northwestward over

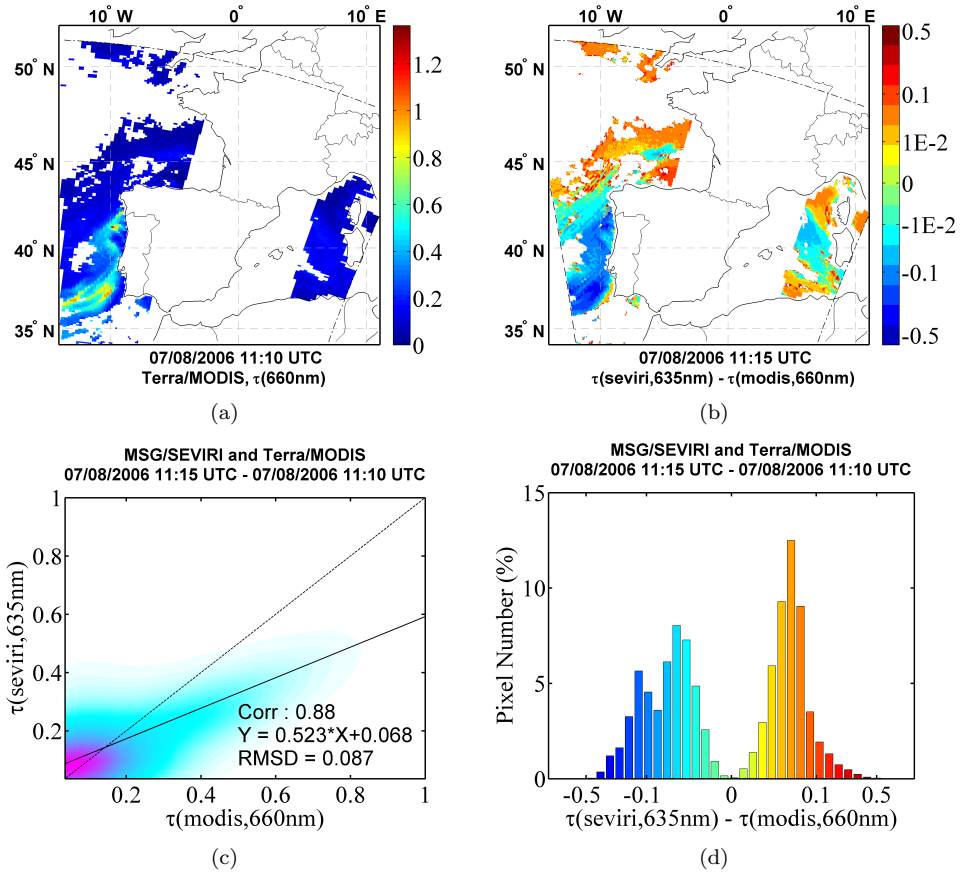


Figure 4.3: Map (resolution $\sim 10 \times 10 \text{ km}^2$) of AOD at 660 nm ('best' solution) from MODIS aerosol product (a), and comparison of the retrieved AOD from MSG-SEVIRI (11:15 UTC) and MODIS (11:10 UTC), for the smoke plume from forest-fires in Portugal advected over the Atlantic Ocean on 7 August 2006. (b) Map of the AOD difference (resolution $\sim 5 \times 5 \text{ km}^2$). (c) Density scatterplot, with the correlation coefficient, the linear regression coefficients, and the Root Mean Square Difference. (d) Histogram of the AOD difference. The dashed line in the scatterplot represents the identity line, and the solid line is the calculated regression line.

automatic temperature threshold determined by test 1, the "Dense Dust" flag is set to be positive. If the temperature difference is between 0.5 K and 0.7 K, and if the temperature of the pixel is at least 4 K higher than the threshold of test 1, the "Thin Dust" flag is set positive. In all other cases the dust detection result is negative. Figure 4.5 displays the cloud mask obtained, and the results from the dust detection process not only for the dust storm case (Figures 4.5(a) and 4.5(c)), but also for a clear day in the absence of dust (Figures 4.5(b) and 4.5(d)). As can be seen from the figures, the situation was very cloudy during the dust storm event, and the dust detection allowed to isolate the dust plume, as well as the thin layer of dust spread in the plume's surroundings ($\sim 7\%$ of the pixels in total). The clear situation shows the presence of minor false detections of dust due to the presence of thin warm clouds. However, these detections, by their number ($<1\%$ of the pixels), and by the fact they are rather dispersed across the entire study area, already give an indication of a wrong dust detection. In this case the dust flag must not be used to reset to clear pixels which have been screened in the cloud detection process.

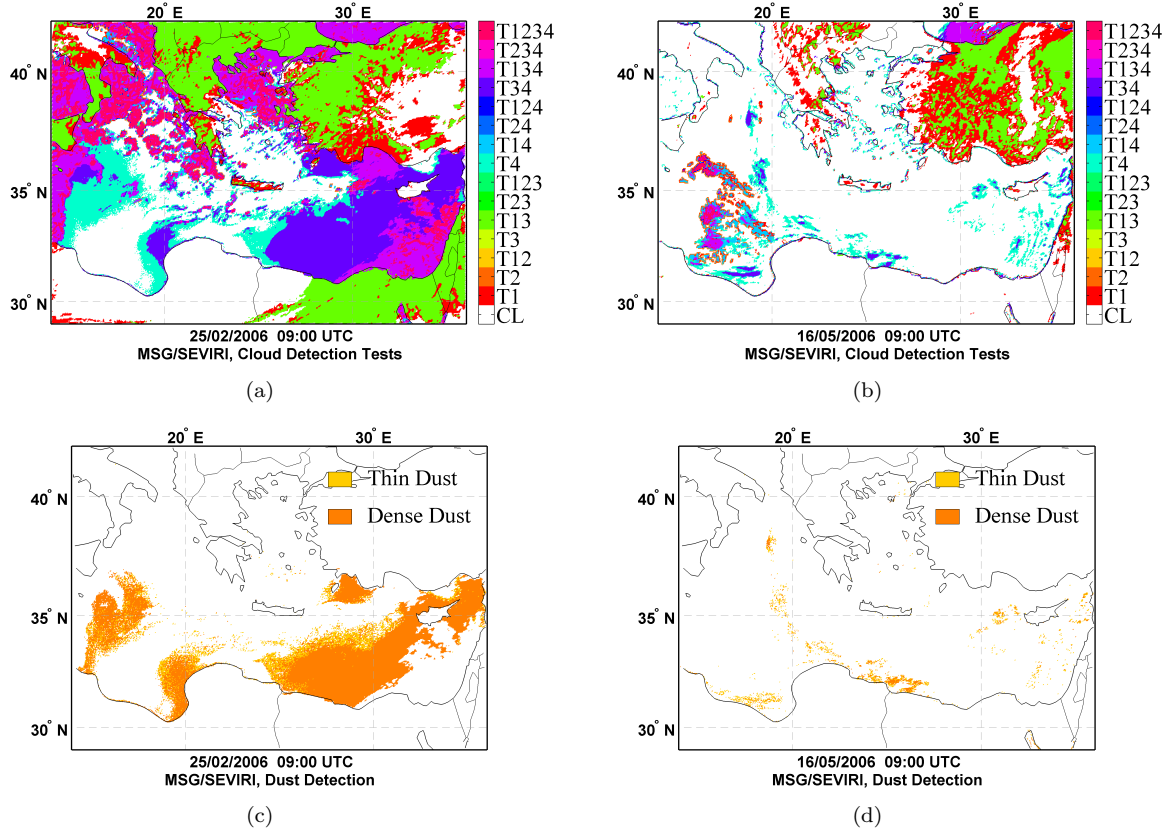


Figure 4.5: Cloud and dust detection results from SARA algorithm for the dust storm over the Mediterranean Sea on 25 February 2006 at 09:00 UTC. (a,b) Cloud Mask and (c,d) Dust Detection maps. See text for further explanation. The cloud tests indicated on the color bar in figures (a) and (b) are described in [Bennouna et al., 2008].

SEVIRI retrieval results

The AOD retrievals for SEVIRI were performed using different aerosol models. For one simulation the fine mode is based on the 'NAMb1', and the algorithm chooses the best coarse mode among 'NAMsoc' (sea salt), 'MODc8' and 'MODc9' (desert dust). For the other simulation the different aerosol types are based on the 'OPAC' set (cf. section 4.2.3). Since the simulations based on the OPAC aerosol models are not very satisfying, the results presented in Figure 4.6 are related to the first simulation mentioned. For most aerosols the near-infrared AOD is rather low, except for large particles such as dust. Figure 4.6(a) displays the AOD map retrieved using SARA for the near-infrared channel of SEVIRI. The AOD at 1640 nm indicates large values in the plume off the Egyptian coast. In the center of the dust cloud, the AOD can be as high as 5, and these values decrease as the dust is dispersed. For this case study, the Ångström coefficient is calculated between the wavelengths 810 nm and 1640 nm. The spatial distribution of the Ångström coefficient is shown in Figure 4.6(b). Low values of the Ångström coefficients indicate the presence of large particles. In the areas where the dust is densest the Ångström coefficient becomes negative, with values reaching a minimum of -0.5. Around the dust plume, the Ångström coefficient mostly ranges between 0 and 0.5. Values close to 0 can be explained by the dominance of marine aerosol or dust, whereas higher Ångström coefficients can probably be associated with polluted air masses. Clean areas with very low optical depth, as well as the dust plume region have a weak contribution of the fine mode aerosol to the total AOD at 500 nm, as opposed to air masses affected by pollution where the Ångström coefficient is usually higher than 0.5 (see Figure 4.6(c)).

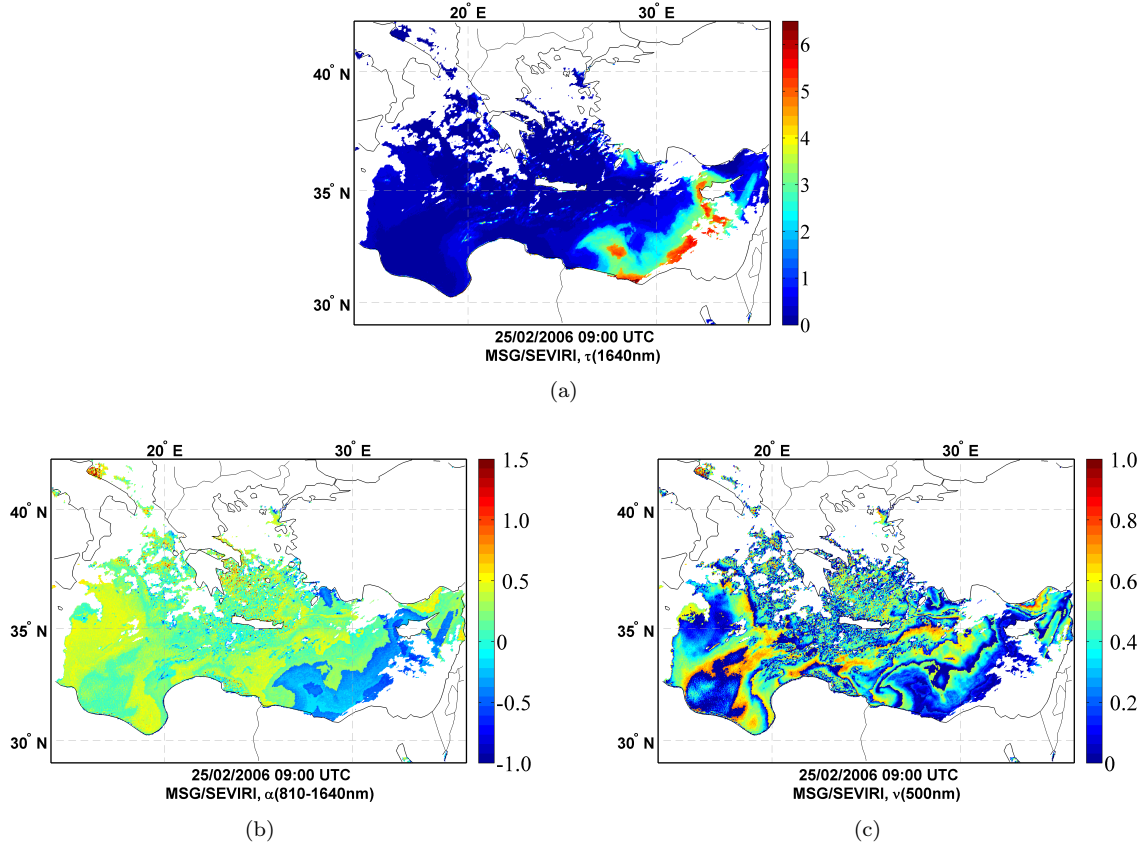


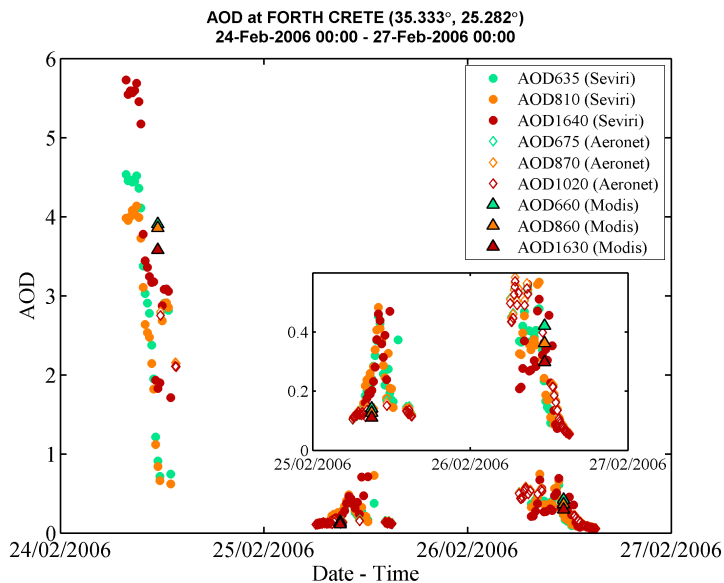
Figure 4.6: Results from SARA retrievals for the dust storm over the eastern Mediterranean on 25 February 2006 at 09:00 UTC: Map (resolution $\sim 5 \times 7 \text{ km}^2$) of (a) AOD at 1640 nm, (b) Ångström coefficient 810-1640 nm, and (c) weight of the Fine/Coarse mode aerosol on AOD at 500 nm.

Validation with AERONET

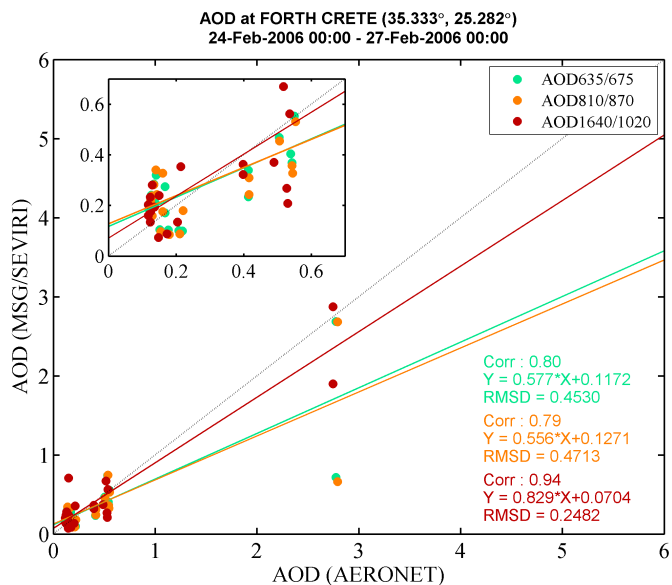
Data from the AERONET station at Forth Crete (35N,25E), located on the north-east coast of the Greek island of Crete, were used to validate the ocean retrieval results for the dust event. The comparison with AERONET is presented in Figure 4.7, with timeseries and scatterplots of results from a three day period from 24 to 27 February 2006. The SEVIRI AOD is presented as the average value for pixels at a distance of less than 10 km from the station. Like for the results presented in the previous section, the comparison is shown only for SARA retrievals using NAM/MODIS sets of aerosol models (fine: 'NAMb1', coarse: 'NAMsoc', 'MODISc8', 'MODISc9'). The timeseries in Figure 4.7(a) shows that the general trend of the AOD measured at Forth Crete is generally well represented by the retrieval using SARA. Some high frequency variations in the SEVIRI AOD, which are not observed in the AERONET data, are probably related to cloud contamination. The scatterplot in Figure 4.7(b) shows that the AOD retrieved with SARA is well correlated (>79%) with AERONET measurements, and the best agreement between the two datasets is found for the near-infrared channels (94% correlation) with a slope of about 0.83 and a bias of 0.07. For the visible wavelength, the AOD retrieved is much lower than the AOD from AERONET, whereas the near-infrared AODs are in good agreement. This could be caused by the aerosol modes used in the aerosol models.

Comparison with MODIS

The results from SARA for the dust event were compared to the MODIS retrievals for the overpass at 09:00 (UTC), the 25th of February. On the map of the AOD at 1630 nm derived from MODIS data (see Figure 4.8), the values reach 4 where the dust layer is the densest. In the area surrounding the dust plume, the presence of dust haze leads to lower AOD values, between 1 and 2. These values are in the same order of magnitude as the AOD at 1640 nm retrieved with SARA, except for some areas in center of the dust cloud where the AOD is lower in MODIS retrievals. Figure 4.9 shows the differences between the two products ($\tau_{seviri,1640} - \tau_{modis,1630}$). For the first comparison (top panel), SARA retrievals used aerosol types from NAM/MODIS sets, and for the second comparison (bottom panel) aerosol types from the OPAC set. Like for the Forest-Fire case, the maps of the AOD difference (Figures 4.9(a) and 4.9(d)), the histograms of the AOD differences (Figures 4.9(b) and 4.9(e)), as well as the scatterplots (Figures 4.9(c) and 4.9(f)) are presented. The map of the AOD differences shows different patterns depending on the aerosol models that were used for the retrieval with SARA. In general, the first simulation (i.e. NAM/MODIS) seems to minimize the differences with the MODIS data, and for both simulations (i.e. NAM/MODIS and OPAC), the absolute difference is largest within the plume region. The differences observed over the dust plume are larger when the OPAC model is used. Outside the plume, large positive differences located on the edge of the cloud mask indicate the presence of cloud contaminated pixels in SARA retrievals. The rough shape of the histogram is similar for the two different simulations. About 70% of the pixels have absolute difference smaller than 0.1 for the first SARA simulation.



(a)



(b)

Figure 4.7: Comparison of the AOD retrieved using SARA with AERONET data at FORTH CRETE for the period 24 - 26 February 2006: (a) Timeseries (26 February 2006). (b) Scatter plots (24 - 26 February 2006). The open diamonds stand for AERONET data, the dots represent SARA retrievals, and the triangles the aerosol product for the MODIS overpass.

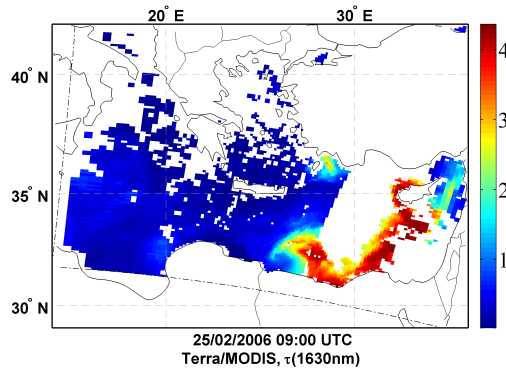


Figure 4.8: Map (resolution $\sim 10 \times 10 \text{ km}^2$) of AOD at 1630 nm ('best' solution) from MODIS aerosol product for the dust storm over the Mediterranean Sea on 25 February 2006 as observed at 09:00 UTC.

For the OPAC results, this percentage is slightly lower. The density scatterplots show that MODIS and SEVIRI retrievals are well correlated.

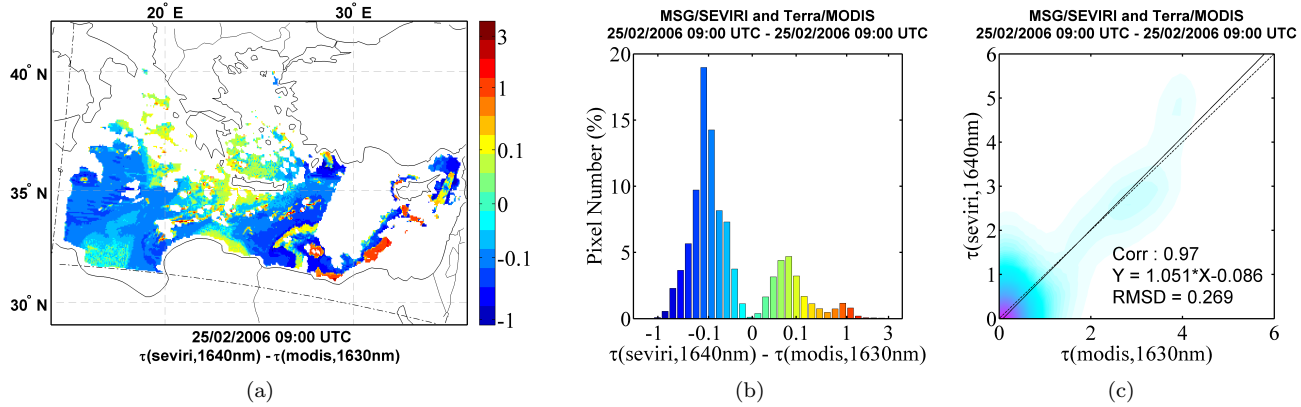


Figure 4.9: Comparison of the retrieved AOD from MSG-SEVIRI and MODIS, for the dust storm over the Mediterranean Sea on 25 February 2006 at 09:00 UTC: (a,d) Map of the AOD difference (resolution $\sim 5 \times 5 \text{ km}^2$). (b,e) Histogram of the AOD difference. (c,f) Density scatterplot, with indication for the correlation coefficient, the linear regression coefficients, and the Root Mean Square Difference. Pictures at the top are related to SARA retrievals obtained using both 'NAM' and 'MODIS' datasets, and at the bottom using the 'OPAC' dataset. The dashed line in the scatterplot represents the identity line, and the solid line is the calculated regression line.

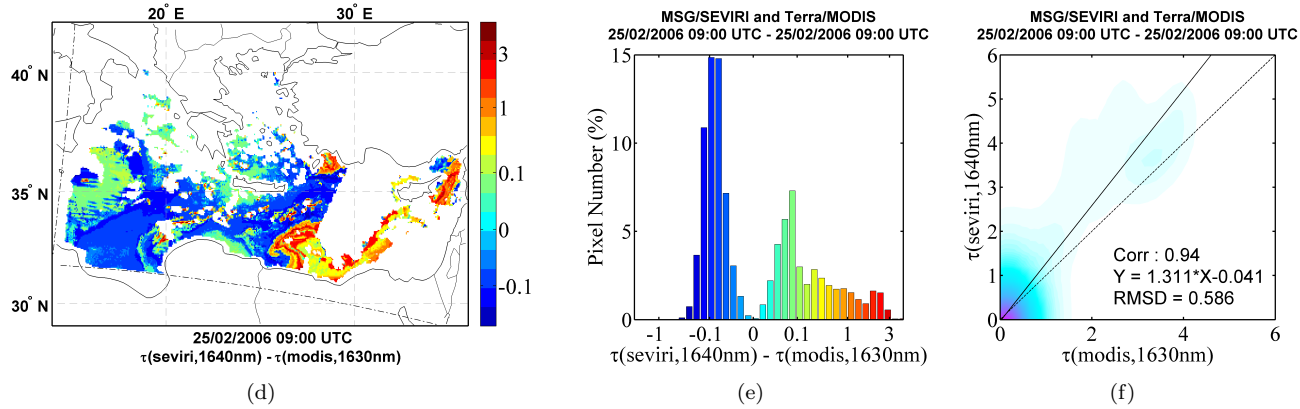


Figure 4.9: Comparison of the retrieved AOD from MSG-SEVIRI and MODIS, for the dust storm over the Mediterranean Sea on 25 February 2006 at 09:00 UTC: (a,d) Map of the AOD difference (resolution $\sim 5 \times 5 \text{ km}^2$). (b,e) Histogram of the AOD difference. (c,f) Density scatterplot, with indication for the correlation coefficient, the linear regression coefficients, and the Root Mean Square Difference. Pictures at the top are related to SARA retrievals obtained using both 'NAM' and 'MODIS' datasets, and at the bottom using the 'OPAC' dataset. The dashed line in the scatterplot represents the identity line, and the solid line is the calculated regression line. (Cont')

The correlation coefficient is larger than 95% for the two simulations. Because the dust event involves high values of the AOD, the RMSD values obtained (0.27 and 0.58) are rather satisfying. The coefficients of the linear regression confirm that AOD values retrieved with SARA are slightly higher than the results obtained with the MODIS algorithm. This difference is negligible in the first simulation, but it represents about 30% of the optical depth when the aerosol model is based on the OPAC. In the second simulation, it was noticed that the algorithm failed to distinguish sea salt from dust particles. This leads to discontinuities in the AOD retrieved over the dust plume. This may also explain the large overestimation of the AOD when the OPAC set of particles is used. The linear regression between MODIS and SEVIRI retrievals, indicate a very good agreement for SARA retrievals using NAM/MODIS aerosol models. The AOD value for the MODIS pixel coincident with the Forth Crete location is shown in the AERONET comparison described in the previous section (see Figure 4.7(a)). For the dust outbreak case, both MODIS and SARA retrievals present satisfactory agreement with AERONET.

Non-Spherical simulations

The effect of particle shape on the retrieval of dustlike tropospheric aerosols is a crucial issue in aerosol remote sensing [Koepke and Hess, 1988]. Several studies have shown that the use of non-spherical models in dust retrievals allow for more accurate fitting of the spectral and angular dependences of the observed intensity. The phase function of desert dust aerosols can be modeled using a mixture of spheroids [Mishchenko et al., 1997] characterized by a certain shape distribution. Inversions from AERONET sunphotometer measurements have shown that in desert plumes the number of particles in the coarse mode with a high aspect ratio dominates [Dubovik et al., 2006].

For the dust storm event presented in this paper, a very simple non-spherical model of randomly oriented spheroids was applied. The single scattering albedo and the expansion coefficients of the scattering matrix for the non-spherical model were calculated with the T-matrix code [Mishchenko et al., 1996, Mishchenko and Travis, 1994]. No shape distribution was used, all particles are assumed to be spheroids with the same shape. The shape aspect of the spheroids is parameterized by their axis ratio which is set to 2. The parameters of the size distribution (i.e. mode radius and standard deviation) for the spheroid model are given in terms of volume equivalent spheres. The gaussian size distribution function was used with the same radius mode and standard deviation as for the spherical model (see Table 4.1 in section 4.2.3). For the dust aerosol labelled 'MODISc8', the phase function calculated with the T-matrix code (i.e. spheroid model) is compared to the phase function obtained with the MIE code (i.e. spherical model) in Figure 4.10. For the three SEVIRI wavelengths, the spheroid and the spherical model differ mainly in their phase function at large scattering angles. As compared to the sphere model, the curve flattens at large scattering angles in the non-spherical case, therefore the back scattered intensity is smaller for these geometries.

Similarly to simulations made with the sphere model, two non-spherical dust

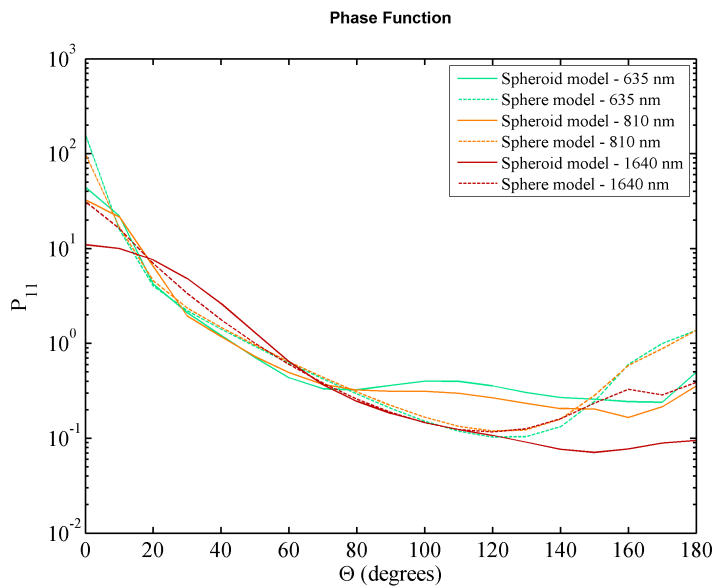


Figure 4.10: Phase Function (P_{11}) of desert dust as a function of scattering angle (Θ), simulated for a sphere (dashed lines) and a spheroid model (solid lines) with a single axis ratio of 2. The different colors indicate the wavelengths of the SEVIRI channels for which the phase function is represented.

aerosol models labeled as 'MODISc8' and 'MODISc9' were used to retrieve the AOD with SARA. The results obtained with the non-spherical retrievals are presented in Figure 4.11. In general, the spatial variations obtained with the non-spherical model remain unchanged as compared to the results of the spherical simulations. However the AOD observed over the dust plume is lower by approximately 25% than for the spherical simulations (see Figure 4.11(a)). The map of the Ångström coefficients (see Figure 4.11(b)) shows a less clear distinction between the oceanic background and the dust cloud than in the spherical case. Although the values of Ångström coefficient are nearly homogeneous over the area, they are slightly lower over the dusty regions (< -0.2) than over clean areas (> 0). As regards the weight of the fine over the coarse mode on the AOD at 500 nm (see Figure 4.11(c)), the maps for the spherical and the non-spherical simulations are very similar, the differences did not exceed 5%. For the comparison with MODIS, in Figure 4.12, the map and the histogram of the AOD differences are similar to the results obtained for the spherical simulations. For the corresponding SEVIRI image, the scattering angle over the area studied varies between 129° and 133° , a range in which the phase function of the spherical and the spheroid model are much alike at 1630 nm. Although the results for the visible channels are not shown for the dust outbreak case, it should be noted that the differences between spherical and non-spherical retrievals from SARA are more notable at 635 nm and 810 nm. Although these differences are of little importance in the near-infrared, the scatterplot (see Figure 4.12(c)) shows that a better agreement is found between MODIS and SARA results when the non-spherical model is used, in particular for the highest AOD values.

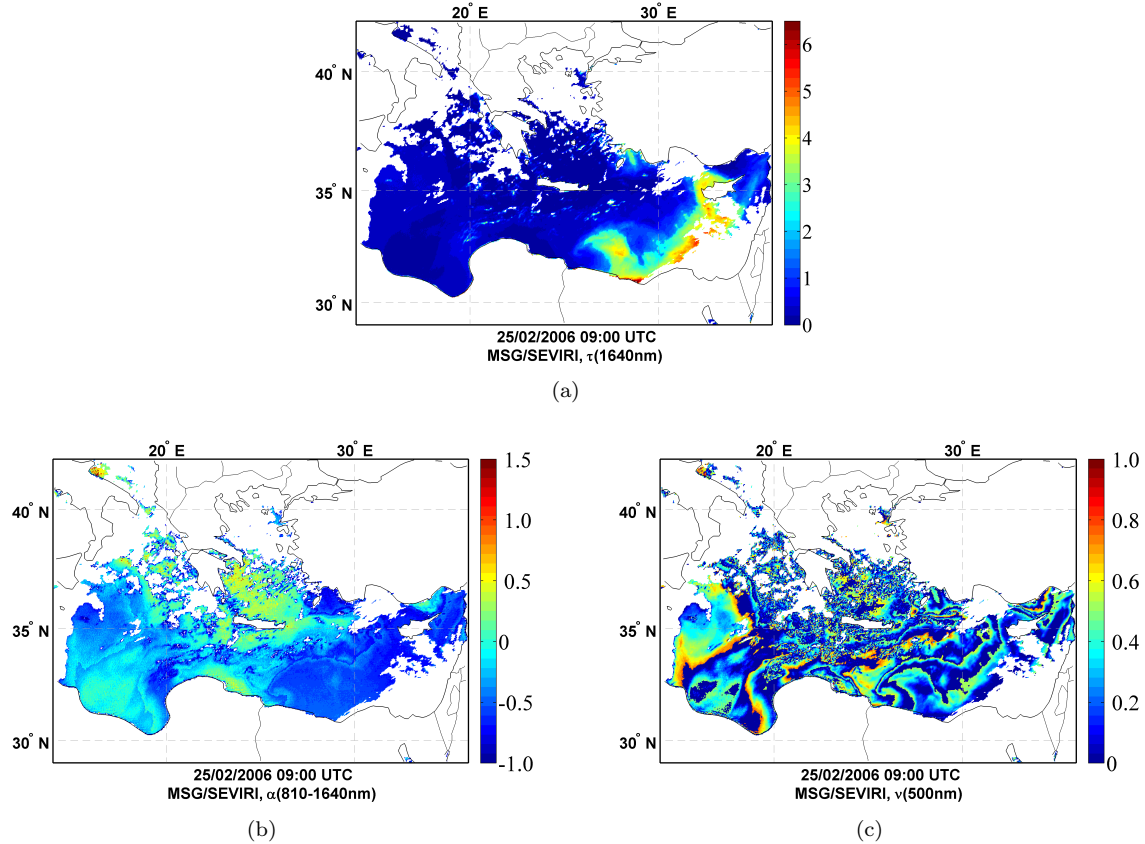


Figure 4.11: Results from SARA retrievals for the dust storm over the eastern Mediterranean on 25 February 2006 at 09:00 UTC: Map (resolution $\sim 5 \times 7 \text{ km}^2$) of (a) AOD at 1640 nm, (b) Ångström coefficient 810-1640 nm, and (c) weight of the Fine/Coarse mode aerosol on AOD at 500 nm.

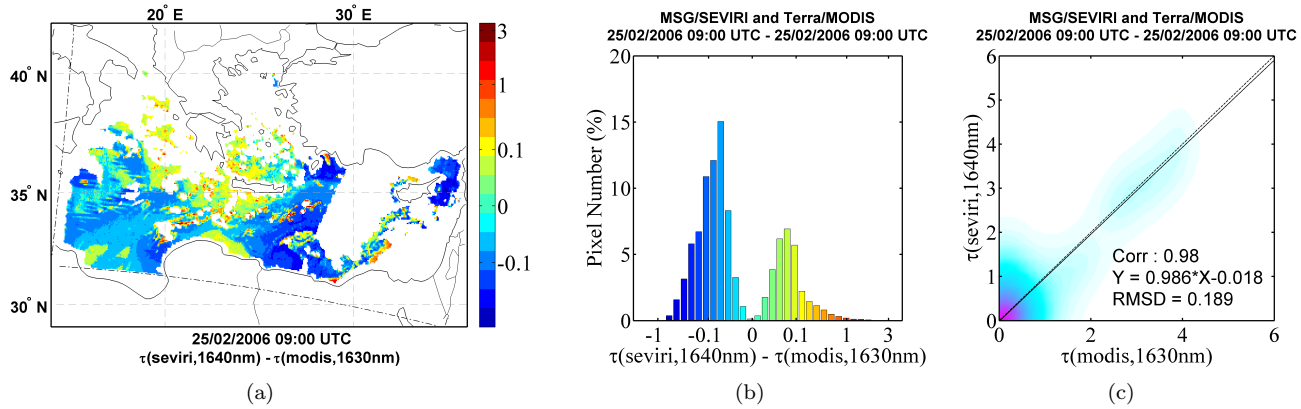


Figure 4.12: Comparison of the retrieved AOD from MSG-SEVIRI and MODIS, for the dust storm over the Mediterranean Sea on 25 February 2006 at 09:00 UTC, with the use of a non-spherical dust model: (a) Map of the AOD difference (resolution $\sim 5 \times 5 \text{ km}^2$). (b) Histogram of the AOD difference. (c) Density scatterplot, with indication for the correlation coefficient, the linear regression coefficients, and the Root Mean Square Difference. The dashed line in the scatterplot represents the identity line, and the solid line is the calculated regression line.

4.5 Conclusions

The approach used in the AATSR aerosol retrieval algorithm over the ocean has been applied to the data from the MSG-SEVIRI instrument through the implementation of the new algorithm SARA. Several sets of LUTs for use with SARA and based on different aerosol models were produced with the DAK radiative transfer model. The results obtained with SARA based on these pre-computed LUTs have demonstrated its capability to derive optical properties such as the aerosol optical depth and the Ångström coefficient over the ocean for case studies related to forest fires and dust storm.

During summer 2006, a forest fire episode in Spain and Portugal has resulted in high AOD values over the Atlantic coast of the Iberian peninsula. The values of AOD retrieved with SARA have been validated against AERONET 'ground-truth' measurements for the coastal station of Cabo da Roca, and showed $\sim 90\%$ correlation in the visible channels. The diurnal variation of the retrievals at the AERONET location are in very good agreement with the AERONET trends (bias of about 0.07). According to MODIS comparisons, the spatial variations of the AOD related to the transport of smoke over the ocean, are well reproduced by the SARA algorithm with approximately 87% correlation. Other parameters derived from the retrievals such as the Ångström coefficient and the contribution of the fine mode to the total AOD at 500 nm, provide additional and consistent information which confirms the dominance of fine aerosol particles in the smoke plume and their important contribution to the total AOD at 500 nm.

The second case study is related to the dust outbreak across the eastern Mediterranean in February 2006. This case study required the implementation of a desert dust detection routine which provides a satisfactory discrimination between dust and clouds over the ocean for the studied event. The AOD retrieved using SARA is in very good agreement with MODIS retrievals, which is further improved by using a non-spherical model to represent the coarse mode for the dust aerosol type: 98% correlation and a bias of about 0.02 for the near-infrared channel. For the desert dust case study, cloud contamination during the event prevented to draw solid conclusions from the comparison with the ground measurement timeseries. However, the general trends of the AOD provided by SARA retrievals agree reasonably with observations made at the AERONET site of Forth Crete. According to the Ångström coefficient derived from the retrievals, the coarse mode was found dominant where the dust was densest, and its fraction vanished as the dust was mixing with the surrounding polluted air masses. Due to the particular range of scattering angles, non-spherical and spherical simulations produced similar results for the near-infrared wavelength in this study. The impact of using this non-spherical model in SARA retrievals over the ocean should be further investigated with applications to other desert dust events presenting different illumination-observation geometries. Moreover, when non-spherical aerosol types were used for dust, the algorithm preferentially chose one size among the two coarse modes (i.e. 'MODISc8' or 'MODISc9'). So both the size and phase function of the aerosol a priori play an important role in the determination of the 'best' aerosol model in the algorithm. The values of the retrieved AOD are found not

significantly dependent on the aerosol model. Meanwhile the ability to retrieve the aerosol type certainly requires further development and additional studies.

Acknowledgements

The authors would like to thank the KNMI for providing the SEVIRI data. We express our gratitude to the Aerosol Robotic Network (AERONET) and the principal investigators of the different sites, as well as the NASA and the MODIS Science Teams for making available the aerosol data used in this study. Financial support from the SRON (project number EO-077) is gratefully acknowledged.

Chapter 5

Aerosol retrievals over land: exploration of a method and application

Abstract

In this chapter the exploration and preliminary application of a method for aerosol retrieval over land using SEVIRI data are presented. With this purpose, in the SARA algorithm the surface correction over land is determined using a global surface reflectance database based on MODIS/MISR observations. This method allows to derive the AOD from the first visible channel of MSG-SEVIRI with a frequency of 15 minutes, and was applied over Europe for the summer of 2006. In general, these results correlate moderately with AERONET ground-based measurements (0.4-0.8). As regards spatial variations, the SEVIRI AOD shows reasonable consistency with the MODIS aerosol product. According to both comparisons with MODIS and AERONET, the SEVIRI AOD retrieved with SARA is overestimated, and SARA is unable to produce satisfactory retrievals under low AOD conditions (<0.15). Moreover, the timeseries show that cloud contamination remains a critical issue in the retrievals. Further implementations are needed to better estimate the surface effect, and to include AOD retrievals for the second visible channel and the near-infrared channel of SEVIRI.

5.1 Introduction

Although 70% of the Earth surface is covered by oceans, the largest number and variety of aerosol particles originate from land sources. Satellites are the only tools capable of providing data for the description of the size distribution and chemical composition of aerosols over large scales. Satellite detection of aerosols over water is a well-established technique (cf. Chapter 4), whereas retrievals over land are generally difficult to perform due to a poor contrast, or because the reflectance of the surface background is generally greater than that due to the aerosol layer. For this reason, the retrievals of aerosol properties from satellite-based measurements has for long been limited to applications over the ocean or dark vegetation.

So far, aerosol information derived from satellite measurements in the visible and the near-infrared range, has mainly been retrieved using passive remote sensing techniques. To correct the satellite signal for the contribution of the surface, an aerosol retrieval algorithm over land can use *a priori* values from a surface reflectance database. Among the current databases: Koelemeijer et al. [2003] proposed a surface reflectivity database derived from the visible wavelengths of the GOME (Global Ozone Monitoring Experiment) instrument; the high angular sampling obtained from the combination of data from the two MODIS (MODerate resolution Imaging Spectroradiometer) instruments flown on Terra and Aqua, and MISR (Multi-angle Imaging SpectroRadiometer), allowed the construction of a surface BRDF (Bi-Directional Reflectance Distribution Functions)/albedo parameter database which constitutes a realistic land surface parametrization of the surface anisotropy [Wanner et al., 1997]. However, due to the lack of surface reflectance databases, several techniques based on spectral, angular, or polarization properties have been proposed to separate the surface from the aerosol contribution in the absence of a surface *a priori*. For MODIS, [Kaufman et al., 1997a] describes a method based on the properties of the visible (blue) to the mid-infrared (2.1 μm) reflectance ratio of over land. With bi-angular and multian-gle observation capabilities of ATSR (Along Track Scanning Radiometer) and MISR (Multi-angle Imaging SpectroRadiometer), the directional signature can be used to discriminate between the radiation originating from the surface and the atmospheric contribution [Veefkind, 1999, Martonchik et al., 2002]. As compared to atmospheric scattering, much less polarized light emerges from the reflection of natural light on ground surfaces. As a result, polarized radiances such as those from POLDER (POLarization and Directionality of the Earths Reflectances) facilitate the correction for ground contribution to the TOA reflectance [Deuzé et al., 2001]. The launch of the CALIPSO (Cloud-Aerosol Lidar and Infrared Pathfinder Satellite Observation) spacecraft which carries the CALIOP (Cloud-Aerosol Lidar with Orthogonal Polarization) lidar offers direct applications of active remote sensing from space to provide accurate information on the vertical distribution of aerosols and clouds with a global coverage.

The greatest advantage of the SEVIRI (Spinning Enhanced Visible Radiometer) instrument onboard the MSG (Meteosat Second Generation) is its unprecedented repeat cycle of 15 minutes over a full Earth disk. The single-view radiometer MSG-SEVIRI is designed to measure the radiance for 12 spectral channels for a hemispheric

region encompassing Africa, most of Europe and the Atlantic ocean at a spatial resolution of 3 km at the subsatellite point. With the combination of excellent spatial, temporal, and spectral resolutions, the multispectral geostationary observations of this sensor provide important inputs for weather forecasts and climate models, and for understanding of the transport and the dispersion of atmospheric pollution. In the framework of aerosol retrievals, the three solar channels of MSG-SEVIRI (635 nm, 810 nm and 1640 nm) are expected to provide useful information as regards urban and rural pollution over mid-latitude Europe and the Mediterranean basin, Saharan dust from North Africa, or the tropical and sub-tropical forest-fires in the African savanna.

The objective of this chapter is to present the exploration of a method for the derivation of aerosol optical properties over land surfaces from MSG-SEVIRI data. This method, which is based on the use of the MODIS surface reflectance database, has been applied to obtain preliminary results for aerosol optical depth (AOD) over land. The chapter starts with a short description of the methodology used in the first-stage retrievals of the SEVIRI Aerosol Retrieval Algorithm (SARA) over land. Aerosol information is derived for cloud-free areas, and cloud-contaminated data are filtered using the cloud screening technique described by [Bennouma et al. \[2008\]](#) (for details see Chapter 3). In the retrieval procedure applied over land, radiative transfer simulations provide pre-calculated tables of the optical properties of the atmosphere for two different types of aerosols and under different aerosol load conditions. The surface correction assumes a Lambertian surface, with reflectance values based on (solar) zenith angle dependent albedo values, reconstructed using the parametrization of the MODIS BRDF/Albedo product for the illumination geometry of MSG-SEVIRI. The preliminary results obtained with the SARA algorithm show the aerosol optical depth derived from the first visible channel of SEVIRI over Europe in the summer of 2006. The AOD retrieved with SARA is evaluated against measurements from several AERONET stations across Europe. For the same period, the differences between MODIS and SEVIRI aerosol retrievals are also presented for a MODIS overpass over western Europe.

5.2 Method and algorithm description

5.2.1 Simulation of the satellite signal

Away from *hot spot* geometry conditions (cf. definition in 2), a land surface can be considered to reflect like a Lambertian surface. For a Lambertian surface the fraction reflected by the surface is independent of the viewing geometry. The TOA reflectance above a plane parallel homogeneous atmosphere overlying a Lambertian surface is modeled using the formulation proposed by [Chandrasekhar \[1960\]](#):

$$\rho = \rho_{atm} + \frac{\rho_{sfc}}{1 - S_{atm} \cdot \rho_{sfc}} T_{tot} \quad (5.1)$$

In this equation, ρ_{atm} is the atmosphere intrinsic reflectance, T_{tot} is the transmission function of the atmosphere, S_{atm} the spherical albedo of the atmosphere, and ρ_{sfc} is the albedo of the underlying surface. The optical properties of the atmosphere ρ_{atm} , T_{tot} and S_{atm} are calculated using a radiative transfer model (see next section). The values used for ρ_{sfc} are based on the MODIS BRDF/albedo product (detailed description in section 5.2.3).

5.2.2 Aerosol models and atmospheric optical properties

The Doubling and Adding KNMI (Royal Netherlands Meteorological Institute) radiative transfer model (DAK) [Stammes, 2001], is used to compute the optical properties of the atmosphere for different aerosol burdens. In the radiative transfer simulations, the atmosphere contains both gases and aerosol particles, and the aerosol particles are confined to the lowest 2 km of the atmosphere. The characteristics of the gaseous phase are based on the mean winter and summer conditions described by the classic Midlatitude Winter (MLW) and Midlatitude Summer (MLS) profiles [McClatchey et al., 1972]. The optical characteristics of the aerosol media are calculated using the Mie code of de Rooij and van der Stap [1984] for a polydispersed aerosol consisting of spherical particles distributed according to a monomodal lognormal number size distribution:

$$n(r) = \frac{dn}{dr} = \frac{1}{r \cdot \sqrt{2\pi} \cdot \ln \sigma_g} \exp \frac{-(\ln r - \ln \bar{r}_g)^2}{2 \cdot \ln^2 \sigma_g} \quad (5.2)$$

Two different aerosol types based on the OPAC database [Hess et al., 1998] are used for the retrievals over land. The water soluble aerosol type 'OPACwaso' is used to represent the anthropogenic component of the ambient aerosol, whereas the sea salt aerosol type 'OPACssam' accounts for the contribution of the natural source, here considered to be of marine origine. Table 5.1 summarizes the physical and optical properties associated with these two aerosol types. The atmospheric properties ρ_{atm} , T_{tot} , and S_{atm} are calculated individually for these two aerosol types, and are stored in two separate LUTs. ρ_{atm} and T_{tot} are directly obtained from the DAK output, with a surface reflectance parameter set to 0 in DAK input data. For a given atmospheric state, the spherical albedo of the atmosphere S_{atm} is derived from the results of 3 different radiative transfer simulations obtained successively with a surface reflectance value of 0, 0.5 and 1, using equation 5.1:

$$S_{atm} = 1 + \frac{(\rho_{\rho_{sfc}=0.5} - \rho_{\rho_{sfc}=0})}{(\rho_{\rho_{sfc}=0.5} - \rho_{\rho_{sfc}=1})} \quad (5.3)$$

The parameter values of the LUTs are tabulated for multiple observation geometries (15 solar and viewing zenith angles, 37 azimuth angles), and different atmospheric conditions characterized by the aerosol optical depths at the reference wavelength of 500 nm (τ_{500}) in the range of 0 to 6.

Table 5.1: Size distribution parameters and microphysical properties for the aerosol models used to generate the different LUTs.

LUT Label	$R_g(\mu m)$	σ_g	$m(\lambda) = n + ik$		
			635 nm	810 nm	1640 nm
OPACwaso	0.03	2.24	1.40 + i0.00212	1.39 + i0.00327	1.37 + i0.00633
OPACssam	0.42	2.03	1.35 + i0.00000	1.35 + i0.00000	1.33 + i0.00015

5.2.3 Land surface albedo

Land surface albedo describes the fraction of incoming solar energy reflected at a given point and time [Wang et al., 2004] i.e. time of the day and season. It is strongly dependent on the solar zenith angle and the three-dimensional structure of the vegetation canopy. Strahler et al. [1999] describes the theoretical basis of the algorithm used for the derivation of the land surface albedo from atmospherically corrected and cloud-cleared radiances from combined observations of the MODIS and MISR instruments. In this algorithm the satellite observations are coupled with semi-empirical models to describe the shape of the BRDF and the corresponding integrals that can be used to derive the spectral albedo of the surface. The semi-empirical models are based on the Ross-Li semi-empirical kernel-driven models of Roujean et al. [1992], in which the BRDF of the surface (R_{sfc}) is expressed by the sum of three kernels corresponding to the basic scattering modes:

$$R_{sfc}(\lambda, \theta_s, \theta_v, \phi_r) = f_{iso}(\lambda) + f_{vol}(\lambda) \cdot K_{vol}(\theta_s, \theta_v, \phi_r) + f_{geo}(\lambda) \cdot K_{geo}(\theta_s, \theta_v, \phi_r) \quad (5.4)$$

where f_{iso} , f_{vol} and f_{geo} are the weighting parameters for isotropic scattering, volume scattering (i.e. interleaf effect), and geometric-optical scattering (i.e. intercrown effect) respectively. The kernels K_{vol} and K_{geo} represent the Ross-Thick [Ross, 1981] and the Li-Sparse [Li and Strahler, 1992] kernels respectively.

One of the standard products of this algorithm is the global MODIS BRDF/Albedo data product (MCD43C1). The MCD43C1 product is a 16-day 0.05° gridded product which provides a set of the 3 parameters f_{iso} , f_{vol} , and f_{geo} for each of the first 7 bands of the MODIS instrument. These parameters can be used to calculate the white and the black sky albedo. The black sky albedo represents the albedo under a fully direct illumination (i.e. in the absence of a diffuse component of the radiation). The black sky albedo is thus a function of the solar zenith angle. The white sky albedo corresponds to the albedo of the surface under a completely diffuse and isotropic illumination. Although the actual albedo of a surface can be accurately represented by a value interpolated between the black and white sky albedo, under most situations the black sky albedo provides a reasonable estimation of the surface albedo that can

be used in the surface correction step. Therefore, in equation 5.1, the value of the surface reflectance ρ_{sfc} is approximated by the value of the black sky albedo, which is determined from the parametrization of the MODIS/BRDF albedo product for coincident MODIS and SEVIRI pixels, using:

$$\rho_{sfc}(\theta_s, \lambda) = \sum_{k=1}^3 f_k(\lambda) \cdot h_k(\theta_s) \quad (5.5)$$

in which h_k corresponds to the kernel integrals specific to the kernel driven models.

5.2.4 Retrieval assumptions

Decoupling aerosol and molecular scattering

In the retrieval process, the intrinsic reflectance of the atmosphere ρ_{atm} , also called path reflectance of the atmosphere, is decomposed into the sum of ρ_{ray} the path radiance of a purely molecular atmosphere, and ρ_{aer} the path reflectance accounting only for the aerosol constituents of the atmosphere:

$$\rho_{atm}(\lambda) = \rho_{ray}(\lambda) + \rho_{aer}(\lambda) \quad (5.6)$$

Therefore, the spherical albedo of the atmosphere can be expressed with a similar expression:

$$S_{atm}(\lambda) = S_{ray}(\lambda) + S_{aer}(\lambda) \quad (5.7)$$

External aerosol mixture

In addition, the path reflectance estimate for a mixture of two aerosol types is the weighted average of the path reflectance from each of the two aerosol types:

$$\rho_{aer}(\lambda) = \nu \cdot \rho_f(\lambda) + (1 - \nu) \cdot \rho_c(\lambda) \quad (5.8)$$

in which ν is the weight of the reflectance due to the aerosol type representing the fine mode ρ_f , and ρ_c represents the reflectance related to the coarse mode aerosol. Hence the spherical albedo of the atmosphere due to the aerosol mixture can be written as:

$$S_{aer}(\lambda) = \nu \cdot S_f(\lambda) + (1 - \nu) \cdot S_c(\lambda) \quad (5.9)$$

5.2.5 Minimization process and AOD retrieval

The signal measured by the satellite ρ^{meas} , is compared to the modeled TOA reflectance ρ^{lut} calculated using the LUT data for different atmospheric states, and the

algorithm finds the aerosol model that minimizes the error ϵ formulated by:

$$\epsilon_{\nu, f, c, \tau_{500}} = \sum_{i=1}^n \left(\frac{\rho^{meas}(\lambda_i) - \rho^{lut}(\lambda_i, \tau_{500})}{\rho^{meas}(\lambda_i) - \rho_0^{lut}(\lambda_i) + 0.01} \right)^2 \quad (5.10)$$

where ρ_0 is the TOA reflectance of the underlying surface-atmosphere system, in the absence of aerosols. The so-called 'best' aerosol model determines the aerosol mixture which is used to derive the relation between the top of the atmosphere reflectance and the AOD. For weakly absorbing aerosols and small optical depths, the SARA algorithm assumes a linear dependance of the top of the atmosphere reflectance on the aerosol optical depth [Durkee et al., 1986, Veefkind, 1999]. Under such conditions, the top of the atmosphere reflectance is:

$$\rho(\lambda) = \rho_0(\lambda) + C(\lambda) \cdot \tau(\lambda) \quad (5.11)$$

The spectral constant C is calculated for the interpolated observation geometry, and depends on the value of the surface reflectance as well as on the aerosol type.

5.3 Aerosol observations over Europe for summer 2006

5.3.1 Results

In the current state of development of the SARA algorithm, only the AOD in the first visible channel (635 nm) of SEVIRI can be retrieved with some degree of confidence. At 810 nm and 1640 nm, the relative contribution of the surface to the total signal is very large, and the difference between the spectral bands of SEVIRI (810 nm, 1640 nm) and MODIS (860 nm, 1640 nm) can strongly affect the accuracy of the surface correction based on the MODIS surface *a priori*. As a result, deviations from the surface *a priori* induce large errors and the AOD is not properly retrieved at those wavelengths. Figure 5.1 shows an example of the spatial distribution of the AOD over Europe at 635 nm as retrieved from SEVIRI by SARA. In this example, the highest AOD values (0.4-0.8) are observed over England, central Germany, northern France, and the Po Valley. For some areas (e.g. Netherlands, Spanish North Atlantic coast), as compared to AOD values retrieved over the ocean, the values of the AOD over land seem rather low, and the AOD gradient between the land and ocean appear discontinuous. This suggests an overestimation of the surface correction, which could also explain the negative values of the AOD obtained over Ireland, The Netherlands, the southwest of France, and Hungaria. For this case, the high and spatially dispersed AOD values observed over Spain and north Africa occur near cloud edges where strong gradients exist and transition between aerosol and cloud causes undetermined clouds.

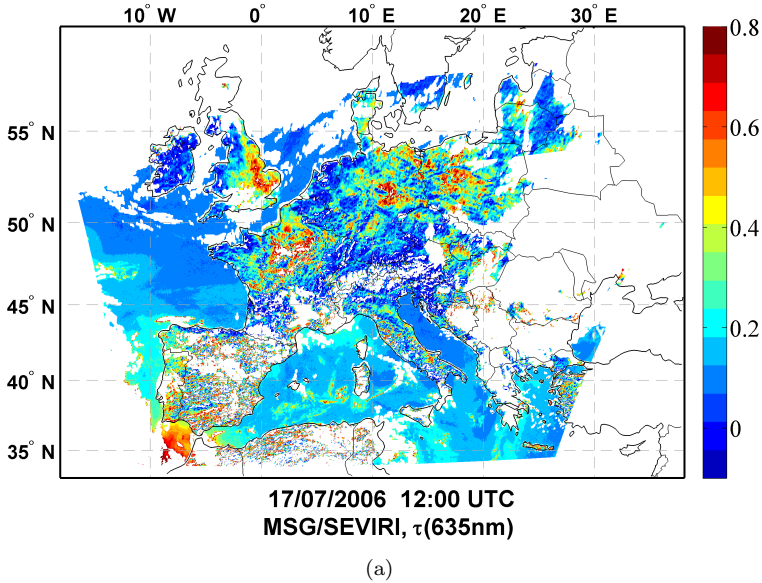


Figure 5.1: Results from SARA retrievals over Europe on 17 July 2006 at 11:15 UTC. Map (resolution $\sim 5 \times 7 \text{ km}^2$) of AOD at 635 nm.

5.3.2 Evaluation against AERONET

To evaluate the AOD results obtained with the SARA algorithm, the latter were compared to AERONET timeseries from different European sites for the months of June, July and August 2006. The map location of the AERONET stations chosen for this study is presented in Figure 5.2, namely: Avignon, Carpentras, Ispra, Modena, Chilbolton, Cabauw, Mainz, and Laegeren.

The surface reflectance values inferred from the MODIS/BRDF albedo parametrization (cf. section 5.2.3), for the SEVIRI pixels collocated with the different AERONET sites, are presented in Figure 5.3. For each AERONET site, the variations of the surface reflectance over the day describe different shapes. These shapes are representative of the reflective properties of the local land cover type for the illumination geometry associated with the SEVIRI pixel. The diurnal variations of the surface reflectance form a bell shape (e.g. Avignon) or a bowl shape (e.g. Carpentras), and in both cases the surface reflectance presents high values at large solar zenith angles. Each day is represented with a different color, and the missing data points indicate cloud contamination, because the SARA algorithm does not apply the surface correction when a SEVIRI pixel is considered as cloud contaminated by cloud detection tests.

For each ground site, the study compares 15-minute average AERONET data at 675 nm, with the AOD at 635 nm retrieved from SARA for the SEVIRI pixel nearest to the sunphotometer. Prior to comparison, SEVIRI retrievals were filtered to

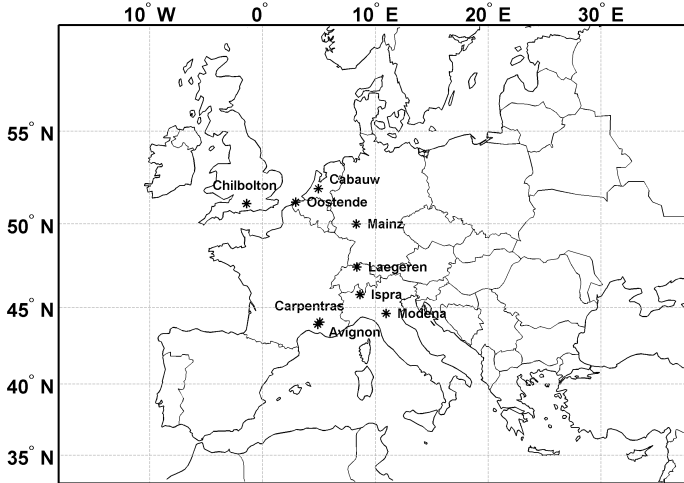


Figure 5.2: Map showing the locations of the different AERONET sites used to test the SEVIRI AOD results of the SARA algorithm over land.

remove remaining cloud contaminated data. In the postprocessing, AOD values above 1 having more than one cloudy-pixel among the neighbouring pixels, were excluded from the comparison. The timeseries are shown in Figure 5.4, and scatterplots are represented in Figure 5.5. The best correlation between SEVIRI and AERONET is found for the Avignon station, where the two datasets are strongly correlated (80%). For all other stations, the correlation coefficient is generally lower, in the range of 40 to 60%. The poor correlations can be explained by the large number of small AOD values measured at the ground-based stations. For clean aerosol conditions, SARA finds the best model to corresponds to the lowest AODs from the LUT (0.02 and 0.05 at 500 nm). However, the interpolation step described by equation 5.11 produces appropriate AOD values. In such conditions, the retrieval method is more sensitive to surface correction accuracy. Consequently, the AOD value retrieved is often either negative or very high. For low-AOD conditions occurring at the beginning or at the end of the day, the AOD retrieved is negative as a result of the increasing surface reflectance at these times of the day. According to the regression lines, the bias is below 0.1 for most locations, and in general the SARA algorithm tends to overestimate the AOD as compared to AERONET.

5.3.3 Evaluation against MODIS

Figure 5.7 shows collocated SEVIRI and MODIS AOD retrievals at 635 nm and 660 nm respectively, for the MODIS overpass of 17 July 2006 at 10:50. In this case,

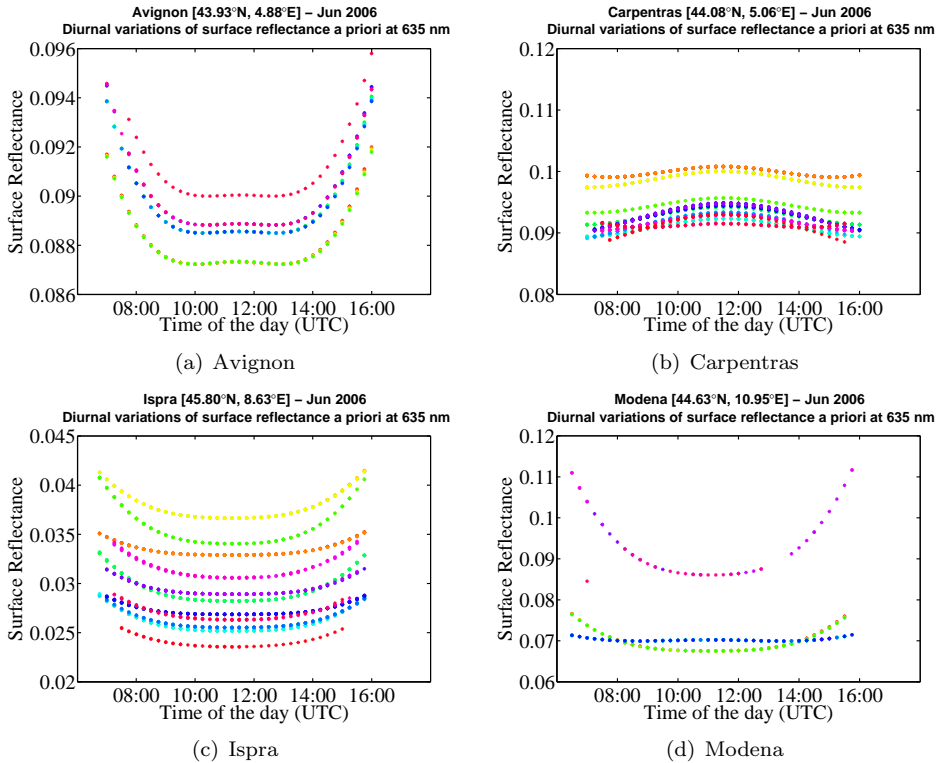


Figure 5.3: Diurnal variations of the surface reflectance inferred from the MODIS BRDF/Albedo parametrization, for SEVIRI pixels coincident with different AERONET sites in Europe for summer 2006: (a) Avignon (b) Carpentras (c) Ispra (d) Modena (e) Chilbolton (f) Cabauw (g) Mainz (h) Laegeren. Each color corresponds to a different day.

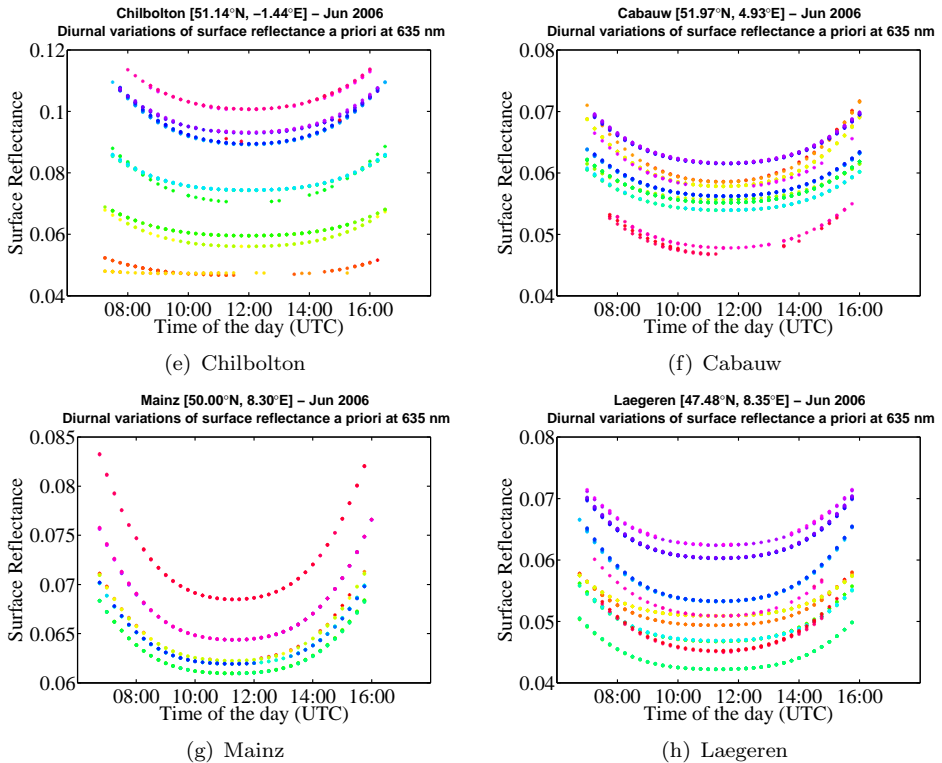


Figure 5.3: Diurnal variations of the surface reflectance inferred from the MODIS BRDF/Albedo parametrization, for SEVIRI pixels coincident with different AERONET sites in Europe for summer 2006: (a) Avignon (b) Carpentras (c) Ispra (d) Modena (e) Chilbolton (f) Cabauw (g) Mainz (h) Laegeren. Each color corresponds to a different day. (Cont')

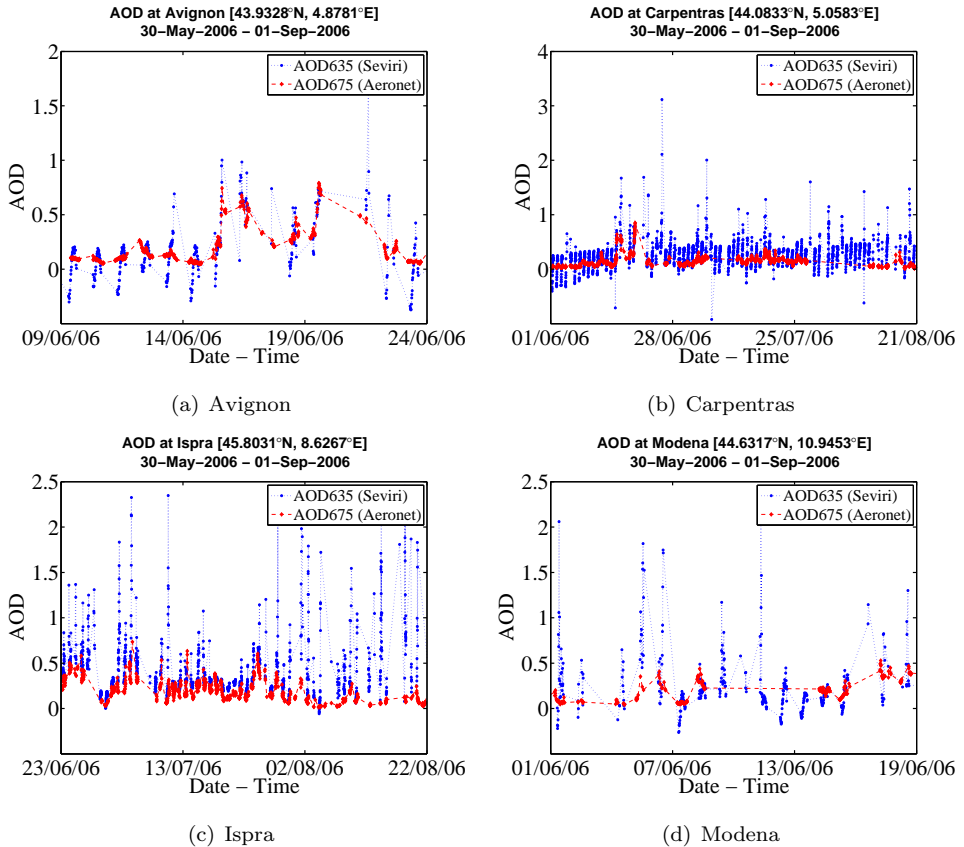


Figure 5.4: Timeseries of the AOD retrieved using SARA at the SEVIRI pixels coincident with AERONET locations for the summer of 2006 (June, July and August): (a) Avignon (b) Carpentras (c) Ispra (d) Modena (e) Chilbolton (f) Cabauw (g) Mainz (h) Laegeren. The red diamonds stand for AERONET data, the blue dots represent SARA retrievals.

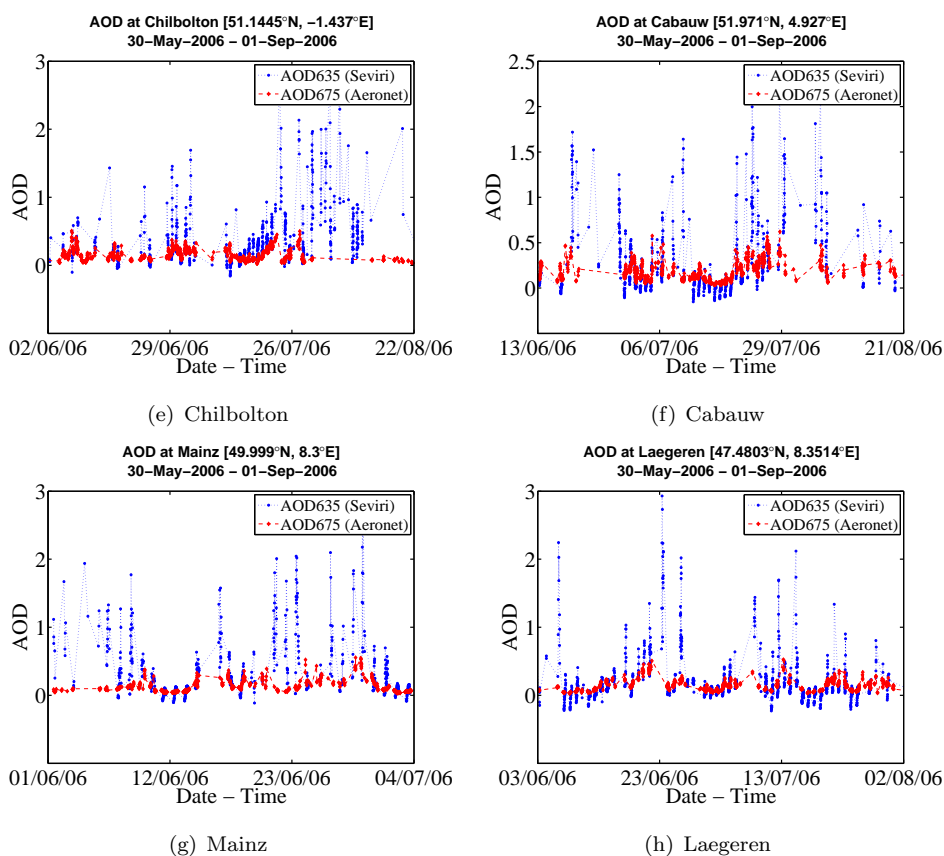


Figure 5.4: Timeseries of the AOD retrieved using SARA at the SEVIRI pixels coincident with AERONET locations for the summer of 2006 (June, July and August): (a) Avignon (b) Carpentras (c) Ispra (d) Modena (e) Chilbolton (f) Cabauw (g) Mainz (h) Laegeren. The red diamonds stand for AERONET data, the blue dots represent SARA retrievals. (Cont¹)

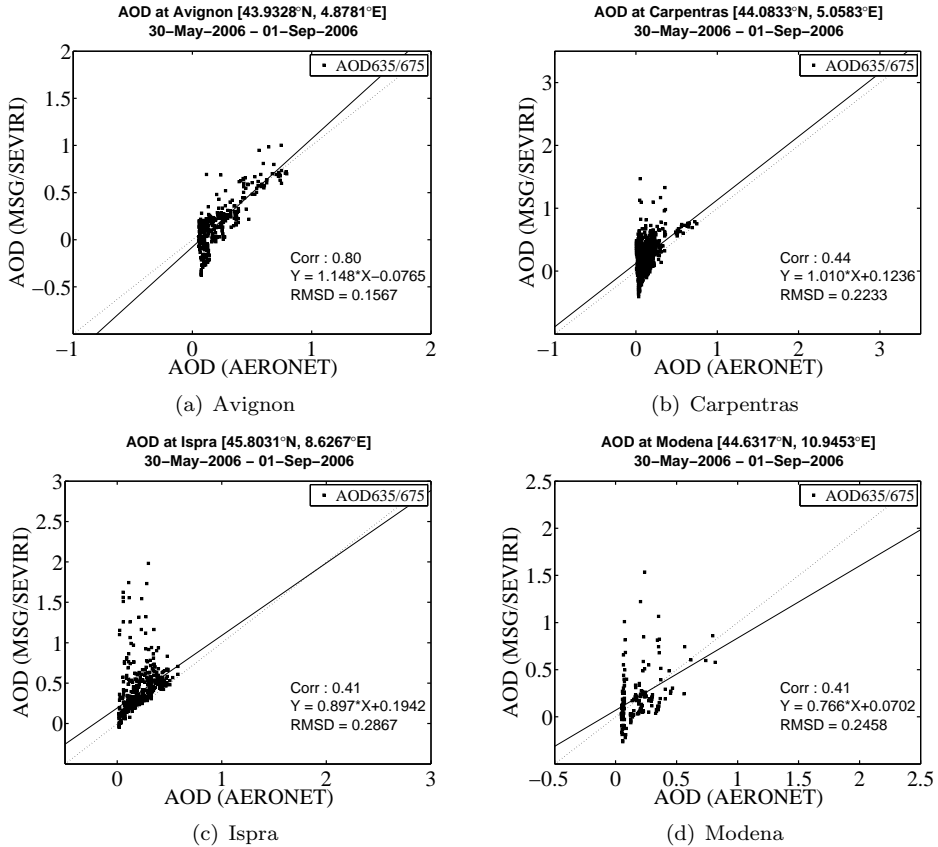


Figure 5.5: Scatterplot of the AOD retrieved using SARA for SEVIRI pixels coincident with AERONET locations site for the summer of 2006 (June, July and August): (a) Avignon (b) Carpentras (c) Ispra (d) Modena (e) Chilbolton (f) Cabauw (g) Mainz (h) Laegeren. On each graph, the correlation coefficient and the linear regression equation are indicated. The dashed line in the scatterplot represents the identity line, and the solid line is the calculated regression line.

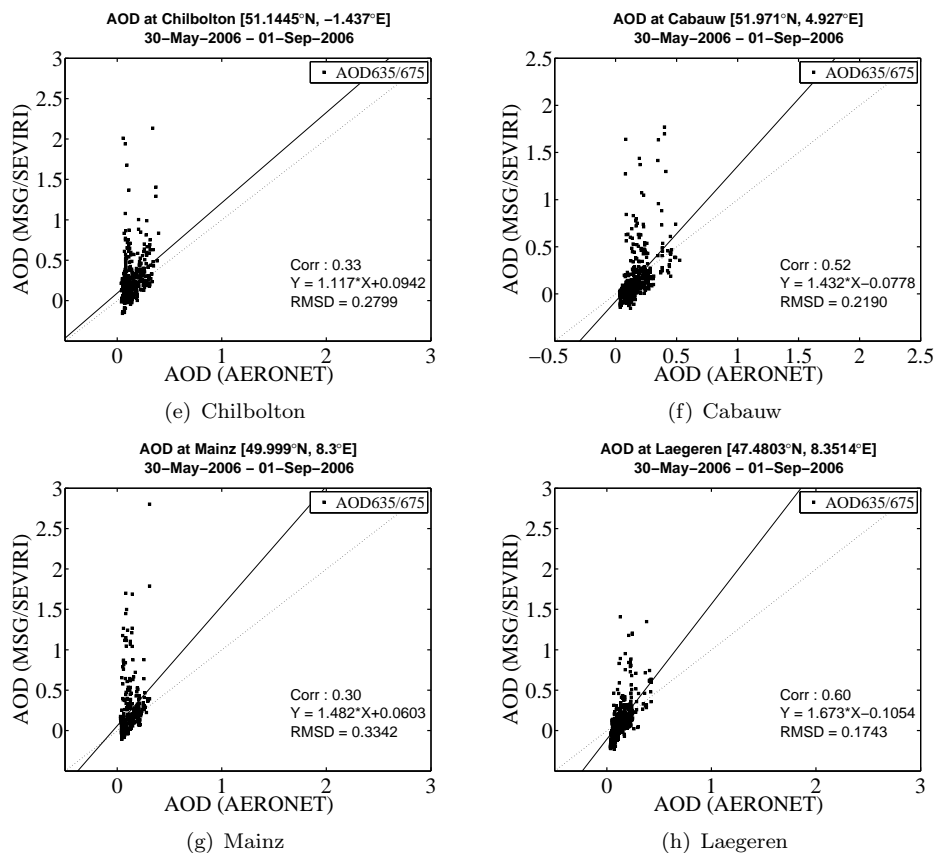


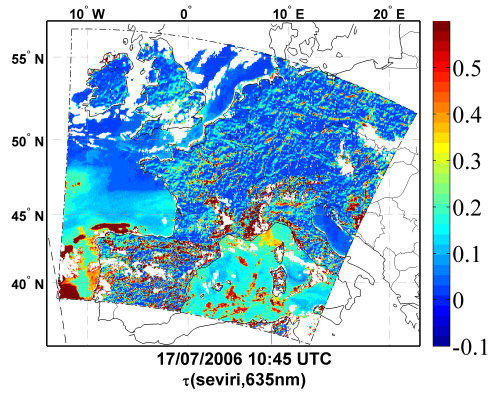
Figure 5.5: Scatterplot of the AOD retrieved using SARA for SEVIRI pixels coincident with AERONET locations for the summer of 2006 (June, July and August): (a) Avignon (b) Carpentras (c) Ispra (d) Modena (e) Chilbolton (f) Cabauw (g) Mainz (h) Laegeren. On each graph, the correlation coefficient and the linear regression equation are indicated. The dashed line in the scatterplot represents the identity line, and the solid line is the calculated regression line. (Cont')

MODIS detects AOD values in the range of 0.1 to 0.2 over central England, the northern part of France, the Netherlands and eastern Germany. The highest AOD values are found over Paris, the Po valley, the southwestern part of France and northeastern part of Spain, where AOD values are mainly above 0.3 reaching up to 0.4. For regions where the MODIS aerosol product shows AOD values below 0.15, the SEVIRI AOD is higher and more homogeneous than that of MODIS. Thus AOD spatial patterns over the northern regions are in general less clear on the map of the SEVIRI AOD. However, the highest AOD values retrieved by MODIS over Italy, France and Spain are well detected by SARA. In addition the high AOD spatial variations over land presumably reveal accuracy problems in the surface correction. The AOD transition between land and ocean surfaces observed over the Atlantic coast of France and Spain, is likely due to underestimation of the AOD over land. According to this comparison, AOD spatial variations seem better represented by the MODIS product. This can be partly explained by the high resolution of the MODIS instrument as compared to SEVIRI, but also by the simplifications and assumptions used by SARA in the surface correction process over land.

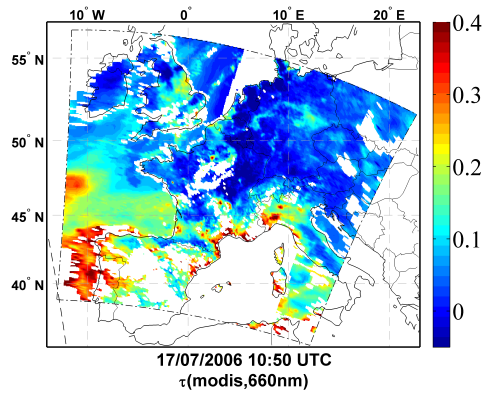
For the same MODIS granule, the map of the AOD difference between MODIS and SEVIRI retrievals and its associated histogram are presented in Figure 5.7. In general, the two sets of data differ by less than ± 0.2 in AOD. On the difference map, the most obvious pattern concerns extremely low AOD values (< 0.1) from MODIS which correspond to significantly larger AOD values for SEVIRI. This difference can be between 0.1 and 0.2. For higher values of the MODIS AOD (> 0.1) the difference between the two instruments is smaller and remains in the range of -0.1 to 0.1. Large differences (> 0.5) are observed near cloud edges, and therefore are anticipated to be due to time difference (5 minutes), the use of different cloud detection algorithms for the two sensors, as well as instrument resolution.

5.4 Conclusion

A simple approach using a surface correction based on the MODIS albedo database has been explored and applied to the SEVIRI data over Europe. The AOD retrieved with this method correlated moderately with AERONET measurements from several European sites. The correlation coefficient is in the range of 0.4 to 0.8. SEVIRI AOD traces quite well AERONET AOD timeseries, but SEVIRI AOD is generally high compared to AERONET, and tends to show very high AODs (> 1). In the present case, AODs with values above 1.5 are likely to result from cloud contaminated data that were not identified as cloudy by the cloud detection process. Screening all AOD retrievals above 1.5 (these figures are not shown in the chapter) have considerably increased the correlation coefficients, by 20% for some locations. Regarding other AOD overestimations, they are suspected to occur because of the surface effect which is not well accounted for in the assumptions of the algorithm. The comparison with MODIS has principally confirmed that in its current implementation state, SARA is not suitable for the retrieval of low AOD values (< 0.15). It should be noted that these results have been obtained with a very simplified formulation of the surface reflectance,



(a)



(b)

Figure 5.6: Map of AOD from (a) MSG-SEVIRI (10:45 UTC) and (b) MODIS (10:50 UTC) on 17 July 2006.

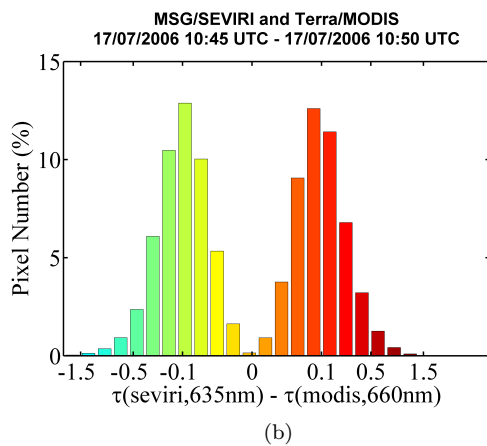
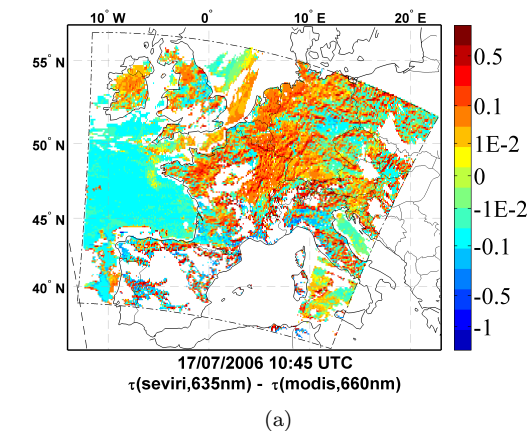


Figure 5.7: Comparison of the retrieved AOD from MSG-SEVIRI (10:45 UTC) and MODIS (10:45 UTC) on 17 July 2006: (a) Map of the AOD difference (resolution $\sim 5 \times 5 \text{ km}^2$). (b) Histogram of the AOD difference.

which considers a surface illuminated by a direct beam. It can be expected to improve the accuracy of the retrievals by using a more complex parametrization of the surface reflectance, such as a linear combination of the "black sky" and the "white sky" MODIS albedo to account as well for the diffuse component of the illumination. The resolution of the surface reflectance database (0.05°) can also be responsible for the poor accuracy of the surface correction. In the next implementation step, it should be considered to exploit the three solar channels of SEVIRI. By means of iterations, the use of the three channels would allow to tune and adapt more accurately the surface reflectance for the SEVIRI spectral bands.

Chapter 6

Conclusion and Outlook

Among the new generation of atmosphere sensors, the SEVIRI (Spinned Enhanced Visible and Infrared Imager) carried on the European spacecraft MSG (Meteosat Second Generation) has the capability to produce 15-minute measurements of the top of the atmosphere radiance over an entire Earth disk, with a high spatial resolution of $3 \times 3 \text{ km}^2$ at nadir. These observations are expected to provide valuable information on aerosol properties and their diurnal variations.

In this thesis the development and the validation of the SEVIRI Aerosol Retrieval Algorithm (SARA), dedicated to the retrieval of aerosol optical properties from geostationary images acquired by MSG-SEVIRI was presented. In its current implementation, SARA allows the retrieval of the aerosol optical depth in the three solar channels of MSG-SEVIRI over the ocean and in the first visible channel over land.

The algorithm can only be applied over cloud free land and ocean surfaces, for which a stand-alone cloud detection procedure has been implemented. The technique used is a modified version of the cloud detection technique applied in the aerosol retrieval algorithm for ATSR-2 and AATSR [Curier et al., 2009] based on the work of Koelemeijer et al. [2001] and Robles-Gonzalez [2003]. Several reflectance and temperature tests are applied, which are different for scenes over land and ocean surfaces. The detection procedure was applied over Europe for several periods during different seasons of 2006, and compared with the cloud mask from the SEVIRI cloud product of Meteo-France and with the MODIS cloud product. The comparison shows that the overall ability of this technique to identify cloud contaminations is satisfactory. The disagreement between the three cloud masks was found to be within 5 to 15 %. In general, the main differences were observed near cloud edges and broken cloud fields. Moreover, obvious cloud mask defects in the cloud mask generated by SARA suggest that an improved version of this stand-alone algorithm should consider the use of latitudinally dependent temperature thresholds over the ocean, as it was done for land. Displacing or modifying the size of the study area within the MSG disk could affect the accuracy and the efficiency of the cloud mask. Because this study was focused over the European region, the technique should also be tested over other

regions, and in particular over very bright surfaces such as desert or snow/ice areas.

The principle of the retrieval of aerosol properties as implemented in SARA, relies on a least-squares minimization of the error between SEVIRI measured and simulated reflectances, for predefined aerosol models and under different aerosol load conditions. The most challenging task of inversion algorithms for aerosol retrieval remains the separation of the surface from the atmospheric contribution. Consequently, aerosol retrievals require an accurate estimation the surface reflectance, as well as an appropriate formulation for the interactions between the surface and the atmosphere. SEVIRI is a single-view instrument, each SEVIRI pixel within the MSG disk is seen under a different viewing angle, and the illumination geometry associated with a pixel varies during the course of the day. As a result, the surface reflectance cannot be directly inferred from SEVIRI radiances, and aerosol retrievals require additional information on the surface reflective properties. So far, no available surface reflectance database based on MSG-SEVIRI data is available. Such a database would allow for the correction for the surface effect, to take the full advantage of the high temporal resolution of 15 minutes.

In SARA, the top of the atmosphere reflectance over the ocean, is determined from the model of [Tanré et al. \[1979\]](#), and the Lambertian approximation of [Chandrasekhar \[1960\]](#) is applied over land. Over dark surfaces, such as the ocean, the surface reflectance can be parametrized relatively easily. The surface reflectance over the ocean accounts for the specular reflection of a wavy ocean surface, the reflectance of oceanic whitecaps, and sub-surface scattering. The wave slope distribution is described by the widely used wind speed dependent formulation of [Cox and Munk \[1954\]](#), foam reflectance is based on measurements of [Whitlock et al. \[1982\]](#), and sub-surface scattering is a function of the chlorophyll concentration [[Baker and Smith, 1982](#), [Morel, 1988](#)] estimated from the monthly climatological chlorophyll concentration database from SeaWiFS [[Campbell et al., 1995](#)]. Over land, the reflective properties of the Earth's surface can vary very much with the land cover type. SEVIRI has spectral channels in the visible and the near-infrared similar to those of MODIS (Moderate resolution Imaging Spectroradiometer). Therefore, an approach was explored that uses the global MODIS BRDF/albedo database as a surface *a priori* in the surface correction process of SARA over land [[Schaaf et al., 2002](#)]. This database includes a parametrization of the surface reflective properties, the so-called "black sky" and "white sky" albedo, based on the fitting of semi-empirical models to MODIS and MISR data. As regards atmospheric optical properties, they were pre-calculated based on DAK (Doubling-Adding KNMI) radiative transfer simulations, using different aerosol models from the literature [[de Leeuw et al., 1989](#), [Hess et al., 1998](#), [Remer et al., 2006](#)] and different ranges of aerosol concentrations. The shape of the phase functions is determined by MIE theory for spherical particles [[Mie, 1908](#)], using the Mie code of [de Rooij and van der Stap \[1984\]](#), except for the desert dust aerosol type, for which the description of the phase function results from T-matrix calculations [[Mishchenko et al., 1996](#)]. All reflectance and transmittance data describing the atmospheric optical properties for the three SEVIRI channels were stored in the form of look-up tables (LUTs). Each LUT refers to a different aerosol type, and is used by SARA to correct for scattering and absorption due to atmospheric constituents,

i.e., gases and aerosol. SARA was implemented in such a way that it considers the aerosol constituent to be an external mixture of two monomodal aerosols: a coarse mode and a fine mode, thus representing a natural and an anthropogenic component, respectively. SARA estimates the surface reflectance and interpolates the LUT values for the specific geometry of each pixel. The aerosol mixture that best fits the satellite measurement determines the model used to calculate the SEVIRI AOD.

The methodology for AOD retrievals over the ocean is based on the single-view algorithm developed by [Veefkind and de Leeuw \[1998\]](#) for ATSR-2 (Along Track Scanning Radiometer). The applicability of the SARA algorithm over the ocean was evaluated for two case studies for which both the AOD and the Ångström coefficient were derived.

The first case study deals with observations made during forest-fire episodes in Spain and Portugal. The smoke of these fires was advected off the Atlantic coast, and high values of both AOD (>0.4) and Ångström coefficient (>0.8) were detected from the visible radiances of SEVIRI over the smoke plume. These observations confirmed the expected dominance of small aerosol particles and their large impact on the total aerosol optical depth. The values and diurnal variations of the SEVIRI AOD during this episode correlate very well with the timeseries of available AERONET data observed in the region. This comparison shows that SARA provides better results than MODIS in this particular case. In these retrievals, a mixture of sea salt and water-soluble aerosol types was considered. However, biomass burning aerosols are a complex mixture of non-soluble and water-soluble organic and inorganic compounds. Although AOD retrievals have provided satisfactory results over the smoke plume, a new LUT dedicated to biomass burning retrievals should be built and tested.

The second case study is that of a desert dust outbreak in the eastern Mediterranean sea. For this case study several desert dust models were tested, and the effect of the non-sphericity of dust particles on the retrievals was also investigated. Over the dust cloud, aerosols strongly influence the satellite measurement in the near-infrared channel, and the AOD retrieved for this spectral band reaches values up to 5. The Ångström coefficient presented very low negative values ($-0.5-0$). Due to the occurrence of cloud contaminations, the agreement with AERONET data was less convincing than for the forest-fire case. However the general day-to-day trends of the AOD appeared reasonably reproduced by SARA. As regards spatial variations of the SEVIRI AOD, they were in good agreement with MODIS retrievals (correlation coefficient $>95\%$). The use of non-spherical models appears to produce lower values of the SEVIRI AOD, and leads to a slightly improved agreement with MODIS.

As mentioned, over land a methodology based on the use of the surface reflectance database of MODIS has been explored. With this method, SARA retrieves the AOD from the visible channel of SEVIRI at 0.635 nm, and an evaluation of the results obtained was carried out using data over Europe for the summer of 2006. The comparison with several AERONET locations across Europe shows that there is a moderate correlation between the SEVIRI AOD and ground-based AERONET AOD timeseries (40-80%). Ground-based measurements indicate low-AOD conditions frequently occurred during the study period, and this can partly explain the weak correlations

between SEVIRI and AERONET data. Under such atmospheric conditions, the relative contribution of aerosols to the TOA reflectance is small, and therefore the retrieval is more sensitive to errors in the estimate of the surface reflectance. This can lead to large under- or over-estimation of the AOD. For larger AODs (> 0.2), the SARA algorithm produces satisfactory results although, as compared to AERONET, there seems to be an overestimation of the AOD by SARA. The comparison of the spatial variations between the SEVIRI AOD and the MODIS aerosol product have demonstrated that the major spatial patterns of the AOD are captured by SEVIRI, but the differences between the AOD values obtained for the two retrievals are quite large, and mostly in the range of -0.2 to 0.2 . In general, high values of the MODIS AOD are underestimated by SEVIRI, whereas for MODIS low-AOD conditions the AOD is overestimated by SARA. Preliminary AOD results over land are promising, but more work is required to achieve accurate AOD retrievals using this method. At this stage of the implementation, the surface correction is simply performed using the MODIS "black sky" albedo, which implies the assumption of a pure direct illumination. The errors introduced by this assumption could be critical, in particular for large solar zenith angles (i.e. air mass factor impact), or under high AOD conditions. More adequate retrievals should consider a diffuse component of the illumination in the estimation process of the surface reflectance. This could be taken into account, for instance, by approximating the surface reflectance as a linear combination of the white and the black sky albedo, weighted by the fraction of the diffuse to the total incident radiation at the surface level. In addition, extra implementation work is needed to include the use of the 810 nm and 1640 nm SEVIRI channels, both to tune the surface reflectance estimate for the specific wavelengths of SEVIRI, and to obtain AOD retrievals at these wavelengths.

Bibliography

- M. Aceves and J.O. Grimalt. Seasonally dependent size distributions of aliphatic and polycyclic aromatic hydrocarbons in urban aerosols from densely populated areas. *Environmental Science & Technology*, 27(13):2896–2908, 1993. [9](#)
- A.S. Ackerman, O.B. Toon, D.E. Stevens, A.J. Heymsfield, V. Ramanathan, and E.J. Welton. Reduction of Tropical Cloudiness by Soot. *Science*, 288(5468):1042, 2000. [19](#)
- S.A. Ackerman, K.I. Strabala, W.P. Menzel, R.A. Frey, C.C. Moeller, and L.E. Gumley. Discriminating clear sky from clouds with modis. *Journal of Geophysical Research*, 103(D24):32141–32157, 1998. [70](#)
- J. Al-Saadi, J. Szykman, R.B. Pierce, C. Kittaka, D. Neil, D.A. Chu, L. Remer, L. Gumley, E. Prins, L. Weinstock, et al. Improving National Air Quality Forecasts with Satellite Aerosol Observations. *Bulletin of the American Meteorological Society*, 86(9):1249–1261, 2005. [27](#)
- B.A. Albrecht. Aerosols, Cloud Microphysics, and Fractional Cloudiness. *Science*, 245(4923):1227–1230, 1989. [18](#)
- D.M.A. Aminou. MSG’s SEVIRI instrument. *ESA Bulletin(0376-4265)*, pages 15–17, 2002. [30](#), [162](#)
- M.O. Andreae. The ocean as a source of atmospheric sulfur compounds. *The Role of Air-Sea Exchange in Geochemical Cycling*, pages 331–362, 1986. [6](#)
- M.O. Andreae. Climatic effects of changing atmospheric aerosol levels. *World Survey of Climatology*, 16:341–392, 1995. [2](#), [3](#), [169](#)
- M.O. Andreae and H. Raemdonck. Dimethyl Sulfide in the Surface Ocean and the Marine Atmosphere: A Global View. *Science*, 221(4612):744–747, 1983. [6](#)
- E. L. Andreas. A new sea spray generation function for wind speeds up to 32ms-1. *Journal of Physical Oceanography*, 28:21752184, 1998. [9](#)
- C. Bacour, F.M. Bréon, and F. Maignan. Normalization of the directional effects in NOAA–AVHRR reflectance measurements for an improved monitoring of vegetation cycles. *Remote Sensing of Environment*, 102(3-4):402–413, 2006. [41](#)

- K.S. Baker and R.C. Smith. Bio-optical classification and model of natural waters. 2. *Limnology and Oceanography*, 27(3):500–509, 1982. [88](#), [136](#)
- R. L. Bankert. Cloud classification of avhrr imagery in maritime regions using a probabilistic neural network. *Journal of Applied Meteorology*, 33:909–918, 1994. [48](#)
- A.M. Bass and R.J. Paur. The ultraviolet cross-sections of ozone: I, II. In *Atmospheric Ozone, Proceedings of the Quadrennial Ozone Symposium Held in Halkidiki, Greece, 3–7 September 1984*, pages 606–616, 1984. [44](#)
- T.S. Bates, B.J. Huebert, J.L. Gras, F.B. Griffiths, and P.A. Durkee. International Global Atmospheric Chemistry (IGAC) Project’s First Aerosol Characterization Experiment (ACE 1): Overview. *Journal of Geophysical Research*, 103(D13), 1998a. [21](#)
- T.S. Bates, V.N. Kapustin, P.K. Quinn, D.S. Covert, D.J. Coffman, C. Mari, P.A. Durkee, W.J. De Bruyn, and E.S. Saltzman. Processes controlling the distribution of aerosol particles in the lower marine boundary layer during the First Aerosol Characterization Experiment (ACE 1). *Journal of Geophysical Research*, 103(D13), 1998b. [6](#)
- N. Bellouin, O. Boucher, J. Haywood, and M.S. Reddy. Global estimate of aerosol direct radiative forcing from satellite measurements. *Nature(London)*, 438(7071): 1138–1141, 2005. [16](#)
- Y.S. Bennouna, R.L. Curier, G. de Leeuw, J. Piazzola, R. Roebeling, and P. de Valk. An automated day-time cloud detection technique applied to MSG-SEVIRI data over Western Europe. *International Journal of Remote Sensing*, 2008. Accepted for publication: October 2008. [82](#), [98](#), [100](#), [117](#), [165](#)
- C.F. Bohren and D.R. Huffman. Absorption and Scattering of Light by Small Particles. *John Wiley & Sons. Inc., USA*, 1983. [12](#)
- D.W. Bond, S. Steiger, R. Zhang, X. Tie, and R.E. Orville. The importance of NO_x production by lightning in the tropics. *Atmospheric Environment*, 36(9):1509–1519, 2002. [7](#)
- J. Bösenberg, A. Ansmann, J.M. Baldasano, D. Balis, C. Böckmann, B. Calpini, A. Chaikovsky, P. Flamant, A. Hågård, V. Mitev, et al. EARLINET: A European Aerosol Research Lidar Network. *Advances in Laser Remote Sensing*, pages 155–158, 2001. [23](#)
- E. Buijsman, J.P. Beck, L. Bree, F.R. Cassee, R.B.A. Koelemeijer, J. Matthijsen, R. Thomas, and K. Wieringa. Particulate Matter: a closer look. 2005. [20](#)
- J.P. Burrows, M. Weber, M. Buchwitz, V. Rozanov, A. Ladstätter-Weissenmayer, A. Richter, R. DeBeek, R. Hoogen, K. Bramstedt, K.U. Eichmann, et al. The Global Ozone Monitoring Experiment (GOME): Mission Concept and First Scientific Results. *Journal of the Atmospheric Sciences*, 56(2):151–175, 1999. [23](#)

- J.W. Campbell, J.M. Blaisdell, and M. Darzi. Level-3 SeaWiFS Data Products: Spatial and Temporal Binning Algorithms. *NASA Technical Memorandum*, 104566: 73, 1995. [46](#), [88](#), [136](#)
- C.K. Chan, Z. Ha, and M.Y. Choi. Study of water activities of aerosols of mixtures of sodium and magnesium salts. *Atmospheric Environment*, 34(28):4795–4803, 2000. [6](#)
- S. Chandrasekhar. Radiative Transfer. 1960. [40](#), [117](#), [136](#)
- D.A. Chu, Y.J. Kaufman, C. Ichoku, L.A. Remer, D. Tanré, and B.N. Holben. Validation of MODIS aerosol optical depth retrieval over land. *Geophys. Res. Lett*, 29(12):8007, 2002. [92](#)
- A.R. Chughtai, G.R. Williams, M.M.O. Atteya, N.J. Miller, and D.M. Smith. Carbonaceous particle hydration. *Atmospheric Environment*, 33(17):2679–2687, 1999. [7](#)
- P. Chylek and J. Coakley. Aerosols and climate. *Science*, 183:75–77, 1974. [18](#)
- A.D. Clarke, Y. Shinozuka, V.N. Kapustin, S. Howell, B. Huebert, S. Doherty, T. Anderson, D. Covert, J. Anderson, X. Hua, et al. Size distributions and mixtures of dust and black carbon aerosol in Asian outflow: Physiochemistry and optical properties. *Journal of Geophysical Research*, 109(D15):1–20, 2004. [7](#)
- J.A. Coakley and F.P. Bretherton. Cloud cover from high-resolution scanner data: Detection and allowing for partially filled fields of view. *Journal of Geophysical Research*, 87:4917–4932, 1982. [48](#)
- C. Cox and W. Munk. Measurement of the Roughness of the Sea Surface from Photographs of the Sun’s Glitter. *MEASUREMENT*, 1954. [41](#), [86](#), [89](#), [136](#)
- L. Curier, G. de Leeuw, P. Kolmonen, A. M. Sundström, L. Sochageva, and Y. Benouna. *Satellite Aerosol Remote Sensing Over Land*, chapter Aerosol retrieval over land using the ATSR dual-view algorithm. Springer-Praxis (Berlin), 2009. In press. [81](#), [135](#)
- R.L. Curier, P. Veefkind, R. Braak, B. Veihelmann, O. Torres, and G. de Leeuw. Retrieval of aerosol optical properties from OMI radiances using a multi-wavelength algorithm: Application to Western Europe. *Journal of Geophysical Research*, 2008. [25](#)
- G.A. D’Almeida. Desert aerosol: characteristics and effects on climate. *Paleoclimatology and paleometeorology: Modern and past patterns of global atmospheric transport*, pages 311–38, 1987. [4](#)
- J.F. de Haan, P.B. Bosma, and J.W. Hovenier. The adding method for multiple scattering calculations of polarized light. *Astron. Astrophys*, 183:371–391, 1987. [43](#), [84](#)

- G. de Leeuw. Vertical profiles of giant particles close above the sea surface. *Tellus B*, 38, 1986. [9](#)
- G. de Leeuw, K.L. Davidson, S.G. Gathman, and R.V. Noonkester. Modeling of aerosols in the marine mixed-layer. pages 287–294, 1989. [82](#), [136](#)
- G. de Leeuw, R. Schoemaker, L. Curier, Y.S. Bennouna, R. Timmermans, M. Schaap, P. Bultjes, and R.B.A. Koelemeijer. Aatsr derived aerosol properties over land. In *the Envisat Symposium 2007*, 23 - 27 April 2007. (ESA SP-636, July 2007), paper 461895. [78](#)
- W.A. de Rooij and C. van der Stap. Expansion of Mie scattering matrices in generalized spherical functions. *Astron. Astrophys*, 131:237–248, 1984. [84](#), [118](#), [136](#)
- S.F.J. De Wekker, D.G. Steyn, and S. Nyeki. A Comparison Of Aerosol-Layer And Convective Boundary-Layer Structure Over A Mountain Range During Staaarte'97. *Boundary-Layer Meteorology*, 113(2):249–271, 2004. [10](#)
- P. DeCarlo, J.G. Slowik, D.R. Worsnop, P. Davidovits, and J.L. Jimenez. Particle Morphology and Density Characterization by Combined Mobility and Aerodynamic Diameter Measurements. Part 1: Theory. *Aerosol Science and Technology*, 38(12): 1185–1205, 2004. [83](#)
- S. Decesari, M.C. Facchini, E. Matta, M. Mircea, S. Fuzzi, A.R. Chughtai, and D.M. Smith. Water soluble organic compounds formed by oxidation of soot. *Atmospheric Environment*, 36(11):1827–1832, 2002. [7](#)
- M. Derrien. Automatic cloud detection applied to noaa-11 avhrr imagery. *Remote Sensing Environment*, (21):246–267, 1993. [48](#), [51](#), [53](#)
- M. Derrien and H. le Gléau. Msg/seviri cloud mask and type from safnwc. *International Journal of Remote Sensing*, 26(21):4707–4732, 2005. [60](#)
- M. Desbois, G. Seze, and G. Szejwach. Automatic classification of clouds on meteosat imagery: Application to high-level clouds. *Journal of Applied Meteorology*, 21:401–412, 1982. [48](#)
- P.Y. Deschamps, F.M. Breon, M. Leroy, A. Podaire, A. Bricaud, J.C. Buriez, and G. Seze. The POLDER mission: instrument characteristics and scientific objectives. *Geoscience and Remote Sensing, IEEE Transactions on*, 32(3):598–615, 1994. [25](#), [26](#)
- S.G. DeSouza-Machado, L.L. Strow, S.E. Hannon, and H.E. Motteler. Infrared dust spectral signatures from AIRS. *Geophys. Res. Lett*, 33:L03801, 2006. [98](#)
- J.L. Deuzé, M. Herman, P. Goloub, D. Tanré, and A. Marchand. Characterization of aerosols over ocean from POLDER/ADEOS-1. *Geophysical Research Letters*, 26 (10), 1999. [26](#)

-
- J.L. Deuzé, F.M. Breon, C. Devaux, P. Goloub, M. Herman, B. Lafrance, F. Maignan, A. Marchand, F. Nadal, G. Perry, et al. Remote sensing of aerosols over land surfaces from POLDER-ADEOS-1 polarized measurements. *Journal of Geophysical Research*, 105:4913–4926, 2001. [26](#), [42](#), [116](#)
- R.B. Devlin, A.J. Ghio, H. Kehrl, G. Sanders, and W. Cascio. Elderly humans exposed to concentrated air pollution particles have decreased heart rate variability. *European Respiratory Journal*, 21(90400):76–80, 2003. [20](#)
- W.D. Dick, P.J. Ziemann, P.F. Huang, and P.H. McMurry. Optical shape fraction measurements of submicrometre laboratory and atmospheric aerosols. *Measurement Science and Technology*, 9(2):183–196, 1998. [7](#)
- D.J. Diner, J.C. Beckert, T.H. Reilly, C.J. Bruegge, J.E. Conel, R.A. Kahn, J.V. Martonchik, T.P. Ackerman, R. Davies, S.A.W. Gerstl, et al. Multi-angle Imaging SpectroRadiometer (MISR) instrument description and experiment overview. *Geoscience and Remote Sensing, IEEE Transactions on*, 36(4):1072–1087, 1998. [25](#)
- D.R. Doelling, L. Nguyen, and P. Minnis. Calibration Comparisons Between SEVIRI, MODIS, and GOES Data. In *Proc. 2004 EUMETSAT meteorological satellite conference*, 2004. [31](#)
- O. Dubovik and M.D. King. A flexible inversion algorithm for retrieval of aerosol optical properties from sun and sky radiance measurements. *Journal of Geophysical Research*, 105(D16):20676, 2000. [22](#), [91](#)
- O. Dubovik, A. Sinyuk, T. Lapyonok, B.N. Holben, M.I. Mishchenko, P. Yang, T.F. Eck, H. Volten, O. Muñoz, B. Veihelmann, et al. Application of spheroid models to account for aerosol particle nonsphericity in remote sensing of desert dust. *J. Geophys. Res.*, 111, 2006. [108](#)
- D.P. Duda, P. Minnis, Q. Trepte, and S. Sun-Mack. The Continuous Monitoring of Desert Dust using an Infrared-based Dust Detection and Retrieval Method. *Proc. AMS 12th Conf. Atmos. Radiation, (Madison, WI, July 10-14), CD-ROM*, 8, 2006. [98](#)
- P.A. Durkee, D.R. Jensen, E.E. Hindman, and T.H. Vonder Haar. The relationship between marine aerosol particles and satellite-detected radiance. *Journal of Geophysical Research*, 91:4063–4072, 1986. [44](#), [90](#), [121](#)
- E. Ebert. A pattern recognition technique for distinguishing surface and cloud types in the polar regions. *Journal of Climate and Applied Meteorology*, 26:1412–1427, 1987. [48](#), [50](#)
- T. Edwards, R. Browning, J. Delderfield, D.J. Lee, and K.A. Lidiard. The along track scanning radiometer-Measurement of sea-surface temperature from ERS-1. *British Interplanetary Society, Journal (ISSN 0007-084X)*, 43, 1990. [25](#)

- C. Elachi. *Introduction to the Physics and Techniques of Remote Sensing*. New York: John Wiley & Sons, 1987. [21](#)
- J.A. Engel-Cox, C.H. Holloman, B.W. Coutant, and R.M. Hoff. Qualitative and quantitative evaluation of MODIS satellite sensor data for regional and urban scale air quality. *Atmospheric Environment*, 38(16):2495–2509, 2004. [27](#)
- K.F. Evans. The Spherical Harmonics Discrete Ordinate Method for Three-Dimensional Atmospheric Radiative Transfer. *Journal of the Atmospheric Sciences*, 55(3):429–446, 1998. [43](#)
- A. Feijt, P. de Valk, and S. van der Veen. Cloud detection using meteosat imagery and numerical weather prediction model data. *Journal of Applied Meteorology*, 39: 1017–1030, 1999. [48](#)
- J.W. Fitzgerald. Marine aerosols: a review. *Atmospheric environment. Part A, General topics*, 25(3-4):533–545, 1991. [9](#)
- A.I. Flossmann. Interaction of Aerosol Particles and Clouds. *Journal of the Atmospheric Sciences*, 55(5):879–887, 1998. [80](#)
- R.J. Flowerdew and J.D. Haigh. Retrieving land surface reflectances using the ATSR-2: A theoretical study. *Journal of Geophysical Research*, 102(D14):17163–17171, 1997. [41](#)
- P. Forster, V. Ramaswamy, P. Artaxo, et al. Changes in atmospheric constituents and in radiative forcing, Climate Change 2007. *The Physical Science Basis, Contribution of Working Group I to the Fourth Assessment Report of the IPCC*, edited by: Solomon, S., Qin, D., Manning, M., et al., Cambridge University Press, Cambridge, United Kingdom and New York, NY, USA, pages 129–234, 2007. [16](#)
- A. Fresnel. Elementary View of an Ondulatory Theory of Light. *Quarterly Journal of Science*, 23:127–141, 1827. [86](#)
- G.P. Gobbi, F. Barnaba, R. Giorgi, and A. Santacasa. Altitude-resolved properties of a Saharan dust event over the Mediterranean. *Atmospheric Environment*, 34 (29-30):5119–5127, 2000. [96](#)
- G.P. Gobbi, F. Barnaba, R. Van Dingenen, J.P. Putaud, M. Mircea, and M.C. Facchini. Lidar and in situ observations of continental and Saharan aerosol: closure analysis of particles optical and physical properties. *Atmos. Chem. Phys*, 3(21):6, 2003. [10](#)
- G.P. Gobbi, F. Barnaba, and L. Ammannato. The vertical distribution of aerosols, Saharan dust and cirrus clouds at Rome (Italy) in the year 2001. *Atmos. Chem. Phys*, 4:351–359, 2004. [10](#)
- H. Gordon, J. Brown, O. Brown, R. Evans, and R. Smith. A semianalytic radiance model of ocean color. *Journal of Geophysical Research*, 93(D9):10909–10924, 1988. [88](#)

- H.R. Gordon and A. Morel. Remote assessment of ocean color for interpretation of satellite visible imagery: A review. *Springer-Verlag, New York, 114 pp*, 1983. [86](#)
- A.S. Goudie and N.J. Middleton. Saharan dust storms: nature and consequences. *Earth Science Reviews*, 56(1-4):179–204, 2001. [4](#)
- Y. Govaerts, A. Yildirim, M. Clerici, and T. Heinemann. Drift analysis of the MSG/SEVIRI solar channels. *35th COSPAR Scientific Assembly. Held 18-25 July 2004, in Paris, France., p. 1999*, 2004. [31](#)
- J. Gras. Southern Hemisphere tropospheric aerosol microphysics. *Journal of Geophysical Research*, 96(D3):5345–5356, 1991. [9](#)
- W.W. Gregg and N.W. Casey. Global and regional evaluation of the SeaWiFS chlorophyll data set. *Remote Sensing of Environment*, 93(4):463–479, 2004. [46](#)
- M. Griggs. Measurements of atmospheric aerosol optical thickness over water using ERTS-1 data. *Journal of the Air Pollution Control Association*, 25(6):622–6, 1975. [23](#)
- M. Griggs. AVHRR measurements of atmospheric aerosols over oceans. *Final Report Science Applications, Inc., San Diego, CA.*, 1981. [80](#)
- S. Guerzoni and R. Chester. *The Impact of Desert Dust Across the Mediterranean*. Kluwer Academic Publishers, 1996. [96](#)
- P. Gupta, S.A. Christopher, J. Wang, R. Gehrig, Y. Lee, and N. Kumar. Satellite remote sensing of particulate matter and air quality assessment over global cities. *Atmospheric Environment*, 40(30):5880–5892, 2006. [27](#)
- J. Hansen, D. Johnson, A. Lacis, S. Lebedeff, P. Lee, D. Rind, and G. Russell. Climate Impact of Increasing Atmospheric Carbon Dioxide. *Science*, 213(4511):957–966, 1981. [12](#)
- J. Haywood and O. Boucher. Estimates of the direct and indirect radiative forcing due to tropospheric aerosols: A review. *Reviews of Geophysics*, 38(4):513–543, 2000. [16](#), [18](#), [19](#), [162](#)
- L.G. Henyey and J.L. Greenstein. Diffusive radiation in the galaxy. *Astrophysical Journal*, 93:7083, 1941. [41](#)
- J.R. Herman and E.A. Celarier. Earth surface reflectivity climatology at 340-380 nm from TOMS data. *Journal of geophysical research*, 102(D 23):28003–28011, 1997. [40](#)
- J.R. Herman, E. Celarier, and D. Larko. UV 380 nm reflectivity of the Earth’s surface, clouds and aerosols. *Journal of Geophysical Research*, 106(D6), 2001. [40](#)
- M. Hess, P. Koepke, and I. Schult. Optical Properties of Aerosols and Clouds: The Software Package OPAC. *Bulletin of the American Meteorological Society*, 79(5): 831–844, 1998. [9](#), [13](#), [83](#), [118](#), [136](#)

- B. Holben, E. Vermote, Y.J. Kaufman, D. Tanré, and V. Kalb. Aerosol retrieval over land from AVHRR data-application foratmospheric correction. *Geoscience and Remote Sensing, IEEE Transactions on*, 30(2):212–222, 1992. 23
- B.N. Holben, T.F. Eck, I. Slutsker, D. Tanré, J.P. Buis, A. Setzer, E. Vermote, J.A. Reagan, Y.J. Kaufman, T. Nakajima, et al. AERONET-A Federated Instrument Network and Data Archive for Aerosol Characterization. *Remote Sensing of Environment*, 66(1):1–16, 1998. 22, 91
- WA Hoppel, GM Frick, JW Fitzgerald, and RE Larson. Marine boundary layer measurements of new particle formation and the effects nonprecipitating clouds have on aerosol size distribution. *Journal of Geophysical Research - Atmospheres*, 99(D7):14 44314 459, 1994. 6
- W.A. Hovis, F. Clark, D.K. Anderson, R.W. Austin, W.H. Wilson, E.T. Baker, D. Ball, H.R. Gordon, J.L. Mueller, S.Z. El-Sayed, et al. Nimbus-7 Coastal Zone Color Scanner: System Description and Initial Imagery. *Science*, 210(4465):60–63, 1980. 46
- R.B. Husar, D.M. Tratt, B. Schichtel, S.R. Falke, F. Li, D. Jaffe, S. Gasso, T. Gill, N.S. Laulainen, F. Lu, et al. Asian dust events of April 1998. *Journal of Geophysical Research*, 106(D16):18317–18330, 2001. 4
- C. Ichoku, D.A. Chu, S. Mattoo, Y.J. Kaufman, L.A. Remer, D. Tanré, I. Slutsker, and B.N. Holben. A spatio-temporal approach for global validation and analysis of MODIS aerosol products. *Geophys. Res. Lett*, 29(12):8006, 2002. 92
- A. Ignatov, J. Sapper, S. Cox, I. Laszlo, N.R. Nalli, and K.B. Kidwell. Operational Aerosol Observations (AEROBS) from AVHRR/3 On Board NOAA-KLM Satellites. *Journal of Atmospheric and Oceanic Technology*, 21(1):3–26, 2004. 23
- IPCC. *Climate change 2007: The physical science basis . Contribution of Working Group I to the Fourth Assessment Report of the Intergovernmental Panel on Climate Change*. Cambridge University Press, Cambridge, United Kingdom and New York, NY, USA, 2007. Accessed online at <http://www.ipcc.ch/ipccreports/ar4-wg1.htm>, in January 2008. 1, 20, 80
- R. Jaenicke. *Tropospheric Aerosols*. Published by Academic Press, San diego, CA, 1993. 8, 161
- D. Jaffe, J. Snow, and O. Cooper. The 2001 Asian Dust Events: Transport and Impact on Surface Aerosol Concentrations in the US. *Eos, Transactions American Geophysical Union*, 84(46):501–516, 2003. 4
- Y. Jin, C.B. Schaaf, F. Gao, X. Li, A.H. Strahler, W. Lucht, and S. Liang. Consistency of MODIS surface bidirectional reflectance distribution function and albedo retrievals: 1. Algorithm performance. *Journal of Geophysical Research*, 108(D5): 4158, 2003. 41

-
- O.V. Kalashnikova and I.N. Sokolik. Importance of shapes and compositions of wind-blown dust particles for remote sensing at solar wavelengths. *Geophysical Research Letters*, 29(10):38–1, 2002. 83
- M. Kanakidou, J.H. Seinfeld, S.N. Pandis, I. Barnes, F.J. Dentener, M.C. Facchini, R. Van Dingenen, B. Ervens, A. Nenes, C.J. Nielsen, et al. Organic aerosol and global climate modelling: a review. *Atmospheric Chemistry and Physics*, 5(4): 1053–1123, 2005. 7
- Y.J. Kaufman and R.S. Fraser. The Effect of Smoke Particles on Clouds and Climate Forcing. *Science*, 277(5332):1636, 1997. 19
- Y.J. Kaufman and I. Koren. Smoke and Pollution Aerosol Effect on Cloud Cover. *Science*, 313(5787):655–658, 2006. 19
- Y.J. Kaufman, A.E. Remer, L.A.B.C.G. Rong-Rong, L. Flynn, L.N.G.S.F. Center, and M.D. Greenbelt. The MODIS 2.1- μm channel-correlation with visible reflectance for use in remote sensing of aerosol. *Geoscience and Remote Sensing, IEEE Transactions on*, 35(5):1286–1298, 1997a. 25, 116
- Y.J. Kaufman, D. Tanré, H.R. Gordon, T. Nakajima, J. Lenoble, R. Frouin, H. Grassl, B.M. Herman, M.D. King, and P.M. Teillet. Passive remote sensing of tropospheric aerosol and atmospheric correction for the aerosol effect. *Journal of Geophysical Research*, 102(D14):16815–16830, 1997b. 23
- Y.J. Kaufman, D. Tanré, L.A. Remer, E.F. Vermote, A. Chu, and B.N. Holben. Operational remote sensing of tropospheric aerosol over land from EOS moderate resolution imaging spectroradiometer. *Journal of Geophysical Research*, 102(17): 051–17, 1997c. 25, 92
- Y.J. Kaufman, D. Tanré, and O. Boucher. A satellite view of aerosols in the climate system. *Nature*, 419(6903):215–223, 2002. 27, 80
- Y.J. Kaufman, O. Boucher, D. Tanré, M. Chin, L.A. Remer, and T. Takemura. Aerosol anthropogenic component estimated from satellite data. *Geophysical Research Letters*, 32, 2005a. 16
- Y.J. Kaufman, I. Koren, L.A. Remer, D. Rosenfeld, and Y. Rudich. The effect of smoke, dust, and pollution aerosol on shallow cloud development over the Atlantic Ocean. *Proceedings of the National Academy of Sciences*, 102(32):11207–11212, 2005b. 19
- M. Kerker. *The Scattering of Light and Other Electromagnetic Radiation*. 1969. 84
- K.B. Kidwell. NOAA Polar Orbiter Data Users Guide:(TIROS-N, NOAA-6, NOAA-7, NOAA-8, NOAA-9, NOAA-10, NOAA-11, NOAA-12, NOAA-13, and NOAA-14). 1995. 23
- JT Kiehl and K.E. Trenberth. Earth’s Annual Global Mean Energy Budget. *Bulletin of the American Meteorological Society*, 78(2):197–208, 1997. 15, 161

- S. Kim, S. Shen, C. Sioutas, Y. Zhu, and W.C. Hinds. Size Distribution and Diurnal and Seasonal Trends of Ultrafine Particles in Source and Receptor Sites of the Los Angeles Basin. *Journal of the Air & Waste Management Association*, 52(3): 297–307, 2002. [9](#)
- Y. Kim, H. Sievering, and J. Boatman. Volume and surface area size distribution, water mass and model fitting of GCE/CASE/WATOX marine aerosols. *Global Biogeochem. Cycles*, 4:165–177, 1990. [6](#)
- M.D. King, Y.J. Kaufman, D. Tanré, and T. Nakajima. Remote Sensing of Tropospheric Aerosols from Space: Past, Present, and Future. *Bulletin of the American Meteorological Society*, 80(11):2229–2259, 1999. [23](#)
- EG Knox. Childhood cancers and atmospheric carcinogens. *Journal of Epidemiology & Community Health*, 59(2):101–105, 2005. [20](#)
- R.B.A. Koelemeijer, P. Stammes, J.W. Hovenier, and J.F. de Haan. A fast method for the retrieval of cloud parameters using oxygen a-band measurements from the global ozone monitoring instrument. *Journal of Geophysical Research*, 106:3475–3490, 2001. [48](#), [50](#), [82](#), [135](#)
- R.B.A. Koelemeijer, J.F. de Haan, and P. Stammes. A database of spectral surface reflectivity in the range 335–772 nm derived from 5.5 years of GOME observations. *Journal of Geophysical Research*, 108(D2):4070, 2003. [40](#), [41](#), [116](#)
- P. Koepke. Effective reflectance of oceanic whitecaps. *Applied Optics*, 23(11):1816–1824, 1984. [86](#)
- P. Koepke and M. Hess. Scattering functions of tropospheric aerosols- The effects of nonspherical particles. *Applied Optics*, 27(12):2422–2430, 1988. [108](#)
- H. Kohler. *Meteorologische Zeitschrift*, 38:168, 1921. [18](#)
- A.A. Kokhanovsky. Spectral reflectance of whitecaps. *Journal of Geophysical Research*, 109, 2004. [86](#)
- A.A. Kokhanovsky, R.L. Curier, G. de Leeuw, W. M. F. Grey, K.-H. Lee, Y.S. Benouna, R. Schoemaker, and P.R.J. North. The inter-comparison of AATSR dual view aerosol optical thickness retrievals with results from various algorithms and instruments. *International Journal of Remote Sensing*, 2009. In press. [44](#), [90](#)
- I. Koren, Y.J. Kaufman, L.A. Remer, and J.V. Martins. Measurement of the Effect of Amazon Smoke on Inhibition of Cloud Formation. *Science*, 303(5662):1342–1345, 2004. [19](#)
- I. Koren, L.A. Remer, J.Y. Kaufman, Y. Rudich, and J.V. Martins. On the twilight zone between clouds and aerosols. *Geophysical Research Letter*, 34, 2007. [78](#)

-
- K.T. Kriebel. The cloud analysis tool apollo: improvements and validations. *International Journal of Remote Sensing*, 24(12):2389–2408, 2003. [48](#), [50](#), [54](#), [78](#), [82](#)
- J. Kuśmierczyk-Michulec and G. de Leeuw. Aerosol optical thickness retrieval over land and water using Global Ozone Monitoring Experiment (GOME) data. *Journal of Geophysical Research*, 110, 2005. [25](#), [41](#)
- J. Kuśmierczyk-Michulec, M. Schulz, S. Ruellan, O. Krüger, E. Plate, R. Marks, G. de Leeuw, and H. Cachier. Aerosol composition and related optical properties in the marine boundary layer over the Baltic Sea. *Journal of Aerosol Science*, 32(8):933–955, 2001. [13](#)
- T. Lavergne, T. Kaminski, B. Pinty, M. Taberner, N. Gobron, M.M. Verstraete, M. Vossbeck, J.L. Widlowski, and R. Giering. Application to MISR land products of an RPV model inversion package using adjoint and Hessian codes. *Remote Sensing of Environment*, 107(1-2):362–375, 2007. [41](#)
- J. Lenoble. *Radiative transfer in scattering and absorbing atmospheres: Standard computational procedures*. 1985. [42](#)
- G. Lesins, P. Chylek, and U. Lohmann. A study of internal and external mixing scenarios and its effect on aerosol optical properties and direct radiative forcing. *Journal of Geophysical Research*, 107(10):4094, 2002. [7](#)
- P.F. Levelt and R. Noordhoek. OMI Algorithm Theoretical Basis Document Volume I: OMI Instrument, Level 0-1b Processor, Calibration & Operations. Technical report, Tech. Rep. ATBD-OMI-01, Version 1.1, August 2002. [25](#)
- R.C. Levy, L.A. Remer, D. Tanré, Y.J. Kaufman, C. Ichoku, B.N. Holben, J.M. Livingston, P.B. Russell, and H. Maring. Evaluation of the Moderate-Resolution Imaging Spectroradiometer (MODIS) retrievals of dust aerosol over the ocean during PRIDE. *J. Geophys. Res*, 108(D19), 2003. [92](#)
- R.C. Levy, L.A. Remer, J.V. Martins, Y.J. Kaufman, A. Plana-Fattori, J. Redemann, and B. Wenny. Evaluation of the MODIS Aerosol Retrievals over Ocean and Land during CLAMS. *Journal of the Atmospheric Sciences*, 62(4):974–992, 2005. [92](#)
- R.C. Levy, L.A. Remer, S. Mattoo, E.F. Vermote, and Y.J. Kaufman. Second-generation operational algorithm: Retrieval of aerosol properties over land from inversion of Moderate Resolution Imaging Spectroradiometer spectral reflectance. *Journal of Geophysical Research*, 112, 2007. [41](#)
- X. Li and A.H. Strahler. Geometric-optical bidirectional reflectance modeling of the discrete crown vegetation canopy: effect of crown shape and mutual shadowing. *Geoscience and Remote Sensing, IEEE Transactions on*, 30(2):276–292, 1992. [41](#), [119](#)

- P.J. Lioy, J.M. Daisey, and A.T. Element. Toxic Air Pollution: A Comprehensive Study of Non-criteria Air Pollutants. 1987. [9](#)
- M. Lippmann and R.E. Albert. The Effect of Particle Size on the Regional Deposition of Inhaled Aerosols in the Human Respiratory Tract. *American Industrial Hygiene Association Journal*, 30(3):257–275, 1969. [20](#)
- M. Lippmann, D.B. Yeates, and R.E. Albert. Deposition, retention, and clearance of inhaled particles. *British Journal of Industrial Medicine*, 37(4):337, 1980. [20](#)
- M. Lippmann, K. Ito, A. Nadas, and R.T. Burnett. Association of particulate matter components with daily mortality and morbidity in urban populations. *Research Report/ Health Effects Institute*, 95:5–72, 2000. [20](#)
- M. Lippmann, M. Frampton, J. Schwartz, D. Dockery, R. Schlesinger, P. Koutrakis, J. Froines, A. Nel, J. Finkelstein, J. Godleski, et al. The US Environmental Protection Agency Particulate Matter Health Effects Research Centers Program: A Midcourse Report of Status, Progress, and Plans. *Environmental Health Perspectives*, 111:1074–1093, 2003. [20](#)
- D. Llewellyn-Jones, M.C. Edwards, C.T. Mutlow, A.R. Birks, I.J. Barton, and H. Tait. AATSR: Global-Change and Surface-Temperature Measurements from Envisat. *ESA Bulletin*, 105:10–21, 2001. [25](#)
- U. Lohmann and J. Feichter. Global indirect aerosol effects: a review. *Atmospheric Chemistry and Physics*, 5(5):715–737, 2005. [18](#)
- D.R. Longtin, E.P. Shettle, J.R. Hummel, and J.D. Pryce. A Wind Dependent Desert Aerosol Model: Radiative Properties. 1988. [9](#)
- A. Macke, D.L. Mitchell, and L.V. Bremen. Monte Carlo radiative transfer calculations for inhomogeneous mixed phase clouds. *Physics and Chemistry of the Earth, Part B*, 24(3):237–241, 1999. [43](#)
- F. Maignan, F.M. Bréon, and R. Lacaze. Bidirectional reflectance of Earth targets: evaluation of analytical models using a large set of spaceborne measurements with emphasis on the Hot Spot. *Remote Sensing of Environment*, 90(2):210–220, 2004. [41](#)
- J.M. Mäkelä, I.K. Koponen, P. Aalto, and M. Kulmala. One-Year Data of Submicron Size Modes of Tropospheric Background Aerosol in Southern Finland. *Journal of Aerosol Science*, 31(5):595–611, 2000. [8](#)
- J.V. Martonchik, D.J. Diner, R.A. Kahn, T.P. Ackerman, M.M. Verstraete, B. Pinty, and H.R. Gordon. Techniques for the retrieval of aerosol properties over land and ocean using multiangle imaging. *Geoscience and Remote Sensing, IEEE Transactions on*, 36(4):1212–1227, 1998. [26](#)

-
- J.V. Martonchik, D.J. Diner, K. Crean, and M.A. Bull. Regional aerosol retrieval results from MISR. *IEEE Transactions on Geoscience and Remote Sensing*, 40(7): 1520–1531, 2002. [26](#), [116](#)
- R.A. McClatchey, R.W. Fenn, J.E.A. Selby, F.E. Volz, and J.S. Garing. Optical Properties of the Atmosphere. 1972. [44](#), [84](#), [118](#)
- G. Mie. A contribution to the optics of turbid media, especially colloidal metallic suspensions. *Annals of Physics*, 25(4):377–445, 1908. [10](#), [12](#), [84](#), [136](#)
- M. Minnaert. The reciprocity principle in lunar photometry. *The Astrophysical Journal*, 93(3):403–410, 1941. [41](#)
- M. Mishchenko. Light scattering by randomly oriented axially symmetric particles. *Journal of the Optical Society of America*, 1991. [10](#)
- M.I. Mishchenko and L.D. Travis. T-matrix computations of light scattering by large spheroidal particles. *Optics Communications*, 109(1-2):16–21, 1994. [84](#), [108](#)
- M.I. Mishchenko, L.D. Travis, and D.W. Mackowski. T-matrix computations of light scattering by nonspherical particles: a review. *Journal of Quantitative Spectroscopy and Radiative Transfer*, 55(5):535–575, 1996. [108](#), [136](#)
- M.I. Mishchenko, L.D. Travis, R.A. Kahn, and R.A. West. Modeling phase functions for dustlike tropospheric aerosols using a shape mixture of randomly oriented polydisperse spheroids. *J. Geophys. Res.*, 102(16):831–16, 1997. [81](#), [108](#)
- E.C. Monahan and I.Ó. Muircheartaigh. Optimal Power-Law Description of Oceanic Whitecap Coverage Dependence on Wind Speed. *Journal of Physical Oceanography*, 10(12):2094–2099, 1980. [86](#)
- K.D. Moore, K.J. Voss, and H.R. Gordon. Spectral reflectance of whitecaps: their contribution to water-leaving radiance. *J. Geophys. Res.*, 105(C3):6493–6499, 2000. [86](#)
- K.K. Moorthy, S.K. Satheesh, S.S. Babu, and C.B.S. Dutt. Integrated Campaign for Aerosols, gases and Radiation Budget (ICARB): An Overview. *Journal of Earth System Science*, 2008. [22](#)
- A. Morel. Optical modeling of the upper ocean in relation to its biogenous matter content (case I waters). *Journal of Geophysical Research*, 93(C9):10749–10768, 1988. [88](#), [136](#)
- A. Morel and B. Gentili. Diffuse reflectance of oceanic waters. III. Implication of bidirectionality for the remote-sensing problem. *Appl. Opt.*, 35(24):4850–4862, 1996. [86](#)
- A. Morel and L. Prieur. Analysis of variations in ocean color. *Limnol. Oceanogr.*, 22(4):709–722, 1977. [88](#)

- G. Myhre, A. Myhre, and F. Stordal. Historical evolution of radiative forcing of climate. *Atmospheric Environment*, 35(13):2361–2373, 2001. 16
- T. Nakajima, M. Tanaka, and T. Yamauchi. Retrieval of the optical properties of aerosols from aureole and extinction data. *Applied Optics*, 22(19):2951–2959, 1983. 22
- C.D. O’Dowd and G. de Leeuw. Marine aerosol production: a review of the current knowledge. *Philosophical Transactions of the Royal Society A: Mathematical, Physical and Engineering Sciences*, 365(1856):1753–1774, 2007. 6
- J. Ogren. Aerosol Sampling System for WMO Global Atmosphere Watch. 2004. 22
- J.E. O’Reilly, S. Maritorena, B.G. Mitchell, D.A. Siegel, K.L. Carder, S.A. Garver, M. Kahru, and C. McClain. Ocean color chlorophyll algorithms for SeaWiFS. *Journal of Geophysical Research*, 103(C11):24937–24953, 1998. 46
- S.N. Pandis, A.S. Wexler, and J.H. Seinfeld. Dynamics of Tropospheric Aerosols. *The Journal of Physical Chemistry*, 99(24):9646–9659, 1995. 80
- A. Papayannis, D. Balis, V. Amiridis, G. Chourdakis, G. Tsaknakis, C. Zerefos, A. D. A. Castanho, S. Nickovic, S. Kazadzis, and J. Grabowski. Measurements of saharan dust aerosols over the eastern mediterranean using elastic backscatter-raman lidar, spectrophotometric and satellite observations in the frame of the earlinet project. *Atmospheric Chemistry and Physics Discussions*, 5(2):2075–2110, 2005. ISSN 1680-7367. URL <http://www.atmos-chem-phys-discuss.net/5/2075/2005/>. 96
- J.E. Penner, M. Andreae, H. Annegarn, L. Barrie, J. Feichter, D. Hegg, A. Jayaraman, R. Leaitch, D. Murphy, J. Nganga, et al. Aerosols, their direct and indirect effects. *Climate Change*, pages 289–348, 2001. 16
- J. Piazzola and S. Despiau. Contribution of marine aerosols in the particle size distributions observed in Mediterranean coastal zone. *Atmospheric Environment*, 31(18):2991–3009, 1997. 9
- J. Piazzola, P. Forget, and S. Despiau. A sea spray generation function for fetch-limited conditions. *Ann. Geophysicae*, 20(1):121–131, 2002. 9
- U. Pöschl, S. Bhowmik, T. Fehrenbach, T. Franze, E. Mikhailov, U. Schaller, C. Schauer, and A. Zerrath. Carbonaceous Aerosol Components (CARBAERO): Chemical Composition, Reactivity, and Hygroscopicity. *Geophysical Research Abstracts*, 6(01909), 2004. 7
- W. H. Press, B. P. Flannery, S.A. Teukolsky, and W. T. Vetterling. *Numerical Recipes in Fortran, the Art of Scientific Computing*. Cambridge University Press, 1992. 51
- J.M. Prospero. Saharan dust transport over the North Atlantic Ocean and Mediterranean: an overview. *The Impact of Desert Dust Across the Mediterranean*, pages 133–152, 1996. 4

-
- J.M. Prospero, P. Ginoux, O. Torres, S.E. Nicholson, and T.E. Gill. Environmental characterization of global sources of atmospheric soil dust identified with the NIMBUS 7 Total Ozone Mapping Spectrometer (TOMS) absorbing aerosol product. *Rev. Geophys.*, 40(1):1002, 2002. 4, 96
- H. Rahman, B. Pinty, and M.M. Verstraete. Coupled surface-atmosphere reflectance (CSAR) model. 2: Semiempirical surface model usable with NOAA advanced very high resolution radiometer data. *Journal of Geophysical Research (ISSN 0148-0227)*, 98(D11), 1993. 41
- M.R. Rampino and S. Self. Sulphur-rich volcanic eruptions and stratospheric aerosols. *Nature*, 310(5979):677–679, 1984. 2
- C.R.N. Rao, L.L. Stowe, and E.P. McClain. Remote sensing of aerosols over the oceans using AVHRR data Theory, practice and applications. *International Journal of Remote Sensing*, 10(4):743–749, 1989. 23
- M.S. Reddy, O. Boucher, Y. Balkanski, and M. Schulz. Aerosol optical depths and direct radiative perturbations by species and source type. *Geophysical Research Letters*, 32, 2005. 13, 18
- L.A. Remer, D. Tanré, Y.J. Kaufman, C. Ichoku, S. Mattoo, R. Levy, D.A. Chu, B.N. Holben, O. Dubovik, A. Smirnov, et al. Validation of MODIS aerosol retrieval over ocean. *Geophys. Res. Lett.*, 29(12):8008, 2002. 92
- L.A. Remer, Y.J. Kaufman, D. Tanré, S. Mattoo, D.A. Chu, J.V. Martins, R.R. Li, C. Ichoku, R.C. Levy, R.G. Kleidman, et al. The MODIS Aerosol Algorithm, Products, and Validation. *Journal of the Atmospheric Sciences*, 62(4):947–973, 2005. 90, 92
- L.A. Remer, D. Tanré, and Y. Kaufman. Algorithm For Remote Sensing Of Tropospheric Aerosol From Modis: Collection 5. *ATBD-02 Document http://modis.gsfc.nasa.gov/data/atbd/atbd_mod02.pdf*, 2006. 83, 92, 136
- D.W. Reynolds and T.H. Vonder Haar. A bispectral method for cloud parameter determination. *Monthly Weather Review*, 105:446–457, 1977. 48
- C. Robles-Gonzalez. *Retrieval of Aerosol Properties using ATSR-2 Observations and their Interpretation*. PhD thesis, Utrecht University, The Netherlands, 2003. 48, 50, 78, 81, 82, 135
- A. Robock. Volcanic eruptions and climate. *Rev. Geophys.*, 38(2):191–219, 2000. 2
- J. Ross. The Radiation Regime and Architecture of Plant Stands. 1981. 41, 119
- W.B. Rossow and L.C. Garder. Validation of the isccp cloud detections. *Journal of Climate*, 6:2370–2393, 1993. 49

- J.L. Roujean, M. Leroy, and P.Y. Deschamps. A bidirectional reflectance model of the earth's surface for the correction of remote sensing data. *Journal of Geophysical Research*, 97(D 18):20455–20468, 1992. [41](#), [119](#)
- K.G. Ruddick, V. De Cauwer, Y.J. Park, and G. Moore. Seaborne measurements of near infrared water-leaving reflectance: The similarity spectrum for turbid waters. *Limnol. Oceanogr*, 51(2):1167–1179, 2006. [86](#)
- P.B. Russell, P.V. Hobbs, and L.L. Stowe. Aerosol properties and radiative effects in the United States haze plume: An overview of the Tropospheric Aerosol Radiative Forcing Observational Experiment (TARFOX). *Journal of Geophysical Research*, 104:2213–2222, 1999. [22](#)
- V.V. Salomonson, W.L. Barnes, P.W. Maymon, H.E. Montgomery, and H. Ostrow. MODIS: advanced facility instrument for studies of the Earth as a system. *Geoscience and Remote Sensing, IEEE Transactions on*, 27(2):145–153, 1989a. [91](#)
- V.V. Salomonson, W.L. Barnes, P.W. Maymon, H.E. Montgomery, and H. Ostrow. MODIS: advanced facility instrument for studies of the Earth as a system. *Geoscience and Remote Sensing, IEEE Transactions on*, 27(2):145–153, 1989b. [25](#)
- R.W. Saunders and K.T. Kriebel. An improved method for detecting clear sky and cloudy radiances from avhrr data. *Internal Journal of Remote Sensing*, 9(1):123–150, 1988. [48](#), [50](#), [82](#)
- A. Savtchenko, R. Kummerer, P. Smith, S. Kempler, and G. Leptoukh. A-Train data depot-bringing Atmospheric measurements together. pages 4268–4271, 2007. [25](#)
- C.B. Schaaf, F. Gao, A.H. Strahler, W. Lucht, X. Li, T. Tsang, N.C. Strugnell, X. Zhang, Y. Jin, J.P. Muller, et al. First operational BRDF, albedo and nadir reflectance products from MODIS. *Remote Sensing of Environment*, 83(1-2):135–148, 2002. [42](#), [136](#)
- M. Schaap, A. Apituley, R.M.A. Timmermans, R.B.A. Koelemeijer, and G. de Leeuw. Exploring the relation between aerosol optical depth and PM2.5 at Cabauw, The Netherlands. *Atmos. Chem. Phys.*, 9:909925, 2009. [27](#)
- R.A. Schiffer and W.B. Rossow. The international satellite cloud climatology project (isccp): The first project of the world climate research programme. *Bulletin of the American Meteorological Society*, 64:2261–2287, 1983. [48](#)
- J. Schmetz, P. Pili, S. Tjemkes, D. Just, J. Kerkmann, S. Rota, and A. Ratier. An Introduction to Meteosat Second Generation (MSG). *Bulletin of the American Meteorological Society*, 83(7):977–992, 2002. [29](#), [48](#), [82](#)
- J. Schmid. The SEVIRI Instrument. *Proceedings of the 2000 EUMETSAT Meteorological Satellite*, pages 13–32, 2000. [30](#)

-
- M. Schulz, C. Textor, S. Kinne, Y. Balkanski, S. Bauer, T. Berntsen, T. Berglen, O. Boucher, F. Dentener, S. Guibert, et al. Radiative forcing by aerosols as derived from the AeroCom present-day and pre-industrial simulations. *Atmospheric Chemistry and Physics*, 6(12):5225–5246, 2006. 16
- L. Schütz and R. Jaenicke. Particle Number and Mass Distributions above 10- 4 cm Radius in Sand and Aerosol of the Sahara Desert. *Journal of Applied Meteorology*, 13(8):863–870, 1974. 9
- L. Schütz, R. Jaenicke, and H. Pietrek. Saharan dust transport over the North Atlantic Ocean. *Desert dust: Origin, characteristics, and effects on man. Bulletin of the Geological Society of America*,, 1981. 4
- P. Seibert, F. Beyrich, S.E. Gryning, S. Joffre, A. Rasmussen, and P. Tercier. Review and intercomparison of operational methods for the determination of the mixing height. *Atmospheric Environment*, 34(7):1001–1027, 2000. 9
- J.H. Seinfeld and S.N. Pandis. *Atmospheric chemistry and physics. From air pollution to climate change*, chapter Dry Deposition (Aerosols), pages –. 1998a. 4
- J.H. Seinfeld and S.N. Pandis. *Atmospheric chemistry and physics. From air pollution to climate change*, chapter Wet Deposition (Aerosols), pages –. 1998b. 4
- J.H. Seinfeld and S.N. Pandis. *Atmospheric chemistry and physics. From air pollution to climate change*, chapter Properties of Atmospheric Aerosols, page 408. 1998c. 2, 83
- J.H. Seinfeld and S.N. Pandis. *Atmospheric chemistry and physics. From air pollution to climate change*, chapter Properties of Atmospheric Aerosols, page 408. 1998d. 80
- G. Seze and M. Desbois. Cloud cover analysis from satellite imagery using spatial and temporal characteristics of the data. *Journal of Applied Meteorology*, 26:287–303, 1987. 48
- E.P. Shettle and R.W. Fenn. Models for the Aerosols of the Lower Atmosphere and the Effects of Humidity Variations on their Optical Properties. 1979. 7, 13, 83
- M. Sicard, C. Pérez, F. Roca-denbosch, J.M. Baldasano, and D. García-Vizcaino. Mixed-layer depth determination in the Barcelona coastal area from regular lidar measurements: methods, results and limitations. *Boundary-Layer Meteorology*, 119(1):135–157, 2006. 10
- C. Simmer, E. Raschke, and E. Ruprecht. A method for the determination of cloud properties from two-dimensional histograms. *Annalen der Meteorologie*, 18:130–132, 1982. 48
- A. Smirnov, B.N. Holben, T.F. Eck, O. Dubovik, and I. Slutsker. Cloud-screening and quality control algorithms for the AERONET database. *Remote Sensing of Environment*, 73(3):337–349, 2000. 22

- R.C. Smith and K.S. Baker. The bio-optical state of ocean waters and remote sensing. *Limnol. Oceanogr*, 23(2):247–259, 1978. [88](#)
- R.C. Smith and K.S. Baker. Optical Properties of the Clearest Natural Waters(200–800 nm). *Applied Optics*, 20(2):177–184, 1981. [88](#)
- I.N. Sokolik and O.B. Toon. Incorporation of mineralogical composition into models of the radiative properties of mineral aerosols from ultraviolet to infrared wavelengths. *Journal of Geophysical Research*, 104:9423–9444, 1999. [7](#)
- I.N. Sokolik, D.M. Winker, G. Bergametti, and D. Gillette. Introduction to special section- Outstanding problems in quantifying the radiative impacts of mineral dust. *Journal of Geophysical Research*, 106(D16):18015–18028, 2001. [98](#)
- S. Solomon, D. Qin, M. Manning, Z. Chen, M. Marquis, K.B. Averyt, M. Tignor, and H.L. Miller. *IPCC, 2007: Climate Change 2007: The Physical Science Basis. Contribution of Working Group I to the Fourth Assessment Report of the Intergovernmental Panel on Climate Change*. Cambridge University Press, Cambridge, UK, 2007. [16](#), [18](#), [20](#)
- J.W. Spencer. Fourier series representation of the position of the sun. *Search*, 5(5): 172, 1971. [33](#)
- P. Stammes. *Manual for the DAK program*. Royal Netherlands Meteorological Institute, De Bilt, The Netherlands, 2001. [43](#), [81](#), [84](#), [118](#)
- K. Stammes, S.C. Tsay, K. Jayaweera, and W. Wiscombe. Numerically stable algorithm for discrete-ordinate-method radiative transfer in multiple scattering and emitting layered media. *Applied Optics*, 27(12):2502–2509, 1988. [43](#)
- L.L. Stowe, A.M. Ignatov, and R.R. Singh. Development, validation, and potential enhancements to the second-generation operational aerosol product at the National Environmental Satellite, Data, and Information Service of the National Oceanic and Atmospheric Administration. *Journal of Geophysical Research*, 102(16):923–16, 1997. [23](#)
- A.H. Strahler, W. Lucht, C.B. Schaaf, T. Tsang, F. Gao, X. Li, J.P. Muller, P. Lewis, M.J. Barnsley, D. McIver, et al. MODIS BRDF/Albedo Product: Algorithm Theoretical Basis Document Version 5.0. *National Aeronautics and Space Administration*, 1999. [119](#)
- R.B. Stull. *An Introduction to Boundary Layer Meteorology*. 1988. [9](#), [10](#)
- R. Swap, M. Garstang, S. Greco, R. Talbot, and P. Kallberg. Saharan dust in the Amazon Basin. *Tellus B*, 44(2):133–149, 1992. [4](#)
- R.J. Swap, H.J. Annegarn, J.T. Suttles, J. Haywood, C. Helmlinger, M.C. and Hely, P.V. Hobbs, B.N. Holben, J. Ji, M.D. King, et al. The Southern African Regional Science Initiative (SAFARI 2000): overview of the dry season field campaign. *South African Journal of Science*, 98(3 & 4):125–130, 2002. [22](#)

-
- T. Takashima and K. Masuda. Degree of radiance and polarization of the upwelling radiation from an atmosphere-ocean system. *Applied Optics*, 24(15):2423–2429, 1985. [89](#)
- K. Takemata, T. Izumiya, and Y. Kawata. Analysis of ADEOS/POLDER data over land surfaces. *Advances in Space Research*, 26(7):1065–1068, 2000. [41](#)
- I.N. Tang and H.R. Munkelwitz. Aerosol Phase Transformation and Growth in the Atmosphere. *Journal of Applied Meteorology*, 33(7):791–796, 1994. [6](#)
- I.N. Tang, A.C. Tridico, and K.H. Fung. Thermodynamic and optical properties of sea salt aerosols. *Journal of Geophysical Research*, 102(23):269–23, 1997. [6](#)
- D. Tanré, M. Herman, PY Deschamps, and A. De Leffe. Atmospheric modeling for space measurements of ground reflectances, including bidirectional properties. *Applied Optics*, 18(21):3587–3594, 1979. [38](#), [89](#), [136](#)
- D. Tanré, Y.J. Kaufman, M. Herman, and S. Mattoo. Remote sensing of aerosol properties over oceans using the MODIS/EOS spectral radiances. *Journal of Geophysical Research*, 102(D14):16971–16988, 1997. [25](#), [92](#)
- D. Tanré, J. Haywood, J. Pelon, J.F. Leon, B. Chatenet, P. Formenti, P. Francis, P. Goloub, E.J. Highwood, and G. Myhre. Measurement and modeling of the Saharan dust radiative impact: Overview of the Saharan Dust Experiment (SHADE). *Journal of Geophysical Research*, 108(D18):8574, 2003. [22](#), [96](#)
- L.W. Thomason and M.C. Pitts. CALIPSO observations of volcanic aerosol in the stratosphere. Technical report, NASA Center: Langley Research Center, 2008. Document ID: 20080046992; Report Number: Meeting Paper No. 7153-24. [2](#)
- O. Torres, P.K. Bhartia, J.R. Herman, A. Sinyuk, P. Ginoux, and B. Holben. A Long-Term Record of Aerosol Optical Depth from TOMS Observations and Comparison to AERONET Measurements. *Journal of the Atmospheric Sciences*, 59(3):398–413, 2002. [23](#), [25](#), [40](#)
- S. Twomey. The Influence of Pollution on the Shortwave Albedo of Clouds. *Journal of the Atmospheric Sciences*, 34(7):1149–1152, 1977. [18](#), [80](#)
- S.A. Twomey, M. Piegras, and T.L. Wolfe. An assessment of the impact of pollution of global cloud albedo. *Tellus B*, 36:356, 1984. [18](#), [80](#)
- U.S. Geological Survey, 1997. GTOPO30 (Global 30 Arc-Second Elevation Data Set) Documentation available online at <http://eros.usgs.gov/products/elevation/gtopo30.html> (accessed July 4, 2005) . [45](#), [51](#)
- H.C. van de Hulst. *Light scattering by small particles*. John Wiley & Sons., 1957. [84](#)

- M. Vaughan, S. Young, D. Winker, K. Powell, A. Omar, Z. Liu, Y. Hu, and C. Hostetler. Fully automated analysis of space-based lidar data: an overview of the CALIPSO retrieval algorithms and data products. In *Proc. of SPIE Vol*, volume 5575, page 17, 2004. 26
- J.P. Veefkind. *Aerosol satellite remote sensing*. PhD thesis, Utrecht University, The Netherlands, 1999. 25, 41, 44, 90, 116, 121
- J.P. Veefkind and G. de Leeuw. A new algorithm to determine the spectral aerosol optical depth from satellite radiometer measurements. *Journal of Aerosol Science*, 29(10):1237–1248, 1998. 79, 81, 137
- C.A. Velds, P.C.T. van der Hoeven, J.M. Koopstra, W.R. Raaf, and W.H. Slob. *Zonnestraling in Nederland*. Koninklijk Nederlands Meteorologisch Instituut, 1992. 33
- E.F. Vermote, D. Tanré, J.L. Deuzé, M. Herman, and J.J. Morcette. Second Simulation of the Satellite Signal in the Solar Spectrum, 6S: an overview. *Geoscience and Remote Sensing, IEEE Transactions on*, 35(3):675–686, 1997. 43
- J.H. Vincent, P.H.Y. Tsai, and J.S. Warner. Sampling of inhalable aerosol with special reference to speciation. *Analyst(London. 1877. Print)*, 120(3):675–679, 1995. 20
- H. Volten, O. Muñoz, E. Rol, J.F. de Haan, W. Vassen, J.W. Hovenier, K. Muinonen, and T. Nousiainen. Scattering matrices of mineral aerosol particles at 441.6 nm and 632.8 nm. *Journal of Geophysical Research*, 106(D15):17375–17402, 2001. 83
- M. Wang and H.R. Gordon. Radiance reflected from the ocean-atmosphere system: synthesis from individual components of the aerosol size distribution. *Appl. Opt*, 33:7088–7095, 1994. 44, 90
- Z. Wang, X. Zeng, M. Barlage, RE Dickinson, F. Gao, and CB Schaaf. Using MODIS BRDF and Albedo Data to Evaluate Global Model Land Surface Albedo. *Journal of Hydrometeorology*, 5(1):3–14, 2004. 119
- W. Wanner, A.H. Strahler, B. Hu, P. Lewis, J.P. Muller, X. Li, C.L.B. Schaaf, and M.J. Barnsley. Global retrieval of bidirectional reflectance and albedo over land from EOS MODIS and MISR data: Theory and algorithm. *J. Geophys. Res*, 102(17):143–17, 1997. 41, 116
- A.S. Wexler. *Inorganic Components of Atmospheric Aerosols*. PhD thesis, California Institute of Technology, 1991. 6
- KT Whitby and B. Cantrell. Fine particles. In *International Conference on Environmental Sensing and Assessment, Las Vegas, NV, Institute of Electrical and Electronic Engineers*, 1976. 4, 5, 161
- C.H. Whitlock, D.S. Bartlett, and E.A. Gurganus. Sea foam reflectance and influence on optimum wavelength for remote sensing of ocean aerosols. *Geophysical Research Letters*, 9(6):719–722, 1982. 86, 136

- D.M. Winker, J. Pelon, and M.P. McCormick. The CALIPSO mission: Spaceborne lidar for observation of aerosols and clouds. *4893(1):11*, 2003. [26](#)
- WMO. Radiation commission of IAMAP meeting of experts on aerosol and their climatic effects. *World Meteorological Organization Rep. WCP55*, page 2830, 1983. [13](#)
- P. Yang, Q. Feng, G. Hong, G.W. Kattawar, W.J. Wiscombe, M.I. Mishchenko, O. Dubovik, I. Laszlo, and I.N. Sokolik. Modeling of the scattering and radiative properties of nonspherical dust-like aerosols. *Journal of Aerosol Science*, 38(10):995–1014, 2007. [83](#)
- H. Yu, Y.J. Kaufman, M. Chin, G. Feingold, L.A. Remer, T.L. Anderson, Y. Balkanski, N. Bellouin, O. Boucher, S. Christopher, et al. A review of measurement-based assessments of the aerosol direct radiative effect and forcing. *Atmospheric Chemistry and Physics*, 6(3):613–666, 2006. [16](#), [18](#)

List of Figures

1.1	Conceptual representation of the principal size ranges for atmospheric particles and their associated sources, and removal processes, adapted from the work of Whitby and Cantrell [1976]. The blue curve is a plot of the idealized surface area distribution of an atmospheric aerosol, and blue arrows identify the different physical and the chemical processes responsible for aerosol formation and changes in size. Source: http://www.dwanepaulsen.net/blog/category/aerosols/	5
1.2	Number size distributions as described by the trimodal lognormal parametrization proposed by Jaenicke [1993] for urban, rural, remote, desert and marine environments.	8
1.3	Schematic description of light scattering by particles with different size parameters. The size parameter is increasing from left to right. Source: http://hyperphysics.phy-astr.gsu.edu/Hbase/atmos/blusky.html	11
1.4	Sun and Earth emission spectrums. The spectrum of the solar radiation can be approximated by the spectrum of a black-body with a temperature of 6000 K. With this temperature, most of the radiation is emitted between 0.1 and 4 μm and the maximum of energy is reached for a wavelength of approximately 0.48 μm . The spectral distribution of the terrestrial radiation is similar to that of a black-body with a temperature of 288 K. The Earth radiates mainly in a range between 0.5 and 30 μm , and the wavelength of maximum emission is found around 10 μm . Source: http://ockhams-axe.com/global_warming	14
1.5	The global annual energy balance of the Earth. The contributions of the different components are expressed in Wm^{-2} . Straight lines represent either short-wave radiation (black) or long-wave radiation (red), and dotted lines illustrate the vertical heat transport due to evapocondensation processes (latent heat) and uprising warm air masses (sensible heat). Source http://www.hamburger-bildungsserver.de/welcome.phtml?unten=/klima/greenhouse/radiation.html , based on data from Kiehl and Trenberth [1997], Figure 1.2 in Chapter 1 "The Climate System: an Overview" of the Working Group I Report in the 2001 Intergovernmental Panel on Climate Change.	15

1.6	Global average estimates (in $\text{W}\cdot\text{m}^{-2}$) of the contributions from the different radiative forcing components of the Earth climate for the year 2005. For each component, the spatial scale and Level Of Scientific Understanding (LOSU) are presented in the right most columns. The amplitude and the uncertainty of the total net radiative effect due to the anthropogenic contribution is also available. Source: Figure SPM.2 from the Summary of Policymakers of the Working Group I Report in the 2007 Intergovernmental Panel on Climate Change.	17
1.7	Schematic illustration of aerosol radiative effects on climate including the different direct and indirect effects (modified from Haywood and Boucher [2000]). Straight lines represent shortwave radiation, and wavy lines the longwave radiation. Black dots, circles, and stars represent respectively aerosols, cloud droplets, and cloud ice crystals. The precipitation amount is related to the thickness of the grey dashed lines. Source: Figure 2.10 from Chapter 2 "Changes in Atmospheric Constituents and in Radiative Forcing" of the Working Group I Report in the 2007 Intergovernmental Panel on Climate Change.	19
1.8	Description of GEosynchronous Orbit (GEO) and Low Earth Orbit (LEO) satellites. GEO satellites have geosynchronous orbits characterized by their circularity, an altitude of 35000 km directly above the Earth's equator (0° latitude), and a period equal to the revolution period of the Earth. For an observer on the Earth surface, geostationary satellites appear motionless. Orbits of LEO satellites are commonly defined as orbits with an altitude below 2000 km. These orbits are elliptical or circular with a period of the order of a hundred minutes. Polar orbits are LEO orbits for applications with the purpose to view the same place on Earth at the same time each day. Image Credit: Reproduced with permission from Computer Desktop Encyclopedia (c) 2008 The Computer Language Company Inc.	24
2.1	Schematic representation of the scanning principle used by the MSG-SEVIRI instrument, showing the line-by-line process, the spin rate of the satellite, the spatial resolution, and the spatial coverage of the observation. Source: Figure from [Aminou, 2002].	30
2.2	Schematic representation of the illumination-viewing geometry for satellite observations: θ_s and θ_v are the sun and viewing zenith angles, ϕ_s and ϕ_v the azimuth angles for the sun and the satellite.	32
2.3	Observation geometry for MSG-SEVIRI: map of viewing zenith angle (upper panel) and viewing azimuth angle (lower panel).	34
2.4	Maps of scattering angle for MSG-SEVIRI observations for 22 June (summer solstice) and for 22 December (winter solstice) 2006.	36
2.4	Maps of scattering angle for MSG-SEVIRI observations the 22 June (summer solstice) and 22 December (winter solstice) 2006. (Con't)	37
2.5	Schematic representation of the different paths a photon from the sun beam can follow before reaching the satellite sensor.	39

2.6	Map of terrain elevation over Europe, obtained from GTOPO30 data, and remapped for the projection grid of MSG-SEVIRI.	45
2.7	Map of chlorophyll- <i>a</i> concentration over Europe for August 2006, obtained from SeaWiFS data, and remapped for the projection grid of MSG-SEVIRI.	46
3.1	Infrared Gross Temperature Test histograms over Western Europe for 29 October 2006 at 10:00 UTC, in (a) Land case and (b) Sea case. Bars in orange and blue represent the histograms including all land, and sea pixels. Green bars correspond to pixels determined as clear vegetated by test 4 (see text for further explanation).	53
3.2	Dynamic Visible Test histograms over Western Europe for 29 October 2006 at 10:00 UTC, in (a) Land case and (b) Sea case (see text for further explanation).	54
3.3	Dynamic Ratio Test histogram over Western Europe for 29 October 2006 at 10:00 UTC, as applied over sea (see text for further explanation).	55
3.4	Description of the test sequences used in TNO-CDA developed for MSG-SEVIRI, for land pixels. Rectangles represent the data corresponding to a particular group of pixels within the image. These distinctions may be derived from the result of a test, and used as an input for other tests. For the areas suspected to be cloudy by a test, the test flag is set to 1, to 0 otherwise.	56
3.5	Description of the test sequences used in TNO-CDA developed for MSG-SEVIRI, for sea pixels. Rectangles represent the data corresponding to a particular group of pixels within the image. These distinctions may be derived from the result of a test, and used as an input for other tests. For the areas suspected to be cloudy by a test, the test flag is set to 1, to 0 otherwise.	57
3.6	MSG-SEVIRI images over Western Europe for 29 October 2006 at 10:00 UTC, for the 4 channels used in the TNO cloud detection algorithm. (a) channel 1 - VIS0.6 (b) channel 2 - VIS0.8 (c) channel 9 - IR10.8 and (d) channel 10 - IR12.0.	59
3.7	Cloud test results obtained with TNO-CDA, over Western Europe for 29 October 2006 at 10:00 UTC. Each color corresponds to a different combination of tests that have all flagged the same pixel as cloudy. (see Table 3.1 for details).	61
3.8	Comparison of the KNMI/MF and TNO-CDA products over Western Europe for (a) 29 January 2006 at 11:45 UTC, (b) 1 May 2006 at 13:15 UTC, (c) 4 August 2006 at 14:00 UTC and (d) 29 October 2006 at 10:00 UTC. The meaning of the different abbreviations used in the legend are explained in Table 3.2. The percentages represented by the different colors are available in Table 3.3.	63

3.8	Comparison of the KNMI/MF and TNO-CDA products over Western Europe for (a) 29 January 2006 at 11:45 UTC, (b) 1 May 2006 at 13:15 UTC, (c) 4 August 2006 at 14:00 UTC and (d) 29 October 2006 at 10:00 UTC. The meaning of the different abbreviations used in the legend are explained in Table 3.2. The percentages represented by the different colors are available in Table 3.3. (Cont')	64
3.9	Statistical comparison of the KNMI/MF and TNO cloud detection results, over Western Europe for the 4 periods chosen in 2006 ('J', 'M', 'A', and 'O' refer to individual periods for January, May, August, and October, respectively). The abbreviations used in the legend are explained in Table 3.2.	67
3.10	Geographic distribution of the cumulative agreement (in percentage) between KNMI/MF product and TNO product, over Western Europe for one week in (a) January 2006, (b) May 2006 (c) August 2006 and (d) October 2006.	68
3.10	Geographic distribution of the cumulative agreement (in percentage) between KNMI/MF product and TNO product, over Western Europe for one week in (a) January 2006, (b) May 2006 (c) August 2006 and (d) October 2006. (Cont')	69
3.11	Comparison between MSG-SEVIRI (TNO product) and Terra-MODIS cloud detection over Western Europe for (a) 30 January 2006 at 10:00 UTC, (b) 7 May 2006 at 10:45 UTC, (c) 10 August 2006 at 10:00 UTC and (d) 29 October 2006 at 10:00 UTC. The meaning of the different abbreviations used in the legend are explained in Table 3.4. The percentage represented by the different colors are available in Table 3.5.	71
3.11	Comparison between MSG-SEVIRI (TNO product) and Terra-MODIS cloud detection over Western Europe for (a) 30 January 2006 at 10:00 UTC, (b) 7 May 2006 at 10:45 UTC, (c) 10 August 2006 at 10:00 UTC and (d) 29 October 2006 at 10:00 UTC. The meaning of the different abbreviations used in the legend are explained in Table 3.4. The percentage represented by the different colors are available in Table 3.5. (Cont')	72
3.12	Comparison between MSG-SEVIRI (KNMI product) and Terra-MODIS cloud detection over Western Europe for (a) 7 May 2006 at 10:45 UTC, (b) 10 August 2006 at 10:00 UTC and (c) 29 October 2006 at 10:00 UTC. The meaning of the different abbreviations used in the legend are explained in Table 3.6. The percentage represented by the different colors are available in Table 3.7.	75
3.12	Comparison between MSG-SEVIRI (KNMI product) and Terra-MODIS cloud detection over Western Europe for (a) 7 May 2006 at 10:45 UTC, (b) 10 August 2006 at 10:00 UTC and (c) 29 October 2006 at 10:00 UTC. The meaning of the different abbreviations used in the legend are explained in Table 3.6. The percentage represented by the different colors are available in Table 3.7. (Cont')	76

4.1	True Color image from the MODIS Terra/Aqua collection (a) and results from SARA retrievals (b,c,d) for the smoke plume from forest-fires in Portugal advected over the Atlantic Ocean on 7 August 2006 at 11:15 UTC. Map (resolution $\sim 5 \times 7 \text{ km}^2$) of (b) AOD at 635 nm, (c) Ångström coefficient 635-810 nm, and (d) weight of the Fine/Coarse mode aerosol on the AOD at 500 nm.	94
4.2	Comparison of the AOD retrieved using SARA with AERONET data at Cabo da Roca for the period 6 - 8 August 2006: (a) Timeseries (7 August 2006). (b) Scatter plots (6 - 8 August 2006). The open diamonds stand for AERONET data, the dots represent SARA retrievals, and the triangles the aerosol product for the MODIS overpass.	95
4.3	Map (resolution $\sim 10 \times 10 \text{ km}^2$) of AOD at 660 nm ('best' solution) from MODIS aerosol product (a), and comparison of the retrieved AOD from MSG-SEVIRI (11:15 UTC) and MODIS (11:10 UTC), for the smoke plume from forest-fires in Portugal advected over the Atlantic Ocean on 7 August 2006. (b) Map of the AOD difference (resolution $\sim 5 \times 5 \text{ km}^2$). (c) Density scatterplot, with the correlation coefficient, the linear regression coefficients, and the Root Mean Square Difference. (d) Histogram of the AOD difference. The dashed line in the scatterplot represents the identity line, and the solid line is the calculated regression line.	97
4.4	True Color image from the MODIS Terra/Aqua collection for the dust storm over the Mediterranean Sea on 25 February 2006 as observed at 09:00 UTC.	98
4.5	Cloud and dust detection results from SARA algorithm for the dust storm over the Mediterranean Sea on 25 February 2006 at 09:00 UTC. (a,b) Cloud Mask and (c,d) Dust Detection maps. See text for further explanation. The cloud tests indicated on the color bar in figures (a) and (b) are described in [Bennouna et al., 2008].	100
4.6	Results from SARA retrievals for the dust storm over the eastern Mediterranean on 25 February 2006 at 09:00 UTC: Map (resolution $\sim 5 \times 7 \text{ km}^2$) of (a) AOD at 1640 nm, (b) Ångström coefficient 810-1640 nm, and (c) weight of the Fine/Coarse mode aerosol on AOD at 500 nm.	102
4.7	Comparison of the AOD retrieved using SARA with AERONET data at Forth Crete for the period 24 - 26 February 2006: (a) Timeseries (26 February 2006). (b) Scatter plots (24 - 26 February 2006). The open diamonds stand for AERONET data, the dots represent SARA retrievals, and the triangles the aerosol product for the MODIS overpass.	104
4.8	Map (resolution $\sim 10 \times 10 \text{ km}^2$) of AOD at 1630 nm ('best' solution) from MODIS aerosol product for the dust storm over the Mediterranean Sea on 25 February 2006 as observed at 09:00 UTC.	105

4.9	Comparison of the retrieved AOD from MSG-SEVIRI and MODIS, for the dust storm over the Mediterranean Sea on 25 February 2006 at 09:00 UTC: (a,d) Map of the AOD difference (resolution $\sim 5 \times 5 \text{ km}^2$). (b,e) Histogram of the AOD difference. (c,f) Density scatterplot, with indication for the correlation coefficient, the linear regression coefficients, and the Root Mean Square Difference. Pictures at the top are related to SARA retrievals obtained using both 'NAM' and 'MODIS' datasets, and at the bottom using the 'OPAC' dataset. The dashed line in the scatterplot represents the identity line, and the solid line is the calculated regression line.	106
4.9	Comparison of the retrieved AOD from MSG-SEVIRI and MODIS, for the dust storm over the Mediterranean Sea on 25 February 2006 at 09:00 UTC: (a,d) Map of the AOD difference (resolution $\sim 5 \times 5 \text{ km}^2$). (b,e) Histogram of the AOD difference. (c,f) Density scatterplot, with indication for the correlation coefficient, the linear regression coefficients, and the Root Mean Square Difference. Pictures at the top are related to SARA retrievals obtained using both 'NAM' and 'MODIS' datasets, and at the bottom using the 'OPAC' dataset. The dashed line in the scatterplot represents the identity line, and the solid line is the calculated regression line. (Cont')	107
4.10	Phase Function (P_{11}) of desert dust as a function of scattering angle (Θ), simulated for a sphere (dashed lines) and a spheroid model (solid lines) with a single axis ratio of 2. The different colors indicate the wavelengths of the SEVIRI channels for which the phase function is represented.	109
4.11	Results from SARA retrievals for the dust storm over the eastern Mediterranean on 25 February 2006 at 09:00 UTC: Map (resolution $\sim 5 \times 7 \text{ km}^2$) of (a) AOD at 1640 nm, (b) Ångström coefficient 810-1640 nm, and (c) weight of the Fine/Coarse mode aerosol on AOD at 500 nm.	111
4.12	Comparison of the retrieved AOD from MSG-SEVIRI and MODIS, for the dust storm over the Mediterranean Sea on 25 February 2006 at 09:00 UTC, with the use of a non-spherical dust model: (a) Map of the AOD difference (resolution $\sim 5 \times 5 \text{ km}^2$). (b) Histogram of the AOD difference. (c) Density scatterplot, with indication for the correlation coefficient, the linear regression coefficients, and the Root Mean Square Difference. The dashed line in the scatterplot represents the identity line, and the solid line is the calculated regression line.	112
5.1	Results from SARA retrievals over Europe on 17 July 2006 at 11:15 UTC. Map (resolution $\sim 5 \times 7 \text{ km}^2$) of AOD at 635 nm.	122
5.2	Map showing the locations of the different AERONET sites used to test the SEVIRI AOD results of the SARA algorithm over land.	123

5.3	Diurnal variations of the surface reflectance inferred from the MODIS BRDF/Albedo parametrization, for SEVIRI pixels coincident with different AERONET sites in Europe for summer 2006: (a) Avignon (b) Carpentras (c) Ispra (d) Modena (e) Chilbolton (f) Cabauw (g) Mainz (h) Laegeren. Each color corresponds to a different day.	124
5.3	Diurnal variations of the surface reflectance inferred from the MODIS BRDF/Albedo parametrization, for SEVIRI pixels coincident with different AERONET sites in Europe for summer 2006: (a) Avignon (b) Carpentras (c) Ispra (d) Modena (e) Chilbolton (f) Cabauw (g) Mainz (h) Laegeren. Each color corresponds to a different day. (Cont')	125
5.4	Timeseries of the AOD retrieved using SARA at the SEVIRI pixels coincident with AERONET locations for the summer of 2006 (June, July and August): (a) Avignon (b) Carpentras (c) Ispra (d) Modena (e) Chilbolton (f) Cabauw (g) Mainz (h) Laegeren. The red diamonds stand for AERONET data, the blue dots represent SARA retrievals.	126
5.4	Timeseries of the AOD retrieved using SARA at the SEVIRI pixels coincident with AERONET locations for the summer of 2006 (June, July and August): : (a) Avignon (b) Carpentras (c) Ispra (d) Modena (e) Chilbolton (f) Cabauw (g) Mainz (h) Laegeren. The red diamonds stand for AERONET data, the blue dots represent SARA retrievals. (Cont')	127
5.5	Scatterplot of the AOD retrieved using SARA for SEVIRI pixels coincident with AERONET locations site for the summer of 2006 (June, July and August): (a) Avignon (b) Carpentras (c) Ispra (d) Modena (e) Chilbolton (f) Cabauw (g) Mainz (h) Laegeren. On each graph, the correlation coefficient and the linear regression equation are indicated. The dashed line in the scatterplot represents the identity line, and the solid line is the calculated regression line.	128
5.5	Scatterplot of the AOD retrieved using SARA for SEVIRI pixels coincident with AERONET locations for the summer of 2006 (June, July and August): : (a) Avignon (b) Carpentras (c) Ispra (d) Modena (e) Chilbolton (f) Cabauw (g) Mainz (h) Laegeren. On each graph, the correlation coefficient and the linear regression equation are indicated. The dashed line in the scatterplot represents the identity line, and the solid line is the calculated regression line. (Cont')	129
5.6	Map of AOD from (a) MSG-SEVIRI (10:45 UTC) and (b) MODIS (10:50 UTC) on 17 July 2006.	131
5.7	Comparison of the retrieved AOD from MSG-SEVIRI (10:45 UTC) and MODIS (10:45 UTC) on 17 July 2006: (a) Map of the AOD difference (resolution $\sim 5 \times 5$ km ²). (b) Histogram of the AOD difference.	132

List of Tables

1.1	Sources of natural and anthropogenic aerosols with the global annual burden of their emission (after Andreae [1995]).	3
2.1	Spectral features characterizing the SEVIRI channels.	31
3.1	Code signification for the result map of TNO cloud detection algorithm.	61
3.2	Signification of the legend abbreviations used in the comparison maps with the KNMI/MF product (Figures 3.8).	65
3.3	Extent (in pixel percentage) of the different colored areas in the comparison maps with the KNMI/MF product (Figures 3.8).	65
3.4	Meaning of the legend abbreviations used in the comparison maps with the MODIS product (Figure 3.11).	73
3.5	Extent (in pixel percentage) of the different colored areas in the comparison maps with the MODIS product (Figure 3.11).	73
3.6	Meaning of the legend abbreviations used in the comparison maps with the MODIS product (Figure 3.12).	77
3.7	Extent (in pixel percentage) of the different colored areas in the comparison maps with the MODIS product (Figure 3.12).	77
4.1	Size distribution parameters and microphysical properties for the aerosol models used to generate the different LUTs.	83
4.2	Spectral average extinction cross section (in μm^2) for the different aerosol types and wavelengths of SEVIRI.	84
4.3	Spectral single scattering albedo for the different aerosol types and wavelengths of SEVIRI.	85
4.4	Spectral asymetry parameter for the different aerosol types and wavelengths of SEVIRI.	85
4.5	Variables stored in the LUTs.	87
5.1	Size distribution parameters and microphysical properties for the aerosol models used to generate the different LUTs.	119

Curriculum Vitae

Yasmine Bennouna was born the 18 July 1978 in Rennes, France, where she lived for six years, before moving with her parents and younger sister to Marrakesh, Morocco. During the thirteen years she spent in Marrakesh, she received her primary and secondary education at the French schools, the *Ecole Renoir* and the *Lycée Victor Hugo*.

Around the age of eighteen, she completed her *Baccalauréat* (high school graduation) with a major in science, and soon after, she left for France to start her undergraduate studies. First, she followed a two-year course to prepare for the competitive examination for the French engineering schools, at both the *Lycée Vaucanson* and the *Lycée Descartes* in Tours. Then, she joined the *University of Rennes I* for one year, where she obtained a *DEUG* diploma (French diploma granted after completion of first two years of a bachelor degree) with major in *Sciences of Matter*.

In September 1999, she entered the *Institute for Engineering Sciences of Toulon (ISITV)* to prepare a Master of Science in Ocean and Coastal Engineering. While preparing for this degree, she had the opportunity to gain training experience abroad. She worked for two months as a research assistant within the *Department of Physics and Physical Oceanography* at the *Memorial University of Newfoundland (MUN)*, in Saint John's, Canada, and for six months at the *Marine Science Research Centre (MSRC)* at the *State University of New York (SUNY)* at Stony Brook, United States. During her graduate studies, she also gave private lessons in mathematics, physics and chemistry, for elementary and secondary level students. With the aim of pursuing a research career, she attended in 2004 a course within the French Research Master program (*DEA*), with emphasis on *Marine Environmental Sciences*.

One year later, she started her PhD in atmospheric physics at the *Netherlands Organisation for Applied Scientific Research (TNO)*, in The Hague. She was enrolled in the research activities of the *Electro-Optics group* of *TNO, Defence Security and Safety*, to carry out a research project in the field of satellite aerosol remote sensing. She held this position until the beginning of 2009. The related work, which is described in the present thesis, was conducted in the framework of a dual-doctoral degree program between the Dutch *Eindhoven University of Technology (TUE)* and the French *University of the South Toulon Var (USTV)*. Currently she is continuing research on the same topic within the *Atmospheric Optics Group (GOA)* at the *University of Valladolid (UVA)* in Spain.

Colophon

Text and cover of this manuscript were prepared in LateX, using the MikTeX distribution, version 2.7.

Graph and map illustrations were generated using the Matlab software, version 7.5 (R2007b).

Cover and bookmark show the picture of a child drawing, by So Long Hin, 5th price of the *17th Tunza International Children's Painting Competition on Environment* (2008), organized by the *United Nations Environment Programme (UNEP)*.